

Wireless Communications and Mobile Computing

# Antennas and Circuits for 5G Mobile Communications

Lead Guest Editor: Lei Ge

Guest Editors: Jianpeng Wang, Mingjian Li, Ting-Yen Shih, and Shichang Chen





---

# **Antennas and Circuits for 5G Mobile Communications**

Wireless Communications and Mobile Computing

---

## **Antennas and Circuits for 5G Mobile Communications**

Lead Guest Editor: Lei Ge

Guest Editors: Jianpeng Wang, Mingjian Li, Ting-Yen Shih,  
and Shichang Chen



---

Copyright © 2018 Hindawi. All rights reserved.

This is a special issue published in “Wireless Communications and Mobile Computing.” All articles are open access articles distributed under the Creative Commons Attribution License, which permits unrestricted use, distribution, and reproduction in any medium, provided the original work is properly cited.

## Editorial Board

- Javier Aguiar, Spain  
Wessam Ajib, Canada  
Muhammad Alam, China  
Eva Antonino-Daviu, Spain  
Shlomi Arnon, Israel  
Leyre Azpilicueta, Mexico  
Paolo Barsocchi, Italy  
Alessandro Bazzi, Italy  
Zdenek Becvar, Czech Republic  
Francesco Benedetto, Italy  
Olivier Berder, France  
Ana M. Bernardos, Spain  
Mauro Biagi, Italy  
Dario Bruneo, Italy  
Jun Cai, Canada  
Zhipeng Cai, USA  
Claudia Campolo, Italy  
Gerardo Canfora, Italy  
Rolando Carrasco, UK  
Vicente Casares-Giner, Spain  
Dajana Cassioli, Italy  
Luis Castedo, Spain  
Ioannis Chatzigiannakis, Greece  
Lin Chen, France  
Yu Chen, USA  
Hui Cheng, UK  
Luca Chiaraviglio, Italy  
Ernestina Cianca, Italy  
Riccardo Colella, Italy  
Mario Collotta, Italy  
Massimo Condoluci, Sweden  
Bernard Cousin, France  
Telmo Reis Cunha, Portugal  
Igor Curcio, Finland  
Laurie Cuthbert, Macau  
Donatella Darsena, Italy  
Pham Tien Dat, Japan  
André de Almeida, Brazil  
Antonio De Domenico, France  
Antonio de la Oliva, Spain  
Gianluca De Marco, Italy  
Luca De Nardis, Italy  
Alessandra De Paola, Italy  
Liang Dong, USA
- Trung Q. Duong, Sweden  
Mohammed El-Hajjar, UK  
Oscar Esparza, Spain  
Maria Fazio, Italy  
Mauro Femminella, Italy  
Manuel Fernandez-Veiga, Spain  
Gianluigi Ferrari, Italy  
Ilario Filippini, Italy  
Jesus Fontecha, Spain  
Luca Foschini, Italy  
A. G. Fragkiadakis, Greece  
Sabrina Gaito, Italy  
Óscar García, Spain  
Manuel García Sánchez, Spain  
L. J. García Villalba, Spain  
José A. García-Naya, Spain  
Miguel Garcia-Pineda, Spain  
A.-J. García-Sánchez, Spain  
Piedad Garrido, Spain  
Vincent Gauthier, France  
Carlo Giannelli, Italy  
Carles Gomez, Spain  
Juan A. Gomez-Pulido, Spain  
Ke Guan, China  
Daojing He, China  
Paul Honeine, France  
Sergio Ilarri, Spain  
Antonio Jara, Switzerland  
Xiaohong Jiang, Japan  
Minho Jo, Republic of Korea  
Shigeru Kashihara, Japan  
Dimitrios Katsaros, Greece  
Minseok Kim, Japan  
Mario Kolberg, UK  
Nikos Komninos, UK  
Juan A. L. Riquelme, Spain  
Pavlos I. Lazaridis, UK  
Tuan Anh Le, UK  
Xianfu Lei, China  
Hoa Le-Minh, UK  
Miguel López-Benítez, UK  
Martín López-Nores, Spain  
Javier D. S. Lorente, Spain  
Tony T. Luo, Singapore
- Maode Ma, Singapore  
Imadeldin Mahgoub, USA  
Pietro Manzoni, Spain  
Álvaro Marco, Spain  
Gustavo Marfia, Italy  
Francisco J. Martinez, Spain  
Davide Mattera, Italy  
Michael McGuire, Canada  
Nathalie Mitton, France  
Klaus Moessner, UK  
Antonella Molinaro, Italy  
Simone Morosi, Italy  
Kumudu S. Munasinghe, Australia  
Enrico Natalizio, France  
Keivan Navaie, UK  
Thomas Newe, Ireland  
Wing Kwan Ng, Australia  
Tuan M. Nguyen, Vietnam  
Petros Nicolaitidis, Greece  
Giovanni Pau, Italy  
Rafael Pérez-Jiménez, Spain  
Matteo Petracca, Italy  
Nada Y. Philip, UK  
Marco Picone, Italy  
Daniele Pinchera, Italy  
Giuseppe Piro, Italy  
Vicent Pla, Spain  
Javier Prieto, Spain  
Rüdiger C. Prys, Germany  
Junaid Qadir, Pakistan  
Sujan Rajbhandari, UK  
Rajib Rana, Australia  
Luca Reggiani, Italy  
Daniel G. Reina, Spain  
Abusayeed Saifullah, USA  
Jose Santa, Spain  
Stefano Savazzi, Italy  
Hans Schotten, Germany  
Patrick Seeling, USA  
Muhammad Z. Shakir, UK  
Mohammad Shojafar, Italy  
Giovanni Stea, Italy  
Enrique Stevens-Navarro, Mexico  
Zhou Su, Japan



---

Luis Suarez, Russia  
Ville Syrjälä, Finland  
Hwee Pink Tan, Singapore  
Pierre-Martin Tardif, Canada  
Mauro Tortonesi, Italy

Reza Monir Vaghefi, USA  
Juan F. Valenzuela-Valdés, Spain  
Aline C. Viana, France  
Enrico M. Vitucci, Italy  
Honggang Wang, USA

Jie Yang, USA  
Sherali Zeadally, USA  
Jie Zhang, UK  
Meiling Zhu, UK

# Contents

## **Antennas and Circuits for 5G Mobile Communications**

Lei Ge , Jianpeng Wang, Mingjian Li, Ting-Yen Shih, and Shichang Chen  
Editorial (2 pages), Article ID 3249352, Volume 2018 (2018)

## **Low-Profile Flexible UHF RFID Tag Design for Wristbands Applications**

Guan-Long Huang, Chow-Yen-Desmond Sim , Shu-Yao Liang, Wei-Sheng Liao, and Tao Yuan  
Research Article (13 pages), Article ID 9482919, Volume 2018 (2018)

## **Reconfigurable Magneto-Electric Dipole Antennas for Base Stations in Modern Wireless Communication Systems**

Lei Ge , Xujun Yang, Zheng Dong, Dengguo Zhang , and Xierong Zeng  
Review Article (8 pages), Article ID 2408923, Volume 2018 (2018)

## **A Low VSWR and High Efficiency Waveguide Feed Antenna Array**

Zhao Xiao-Fang , Liu Hua-Zhu , Li Yi, Zhou Shi-Gang, and Chow-Yen-Desmond Sim   
Research Article (7 pages), Article ID 7867091, Volume 2018 (2018)

## **A Reactance Compensated Three-Device Doherty Power Amplifier for Bandwidth and Back-Off Range Extension**

Shichang Chen, Weiwei Wang, Kuiwen Xu, and Gaofeng Wang   
Research Article (10 pages), Article ID 8418165, Volume 2018 (2018)

## **CORDIC-Based Multi-Gb/s Digital Outphasing Modulator for Highly Efficient Millimeter-Wave Transmitters**

Dixian Zhao  and Pingyang He  
Research Article (6 pages), Article ID 7216870, Volume 2018 (2018)

## **Design of a Novel Miniaturized Frequency Selective Surface Based on 2.5-Dimensional Jerusalem Cross for 5G Applications**

Peng Zhao, Yihang Zhang , Rongrong Sun, Wen-Sheng Zhao, Yue Hu, and Gaofeng Wang   
Research Article (6 pages), Article ID 3485208, Volume 2018 (2018)

## **A Doherty Power Amplifier with Large Back-Off Power Range Using Integrated Enhancing Reactance**

Wa Kong, Jing Xia , Fan Meng, Chao Yu , Lixia Yang, and Xiaowei Zhu  
Research Article (8 pages), Article ID 3968308, Volume 2018 (2018)

## **Single-Layer, Dual-Port, Dual-Band, and Orthogonal-Circularly Polarized Microstrip Antenna Array with Low Frequency Ratio**

Min Wang , Dao-Yu Wang, Wen Wu, and Da-Gang Fang  
Research Article (10 pages), Article ID 5391245, Volume 2018 (2018)

## **Magnetolectric Dipole Antenna with Dual Polarization and High Isolation**

Xujun Yang, Lei Ge , Dengguo Zhang , and Chow-Yen-Desmond Sim   
Research Article (7 pages), Article ID 4765425, Volume 2018 (2018)

**A Wide Stopband Balun Bandpass Filter with Its Application to Balanced Quasi-Yagi Antenna**

Gang Zhang , Zhenyao Qian, Yushou Chen , and Yang Zhao 

Research Article (7 pages), Article ID 4725072, Volume 2018 (2018)

**A Compact Differential-Mode Wide Stopband Bandpass Filter with Good and Wideband Common-Mode Suppression**

Gang Zhang , Yang Zhao , and Wei Yan

Research Article (4 pages), Article ID 4032183, Volume 2018 (2018)

**Uplink Multiuser MIMO-OFDM System in the Presence of Phase Noises, Power Imbalance, and Correlation**

Xiaoming Chen , Andreas Wolfgang, and Tommy Svensson 

Research Article (8 pages), Article ID 3650307, Volume 2018 (2018)

**Impact of Probe Configurations on Maximum of Test Volume Size in 3D MIMO OTA Testing**

Weimin Wang, Huaqiang Gao, Yongle Wu, and Yuanan Liu

Research Article (9 pages), Article ID 2716149, Volume 2017 (2018)

## Editorial

# Antennas and Circuits for 5G Mobile Communications

**Lei Ge** <sup>1</sup>, **Jianpeng Wang**,<sup>2</sup> **Mingjian Li**,<sup>3</sup> **Ting-Yen Shih**,<sup>4</sup> and **Shichang Chen**<sup>5</sup>

<sup>1</sup>College of Electronic Science and Technology, Shenzhen University, Shenzhen, China

<sup>2</sup>Ministerial Key Laboratory of JGMT, Nanjing University of Science and Technology, Nanjing, China

<sup>3</sup>Department of Electrical and Computer Engineering, University of Wisconsin-Madison, Madison, USA

<sup>4</sup>Department of Electrical and Computer Engineering, University of Idaho, Moscow, USA

<sup>5</sup>Key Laboratory of RF Circuits and Systems of the Ministry of Education of China, Microelectronic CAD Center, Hangzhou Dianzi University, Hangzhou, China

Correspondence should be addressed to Lei Ge; [leige@szu.edu.cn](mailto:leige@szu.edu.cn)

Received 15 May 2018; Accepted 15 May 2018; Published 7 June 2018

Copyright © 2018 Lei Ge et al. This is an open access article distributed under the Creative Commons Attribution License, which permits unrestricted use, distribution, and reproduction in any medium, provided the original work is properly cited.

With the blooming of wireless technologies for communications, the fifth-generation (5G) mobile communications have become one of the hottest topics in recent years. For any wireless devices and systems, antennas, filters, amplifiers, mixers, and so on are crucial components for the RF front-end. Thus the demand for different kinds of advanced and high-performance antennas and circuits is increasing exponentially. However, most conventional designs have difficulty to satisfy those stringent requirements of the 5G mobile communications on bandwidth, radiation pattern, size, and cost. High-performance antennas and circuits for 5G mobile applications are therefore very attractive for researchers from both academic and industrial areas. This special issue solicits high-quality contributions regarding the design of microwave and millimeter-wave antennas and circuits for the upcoming communication systems.

In this special issue, we have 5 papers investigating antennas for 5G mobile communications. Specifically, in “Reconfigurable Magneto-Electric Dipole Antennas for Base Stations in Modern Wireless Communication Systems”, the authors reviewed several reconfigurable directional antennas for base station applications. The results showed that magneto-electric dipole antennas provide wide bands, high gains, and well-controlled radiation patterns and are suitable to be employed in reconfigurable base station antennas.

In “Magnetolectric Dipole Antenna with Dual Polarization and High Isolation”, the authors aimed at modeling and analyzing a novel dual-polarized antenna element which was suitable to be applied in the further 5G mobile base stations.

The work in the paper titled “Single-Layer, Dual-Port, Dual-Band, and Orthogonal-Circularly Polarized Microstrip Antenna Array with Low Frequency Ratio” proposed a method to realize an orthogonal-circularly polarized antenna array with dual bands.

The paper with the title of “A Low VSWR and High Efficiency Waveguide Feed Antenna Array” introduced a high-efficiency slot antenna array by using waveguide feed. The radiation efficiency could achieve as high as larger than 80%.

The paper “Low Profile Flexible UHF RFID Tag Design for Wristbands Applications” presented a low profile RFID tag antenna for healthcare applications. The proposed slotted design can easily allow the tag’s input impedance to be tuned to the complex impedance of typical UHF RFID chips.

In this special issue, we have 4 papers investigating passive and active radio-frequency (RF) circuits for 5G communications. Specifically, in “A Reactance Compensated Three-Device Doherty Power Amplifier for Bandwidth and Back-Off Range Extension”, the authors proposed a new broadband Doherty power amplifier topology with extended back-off range. Underlying bandwidth extension mechanism of the proposed configuration was comprehensively analyzed.

In the paper titled “A Doherty Power Amplifier with Large Back-Off Power Range Using Integrated Enhancing Reactance”, a symmetric Doherty power amplifier based on integrated enhancing reactance (IER) was proposed for large back-off applications.

The work in “A Compact Differential-Mode Wide Stopband Bandpass Filter with Good and Wideband Common-Mode Suppression” aimed at presenting a new coupling topology to realize a differential-mode bandpass filter by integrating a pair of half-wavelength microstrip transmission lines and two multimode resonators.

In the paper with the title of “A Wide Stopband Balun Bandpass Filter with Its Application to Balanced Quasi-Yagi Antenna”, the authors utilize the out-of-phase open-ended microstrip line and the resonant characteristics of the triple-mode resonators to realize a new microstrip balun bandpass filter with a wide stopband.

In this special issue, 2 papers aim at RF systems for 5G mobile communications. In “Uplink Multiuser MIMO-OFDM System in the Presence of Phase Noises, Power Imbalance, and Correlation”, the effects of phase noises (PNs), power imbalances, and correlations on multiuser orthogonal frequency division multiplexing (OFDM) multiple-input multiple-output (MIMO) systems were studied. And the analytical results were verified by simulations.

The paper “CORDIC-Based Multi-Gb/s Digital Outphasing Modulator for Highly Efficient Millimeter-Wave Transmitters” described a high-speed CORDIC-based digital outphasing modulator. The complete outphasing modulator was fully custom designed in 40 nm CMOS, which could be integrated in a millimeter-wave outphasing transmitter to enhance the system average efficiency. Tested with 10.56 Gb/s 64-QAM, the presented work achieved an EVM of 3.2% and fulfilled the IEEE 802.11ad spectral mask requirements.

Two other papers of this special issue investigate over-the-air (OTA) test of MIMO technology and frequency selective surfaces for 5G applications, respectively. Specifically, the paper “Impact of Probe Configurations on Maximum of Test Volume Size in 3D MIMO OTA Testing” presented a method to determine the maximum of test volume size (MTVS) and investigated the impact of probe configurations on MTVS in order to obtain larger MTVS in the OTA testing.

In the paper “Design of a Novel Miniaturized Frequency Selective Surface Based on 2.5-Dimensional Jerusalem Cross for 5G Applications”, a compact frequency selective surface (FSS) for the application to 5G antenna radomes was proposed based on 2.5-dimensional Jerusalem cross.

*Lei Ge  
Jianpeng Wang  
Mingjian Li  
Ting-Yen Shih  
Shichang Chen*

## Research Article

# Low-Profile Flexible UHF RFID Tag Design for Wristbands Applications

Guan-Long Huang,<sup>1</sup> Chow-Yen-Desmond Sim ,<sup>2</sup> Shu-Yao Liang,<sup>3</sup>  
Wei-Sheng Liao,<sup>2</sup> and Tao Yuan<sup>4</sup>

<sup>1</sup>ATR National Key Lab. of Defense Technology, College of Information Engineering, Shenzhen University, Shenzhen 518060, China

<sup>2</sup>Department of Electrical Engineering, Feng Chia University, Taichung 40724, Taiwan

<sup>3</sup>Master's Program, College of Information and Electrical Engineering (Industrial R&D), Feng Chia University, Taichung, Taiwan

<sup>4</sup>College of Information Engineering, Shenzhen University, Shenzhen 518060, China

Correspondence should be addressed to Chow-Yen-Desmond Sim; [cysim@fcu.edu.tw](mailto:cysim@fcu.edu.tw)

Received 14 December 2017; Revised 4 April 2018; Accepted 7 May 2018; Published 7 June 2018

Academic Editor: Mingjian Li

Copyright © 2018 Guan-Long Huang et al. This is an open access article distributed under the Creative Commons Attribution License, which permits unrestricted use, distribution, and reproduction in any medium, provided the original work is properly cited.

In this study, a low-profile ultrahigh frequency (UHF) radio-frequency identification (RFID) tag antenna designed for wristbands in healthcare applications is proposed. The radiator is based on the open-slot cavity technique that is composed of a slotted patch (double-T slots) loaded onto a flexible open cavity. The proposed slotted design can easily allow the tag's input impedance to be tuned to the complex impedance of typical UHF RFID chips. The proposed tag antenna has a size of  $86 \text{ mm} \times 25 \text{ mm} \times 1.6 \text{ mm}$  ( $0.26\lambda_0 \times 0.07\lambda_0 \times 0.004\lambda_0$ ) at 915 MHz, and it can yield a maximum reading range of 8 m (stand alone in free-space condition), 6.6 m (when placed on the human wrist in free-space condition), and up to 3 m (when placed on the human wrist in a crowded condition).

## 1. Introduction

The long-term health care system has been the topic of interest discussed in recent years, and it is also now one of the most important issues in highly developed region, because the health care system in many countries has not been yet fully designed to cope with their long-term care issues. Therefore, there is a need to develop a good RFID tracking system that may require wearable devices such as a flexible RFID tag that can be used as a wristband for the patients.

In order to design an appropriate wearable RFID tag, it must be flexible and able to withstand the human body effects (or also known as on-body effects). Because of the complexity in dielectric constant within the human body (for example skin, fat, muscle, and bones), it will absorb or mitigate the electromagnetic (EM) wave emitted/received by the RFID tag. Furthermore, if the wearable RFID tag is in close proximity or directly in contact with the human body

(on-body), the electrical wavelength, impedance matching, and radiation efficiency of the RFID tag will be deteriorated [1, 2]. The effects on the realized gain of an RFID tag when attached onto different body regions (arm, forearm, forehead, neck, abdomen, and stern) of a thin female volunteer were reported in [3], and they show that the stern region has the worst gain, whereas the leg region has the best gain, because of the larger content of fat tissues.

Due to the on-body effects, many different methods and techniques have been proposed to improve the performances (e.g., gain and reading range) of the RFID tag when it is at on-body condition [4, 6–12]. The easiest way to improve the reading range for on-body RFID tag monitoring application is to use an active RFID tag assisted by battery as reported in [6]; however, such method will increase the cost and thickness (profile) of the RFID tag. To achieve passive on-body RFID tag (without the assistance of battery), a planar tag antenna that is based on a suspended patch fed via a nested slot has been investigated in [7]. Even though the layout of [7]

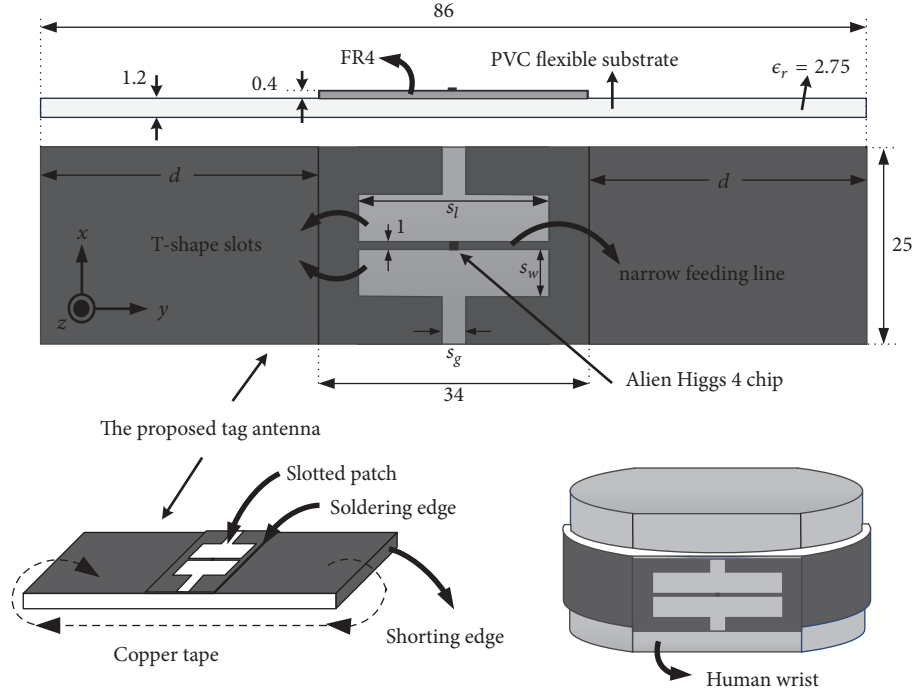


FIGURE 1: Geometry of the proposed tag antenna, and when it is attached to a human wrist,  $d = 26$ ,  $s_l = 24$ ,  $s_w = 6$ ,  $s_g = 3$ . Unit: mm.

allows it to host the sensors and the slot design can be easily tuned to achieve good inductive reactance, the antenna must be electrically isolated from the skin via a 4 mm thick silicone substrate. A balanced slot-antenna concept was studied in [8] for complex environment (e.g., meat, water); however, the planar size of this tag antenna is 120 mm  $\times$  30 mm. To achieve a reading range of approximately 3.9 m (effective isotropic radiated power, EIRP 4W) when attached to the stern of a human body, a four-element PIFA array tag has been reported [9], and it has a planar size of 85.5 mm  $\times$  54 mm.

Recently, the technique of applying open-slot cavity technique for achieving on-body RFID tag designs has been reported [10–12]. To achieve compact size of 40 mm  $\times$  50 mm  $\times$  3 mm ( $0.12\lambda_0 \times 0.14\lambda_0 \times 0.01\lambda_0$ ), the work in [10] has applied the vertical folded coupled shorted patch cavity technique, in which when attached to a human chest can achieve reading range of up to 5.1 m (EIRP 4W). As for the cavity-slot design in [11], the patches are etched on 0.4 mm thin FR4 substrate and loaded on a 1.4 mm thick foam substrate. Nevertheless, the dimensions of [11] are 116 mm  $\times$  40 mm and when attached to a human abdomen can achieve maximum reading range ( $R_{max}$ ) of up to 3.5 m (EIRP 4W). As far as the author's concern, very few authors have investigated on passive RFID tag that can be applied on the wristband of a human body. In [12], two tapered structures were used to form an open-cavity structure. To achieve small size characteristics of 51.1 mm  $\times$  21.3 mm  $\times$  0.64 mm, [12] has used high dielectric constant substrate (ARLON AD1000,  $\epsilon_r = 10.2$ ), and, when attached to a human wrist, it can only yield  $R_{max}$  of up to 2.1 m (EIRP 3.23W). Nevertheless, there is no detailed reported work that has integrated a flexible wristband to a passive RFID tag that can yield  $R_{max}$  of up to 4 m with EIRP  $<$  3W.

Therefore, in this paper, an extension of the work reported in [11] is proposed in this paper. Instead of using a rigid substrate, the slotted patch that is etched on 0.4 mm thin FR4 substrate is loaded onto a thin 1.2 mm flexible PVC (PolyVinyl Chloride) plastic substrate ( $\epsilon_r = 2.75$ ), and the open-slot cavity is formed by covering the PVC with adhesive copper tape. The advantages of this extended work as compared to the ones in [11, 12] include the following: (1) simple structure design and compact in size, (2) the wristband being flexible, and (3) ease in achieving the desired resonant frequency and impedance matching by simply tuning the slot parameters. Details of the antenna design and its corresponding simulation and measurement results (in free-space and wristband conditions) will be discussed further.

## 2. Antenna Structure

As aforementioned, the proposed tag antenna proposed here is an extension of the work in [11], and its geometry (including how it is attached to a human wrist) is defined in Figure 1. Here, the bottom surface (ground) of the flexible substrate is fully metalized by using the adhesive copper tape, and the two open-ends of this ground are shorted to the two rectangular copper tapes attached on the top surface (left and right sections, each has size of 26 mm  $\times$  25 mm) of the PVC. Thereafter, the two open-ends of these two copper tapes (top left and right sections) are then soldered to the two open edges of the slotted patch. By shorting the top and bottom metallic surfaces (see Figure 1), the achieved inductive reactance will compensate the tag chip's capacitive reactance.

As indicated in Figure 1, the slotted patch is formed by loading two symmetrical T-shaped slots into a 34 mm  $\times$

TABLE 1: Various electrical properties of human wrist/arm phantom at 915 MHz.

	Dielectric Constant	Loss Tangent	Conductivity (S/m)
Skin (dry)	41.3	0.415	0.87
Fat	5.46	0.185	0.05
Muscle	55	0.339	0.94
Bone Cortical	12.44	0.229	0.145
Bone Cancellous	20.75	0.325	0.34
Bone Marrow	5.5	0.145	0.04

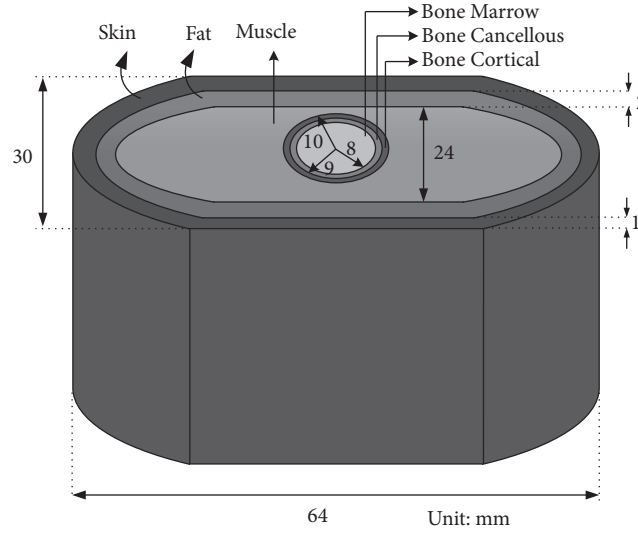


FIGURE 2: Various parameters (skin, fat, muscle, and bones) with reference to a human wrist/arm [4, 5] and its corresponding geometry.

25 mm rectangular patch. Each T-shaped slot is comprised of a vertical (6 mm  $\times$  3 mm) slot and a horizontal (6 mm  $\times$  24 mm) slot section. Therefore, a very narrow (1 mm) feeding line is formed between the two T-shaped slots, which is designated for connecting to the tag chip (Alien Higgs 4, SOT232 package,  $Z = 8 - j142 \Omega$ ). It is noteworthy that the two T-shaped slots also provide an extra degree of freedom to tune to the desired conjugate match and working frequency. The geometry of how the proposed wristband tag antenna is attached to a human wrist is also shown in Figure 1. The exact detailed structure of a human wrist/arm (skin, fat, muscle, and bones) phantom at 915 MHz, corresponding to its geometry such as substrate layers and thickness, is shown in Figure 2 [4, 5]. Its various electrical properties such as dielectric constant, loss tangent, and conductivity are also shown in Table 1. All simulations performed in this work are via the commercially available (high frequency structure simulator) HFSS software.

### 3. Results and Discussion

Figure 3 shows the simulated and measured return losses of the proposed tag antenna in planar form (free-space condition, FSC). The simulated and measured return losses when attaching this tag antenna to a human wrist are also plotted in this figure. When comparing the impedance

bandwidths, the simulated 6-dB return loss bandwidth in FSC was 5.2% (0.89–0.938 GHz), while the measured one was 3.9% (0.9–0.936 GHz). The slight differences between the two results may be due to fabrication tolerance and unexpected effects, especially when the slotted patch was soldered to the two copper tapes located on the top surface of the PVC. Nonetheless, the measured resonant mode of the proposed one in FSC was 914 MHz, while the measured one on human wrist was slightly lower at 904 MHz. Notably, the simulated 6-dB return loss bandwidth of proposed tag antenna attached to human wrist was 6.2% (0.88–0.937 GHz), and its corresponding measured one was 5.3% (0.88–0.928 GHz). Here, the differences between the two results can be attributed to the under estimated parameters (dielectric constant, loss tangent, and conductivity) given in [4, 5]. Furthermore, as shown in Figure 4, the measurement that we have conducted was by applying the 1/4 wavelength balun technique studied in [13], which may yield slight inaccuracy during actual measurement.

To validate the above results, Figures 5(a) and 5(b) show the input resistance and reactance of the proposed tag antenna, respectively, corresponding to the ones shown in Figure 3. As depicted in Figure 5(a), even though the results for the measured input resistance in FSC and human wrist are higher (approximately 9.3  $\Omega$  and 13  $\Omega$ , respectively) than the tag chip resistance (8  $\Omega$ ), their respective reactance as shown

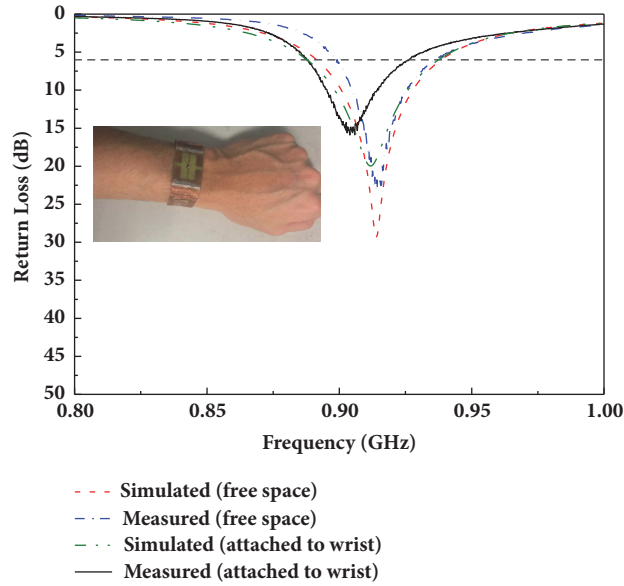


FIGURE 3: Simulated and measured return losses of the proposed tag antenna at free-space (planar form) and attached to wrist conditions.

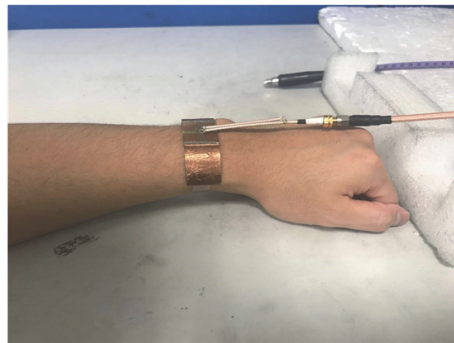


FIGURE 4: Measurement of the proposed tag antenna on human wrist by applying the 1/4 wavelength balun technique [13].

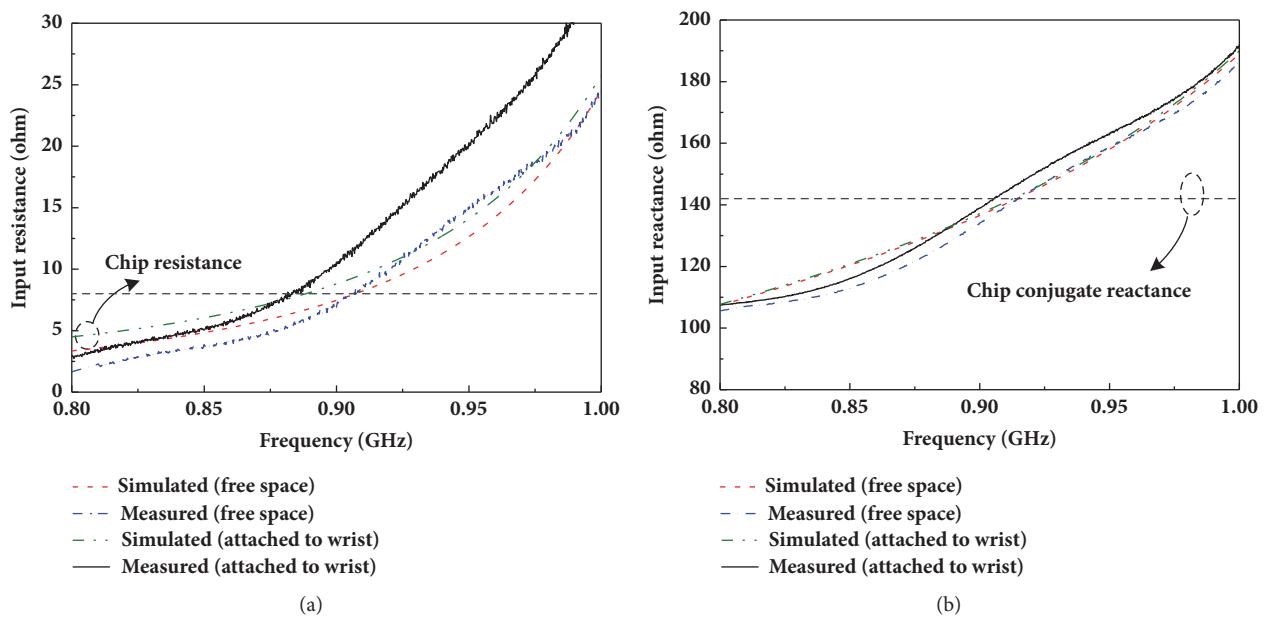


FIGURE 5: Simulated and measured input impedance of the proposed tag antenna in FSC and when attached to human wrist: (a) resistance and (b) reactance.

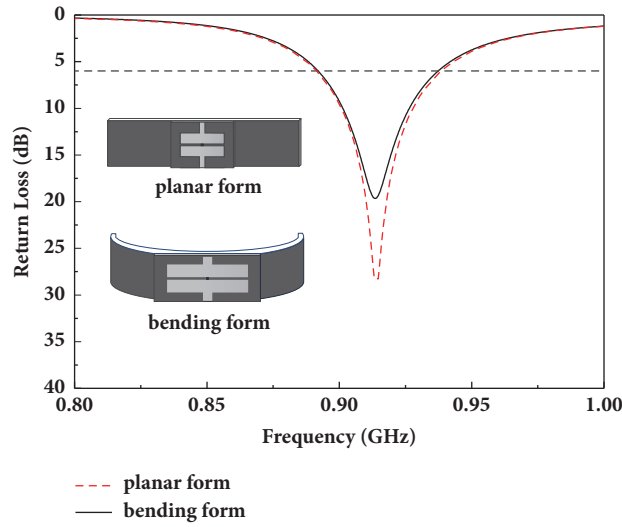


FIGURE 6: Simulated return losses of the proposed tag antenna in FSC and in planar form and bending form.

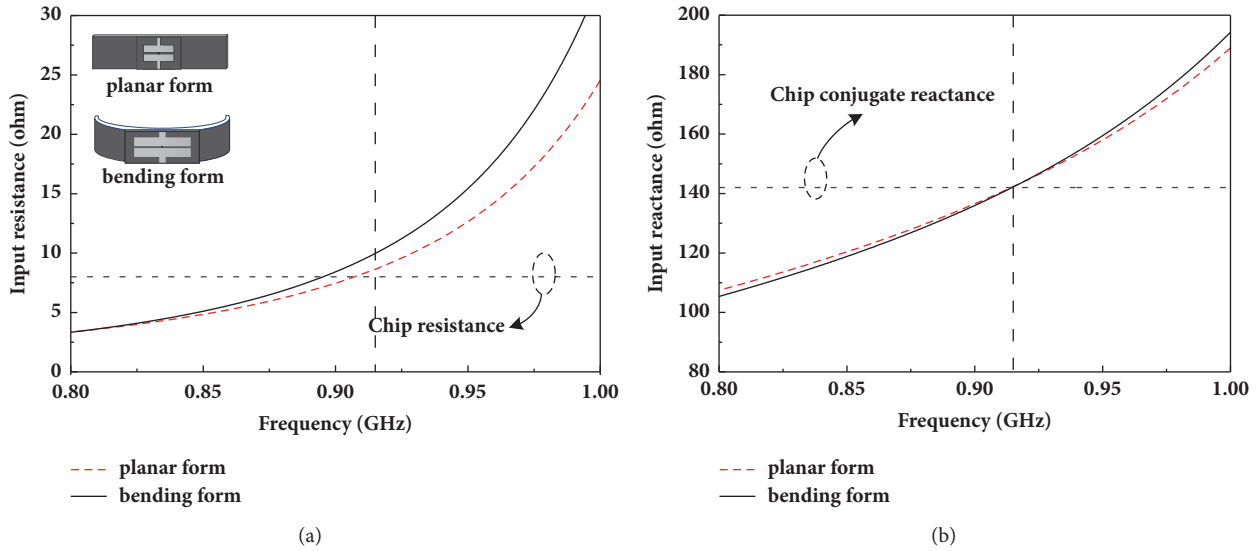


FIGURE 7: Simulated input resistance and reactance of proposed tag antenna in FSC in planar form and bending form.

in Figure 5(b) is very much well conjugate with the tag chip reactance ( $-j142 \Omega$ ) at around 915 MHz.

**3.1. Effects of Bending the Tag Antenna.** Figure 6 shows the simulated return losses of proposed antenna in FSC, when the antenna is simply a planar type (no bending) and when it is bent to conform to a normal human wrist. As depicted in this figure, bending the proposed tag antenna will only slightly affect the impedance matching, which can be clearly explained in Figure 7(a), showing a slightly deviated input resistance value at around 915 MHz, whereas its corresponding reactance remains unchanged, as shown in Figure 7(b).

**3.2. Effects of Tuning the Parameter  $d$ .** To allow this proposed tag antenna to be able to work across the desired UHF RFID

frequency band (902–928 MHz), it is important to identify the one parameter of the tag antenna structure that can easily aid in tuning the excited resonant frequency. As depicted in Figure 8, it is realized that increasing parameter  $d$  from 24 mm to 28 mm (with a step increment of 2 mm), meaning also that the total length of tag antenna will also be increased from 82 mm to 90 mm, can allow linear shifting of the resonant frequency to the lower frequency from 950 MHz to 880 MHz. To further understand this phenomenon, the simulated input resistance and input reactance of the proposed tag antenna when tuning parameter  $d$  are also presented in Figures 9(a) and 9(b), respectively. By further observing these two figures, it is also realized that increasing  $d$  will linearly decrease both the input resistance and reactance of the proposed tag antenna, respectively, which explains the shift to the lower frequency band.

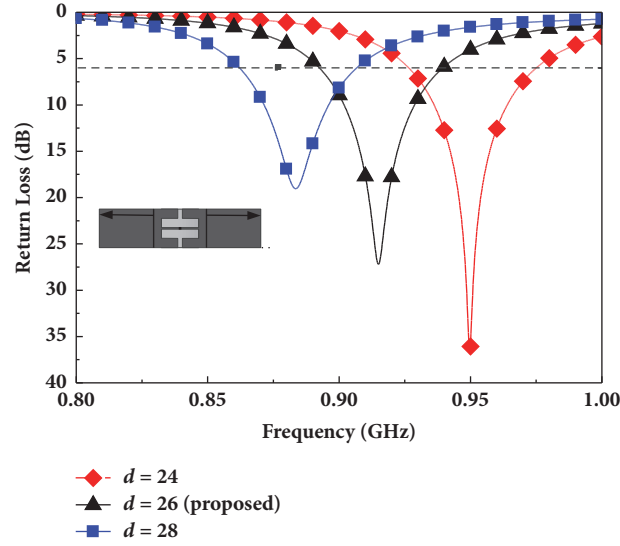


FIGURE 8: Simulated return losses of the proposed tag antenna when tuning parameter  $d$ . Unit: mm.

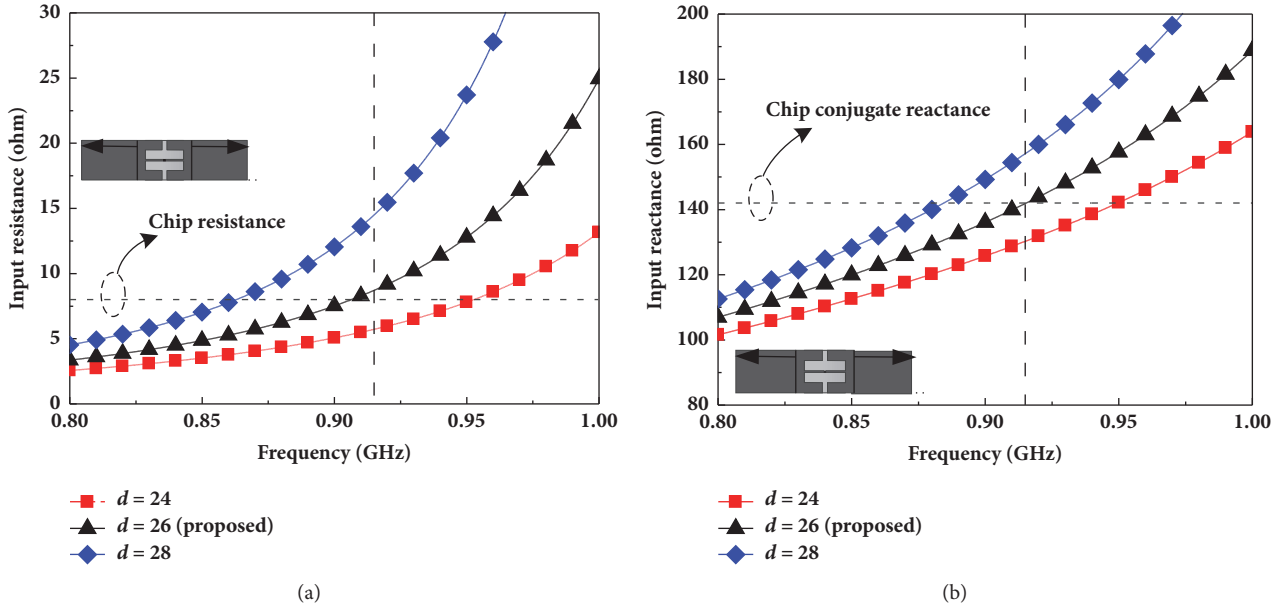


FIGURE 9: Simulated impedance of proposed tag antenna when tuning parameter  $d$ , (a) input resistance and (b) input reactance. Unit: mm.

As for the reason why increasing the parameter  $d$  can decrease the resistance and reactance, one can see from Figure 1 that the proposed tag antenna is a folded type, thus, increasing parameter  $d$  which will also increase the folded surface area (top and bottom), resulting in an increase in capacitive reactance. Thus, once the capacitive reactance ( $X_C$ ) is increased, the inductive reactance ( $X_L$ ) of this proposed tag antenna will be decreased. As the inductive reactance  $X_L = 2\pi f L$ , a decrease in  $X_L$  will obviously result in a decreased frequency. Notably, reducing the overall reactance of the proposed tag antenna by increasing parameter  $d$  may be the main reason why the resistive value is also decreased. Another explanation can also be related to the electrical wavelength, which indicates that the longer the electrical

length (including the length  $d$ ), the longer the wavelength, thus achieving lower frequency.

Therefore, this proposed tag antenna has possessed the advantage of ease in tuning the resonance frequency.

**3.3. Effects of Tuning Parameter  $S_l$ .** As aforementioned, the slotted patch is responsible for tuning the impedance matching of the proposed tag antenna. As the slotted patch is composed of two symmetrical T-shaped slots, tuning any of its slots' parameters ( $S_l$ ,  $S_w$ , and  $S_g$ ) requires both T-shaped slots to be tuned at the same time; however, the width of narrow feeding line must remain constant at 1 mm for ease in attaching the tag chip that has the same width of 1 mm. The simulated effects of tuning the parameter  $S_l$  are first

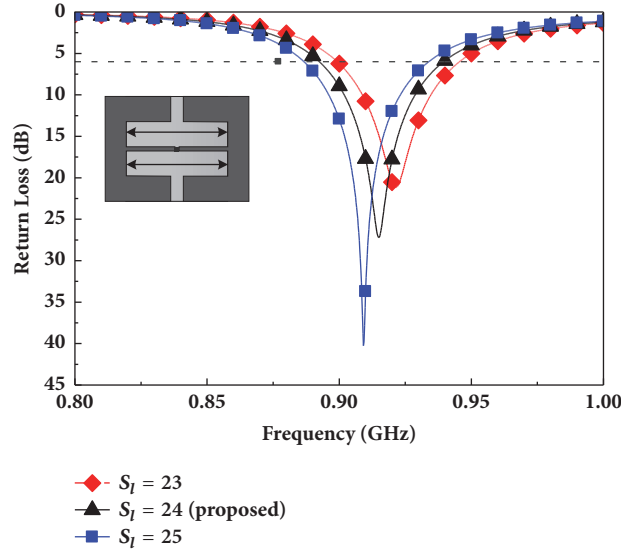


FIGURE 10: Simulated return losses of the proposed tag antenna when tuning parameter  $S_l$ . Unit: mm.

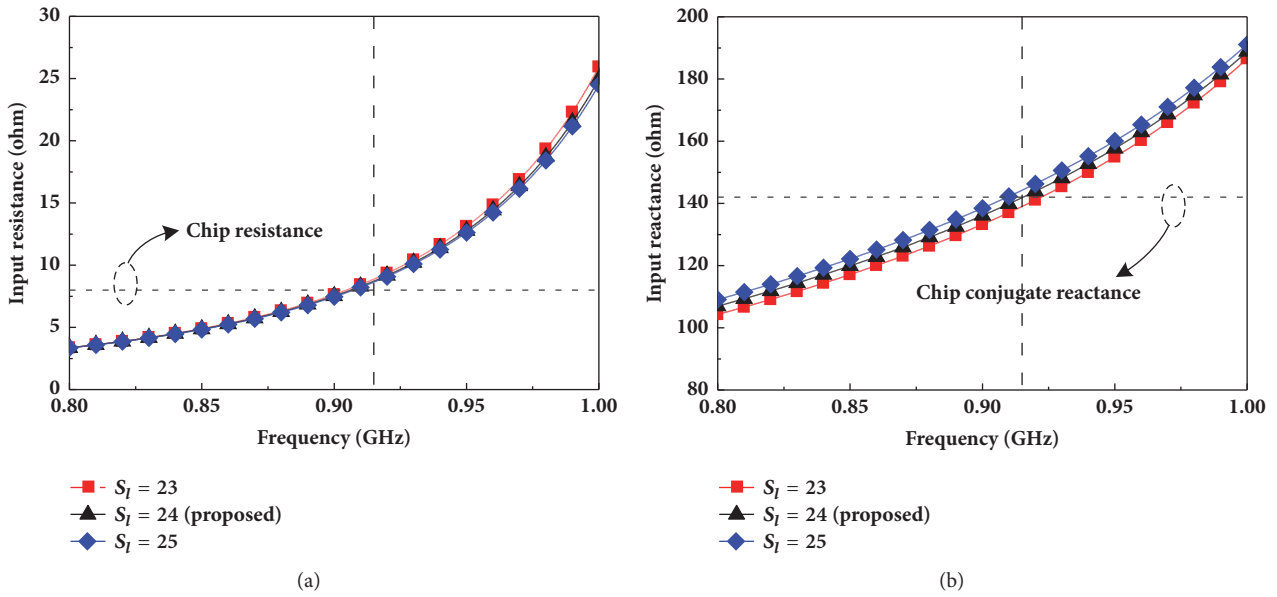


FIGURE 11: Simulated impedance of proposed tag antenna when tuning parameter  $S_l$ , (a) input resistance and (b) input reactance. Unit: mm.

investigated and shown in Figures 10 and 11, while the other two parameters ( $S_w$ , and  $S_g$ ) remain constant.

As depicted in Figure 10, it is realized that increasing parameter  $S_l$  from 23 mm to 25 mm (with a step increment of 1 mm) can allow linear shifting of the resonant frequency to the lower frequency from 921 MHz to 909 MHz. Its corresponding simulated input resistance and input reactance are also plotted in Figures 11(a) and 11(b), respectively. By further observing these two figures, it is realized that tuning  $S_l$  will not affect the input resistance values at 915 MHz, but rather the input reactance at 915 MHz has slightly raised as  $S_l$  increases. In addition to that, the entire input reactance has

shifted to the lower frequency, which validated with the trend observed in Figure 10.

**3.4. Effects of Tuning Parameter  $S_w$ .** Figure 12 shows the effects on the return losses of the proposed tag antenna when increasing the slot's parameter  $S_w$  from 5 mm to 7 mm (with a step increment of 1 mm). Here, increasing  $S_w$  will allow slight linear shifting of the resonant frequency to the upper frequency from 906 MHz to 923 MHz. To further understand this phenomenon, the simulated input resistance and input reactance of the proposed tag antenna when tuning parameter  $S_w$  are also presented in Figures 13(a) and 13(b),

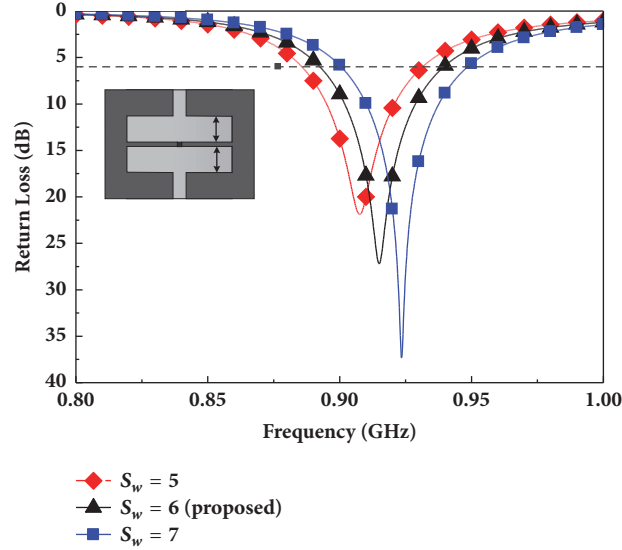


FIGURE 12: Simulated return losses of the proposed tag antenna when tuning parameter  $S_w$ . Unit: mm.

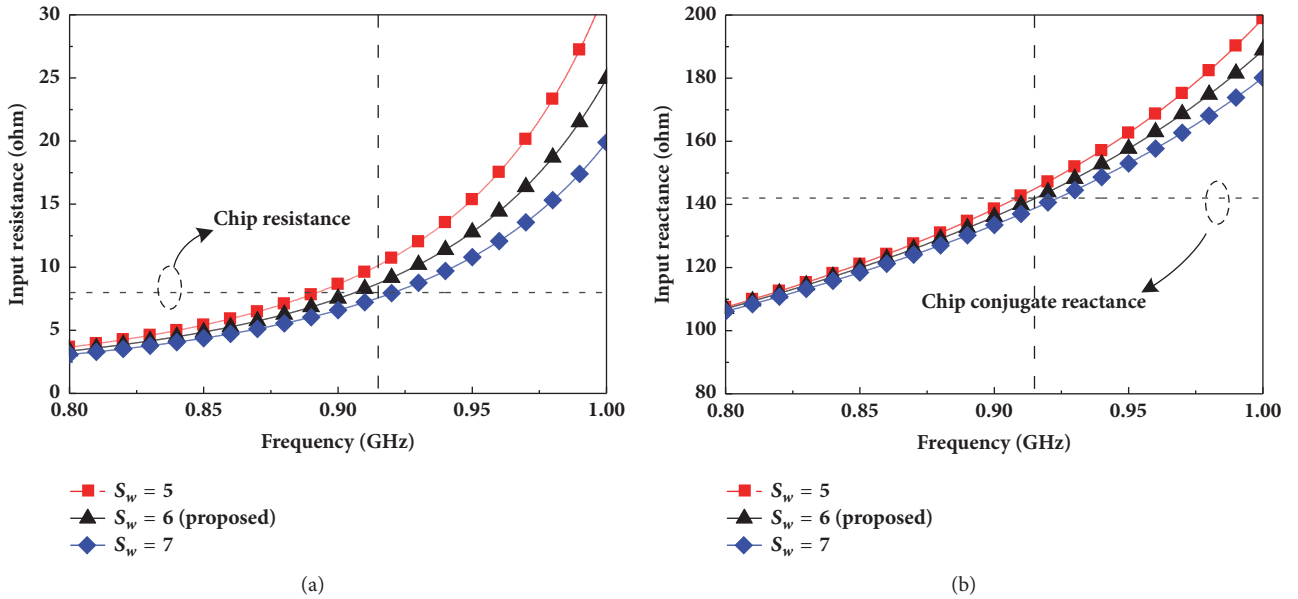


FIGURE 13: Simulated impedance of proposed tag antenna when tuning parameter  $S_w$ . (a) Input resistance and (b) input reactance. Unit: mm.

respectively. By further observing these two figures, it is also realized that increasing  $S_w$  will linearly shift the entire input resistance and reactance of the proposed tag antenna to the higher frequency band.

**3.5. Effects of Tuning Parameter  $S_g$ .** The effects on the return losses of the proposed tag antenna when increasing the slot's parameter  $S_g$  from 2 mm to 4 mm (with a step increment of 1 mm) are shown in Figure 14. In this figure, it is realized that increasing parameter  $S_g$  can allow linear shifting of the resonant frequency to the higher frequency from 910 MHz to 920 MHz. From its corresponding simulated input resistance and input reactance plotted in Figures 15(a) and

15(b), respectively, it is also realized that increasing  $S_g$  will also linearly shift the entire input resistance and reactance of the proposed tag antenna to the higher frequency band.

Therefore, from the above parametric results, the following conclusions can be drawn: (1) tuning  $d$  can easily achieve good resonant frequency and operating bands across the entire UHF RFID band in EPC Gen 2 (Electronic Product Code Generation 2, 860–960 MHz), (2) tuning  $S_l$  will only affect the input reactance while the input resistance remains constant, and (3) tuning both  $S_w$  and  $S_g$  will affect input reactance and resistance values.

**3.6. Simulated Radiation Patterns.** The simulated radiation patterns at 915 MHz (in three different principle planes) of

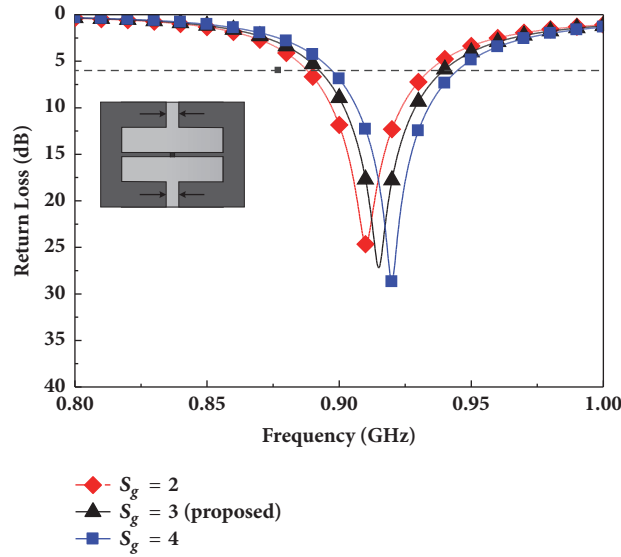


FIGURE 14: Simulated return losses of the proposed tag antenna when tuning parameter  $S_g$ . Unit: mm.

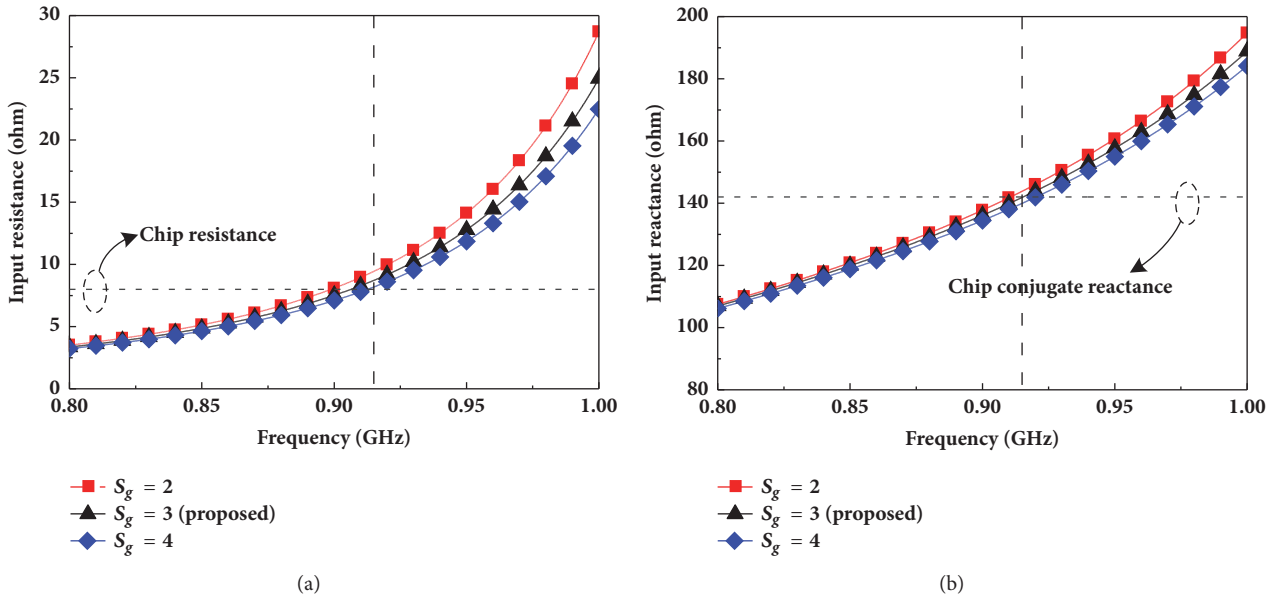


FIGURE 15: Simulated impedance of proposed tag antenna when tuning parameter  $S_g$ , (a) input resistance and (b) input reactance. Unit: mm.

the proposed tag antenna in planar form and attached to a human wrist phantom (indicated in Figure 2 and Table 1) are shown in Figures 16 and 17, respectively, and all values are normalized with respect to their peak gain. As shown in Figure 16, good omnidirectional patterns for  $E_\phi$  were observed in the  $x$ - $z$  plane, while good broadside patterns in the  $\pm z$  directions were observed for  $E_\theta$  in the  $y$ - $z$  plane. Obvious bidirectional patterns were also observed in its corresponding  $x$ - $y$  plane. As depicted in Figure 17, both the  $x$ - $z$  and  $y$ - $z$  planes have shown an obvious decrease in signal strength (approximately 5 to 6 dB) in the  $-z$  direction ( $\theta = 180^\circ$ ) as compared with its corresponding boresight direction

( $+z, \theta = 0^\circ$ ). By comparing these two figures, it can be denoted that the human wrist can absorb the signal strength (EM wave) that is propagating towards the wrist (in the  $-z$  direction). Furthermore, the boresight signal strength (or peak gain at  $+z$  direction) has also been reduced from  $-4.62$  dBi to  $-6.87$  dBi, due to the effects of the human wrist.

**3.7. Measured Maximum Reading Range of Proposed Tag Antenna.** To perform the maximum reading range ( $R_{max}$ ) of this proposed tag antenna in a more accurate manner, two experiments were setup via a commercially available equipment known as “Voyantic Tagformance Pro”, which is

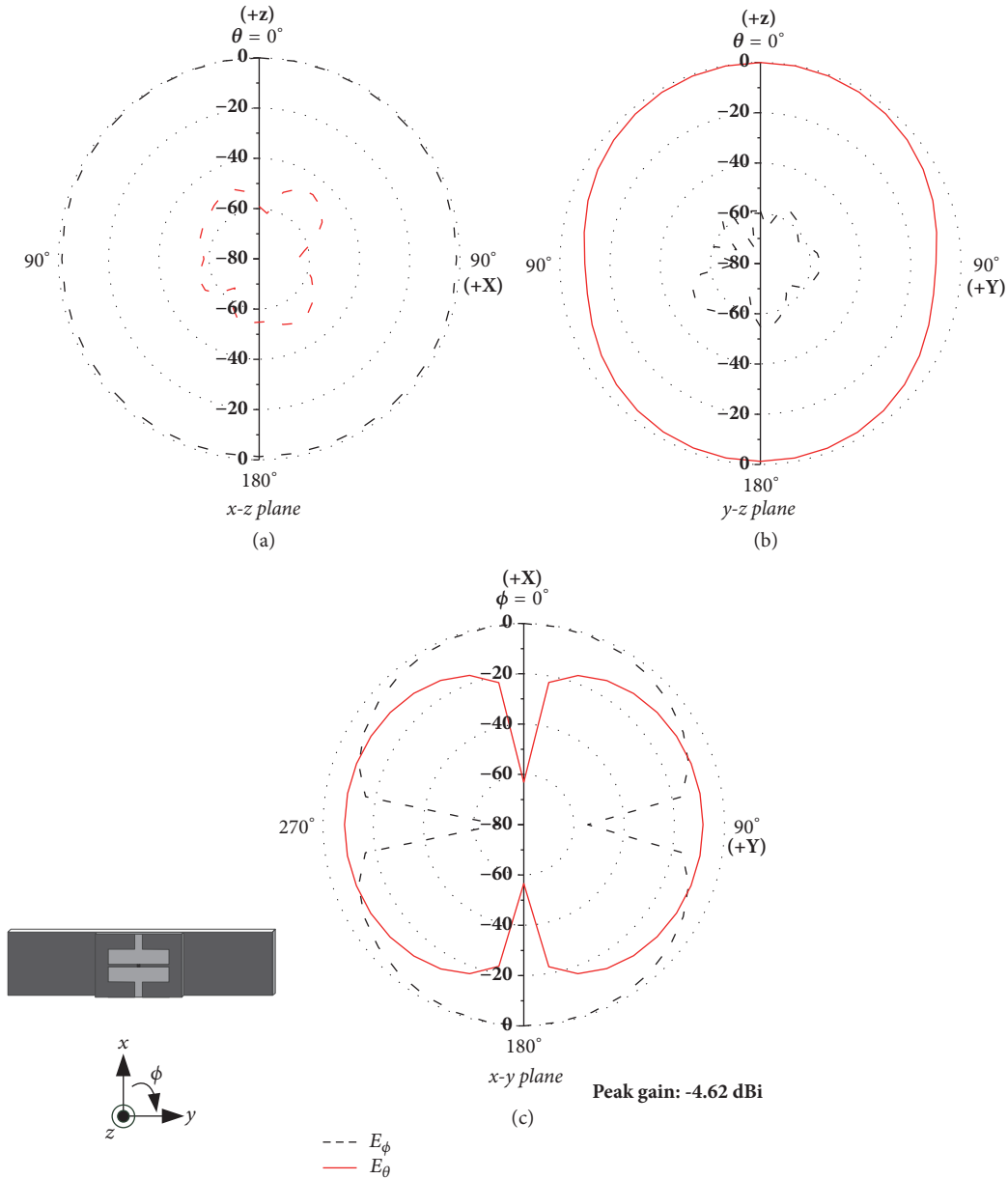


FIGURE 16: Simulated radiation patterns (normalized) of the proposed tag antenna (planar form) at 915 MHz.

an all-in-one test and measurement device for UHF RFID tag antenna [14]. The first setup of the measurement is as shown in Figure 18, in which the proposed tag antenna was attached to a piece of fresh pork. Even though the thicknesses of skin, fat, and muscle of this fresh pork are not the same as human wrist, the reason for using pork is because its electrical properties (fat and muscle) are very much closer to the human ones. Furthermore, it is very easy to obtain, rather than the commercialized hand phantom that is very expensive and not available to the authors. The illustration of this equipment setup is shown in Figure 19, in which a standard horizontal linearly polarized transmitting antenna (7.2 dBi gain) was used in this case and connected to an RF

output power of no more than 0.5 W (27 dBm). Thus, the total EIRP (effective isotropic radiation power) applied in this case for the measurement was 2.63 W (34.2 dBm). As for the second setup, the AUT (antenna under test) was simply replaced with a planar type proposed tag antenna without the attached pork.

Figures 20 and 21 show the measurement results obtained by the two experimental setups performed in the “Voyantic Tagformance Pro” chamber. As depicted in Figure 20,  $R_{max}$  of the proposed tag antenna in planar form (FSC) measured across 900–930 MHz were approximately between 6.6 m and 8.0 m. As for the case when it was attached to a piece of pork, its corresponding  $R_{max}$  were measured approximately

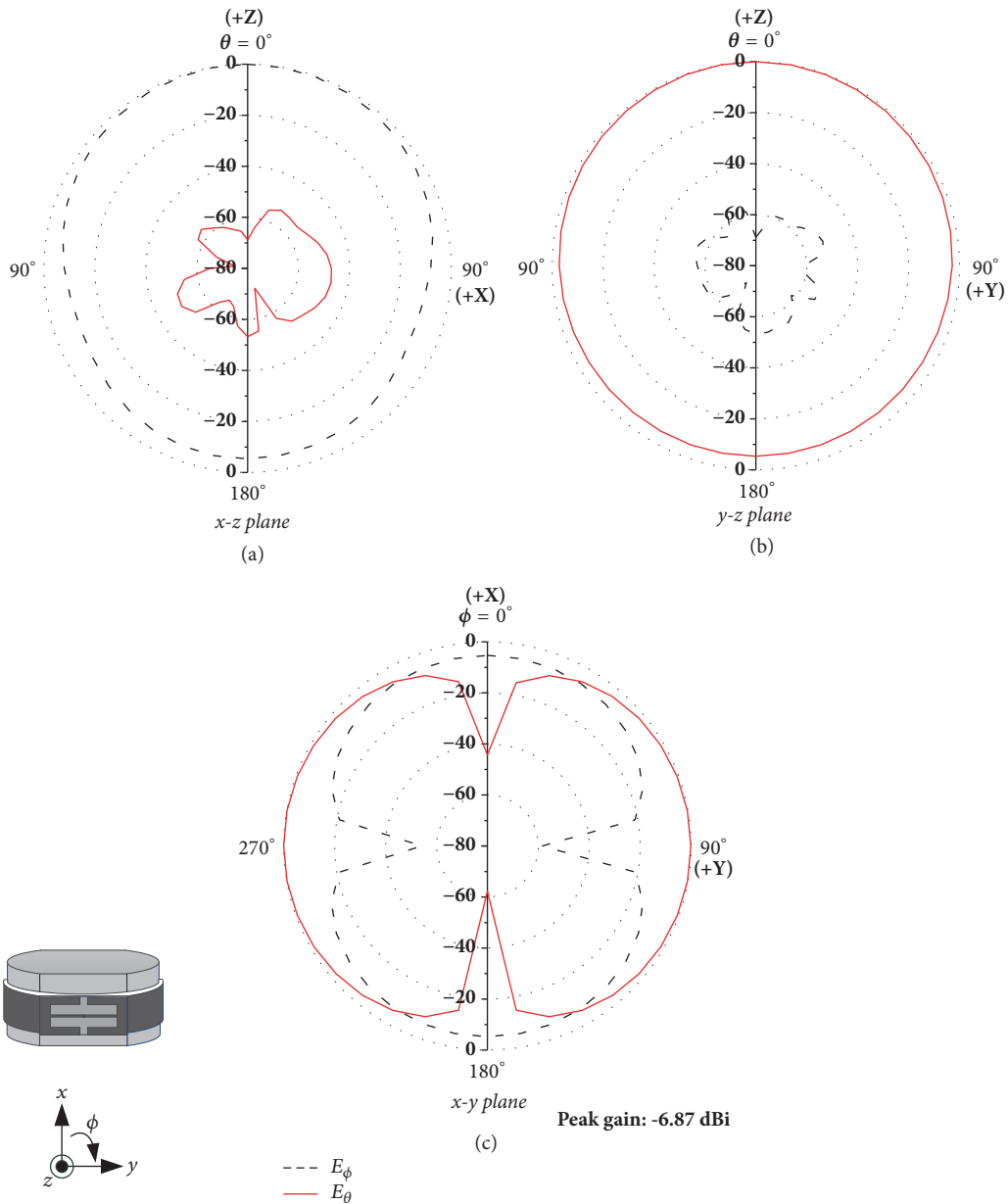


FIGURE 17: Simulated radiation patterns (normalized) of proposed antenna (attached to a human wrist phantom) at 915 MHz.

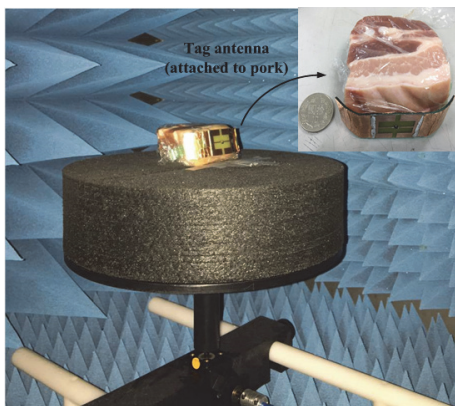


FIGURE 18: Photograph of proposed tag antenna attached to a piece of pork and placed in a “Voyantic Tagformance Pro” chamber [14] ready for measurement.

between 6 m and 6.6 m (across 900–930 MHz). Figure 21 shows the measured  $R_{max}$  of the proposed tag antenna at 915 MHz across the azimuth plane ( $y$ - $z$  plane) for the two setup cases. Here, in planar form (FSC), the boresight direction ( $+z$  direction) has shown  $R_{max}$  of 8 m, and it will slowly mitigate when the  $\theta$  angle has shifted away from boresight direction. In addition to that,  $R_{max}$  will reach a minimum range of approximately 2.2 m when the  $\theta$  angle is at  $90^\circ$  or  $270^\circ$ . As discussed earlier, because of the absorption from the pork, the proposed tag antenna attached to pork has a lower  $R_{max}$  of 6.6 m as compared with the planar form case at boresight direction. Furthermore, this absorption by the pork will become more prominent for the  $-z$  direction, showing a reduced  $R_{max}$  of 4.08 m, as compared with the planar form case with  $R_{max} = 7.18$  m. From the above results, because the proposed tag antenna (for the two setup cases) has shown

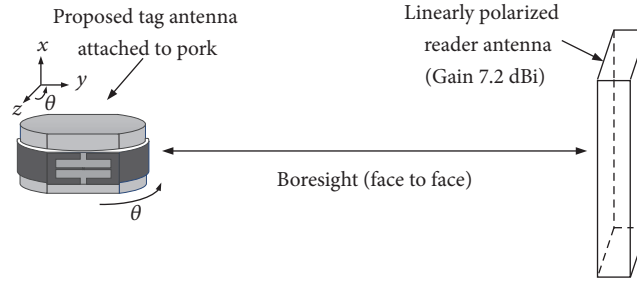


FIGURE 19: The illustration of proposed tag antenna attached to a piece of pork and placed in a “Voyantic Tagformance Pro” chamber that has a linearly polarized reader antenna with EIRP = 2.63 W.

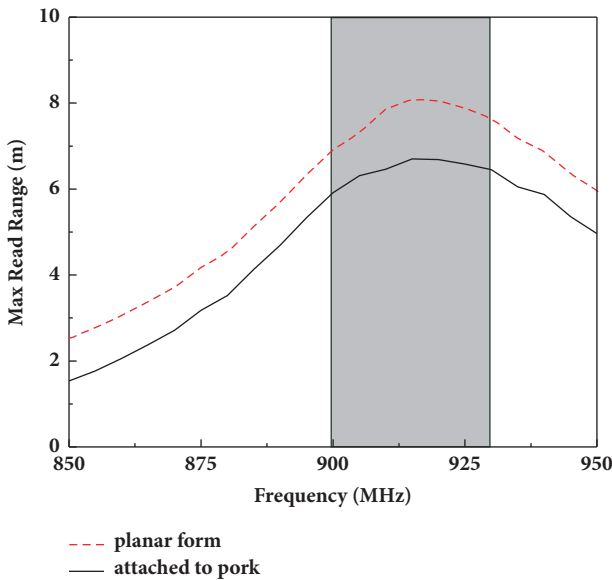


FIGURE 20: Maximum reading range measurement of the proposed tag antenna (with and without attached to a piece of pork) performed by a “Voyantic Tagformance Pro” chamber [14].

minimum  $R_{max}$  of at least 2 m (EIRP 2.63 W) across the entire azimuth, it is therefore suitable for incorporating into the healthcare applications for tracking/monitoring the patients.

To further validate the above results, the proposed antenna was placed into the wrist of three volunteers standing in a non-free-space condition (non-FSC) environment. As shown in Figure 22, the volunteers were standing in the middle of two rows of metal tables in the laboratory, creating a narrow and crowded environment with multipath condition. From the measurement via an RFID reader system (Favite) with 2.63W (34.2 dBm) EIRP, the measured distances performed on these three different students were 3.1 m, 3 m, and 3.2 m, which are approximately half the distance measured in FSC using the “Voyantic Tagformance Pro” chamber. However, one needs to take note that these measurements were taken in a very undesirable condition (narrow and crowded environment with metal walls on both sides), and thus the results obtained may vary across different environments.

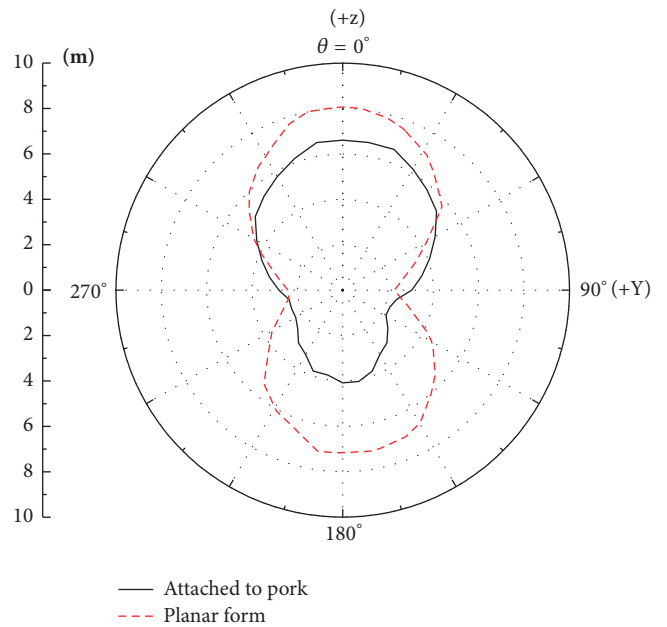


FIGURE 21: Measured reading ranges of the proposed tag antenna for the two setup cases at 915 MHz across the azimuth plane ( $y$ - $z$  plane) performed by the “Voyantic Tagformance Pro” chamber.

#### 4. Conclusions

A simple low-profile flexible RFID tag antenna has been successfully studied for working in the UHF band (902–928 MHz). The proposed open-slot cavity design of this tag antenna has the advantages of ease in impedance matching and tuning to the desired frequency band. The 6-dB return loss bandwidth of the proposed tag antenna when attached to a human wrist was 5.3% (0.88–0.928 GHz). In free-space condition, the experimental result shows that the proposed tag antenna can exhibit good reading ranges of between 2.2 m and 6.6 m. In a narrow and crowded environment with metal walls on both sides, at boresight direction, the reading range can be up to 3 meters. Therefore, this proposed antenna is a good candidate for tracking/monitoring the patients for future healthcare industry.



FIGURE 22: Measured reading ranges of proposed tag antenna on the wrist of three volunteers in a very narrow and crowded environment with metal tables on both sides.

## Conflicts of Interest

The authors declare that they have no conflicts of interest.

## References

- [1] M. A. Ziai and J. C. Batchelor, "A prototype passive UHF RFID transfer tattoo tag," in *Proceedings of the 5th European Conference on Antennas and Propagation, EUCAP 2011*, pp. 3811–3814, April 2011.
- [2] T. Kellomäki, "On-body performance of a wearable single-layer RFID tag," *IEEE Antennas and Wireless Propagation Letters*, vol. 11, pp. 73–76, 2012.
- [3] S. Amendola, S. Milici, and G. Marrocco, "Performance of epidermal RFID dual-loop tag and on-skin retuning," *IEEE Transactions on Antennas and Propagation*, vol. 63, no. 8, pp. 3672–3680, 2015.
- [4] Y. Jin, J. Tak, and J. Choi, "Compact dual-band antenna for smart wristband application," *Microwave and Optical Technology Letters*, vol. 58, no. 6, pp. 1462–1466, June, 2016.
- [5] <http://niremf.ifac.cnr.it/tissprop/>.
- [6] S. Amendola, G. Bovesecchi, A. Palombi, P. Coppa, and G. Marrocco, "Design, Calibration and Experimentation of an Epidermal RFID Sensor for Remote Temperature Monitoring," *IEEE Sensors Journal*, vol. 16, no. 19, pp. 7250–7257, 2016.
- [7] G. Marrocco, "RFID antennas for the UHF remote monitoring of human subjects," *IEEE Transactions on Antennas and Propagation*, vol. 55, no. 6, pp. 1862–1870, 2007.
- [8] A. Dubok and A. B. Smolders, "Miniaturization of robust UHF RFID antennas for use on perishable goods and human bodies," *IEEE Antennas and Wireless Propagation Letters*, vol. 13, pp. 1321–1324, 2014.
- [9] M. C. Tsai, I. G. Li, C. W. Chiu, and H. C. Wang, "UHF RFID PIFA array tag antenna for human body applications," in *Proceedings of the 15th Int. Symposium on WPMC*, pp. 434–437, September, 2012.
- [10] M. Svanda and M. Polivka, "On-body semi-electrically-small tag antenna for ultra high frequency radio-frequency identification platform-tolerant applications," *IET Microwaves, Antennas & Propagation*, vol. 10, no. 6, pp. 631–637, 2016.
- [11] H. Rajagopalan and Y. Rahmat-Samii, "On-body RFID tag design for human monitoring applications," in *Proceedings of the IEEE Antennas Propagation Soc. Int. Symp.*, pp. 1–4, July, 2010.
- [12] S. Lopez-Soriano and J. Parron, "Low profile UHF RFID tag for wristbands in healthcare applications," in *Proceedings of the 8th European Conference on Antennas and Propagation, EuCAP 2014*, pp. 874–877, April 2014.
- [13] H.-G. Cho, N. R. Labadie, and S. K. Sharma, "Design of an embedded-feed type microstrip patch antenna for UHF radio frequency identification tag on metallic objects," *IET Microwaves, Antennas & Propagation*, vol. 4, no. 9, pp. 1232–1239, 2010.
- [14] "Tagformance-pro," <http://voyantic.com/products/tagformance-pro>.

## Review Article

# Reconfigurable Magneto-Electric Dipole Antennas for Base Stations in Modern Wireless Communication Systems

Lei Ge <sup>1</sup>, Xujun Yang,<sup>1</sup> Zheng Dong,<sup>1</sup> Dengguo Zhang <sup>1</sup>, and Xierong Zeng<sup>2</sup>

<sup>1</sup>College of Electronic Science and Technology, Shenzhen University, Shenzhen, China

<sup>2</sup>College of Material Science and Engineering, Shenzhen University, Shenzhen, China

Correspondence should be addressed to Lei Ge; [leige@szu.edu.cn](mailto:leige@szu.edu.cn)

Received 19 January 2018; Accepted 25 March 2018; Published 15 May 2018

Academic Editor: Luca De Nardis

Copyright © 2018 Lei Ge et al. This is an open access article distributed under the Creative Commons Attribution License, which permits unrestricted use, distribution, and reproduction in any medium, provided the original work is properly cited.

Magneto-electric (ME) dipole antennas, with the function of changing the antenna characteristics, such as frequency, polarization, or radiation patterns, are reviewed in this paper. The reconfigurability is achieved by electrically altering the states of diodes or varactors to change the surface currents distributions or reflector size of the antenna. The purpose of the designs is to obtain agile antenna characteristics together with good directive radiation performances, such as low cross-polarization level, high front-to-back ratio, and stable gain. By reconfiguring the antenna capability to support more than one wireless frequency standard, switchable polarizations, or cover tunable areas, the reconfigurable ME dipole antennas are able to switch functionality as the mission changes. Therefore, it can help increase the communication efficiency and reduce the construction cost. This shows very attractive features in base station antennas of modern wireless communication applications.

## 1. Introduction

Owing to the tremendous evolution of wireless communications, the electromagnetic frequency spectrum is more and more crowded and the communication environment is more and more complex. To improve the communication quality, the fifth-generation (5G) mobile communications were proposed several years ago and will be commercially available in early 2020. In 5G mobile communications, higher transmission speed, higher reliability, and lower delay are required.

There are three ways to increase the communication capacity as shown in Figure 1: (1) using new frequency bands with wider bandwidth; (2) improving the spectrum efficiency; (3) using more radio frequency (RF) cells with smaller size. Because of this, in 5G mobile communications, millimeter-wave bands will be used to increase the frequency bandwidth; multi-input multi-output (MIMO) antennas will be applied to increase the network density. In the past several years, reconfiguration technique applied in RF systems to effectively increase the spectrum efficiency has been demonstrated. Accordingly, reconfiguration technique with the ability to improve the frequency spectrum utilization has aroused

great research interest in both industrial and academic areas. As the front end, antennas play a very important role in any wireless communication system. Antennas with reconfigurable characteristics can effectively enhance the system performance because they are able to adjust the antenna characteristics automatically and make them suitable to complex scenarios. Antennas with the function to dynamically change their operating frequency, polarization, or radiation patterns are needed to improve the channel capacity in communication systems. According to Friis transmission equation,

$$\frac{P_R}{P_T} = (1 - |\Gamma_T|^2)(1 - |\Gamma_R|^2)G_T G_R |\hat{\rho}_T \cdot \hat{\rho}_R|^2 \left(\frac{\lambda}{4\pi r}\right)^2. \quad (1)$$

The transmission efficiency between the transmitter and receiver mainly depends on three factors: impedance matching ( $\Gamma_T$ ,  $\Gamma_R$ ), antenna gain ( $G_T$ ,  $G_R$ ), and polarization matching ( $\hat{\rho}_T$ ,  $\hat{\rho}_R$ ). Therefore, reconfigurable antennas can be basically categorized into three types: (1) frequency reconfigurable antennas [1–5]; (2) polarization reconfigurable antennas [6–11]; (3) pattern reconfigurable antennas [5, 12–18].

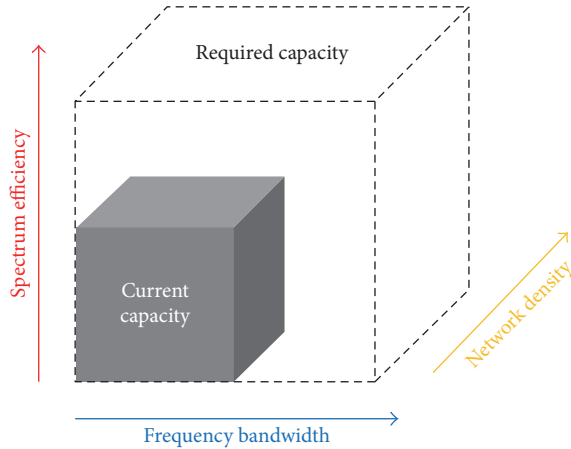


FIGURE 1: Methods for increasing the capacity.

Although many reconfigurable antennas have been proposed, they are usually designed based on microstrip structures [1, 3–5, 9–13, 15, 16]. Due to the narrow bandwidth, they are not appropriate to be applied in base stations. On the other hand, along with the development of wireless communications, antennas with wider bandwidth and good direction radiation patterns are required. Therefore, the conventional directional antenna candidates cannot satisfy the need of reconfigurable base station antennas.

In 2006, Prof. Luk invented a new antenna type specified as the magneto-electric (ME) dipole antenna [19], which consists of a magnetic dipole and an electric dipole. By exciting the complementary dipoles with suitable amplitudes and phases simultaneously, the antenna is able to produce good radiation characteristics over a wide frequency band. Taking advantages of the ME dipole antennas, they are very appreciated for the extensive applications of mobile cellular networks. When combining the ME dipole with reconfiguration technique, consequent reconfigurable ME dipole antennas can be developed for base stations in modern wireless systems. In this paper, three different kinds of reconfigurable ME dipole antennas are reviewed, namely, frequency reconfigurable ME dipole, polarization reconfigurable ME dipole, and beamwidth reconfigurable ME dipoles. In Section 2, a frequency reconfigurable ME dipole antenna is reviewed. In Section 3, several polarization switchable ME dipole antennas are reviewed. In Section 4, three beamwidth reconfigurable ME dipole antennas are reviewed. These designs show attractive features for modern wireless communication systems.

## 2. Frequency Reconfigurable ME Dipole Antenna

In this section, we depict a frequency reconfigurable ME dipole antenna [2]. Figure 2 gives the configuration of the antenna. The wide-narrowband antenna reconfiguration is demonstrated by systematically incorporating a broadband ME dipole antenna and a frequency reconfigurable narrowband dipole antenna. The ME dipole, as a part of the overall antenna structure, plays a crucial role in providing wideband operation. On the other hand, a length-switchable directed

dipole antenna is designed to feature reconfigurable narrow-band operation. A vertically oriented balun is used to feed the dipole. By using a box-shaped cavity, the dipole can generate good unidirectional radiation performance. By dynamically switching the states of PIN diodes embedded in the thin dipole, a changeable effective length is achieved. Besides, the surface current flowed on the thin dipole and the ME dipole can be changed by five groups of switches. Therefore, the antenna can be switched between four narrowband modes and a wideband mode. Notably, when the thin dipole is switched OFF, the ME dipole radiates with a wide band that can cover the operating frequency of the four narrow bands.

The measured reflection coefficients are presented in Figure 3. As observed from the figure, the fractional impedance bandwidth of the wideband mode is 89% and four different narrow bands appear at 0.95, 1.35, 1.7, and 2 GHz, respectively. In addition, the main beam of the radiation patterns is always fixed in the broadside direction with front-to-back ratios of above 20 dB and cross-polarization levels of below  $-22$  dB. Therefore, the design can work in one wideband mode for sensing and four reconfigurable narrowband modes for communications, which is attractive for base stations in cognitive radio.

## 3. Polarization Reconfigurable ME Dipole Antenna

In this section, we present three polarization reconfigurable ME dipole antennas. All the three designs [6–8] are based on similar four-sectional ME dipole geometry, while the polarization reconfiguration is realized by different feed structures and switching methods. The based ME dipole structure is based on the designs in [20, 21].

In [6], a feeding structure of an end-curving cross dipole for excitation of the polarization diversity antenna is proposed, as shown in Figure 4(a). PIN diodes are embedded into the arms of the cross dipole. Diodes can be switched ON or OFF in real time; therefore the RF signals can be coupled from the coaxial cable to the ME dipole. Accordingly, a polarization diversity between horizontal and vertical polarization modes can be produced. An overlapped impedance bandwidth ranging from 1.86 to 2.35 GHz is achieved at both orthogonally polarized states. Furthermore, the antenna presents a good radiation performance with an 8 dBi gain over the whole band.

In [7], another ME dipole antenna with the diversity of polarization is presented, which can operate between one linear polarization (LP) and two orthogonal circular polarizations (CP). In this design, four PIN diodes are embedded into the thin line printed on the diagonal position of four horizontal metal plates for controlling connection or disconnection. When all diodes are in OFF, LP operation is achieved, which means no thin lines are connected. To realize CP radiation, one single thin line is connected at the diagonal parts, perturbation is therefore introduced, and then corresponding left-handed circularly polarization (LHCP) or right-handed circularly polarization (RHCP) can emerge. The proposed design possesses admirable features such as gain stability and good directional radiation patterns.

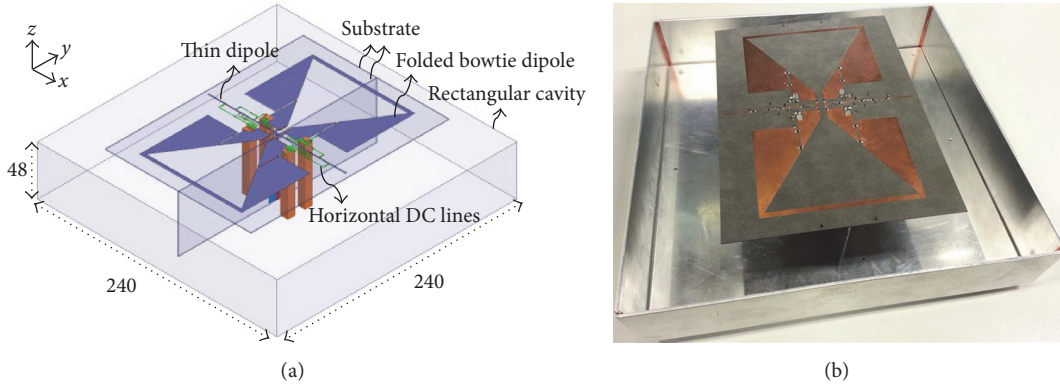


FIGURE 2: Geometry of the frequency reconfigurable ME dipole antenna [2]: (a) 3D view of the design; (b) fabricated prototype.

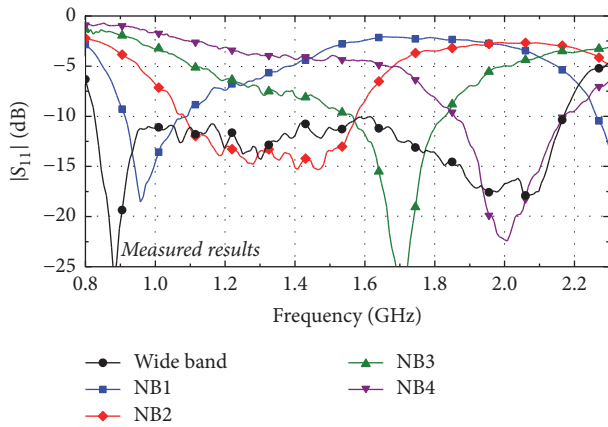


FIGURE 3: Measured  $|S_{11}|$  of the frequency reconfigurable ME dipole antenna.

In [8], the antenna is composed of an ME dipole, a substrate-integrate waveguide (SIW) cavity, and some DC lines as given in Figure 5. The design is comprised of four square metallic patches, four vertically oriented metal posts, and a strip. In this design, two sets of PIN diodes (SW1 and SW2) are used to help connecting or disconnecting the diagonal metal patches with the strip. By controlling the states of the two pairs of switches, one LP and two CP modes can be switched as depicted in Figure 6. When all diodes are ON, LP radiation can emerge. To excite CP modes, one of the two diode groups is ON while another is OFF. Hence, three polarization states can be realized by controlling the states of the switches. The effective overlapped bandwidth is 16% covering 5.07–5.95 GHz for applications of 5G WiFi. The measured antenna gain maintains stability at approximately 8.2 dBi across the band of interest for all operation states.

#### 4. Beamwidth Reconfigurable ME Dipole Antenna

As discussed, frequency reconfigurable and polarization reconfigurable antennas can be designed on the basis of the ME dipole. In this section, we will discuss radiation pattern

reconfiguration based on the ME dipole structure. Conventionally, pattern reconfigurable antennas are mainly designed to switch the radiating direction of the antenna. Furthermore, an antenna, with the ability of electronically controlling its radiation beamwidth, can enhance the communication quality of wireless systems. Thus, beamwidth reconfigurable antennas are demanded for modern base stations. In this section, three different methods are introduced to implement beamwidth reconfiguration of ME dipole antennas.

First, a three-element linear ME dipole array is used to achieve tunable beamwidth [17]. As shown in Figure 7, the linear array is composed of three ME dipoles and a feeding network. The feeding network is able to reset the phase distribution with a power distribution ratio of 1 : 2 : 1 for three antenna elements. The phase difference between Antennas 1 and 3 and Antenna 2 is  $\beta = 0^\circ/50^\circ/108^\circ$ . The operation principle of the antenna can be explained by a simplified three-element linear array. As illustrated in Figure 8, the three elements are located along the  $y$ -axis and the space between them is  $d$ . In this condition, it is assumed that the three antenna elements are all the same and well-isolated. The radiation field in the  $yo$ -plane can be expressed as

$$F(\theta)_T = [a_1 e^{-j(kr_1 + \psi_1)} + a_2 e^{-j(kr_2 + \psi_2)} + a_3 e^{-j(kr_3 + \psi_3)}] f(\theta), \quad (2)$$

where the amplitudes and phases of excitations are  $a_n$  and  $\psi_n$  ( $n = 1, 2, 3$ ) and  $f(\theta)$  is the radiation pattern of a single antenna element. In order to achieve symmetrical radiation pattern in the  $H$ -plane, the amplitudes and phases of Ant 1 and 3 are set to be the same. Assuming  $a_2 = Ma_1 = Ma_3$ ,  $\psi_2 = \psi_1 + \beta = \psi_3 + \beta$ , and the factor of the antenna array is decreased to

$$AF = a_1 [2 \cos(kd \sin \theta) + M \cos \beta - jM \sin \beta]. \quad (3)$$

For different  $\beta$ , the array factor in the  $yo$ -plane is given in Figure 9 with  $d = 0.5\lambda_0$  and  $M = \sqrt{2}$ . Especially, by utilizing the variation of the beam of the array factor and then multiplying the array factor with the pattern of a single element, the reconfiguration of the beamwidth is able to be realized.

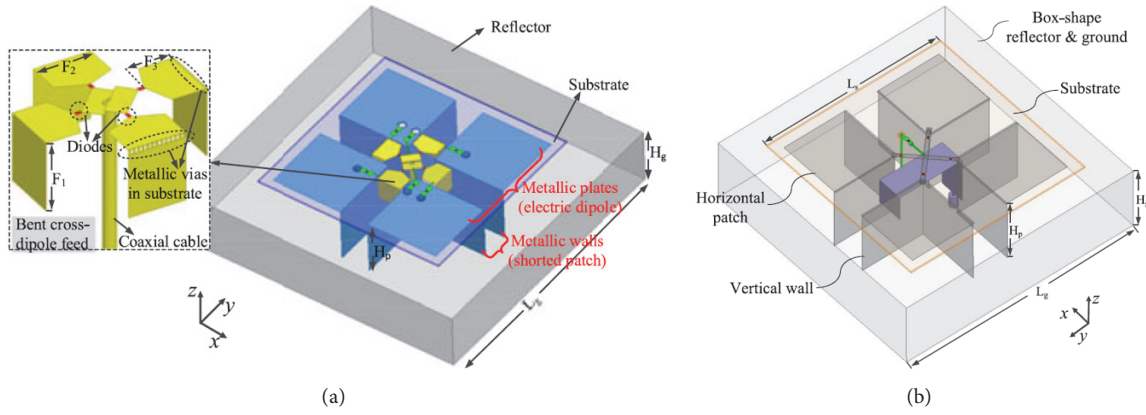


FIGURE 4: Geometry of the polarization reconfigurable ME dipole antennas: (a) the antenna in [6]; (b) the antenna in [7].

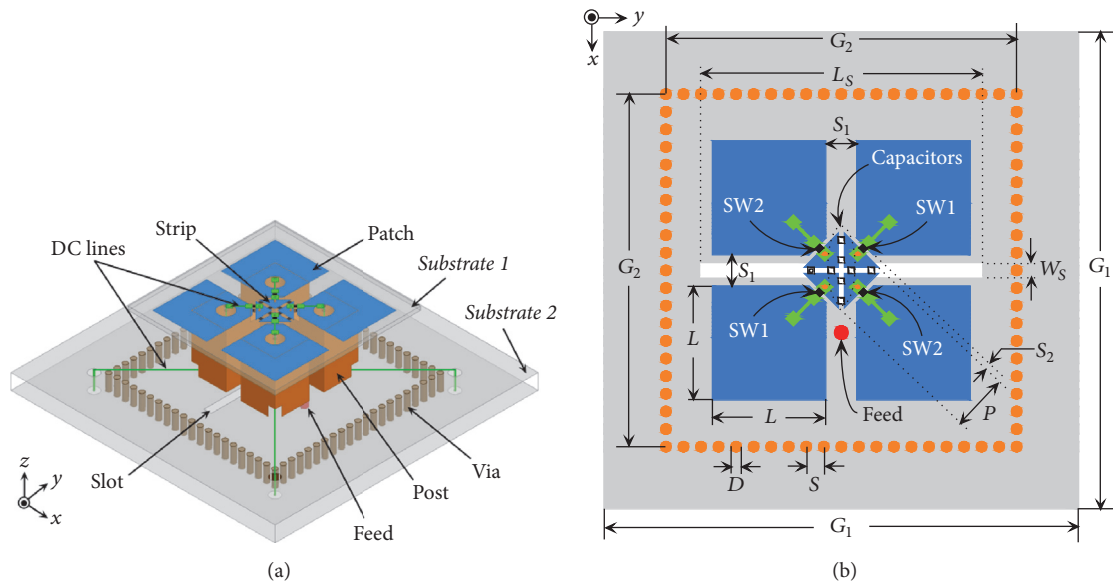


FIGURE 5: Geometry of the polarization reconfigurable ME dipole antenna [8]: (a) 3D view; (b) top view.

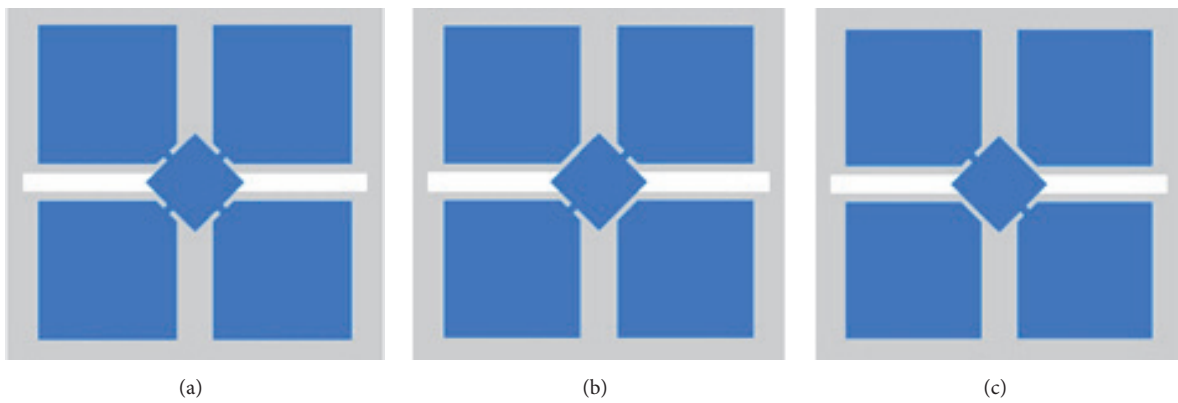


FIGURE 6: Switching states of the polarization reconfigurable ME dipole antenna [8]: (a) LP state; (b) RHCP state; (c) LHCP state.

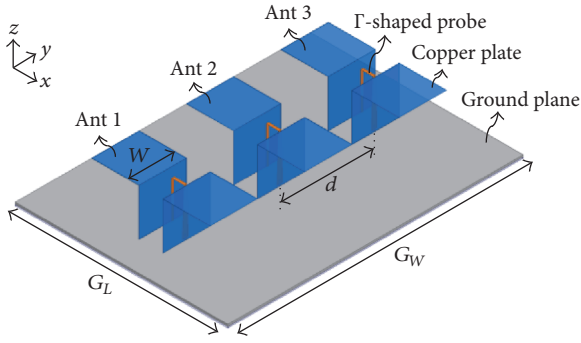


FIGURE 7: Geometry of the three-element linear ME dipole array with beamwidth reconfiguration.

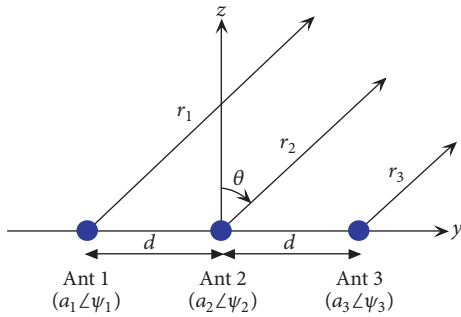


FIGURE 8: Three-element array model.

Secondly, LP and DP ME dipole antennas with the property of a dynamic  $H$ -plane beamwidth control are achieved as shown in Figure 10 [14]. Two tunable parasitic dipoles are put on the sides of a driven ME dipole along its  $H$ -plane. Varactor diodes are loaded on the parasitic thin dipoles to change the strength of the mutual coupling. When changing the state of the varactor diode, the overall radiation pattern of the antenna could be tuned. Different from the first method, this design uses the magnitude distribution instead of the phase distribution in the first method to obtain beamwidth reconfiguration. Figure 11 describes the simplified equivalent circuit of the design. The mutual coupling between the driven and parasitic dipoles is represented by a transformer. Since the varactor diodes are inserted in the parasitic dipoles, the impedance of the parasitic element is able to be varied by means of changing the capacitance of the varactor diodes. Therefore, the magnitude and phase distribution of the driven and parasitic dipoles are decided by the varactor diodes. Consequently, the entire antenna works similarly to a three-element array, where the center element is an ME dipole and the left and right elements are dipoles with an identical magnitude and phase distribution. The capacitance values of the varactor diodes determine the coupling strength and, in turn, the magnitude distribution. Hence, the entire radiation pattern of the antenna could be varied by tuning the power distribution of the dipoles. The simulated radiation patterns in the  $H$ -plane is presented in Figure 12 with different  $C$  (the capacitance value of varactor diodes). We can see that, along with  $C$  which reduces from 4 to 0.8 pF, the 3 dB beamwidth of the proposed antenna rises from  $80^\circ$  to  $160^\circ$ .

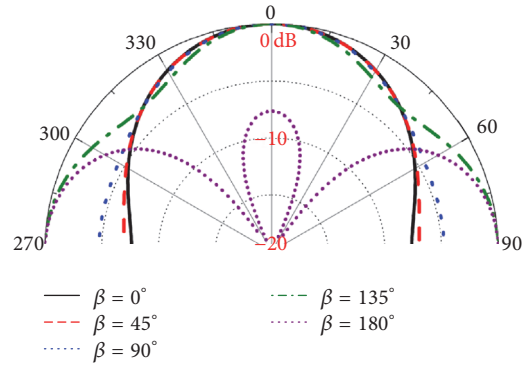


FIGURE 9: Array factor for different  $\beta$  with  $d = 0.5\lambda_0$  and  $M = \sqrt{2}$ .

Finally, an LP design with beamwidth reconfiguration is realized in [18]. As shown in Figure 13, the antenna is composed of a  $\Gamma$ -probe-fed ME dipole. Along its  $H$ -plane, there are three pairs of tunable strip gratings. Each strip is cut into 16 short portions and 15 PIN diodes are inserted into the gaps. When forward biased, the PIN diodes are ON and the strips serve as reflectors. When unbiased, the PIN diodes are OFF and the strips can be seen as transparent for radiating wave. Furthermore, because the PIN diodes on different strips are commanded by separated DC signals, by changing the amplitude of the DC signals, the size of the reflector can be varied as indicated in Figure 14. Therefore, the beamwidth of the proposed antenna could be changed. It should be emphasized that this method for beamwidth reconfiguration is different from the aforementioned. The first two methods are implemented by tuning the amplitude and phase distributions of the parasitic elements, while this design is realized by reconfiguring the size of the reflector. The characteristics of this simple antenna are highly attractive for applications in cellular systems. It has an impedance bandwidth as wide as 40%. The  $H$ -plane beamwidth can be tuned from  $153^\circ$  to  $81^\circ$ .

## 5. Conclusion

In this paper, some reconfigurable ME dipole antennas have been reviewed. A frequency reconfigurable design has been first reviewed, showing a wideband mode for sensing and reconfigurable narrowband modes for communications, which is attractive for base stations in cognitive radio. Secondly, polarization reconfigurable designs which are able to switch between the LP, RHCP, and LHCP states have been reviewed. The designs own the ability of degrading multipath-fading effects and enhancing the system stability and are useful for indoor wireless communication systems and can also be used as antenna elements for the outdoor base stations. Finally, three different beamwidth reconfigurable designs have been reviewed with dynamic control over their radiation beamwidth according to the environment requirement. These designs are attractive for outdoor base stations in future wireless communication systems.

Compared with other reconfigurable directional antenna candidates, the ME dipole owns some very attractive advantages as indicated in Table 1. The ME dipole can obtain wide

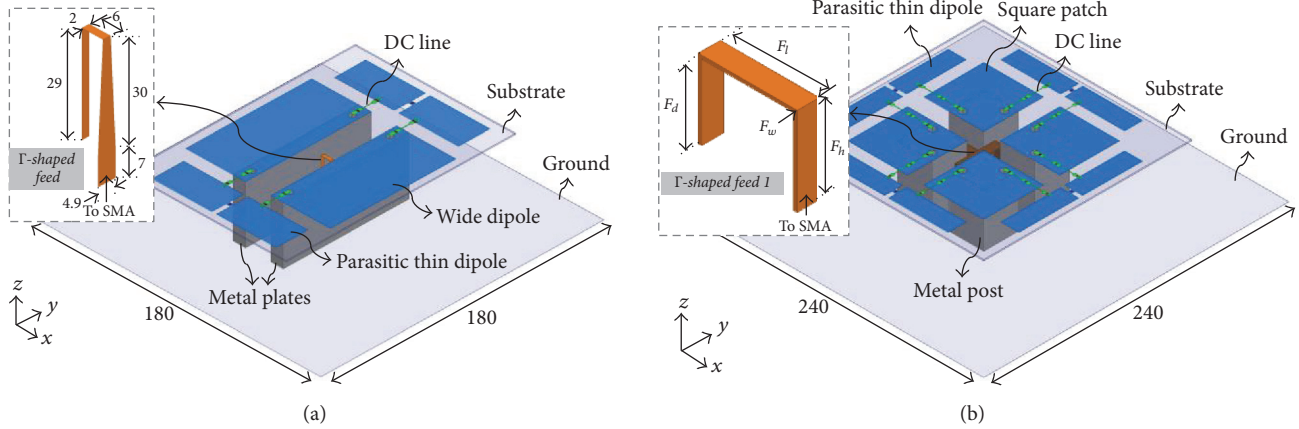


FIGURE 10: Geometry of the linearly polarized and dual-polarized beamwidth reconfigurable ME dipole antennas [14]: (a) LP antenna; (b) DP antenna.

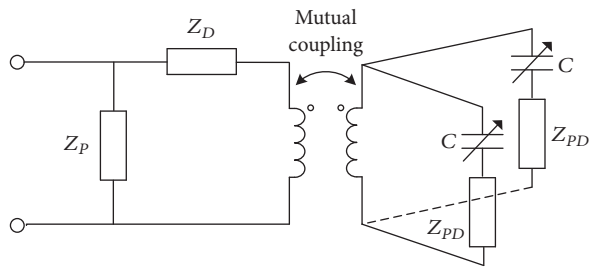


FIGURE 11: Equivalent circuit of the LP antenna.  $Z_D$ ,  $Z_P$ ,  $Z_{PD}$  represent the impedances of the wide planer dipole, shorted quarter-wavelength patch antenna, and the parasitic dipoles, respectively.

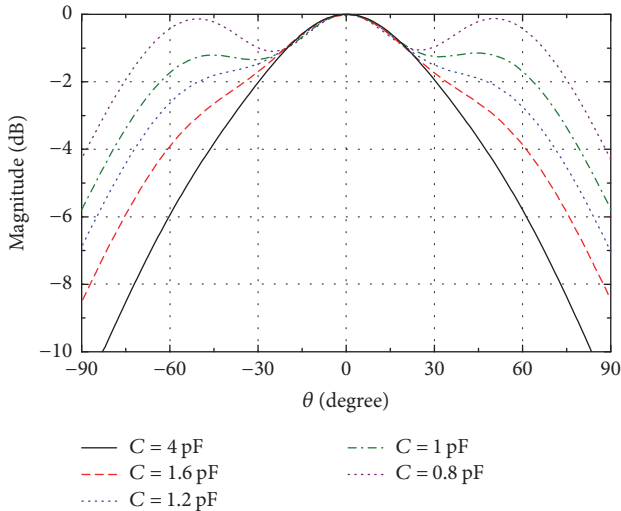


FIGURE 12: Simulated radiation patterns in the  $H$ -plane at 2 GHz with different  $C$ .

bandwidth and excellent unidirectional radiation patterns when designed for reconfigurable antennas. This is attributed to the advantages of the ME dipole. Besides, since the DC biasing lines can be hidden in the metal posts (magnetic dipole), the DC biasing lines can cause ignorable effects on

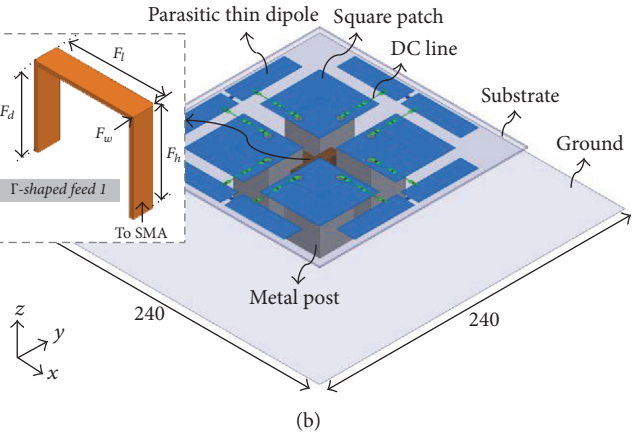


FIGURE 13: Geometry of the beamwidth reconfigurable ME dipole antenna using tunable strip grating.

TABLE 1: Comparison between ME dipole with other reconfigurable directional antenna candidates.

Reconfigurable directional antenna candidates	Bandwidth	Unidirectional radiation patterns (front-to-back ratio, cross-pol)	Difficulty level to be integrated with tuning mechanisms
Patch antenna [1]	Narrow	Poor	Easy
Cavity-backed slot antenna [12]	Fair	Fair	Easy
Yagi-Uda antenna [13]	Fair	Fair	Difficult
Dipole [2]	Wide	Good	Difficult
<i>ME dipole</i>	<i>Wide</i>	<i>Excellent</i>	<i>Fair</i>

the antenna performance. Therefore, the ME dipole is easy to be integrated with tuning mechanisms, especially with

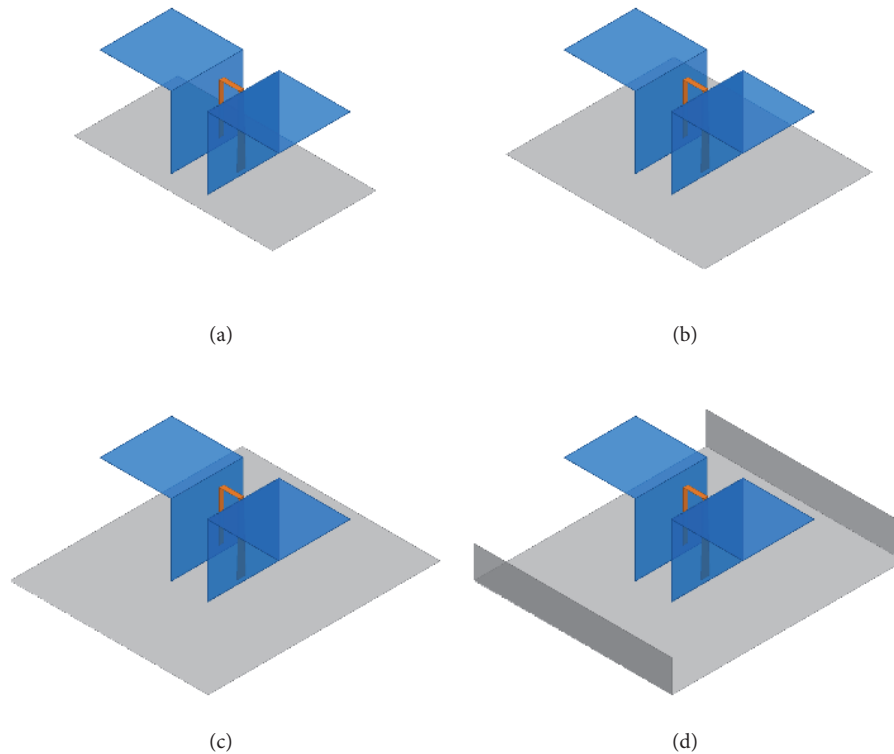


FIGURE 14: Equivalent structures of the antenna in different beamwidth states: (a) State 1; (b) State 2; (c) State 3; (d) State 4.

the electronically controlled switches. As discussed above, the ME dipole shows very attractive features over other directional antenna candidates in reconfigurable base station antenna design. These designs may be useful for base stations in wireless communication systems.

### Conflicts of Interest

The authors declare that they have no conflicts of interest.

### Acknowledgments

The work is supported by the National Natural Science Foundation of China (no. 61601303), Fundamental Research Foundation of Shenzhen (no. JCYJ20160308095149392), Fundamental Research Foundation of Shenzhen (no. JCYJ20170817095519575), and SZU R/D Fund (no. 2016022).

### References

- [1] M. R. Hamid, P. Gardner, P. S. Hall, and F. Ghanem, "Switched-band Vivaldi antenna," *IEEE Transactions on Antennas and Propagation*, vol. 59, no. 5, pp. 1472–1480, 2011.
- [2] L. Ge and K.-M. Luk, "A band-reconfigurable antenna based on directed dipole," *IEEE Transactions on Antennas and Propagation*, vol. 62, no. 1, pp. 64–71, 2014.
- [3] A. T. Kolsrud, M.-Y. Li, and K. Chang, "Dual-frequency electronically tunable CPW-fed CPS dipole antenna," *IEEE Electronics Letters*, vol. 34, no. 7, pp. 609–611, 1998.
- [4] B. Avser and G. M. Rebeiz, "Tunable dual-band antennas for 0.7–1.1-GHz and 1.7–2.3-GHz carrier aggregation systems," *Institute of Electrical and Electronics Engineers. Transactions on Antennas and Propagation*, vol. 63, no. 4, part 2, pp. 1498–1504, 2015.
- [5] K. Chung, Y. Nam, T. Yun, and J. Choi, "Reconfigurable microstrip-patch antenna with frequency and polarization-diversity functions," *Microwave and Optical Technology Letters*, vol. 47, no. 6, pp. 605–607, 2005.
- [6] F. Wu and K.-M. Luk, "A Reconfigurable Magneto-Electric Dipole Antenna Using Bent Cross-Dipole Feed for Polarization Diversity," *IEEE Antennas and Wireless Propagation Letters*, vol. 16, pp. 412–415, 2017.
- [7] F. Wu and K. M. Luk, "Wideband tri-polarization reconfigurable magneto-electric dipole antenna," *Institute of Electrical and Electronics Engineers. Transactions on Antennas and Propagation*, vol. 65, no. 4, pp. 1633–1641, 2017.
- [8] L. Ge, X. Yang, D. Zhang, M. Li, and H. Wong, "Polarization-Reconfigurable Magnetolectric Dipole Antenna for 5G Wi-Fi," *IEEE Antennas and Wireless Propagation Letters*, vol. 16, pp. 1504–1507, 2017.
- [9] W. Lin and H. Wong, "Polarization reconfigurable wheel-shaped antenna with conical-beam radiation pattern," *IEEE Transactions on Antennas and Propagation*, vol. 63, no. 2, pp. 491–499, 2015.
- [10] Y. J. Sung, T. U. Jang, and Y.-S. Kim, "A reconfigurable microstrip antenna for switchable polarization," *IEEE Microwave and Wireless Components Letters*, vol. 14, no. 11, pp. 534–536, 2004.

- [11] U. L. Bombale and S. Gupta, "Broadband planer array with switchable polarizations," *Microwave and Optical Technology Letters*, vol. 49, no. 10, pp. 2415–2419, 2007.
- [12] J.-S. Row and M.-J. Hou, "Design of polarization diversity patch antenna based on a compact reconfigurable feeding network," *IEEE Transactions on Antennas and Propagation*, vol. 62, no. 10, pp. 5349–5352, 2014.
- [13] P. F. Wahid, M. A. Ali, and B. C. DeLoach, "A reconfigurable Yagi antenna for wireless communications," *Microwave and Optical Technology Letters*, vol. 38, no. 2, pp. 140–141, 2003.
- [14] L. Ge and K.-M. Luk, "Linearly polarized and dual-polarized magneto-electric dipole antennas with reconfigurable beamwidth in the H-plane," *Institute of Electrical and Electronics Engineers. Transactions on Antennas and Propagation*, vol. 64, no. 2, pp. 423–431, 2016.
- [15] P.-Y. Qin, Y. J. Guo, A. R. Weily, and C.-H. Liang, "A pattern reconfigurable U-slot antenna and its applications in MIMO systems," *IEEE Transactions on Antennas and Propagation*, vol. 60, no. 2, pp. 516–528, 2012.
- [16] G. Monti, L. Corchia, and L. Tarricone, "A microstrip antenna with a reconfigurable pattern for RFID applications," *Progress in Electromagnetics Research B*, no. 45, pp. 101–116, 2012.
- [17] L. Ge and K. M. Luk, "A three-element linear magneto-electric dipole array with beamwidth reconfiguration," *IEEE Antennas and Wireless Propagation Letters*, vol. 14, pp. 28–31, 2015.
- [18] L. Ge and K. M. Luk, "Beamwidth Reconfigurable Magneto-Electric Dipole Antenna Based on Tunable Strip Grating Reflector," *IEEE Access*, vol. 4, pp. 7039–7045, 2016.
- [19] K. M. Luk and H. Wong, "A new wideband unidirectional antenna element," *International Journal of Microwave and Optical Technology*, vol. 1, no. 1, pp. 35–44, 2006.
- [20] Y. Li and K. M. Luk, "60-GHz Dual-Polarized Two-Dimensional Switch-Beam Wideband Antenna Array of Aperture-Coupled Magneto-Electric Dipoles," *IEEE Transactions on Antennas and Propagation*, vol. 64, no. 2, pp. 554–563, 2016.
- [21] Y. Li and K.-M. Luk, "A 60-GHz wideband circularly polarized aperture-coupled magneto-electric dipole antenna array," *Institute of Electrical and Electronics Engineers. Transactions on Antennas and Propagation*, vol. 64, no. 4, pp. 1325–1333, 2016.

## Research Article

# A Low VSWR and High Efficiency Waveguide Feed Antenna Array

Zhao Xiao-Fang <sup>1</sup>, Liu Hua-Zhu <sup>1</sup>, Li Yi,<sup>1</sup>  
Zhou Shi-Gang,<sup>2</sup> and Chow-Yen-Desmond Sim <sup>3</sup>

<sup>1</sup>School of Electrical Engineering & Intelligentization, Dongguan University of Technology, Dongguan 52380, China

<sup>2</sup>School of Electronics and Information, Northwestern Polytechnical University, Xi'an 710072, China

<sup>3</sup>Department of Electrical Engineering, Feng Chia University, Taichung, Taiwan

Correspondence should be addressed to Liu Hua-Zhu; 654650052@qq.com

Received 11 December 2017; Accepted 31 March 2018; Published 13 May 2018

Academic Editor: Mingjian Li

Copyright © 2018 Zhao Xiao-Fang et al. This is an open access article distributed under the Creative Commons Attribution License, which permits unrestricted use, distribution, and reproduction in any medium, provided the original work is properly cited.

A low VSWR and high efficiency antenna array operating in the Ku band for satellite communications is presented in this paper. To achieve high radiation efficiency and broad enough bandwidth, all-metal radiation elements and full-corporate waveguide feeding network are employed. As the general milling method is used in the multilayer antenna array fabrication, the *E*-plane waveguide feeding network is adopted here to suppress the wave leakage caused by the imperfect connectivity between adjacent layers. A  $4 \times 8$  elements array prototype was fabricated and tested for verification. The measured results of proposed antenna array show bandwidth of 6.9% (13.9–14.8 GHz) for VSWR < 1.5. Furthermore, antenna gain and efficiency of higher than 22.2 dBi and 80% are also exhibited, respectively.

## 1. Introduction

Slotted waveguide antenna array has the advantages such as high power capacity, low transmission loss, and low cross-polarization level. Thus, it is widely used in radar and communication systems [1–3]. However, one of the main drawbacks of conventional slotted waveguide antenna array is its inherently narrow bandwidth because of the long-line effect, and the bandwidth would become narrower with increasing array size. The other drawback of the slotted waveguide antenna arrays is the high fabrication cost, because specialized fabrication technique such as dip-brazing is always applied during the fabricating process.

Recently, corporate-feed hollow-waveguide slot arrays in millimeter wave (mmW) band with multilayer structures have been reported [4–7], and by applying the corporate-feed method, impedance bandwidths of 8% to 12% (at VSWR < 2) can be obtained without exhibiting any beam squint. An efficient antenna fabrication method known as diffusion bonding is used in the antenna array fabrication, and up to 80% of radiation efficiency can be achieved. However,

because it is difficult to achieve high-temperature and uniform pressure during the manufacturing process for a large-scale array, this unique fabrication method is not suitable for array fabrication in the “lower” frequency band, such as those in the Ku band. Therefore, a multilayer corporate-feed slot antenna array was proposed and fabricated by using simple milling process [8–10]. Nonetheless, the wave leakage between layers of this reported antenna array cannot be avoided, because the feeding network used here is an *H*-plane waveguide type.

Recently, a number of antenna array designs working in the Ku band with waveguide feed network have also been reported for satellite system applications [11–15]. Even though all these antenna array designs have been successfully reported, however, they have exhibited certain disadvantages that may compromise the performances. For example, the microstrip antenna element and waveguide feed network have been applied in [11, 12], and they have exhibited element loss and results in lower efficiency. Even though the coupling between elements in [13] is strong, however, that will reduce the performances of the antenna array when the

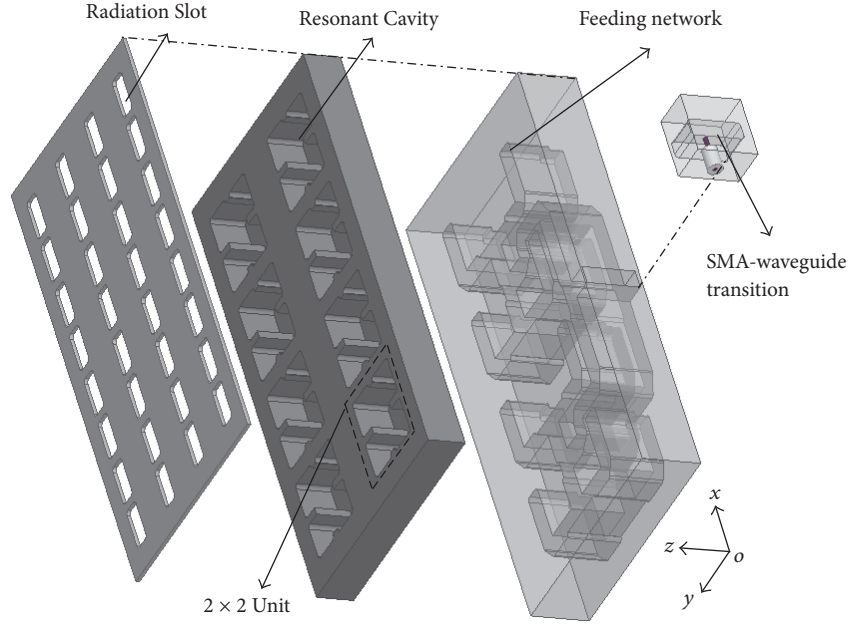


FIGURE 1: Geometry of proposed antenna array in three-dimensional view.

array gets larger. The other disadvantage of this design is its complex structure; thus mass producing this array will be very difficult. In [14], the connected-dipole active array is presented, and when the element is used as passive array fed by a microstrip network, the efficiency will not be high. In [15], the continuous transverse stub array is proposed for satellite communication; however, the structure is also very complicated, and it is not very suitable for small size array design.

Therefore, in this paper, an aperture size  $110 \times 55 \text{ mm}^2$  corporate-feed slot antenna array with  $E$ -plane waveguide feeding network is presented. The proposed antenna array is composed of three layers, namely, radiating slots layer, cavity layer, and a feeding network layer. Here,  $E$ -plane waveguide feeding network is used to reduce wave leakage considering there are gaps between adjacent layers in real fabrication. An antenna prototype is fabricated by applying the simple milling process. Experimental results show that the proposed antenna exhibits low VSWR and high radiation efficiency ( $>80\%$ ) characteristics. Details of the antenna design and measurement results are shown in the following sections.

## 2. Antenna Array Configuration and Design

Figure 1 shows the three-dimensional (3D) view of proposed antenna array structure. The antenna array is a multilayer type composed mainly of three layers, namely, the antenna radiation slots, resonant cavity, and feeding network, from top to bottom, respectively. The  $2 \times 2$  element subarrays employed as one unit here are for the purpose of minimizing the occurrence of grating lobe as much as possible [4, 8]. The design of feeding network adopts the  $E$ -plane waveguide type, so that wave leakage can be prevented after the assembly.

There is also a SMA-waveguide transition at one side to convert the waveguide port to SMA port.

Figure 2 shows the  $2 \times 2$  subarray configuration with related structural parameters, and it is also comprised of three parts. The working mechanisms of the proposed subarray are as follows: (1) the energy is coupled from the  $E$ -plane waveguide at the bottom layer to the resonant cavity located at the middle layer via the coupling slot; (2) there are two pairs of side walls in the cavity for the purpose of splitting the resonant higher mode, which is similar to those reported in [4, 8]; (3) the  $2 \times 2$  radiation slots on the top share the same resonant cavity. Due to the fact that the higher mode resonant can also be excited, the radiation slots can be equally excited. Here, the simulated  $E$ -field distributions at the top of radiation slot and in the middle and bottom of the resonant cavity are shown in Figure 3. At the bottom waveguide layer, a small notch ( $c_l \times c_h$ ) is loaded at one corner of the waveguide, and a distance  $d_f$  separates the coupling slot and the waveguide edge. Notably, both parameters are implemented for impedance matching of the antenna.

To fully develop and transform the  $2 \times 2$  subarray into a larger array antenna type, proper  $E$ -plane corporate-feed-network is therefore required. However, the full-corporate  $E$ -plane waveguide feeding networks cannot be simply composed by  $H$ -junctions and  $T$ -junctions as reported in [4, 8], because the output ports of  $T$ -shaped  $E$ -plane waveguide junctions are excited out-of-phase. Figure 4 presents the configuration of proposed full-corporate  $E$ -plane waveguide feeding networks for the  $4 \times 8$  array, and Table 1 gives the full detailed dimensions of the antenna array. It can be seen that, due to space limitation, some of the waveguide bends and junctions are carefully routed. It is also noteworthy that the surface roughness of each mechanic layer is not very

TABLE 1: Dimension parameters for the antenna array (Unit : mm).

$l_a$	$w_a$	$l_c$	$w_c$	$l_s$	$w_s$	$d_1$	$d_2$	$c_h$	$c_l$	$d_f$	$d$
11.5	4.3	23.0	19.4	10.4	5.0	20.6	9.8	1.0	3.8	1.8	5.5

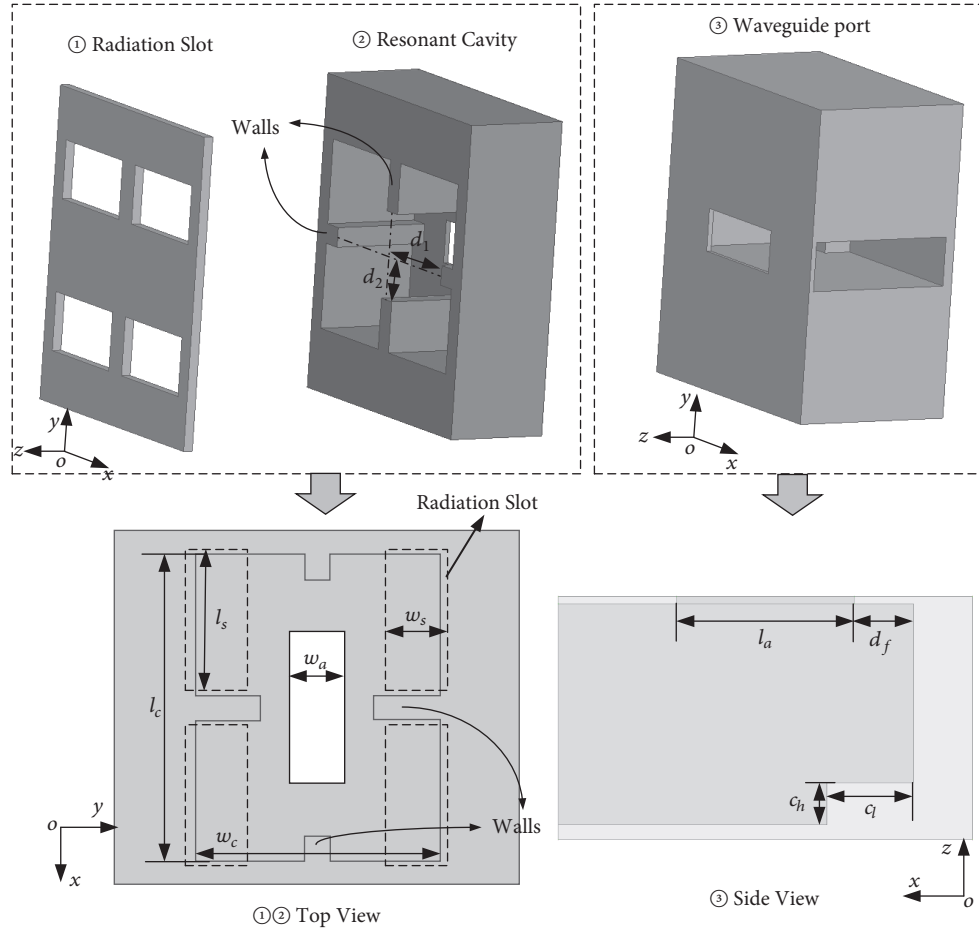


FIGURE 2: Configuration of the  $2 \times 2$  subarray element [16].

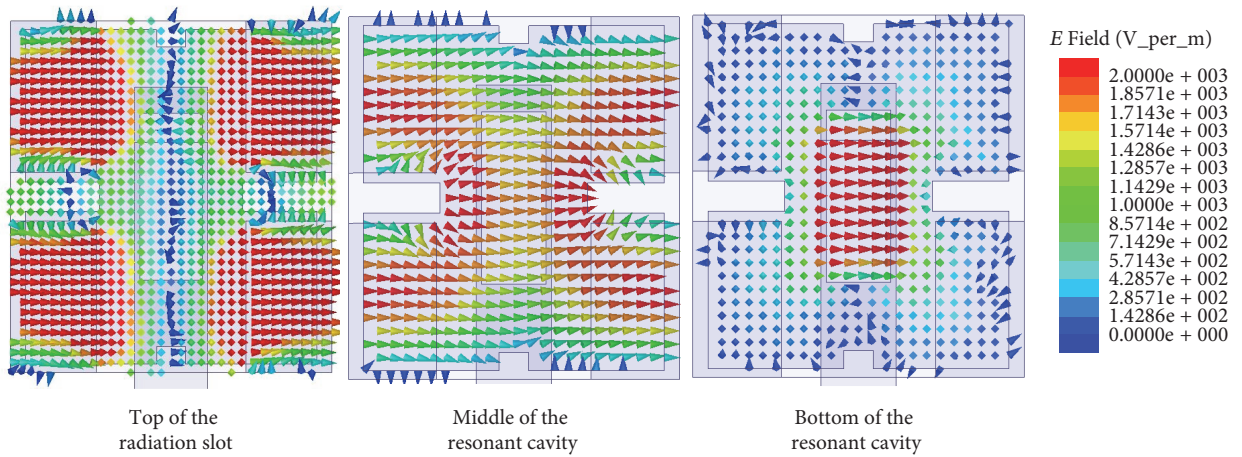


FIGURE 3: Simulated  $E$ -field distribution.

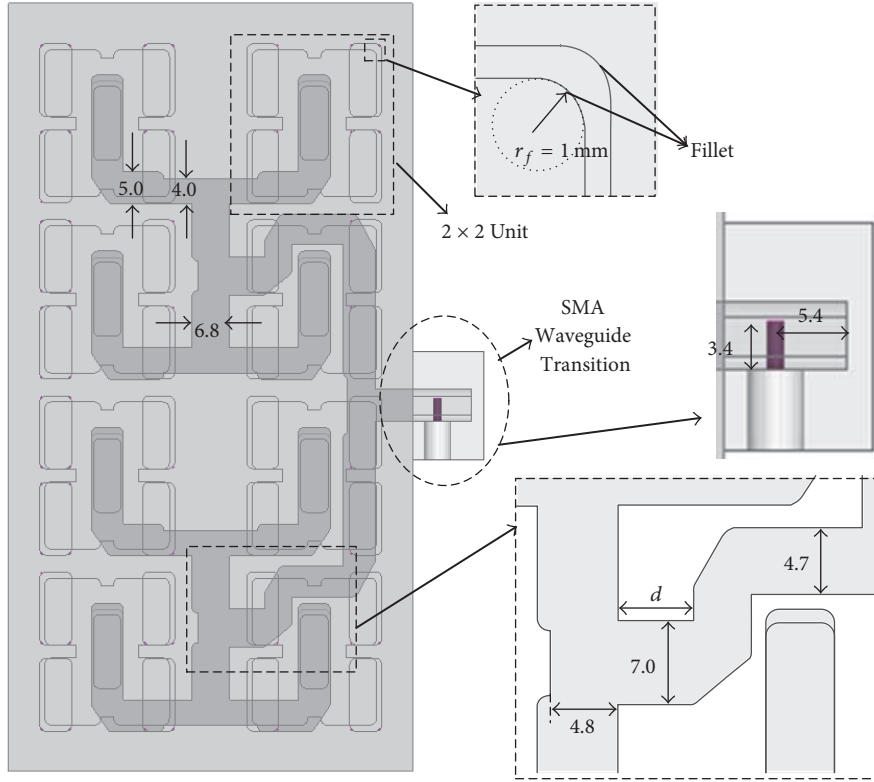


FIGURE 4: Complete  $E$ -plane waveguide feed-networks of the  $4 \times 8$  array.

strict in this work, and thus it is not necessary to use more screws to press two layers very hard together. These factors have therefore contributed to the advantages of this proposed antenna (ease in fabrication), yielding lower fabrication cost.

### 3. Design Evolution and Parametric Studies

To further comprehend the design of this antenna, some of the vital parameters such as  $l_s$ ,  $w_s$ , and  $d_f$  are analyzed and presented. The simulated VSWRs of the  $2 \times 2$  subarray by tuning the length ( $l_s$ ) and width ( $w_s$ ) of radiation slot are given in Figures 5 and 6, respectively. As depicted in Figure 5, tuning  $l_s$  between 9.9 and 11.9 mm can affect the impedance bandwidth of the upper and lower operating frequencies at along VSWR < 1.5 threshold, even though the two resonances at approximately 13.9 and 14.5 GHz are nearly unaffected. In this case, optimum  $l_s$  is chosen to be 10.4 mm, because it can give desirable bandwidth of approximately 13.67–14.68 GHz (along VSWR < 1.5) and exhibit better impedance matching for the two resonances. As shown in Figure 6, an increase in width  $w_s$  by 1 mm (from 4 to 6 mm) will result in shifting the lower resonance to lower frequency band (approximately 14.3 GHz to 13.73 GHz). In addition, tuning  $w_s$  will also highly affect the operating impedance bandwidth. Here, optimum  $w_s$  is chosen to be 5 mm, because it exhibits the widest VSWR < 1.5 bandwidth. Besides tuning the radiation slot  $w_s$ , the simulated results in Figure 7 show that varying distance  $d_f$  (from 0.8 to 2.8 mm) can also exhibit similar resonant

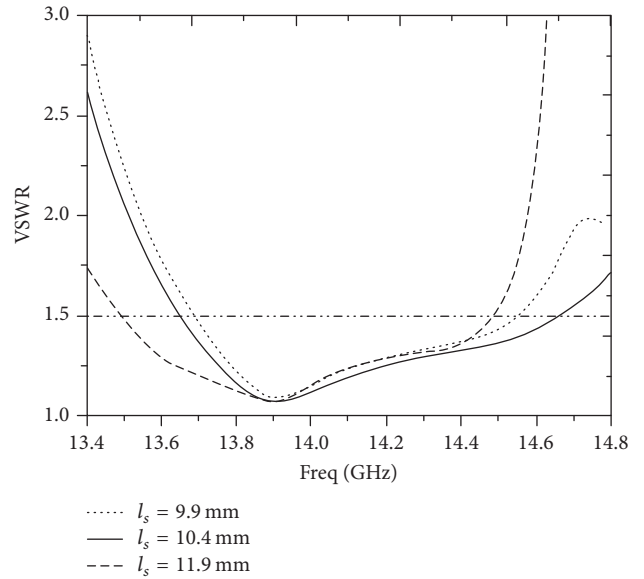


FIGURE 5: Simulated VSWR, varying  $l_s$ .

frequency shifting from approximately 14.3 GHz to 13.7 GHz. Thus, in this case, the optimum  $d_f$  chosen is 1.8 mm.

### 4. Simulated and Measured Results

The  $4 \times 8$  antenna array design was analyzed by using commercial simulator Ansoft HFSS. The parameters shown

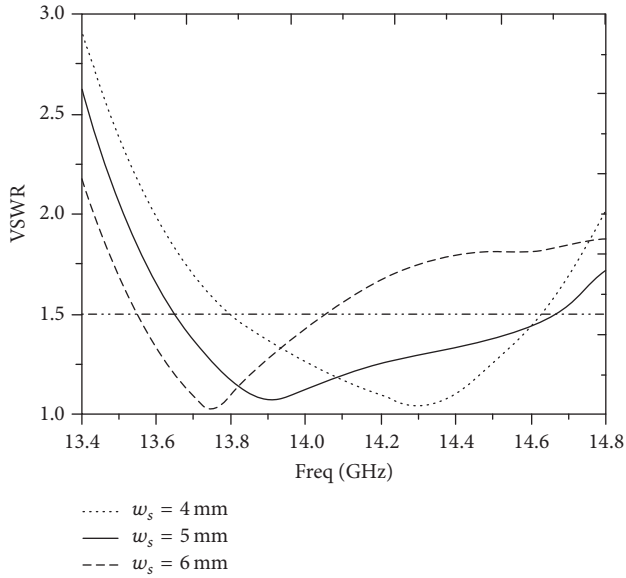


FIGURE 6: Simulated VSWR, varying  $w_s$ .

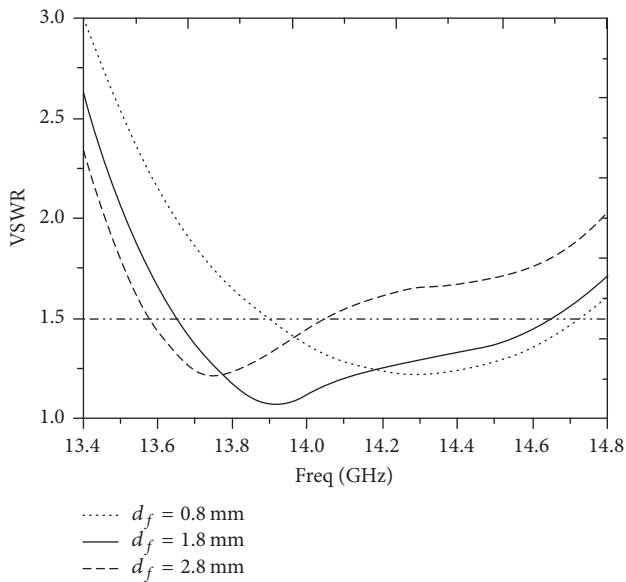


FIGURE 7: Simulated VSWR, varying  $d_f$ .

in Figures 2 and 4 are optimized and the final dimensions are listed in Table 1. Milling technique was applied in this case to fabricate the antenna prototype. As shown in Figure 8, the material used for this prototype antenna is aluminum. Notably, the layer partition of the actual mechanical model is slightly different from the layers shown in Figure 2. This is because in order to suppress the wave leakage between adjacent layers, the waveguides are intentionally split in the middle of the  $E$ -plane of corporate-feed-networks, in which minimal current flow can be attained, so that the gaps caused by the partition and tight electric-contact among the metallic layers are not critical [9].

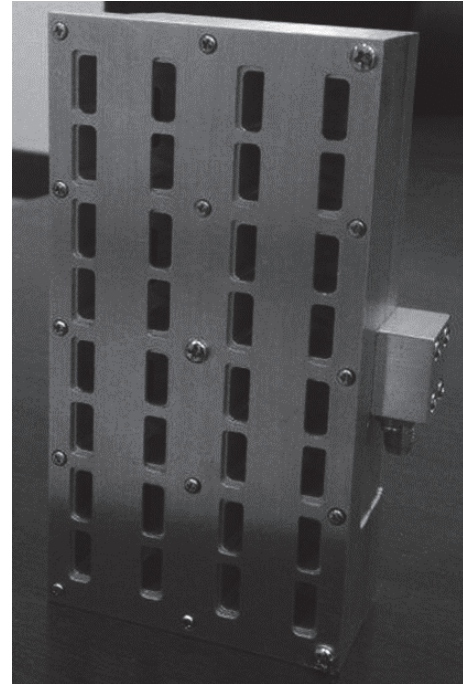


FIGURE 8: Photo picture of proposed antenna array.

The VSWR of the antenna prototype was measured by Agilent N5224A network analyzer. The measured and simulated VSWR results are shown in Figure 9, and good agreement can be observed. For a low VSWR of less than 1.5 ( $VSWR < 1.5$ ), the measured bandwidth of proposed antenna array was 6.9% (13.9–14.8 GHz). The radiation patterns were measured in a far field range anechoic chamber. The simulated and measured radiation patterns in both  $E$ -plane and  $H$ -plane of proposed antenna array at 14.5 GHz (center frequency) are shown in Figure 10. Good validation between the simulated and measured pattern is also observed. In this figure, it is realized that the side lobe level (SLL) is not very low (approximately  $-14$  dB), because each element of the array has exhibited uniform excitation. If lower SLL is required, the tapered distribution (such as Taylor and Chebyshev distribution) technique can be used in the array design. Notably, this technique has been studied in [10], in which an unequal power divided  $T$ -junction was applied in the feeding network. However, the use of this technique will increase the manufacturing difficulty of this work, which is not favourable in this case.

The realized gain of proposed antenna array was measured by applying the conventional gain-comparison method [4]. Figure 11 shows the simulated and measured realized gain and efficiency of proposed antenna array. In this figure, stable gain variations between 22.2 dBi and 22.9 dBi over the operating bandwidth ( $VSWR < 1.5$ ) of 13.9–14.8 GHz were measured. Here, the measured gains are approximately 0.2–0.8 dB lower than the simulated ones. High aperture efficiency of more than 80% is also achieved over the same

TABLE 2: Performance comparison between this work and reference antennas.

Ref	Aperture size (mm <sup>2</sup> )	Freq. (GHz)	BW (%)	VSWR	Eff. (%)	MP	Cost
[4]	75 × 76	58.8–63.9	8.3	<1.5	>80	Hard	High
[8]	146 × 146	14.5–16.1	14.8	<2.0	>80	Medium	Low
[11]	40 × 366	12.2–12.7	4.0*	NA	>63	Easy	Low
[12]	707 × 182	10.8–12.7	16.5	<2.0	>57	Easy	Low
[13]	35 × 35	12–15	21	<2.0	>70	Hard	Low
[15]	229.52 × $\pi$	26–40	40	<2.0	>80	Hard	High
This work	110 × 55	13.9–14.8	6.9	<1.5	>80	Easy	Low

\* Axial Ratio bandwidth, NA: not applicable.

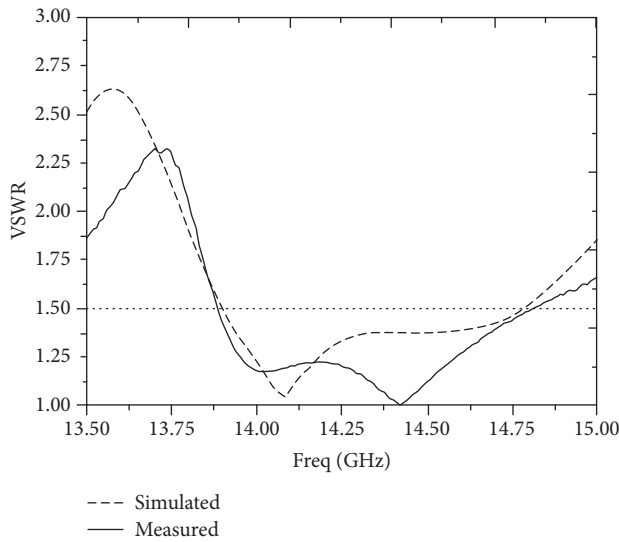


FIGURE 9: Simulated and measured VSWR of proposed antenna array.

operating band (13.9–14.8 GHz), and it can be up to 90% at some frequency points.

Table 2 shows the comparison of performances between the proposed antenna array (this work) and those relevant reported antenna arrays that are also operating in the Ku band. Even though the operating bandwidth of proposed one may have narrower bandwidth than that of [4, 8, 12], by further observing this table, the proposed antenna offers very high radiation efficiency of over 80% in the Ku band (with milling process). From this table, one of the main advantages (novelty) of this proposed work is its ease in fabrication, thus leading to lower manufacturing cost during mass production.

## 5. Conclusion

A multilayer slot antenna array with  $4 \times 8$  elements has been successfully proposed in the Ku band. Full-corporate feed-network is used in this case to achieve desirable bandwidth of 6.9% (VSWR < 1.5) without beam squints. In addition, *E*-plane waveguide is also adopted to prevent wave leakage, which in turn can achieve high radiation efficiency of more than 80%, even though the milling fabrication process was

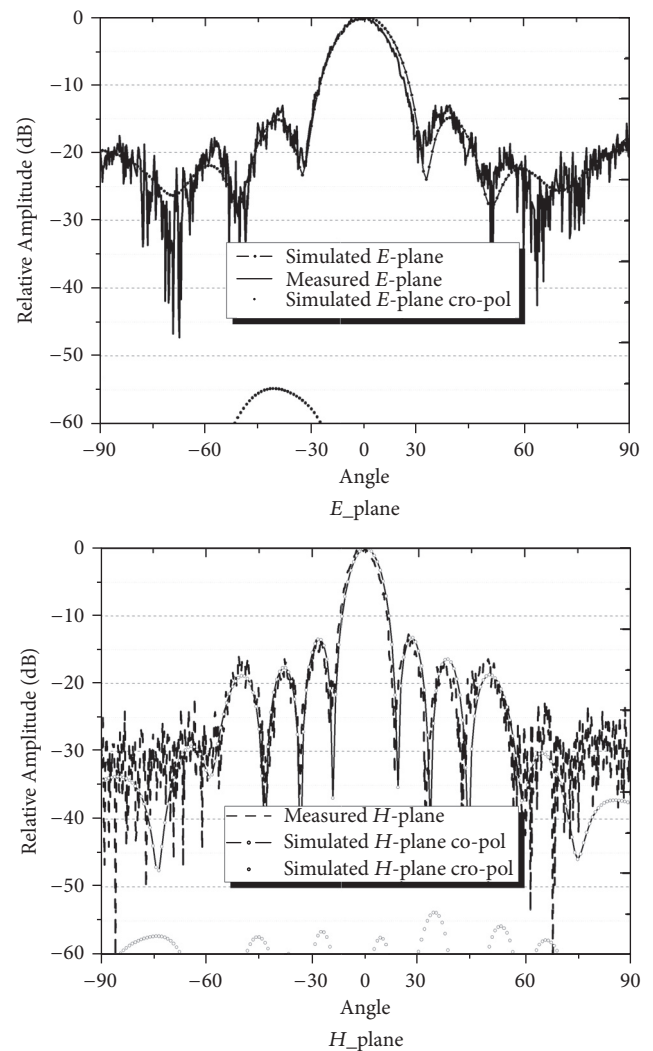


FIGURE 10: Simulated and measured patterns of proposed antenna array [17].

taken into consideration. Due to its compact aperture size and good efficiency, this proposed antenna array is a good candidate for Ku band satellite communications.

## Conflicts of Interest

There are no conflicts of interest related to this paper.

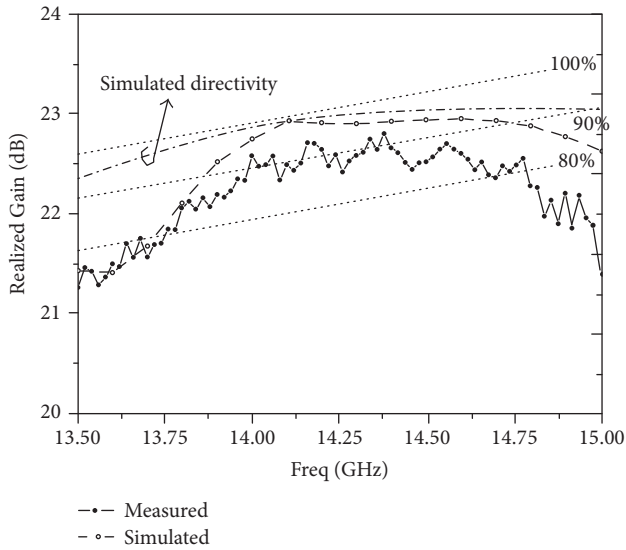


FIGURE 11: Simulated and measured gain and efficiency of proposed antenna array.

## Acknowledgments

This work was supported by the Science and Technology Project of Guangdong Province under Grant nos. 2015A010103019 and 2017A010101038.

## References

- [1] X. Lu, S. Gu, X. Wang, H. Liu, and W. Lu, "Beam-scanning continuous transverse stub antenna fed by a ridged waveguide slot array," *IEEE Antennas and Wireless Propagation Letters*, vol. 16, pp. 1675–1678, 2017.
- [2] W.-J. Gao, J.-J. Jiao, Y.-Z. Han, Y.-K. Deng, Y.-H. Xiong, and X.-M. Liu, "A compact broadband ridged-square-waveguide radiating element for phased array antennas in synthetic aperture radar applications," *Microwave and Optical Technology Letters*, vol. 54, no. 3, pp. 829–833, 2012.
- [3] L. Zhang, Y.-C. Jiao, T. Ni, and W.-L. Liang, "Wideband circularly polarized planar monopole antenna for wireless communication applications," *International Journal of Applied Electromagnetics and Mechanics*, vol. 49, no. 3, pp. 427–434, 2015.
- [4] Y. Miura, J. Hirokawa, M. Ando, Y. Shibuya, and G. Yoshida, "Double-layer full-corporate-feed hollow-waveguide slot array antenna in the 60-GHz band," *IEEE Transactions on Antennas and Propagation*, vol. 59, no. 8, pp. 2844–2851, 2011.
- [5] C. Cui, S.-K. Kim, R. Song, J.-H. Song, S. Nam, and B.-S. Kim, "A 77-GHz FMCW radar system using on-chip waveguide feeders in 65-nm CMOS," *IEEE Transactions on Microwave Theory and Techniques*, vol. 63, no. 11, pp. 3736–3746, 2015.
- [6] H. R. Jha and S. N. Singh, "A high-gain and high-bandwidth waveguide fed longitudinal slot doublets array antenna for X-band," *AEÜ - International Journal of Electronics and Communications*, vol. 70, no. 12, pp. 1622–1629, 2016.
- [7] C. Wu, C. Lu, and W. Cao, "Wideband dual-polarization slot antenna with high isolation by using microstrip line balun feed," *IEEE Antennas and Wireless Propagation Letters*, vol. 16, pp. 1759–1762, 2017.
- [8] H. Guan-Long, Z. Shi-Gang, C. Tan-Huat, and Y. Tat-Soon, "Broadband and high gain waveguide-fed slot antenna array in the Ku-band," *IET Microwaves, Antennas & Propagation*, vol. 8, no. 13, pp. 1041–1046, 2014.
- [9] G.-L. Huang, S.-G. Zhou, and T.-H. Chio, "Waveguide-Fed Cavity Backed Slot Antenna Array with high efficiency in the Ku-band," in *Proceedings of the Joint 2012 IEEE International Symposium on Antennas and Propagation and USNC-URSI National Radio Science Meeting, APSURSI 2012*, Chicago, Ill, USA, July 2012.
- [10] G.-L. Huang, S.-G. Zhou, T.-H. Chio, H.-T. Hui, and T.-S. Yeo, "A low profile and low sidelobe wideband slot antenna array fed by an amplitude-tapering waveguide feed-network," *IEEE Transactions on Antennas and Propagation*, vol. 63, no. 1, pp. 419–423, 2015.
- [11] M. Shahabadi, D. Busuioc, A. Borji, and S. Safavi-Naeini, "Low-cost, high-efficiency quasi-planar array of waveguide-fed circularly polarized microstrip antennas," *IEEE Transactions on Antennas and Propagation*, vol. 53, no. 6, pp. 2036–2043, 2005.
- [12] M. M. Bilgic and K. Yegin, "Low profile wideband antenna array with hybrid microstrip and waveguide feed network for Ku band satellite reception systems," *IEEE Transactions on Antennas and Propagation*, vol. 62, no. 4, pp. 2258–2263, 2014.
- [13] A. U. Zaman and P.-S. Kildal, "Wide-band slot antenna arrays with single-layer corporate-feed network in ridge gap waveguide technology," *IEEE Transactions on Antennas and Propagation*, vol. 62, no. 6, pp. 2992–3001, 2014.
- [14] R. J. Bolt, D. Cavallo, G. Gerini et al., "Characterization of a dual-polarized connected-dipole array for ku-band mobile terminals," *IEEE Transactions on Antennas and Propagation*, vol. 64, no. 2, pp. 591–598, 2016.
- [15] M. Ettorre, F. F. Manzillo, M. Casaletti, R. Sauleau, L. Le Coq, and N. Capet, "Continuous transverse stub array for ka-band applications," *IEEE Transactions on Antennas and Propagation*, vol. 63, no. 11, pp. 4792–4800, 2015.
- [16] S.-G. Zhou, P. Dong, G.-L. Huang, C.-Y. Sim, and J.-Y. Li, "Wideband antenna array with full metal structure and air-filled microstrip feeding network," *IEEE Transactions on Antennas and Propagation*, vol. 65, no. 6, pp. 3041–3048, 2017.
- [17] Y. Wang and Z. Du, "Dual-polarized slot-coupled microstrip antenna array with stable active element pattern," *IEEE Transactions on Antennas and Propagation*, vol. 63, no. 9, pp. 4239–4244, 2015.

## Research Article

# A Reactance Compensated Three-Device Doherty Power Amplifier for Bandwidth and Back-Off Range Extension

Shichang Chen,<sup>1,2</sup> Weiwei Wang,<sup>1</sup> Kuiwen Xu,<sup>1</sup> and Gaofeng Wang <sup>1</sup>

<sup>1</sup>The Key Lab of RF Circuits and Systems of the Ministry of Education of China, Microelectronic CAD Center, Hangzhou Dianzi University, Zhejiang, China

<sup>2</sup>State Key Laboratory of Millimeter Waves, Southeast University, Nanjing, China

Correspondence should be addressed to Gaofeng Wang; [gaofeng@hdu.edu.cn](mailto:gaofeng@hdu.edu.cn)

Received 22 October 2017; Revised 9 March 2018; Accepted 29 March 2018; Published 8 May 2018

Academic Editor: Daniele Pinchera

Copyright © 2018 Shichang Chen et al. This is an open access article distributed under the Creative Commons Attribution License, which permits unrestricted use, distribution, and reproduction in any medium, provided the original work is properly cited.

This paper proposes a new broadband Doherty power amplifier topology with extended back-off range. A shunted  $\lambda/4$  short line or  $\lambda/2$  open line working as compensating reactance is introduced to the conventional load modulation network, which greatly improves its bandwidth. Underlying bandwidth extension mechanism of the proposed configuration is comprehensively analyzed. A three-device Doherty power amplifier is implemented for demonstration based on Cree's 10 W HEMTs. Measurements show that at least 41% drain efficiency is maintained from 2.0 GHz to 2.6 GHz at 8 dB back-off range. In the same operating band, saturation power is larger than 43.6 dBm and drain efficiency is higher than 53%.

## 1. Introduction

As known to all, frequencies are scarce resources nowadays due to the booming of diverse wireless techniques. Therefore, sophisticated modulation schemes must be applied to achieve high data rates in a limited frequency bandwidth. At the same time of enjoying high data throughput, the large peak-to-average power ratios (PAPRs) accompanying these modulations also bring up several undesired effects to hardware implementations. The most evident impact is for power amplifiers (PAs), as they have to operate at large back-off regions to keep good linearity. The by-product of this feature is drastically deteriorated efficiency.

In the past few years, sorts of efficiency-boosting PA solutions such as envelop tracking [1], outphasing [2], and Doherty [3–18] have been reported to fight against efficiency reduction caused by high PAPR signals. Among them, the Doherty PA is considered as one of the best candidates, because it is simple in structure and easy for implementation. Consisting of two amplifiers (carrier and peaking) biased independently, a classical Doherty PA achieves peak efficiencies at both saturation and 6 dB back-off power conditions. This architecture has become the mainstream for base-station

PA designs. Nevertheless, certain communication schemes such as LTE-Advance and upcoming 5G may have several subcarriers; the corresponding PAPR value is still increasing. As a result, techniques like asymmetric subamplifier size [11] and multiway [14–16] for improving back-off range for Doherty PAs have been widely investigated. Large device size for the peaking PA is used in the asymmetric solution. However, it is not easy to find matched devices in practice and the acquirable range improvement is limited. The multiway structure basically brings in several peaking amplifiers and one carrier PA, which is believed to have a large back-off range, whose peak efficiency locations are defined by the number and size of the peaking amplifiers.

Besides, wideband communication is highly demanded today in order to support multiple-band and multifunction operation in a single system. Thereafter, bandwidth enhancement techniques for Doherty PA become hot research topic. In the literature, some efforts on modifying the load modulation networks (LMN) have achieved substantial improvements. However, most of them are still complicated in structures and are mainly limited to conventional two-way Doherty architecture [7–13].

Based on the authors' previous work presented in [18], two novel LMN configurations with shunt compensating reactance are proposed in this paper. By introducing  $\lambda/4$  short line or  $\lambda/2$  open line to the conventional LMN, the modulated impedance can have greatly reduced variation against frequency deviation, therefore improving the overall bandwidth of the Doherty PA. Systematical design concept and comprehensive theoretical analysis of the two new structures are given for good illustration.

The remainder of this paper is organized as follows. Section 2 explains the underlying confinement of the conventional structure and introduces the principle of the proposed designs. In Section 3, a three-device Doherty PA circuit with large high-efficiency back-off range is realized for demonstration. Simulated and measured results are also presented, and decent wideband operational characteristics are successfully obtained. Finally, Section 4 gives the conclusion.

## 2. Proposed Load Modulation Network

**2.1. Background.** As the key element of a Doherty PA, the conventional LMN is made up of two impedance inverters.  $\lambda/4$  transmission lines are generally adopted as a common practice. However, due to the frequency dispersion effect of the  $\lambda/4$  transformers, the conventional LMN is inherently narrow in bandwidth, which finally confines the bandwidth of the entire Doherty PA. In other words, proper load modulation can be maintained only at a single frequency. When the operational frequency deviates from the center ( $f_0$ ), the impedance modulated reduces quickly from the nominal value and PA's efficiency deteriorates as a consequence [6, 7]. Fortunately, it is found that the impedance bandwidth of the LMN can be increased by properly adding a reactive element to neutralize this dispersion. In [6], a LC shunt network is exploited as compensating reactance. However, detailed operational mechanism analysis is not given, and the highest frequency that can support is limited due to the low  $Q$ -factor of the LC resonant circuit.

Two novel LMN topologies with shunt stubs are proposed herein to have extended operational bandwidth. A shunt  $\lambda/4$  short stub and  $\lambda/2$  open stub are connected to the junction point of the subamplifiers, as shown in Figures 1(b) and 1(c), respectively. Detailed analysis will be given to verify the potentiality of the proposed ideas. Based on this, a three-device design with large bandwidth and back-off range is then implemented for verification.

**2.2. Proposed LMN with a Shunt Quarter-Wavelength Short Stub.** As well known, the operation of a Doherty PA is roughly classified into two conditions: low-power and high-power. When the power is low, the carrier amplifier operates only and it completely determines the overall performance.

Define the center frequency as  $f_0$  and the normalized frequency as  $\bar{f} = f/f_0$ . For the typical LMN as shown in Figure 1(a), the impedance seen at the junction point  $Z_{J,\text{conv}}$  is frequency dependent, and its expression is calculated as below according to classic transmission line theory [19]

$$Z_{J,\text{conv}} = Z_L \frac{Z_0 + jZ_L \tan(\bar{f} \cdot \pi/2)}{Z_L + jZ_0 \tan(\bar{f} \cdot \pi/2)}, \quad (1)$$

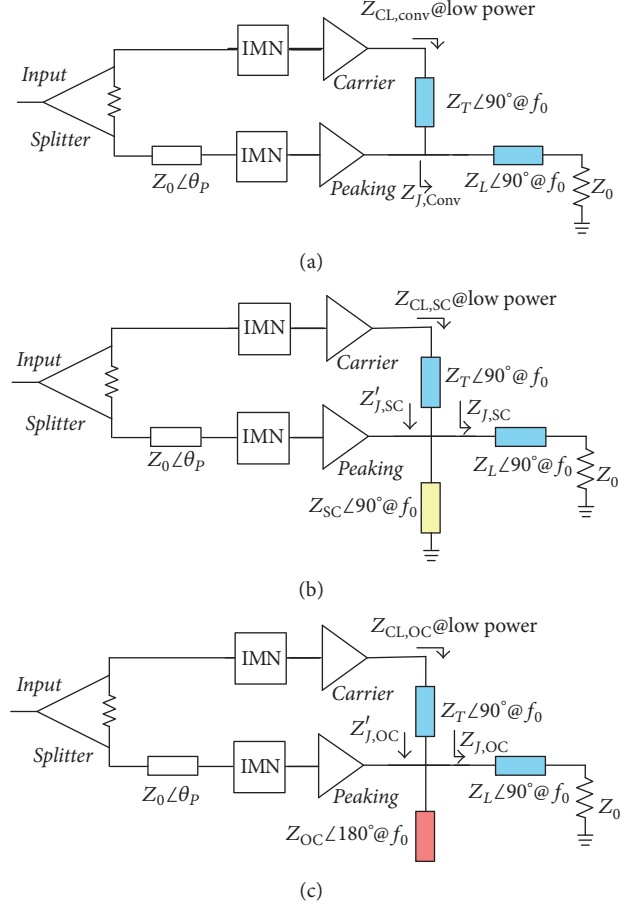


FIGURE 1: Simplified Doherty PA diagrams based on (a) conventional LMN; (b) LMN with  $\lambda/4$  short stub; (c) LMN with  $\lambda/2$  open stub.

where  $Z_L$  is the characteristic impedance of the output  $\lambda/4$  line and  $Z_0$  stands for the load ( $50 \Omega$  typically).

As a consequence, the carrier PA impedance produced by the conventional LMN  $Z_{\text{CL,conv}}$  can be expressed as

$$Z_{\text{CL,conv}} = Z_T \frac{Z_{J,\text{conv}} + jZ_T \tan(\bar{f} \cdot \pi/2)}{Z_T + jZ_{J,\text{conv}} \tan(\bar{f} \cdot \pi/2)}, \quad (2)$$

where  $Z_T$  represents the characteristic impedance of the  $\lambda/4$  line after the carrier PA.

On the other hand, for the proposed LMN shunted with  $\lambda/4$  short line as shown in Figure 1(b), the expression of the impedance for the carrier  $Z_{\text{CL,SC}}$  is now derived using the following equations:

$$Y_{J,\text{SC}} = \frac{1}{Z_{J,\text{SC}}} = \frac{1}{Z_L} \frac{Z_L + jZ_0 \tan(\bar{f} \cdot \pi/2)}{Z_0 + jZ_L \tan(\bar{f} \cdot \pi/2)}, \quad (3)$$

$$Z'_{J,\text{SC}} = \frac{1}{(Y_{J,\text{SC}} - j/Z_{\text{SC}} \tan(\bar{f} \cdot \pi/2))}, \quad (4)$$

$$Z_{CL,SC} = Z_T \frac{Z'_{J,SC} + jZ_T \tan(\bar{f} \cdot \pi/2)}{Z_T + jZ'_{J,SC} \tan(\bar{f} \cdot \pi/2)}, \quad (5)$$

where the subscript SC denotes short circuit condition and  $Z_{SC}$  is the characteristic impedance of the shunt line. Based on (2) and (5), the real and imaginary parts of the carrier impedance against frequency can be extracted by simple mathematical derivations.

Figure 2 depicts the frequency response of  $Z_{CL,SC}$  under different  $Z_{SC}$  values (12, 17, and 22 Ohms) along with that of  $Z_{CL,conv}$ . It needs to stress that the normalized values (to  $Z_0$ ) of  $Z_T$  and  $Z_L$  are unity and  $1/\sqrt{2}$  in this particular comparison, same as the classical Doherty LMN treatment. As can be observed from the figure, in each single case the carrier impedances produced by both cases are maintained around  $100 \Omega$  ( $2Z_0$ ) at the center frequency, agreeing with the classical Doherty PA theory. This is because  $\lambda/4$  short line produces infinite impedance at the center frequency, which has no influence on the modulated impedance. Nevertheless, when the operation frequency deviates from  $f_0$ , the real part of the carrier impedance produced by the conventional LMN decreases sharply. This impedance reduction usually translates to unwanted efficiency degradation and bandwidth reduction. In contrast, by adding the shunt line as compensating reactance, much more stabilized impedances are achieved in a certain band by applying the proposed topological scheme, as indicated by the larger and flatter real part response.

For the imaginary side, all cases exhibit similar capacitive/inductive behaviors at frequencies above/below the center frequency. However, the variation presented by the conventional LMN is much larger than that of the proposed LMNs. From the PA design aspect, a much flatter ohmic and smaller

reactive loading usually means it is easier to design a broadband matching network and achieve larger bandwidth afterwards [7]. At the center frequency, the shunt stub is equivalent to an open-circuit load seen at the junction point; therefore no loading effect occurs. This is demonstrated by the identical load impedances presented at  $f_0$  for all the configurations analyzed.

In the high-power condition, all subamplifiers operate. Suppose the fundamental currents produced by the two sub-amplifier cells are identical, the corresponding impedances can be easily calculated based on the diagram shown in Figures 1(a) and 1(b). Figures 3 and 4 compare the simulated carrier and peaking impedance behaviors at saturation with different LMN schemes, whose real and imaginary parts are monitored separately. It is obvious that the carrier impedance has similar profile to that of the low-power condition. To be specific, impedance variations against frequency deviation are significantly suppressed, for both the imaginary and real parts. On the peaking side, although the conventional design shows relative flatter impedance responses, the variation ratio is not as much as that for the carrier PA. Thus, by optimizing the characteristic impedances of the shunt stub, overall bandwidth enhancement can still be ensured.

### 2.3. Proposed LMN with a Shunt Half-Wavelength Open Stub.

Similar to the configuration shown above, a shunt  $\lambda/2$  open stub can also be used as effective compensating reactance. The theoretical analysis of the configured LMN with a shunt  $\lambda/2$  open stub is much alike to the aforementioned case. Figure 1(c) gives its schematic diagram. The carrier impedance at the low-power condition  $Z_{CL,OC}$  can be derived as

$$Z'_{J,OC} = \frac{1}{\left(\frac{1}{Z_L} \left( (Z_L + jZ_0 \tan(\bar{f} \cdot \pi/2)) / (Z_0 + jZ_L \tan(\bar{f} \cdot \pi/2)) \right) + j \tan(\bar{f} \cdot \pi/2) / Z_{OC} \right)}, \quad (6)$$

$$Z_{CL,OC} = Z_T \frac{Z'_{J,OC} + jZ_T \tan(\bar{f} \cdot \pi/2)}{Z_T + jZ'_{J,OC} \tan(\bar{f} \cdot \pi/2)},$$

where  $Z_{OC}$  is the characteristic impedance of the shunt line and the subscript OC denotes open circuit.

Figure 5 compares the calculated  $Z_{CL,OC}$  behaviors of different  $Z_{OC}$  values (24, 44, and 64 Ohms) along with that of  $Z_{CL,conv}$ . The normalized impedances  $Z_T$  and  $Z_L$  are again unity and  $1/\sqrt{2}$ . It can be seen that, by adopting a proper characteristic impedance (e.g., 44  $\Omega$ ), the modulated impedances from the proposed LMN may have a much flatter response versus frequency than that the conventional LMN can provide. Curves for impedances presented to the carrier and peaking subamplifiers at high-power condition are shown in Figures 6 and 7, respectively. As before, once the characteristic impedance of the shunt stub is appropriately chosen, smaller variation of the carrier impedance is achievable for the proposed topology by contrast with the conventional design. As a consequence, larger bandwidth can

be obtained as impedance matching becomes much easier. In addition, the two compensating methods mentioned above generally have different parameters regarding characteristic impedance and length. In practice, which configuration to use is mainly decided after considering the bandwidth effects and realization convenience overall.

## 3. Circuit Realization

### 3.1. Wideband Three-Device Doherty Power Amplifier Design.

To deal with signals with high PAPRs, total peaking device periphery must be larger than that of the carrier device. Herein, a dual-peaking single-carrier Doherty PA is therefore devised, aiming at large back-off range. In order to have wideband operational capability at the same time, the LMN

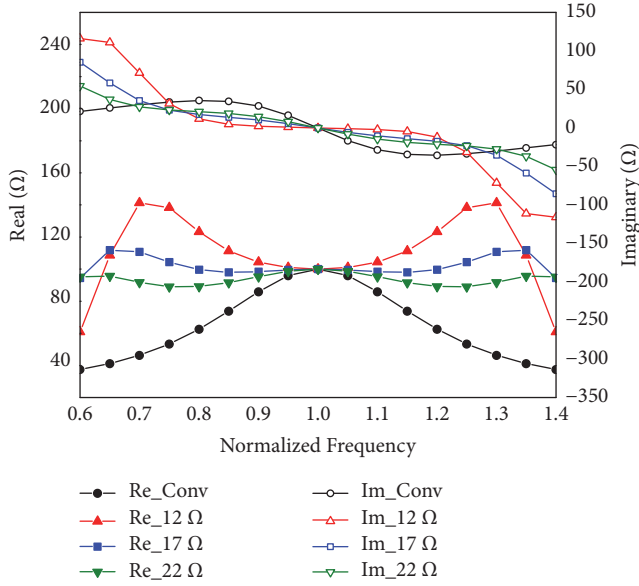


FIGURE 2: Carrier impedance comparison between the conventional LMN and the wideband LMN with a shunt  $\lambda/4$  short stub of different characteristic impedances at low-power condition.

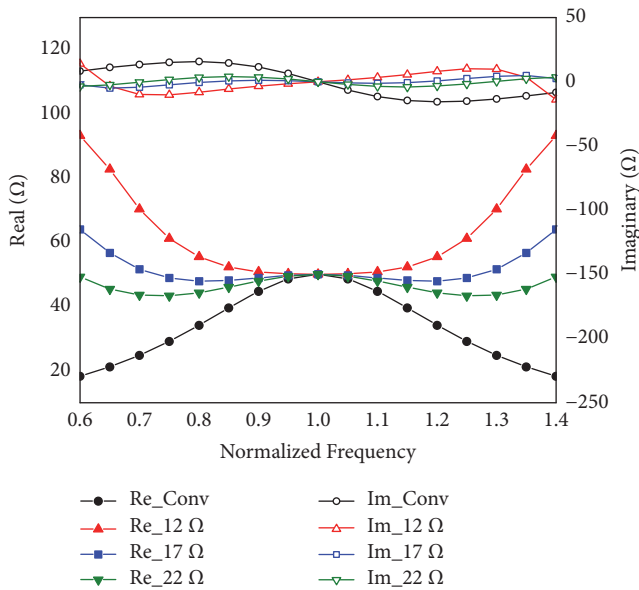


FIGURE 3: Carrier impedance comparison between the conventional LMN and the wideband LMN with a shunt  $\lambda/4$  short stub of different characteristic impedances at high-power condition.

with a shunted short  $\lambda/4$  stub analyzed above is updated to fit a three-way structure, as depicted in Figure 8. Specifically speaking, the carrier PA is placed at the center, whose output is evenly shared by the two symmetrically aligned peaking amplifiers to form load modulation.

It is well acknowledged that the operation of a Doherty PA differs at low-power and high-power regions. For low-power scenario, both peaking PAs are turned off and the carrier PA operates solely. The shunt  $\lambda/4$  line on each branch

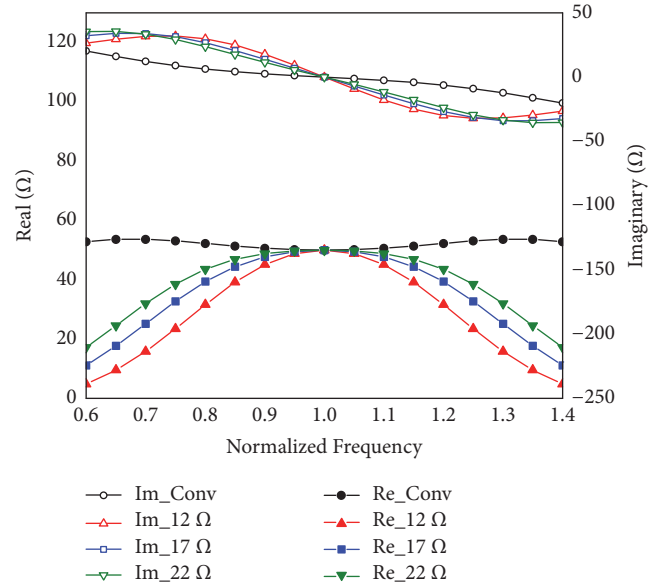


FIGURE 4: Peaking impedances at high-power condition for the conventional LMN and the proposed LMN with a shunt  $\lambda/4$  short stub of different characteristic impedances.

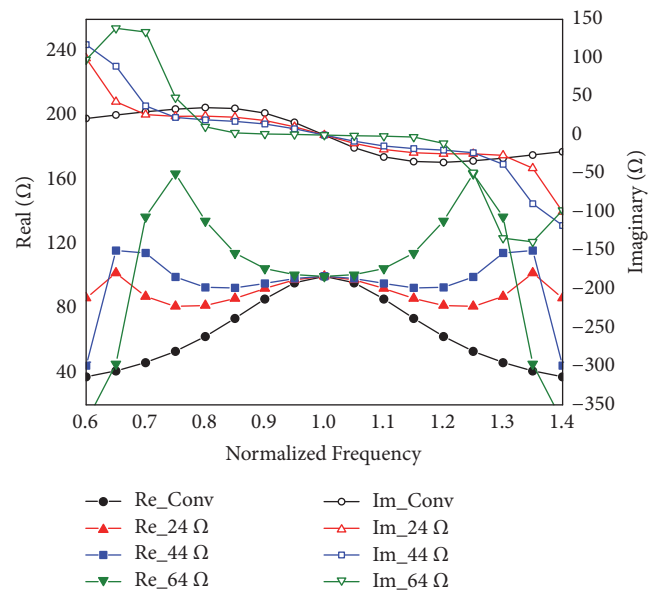


FIGURE 5: Carrier impedance comparison between the conventional LMN and the wideband LMN with a shunt  $\lambda/2$  open stub of different characteristic impedances at low-power condition.

is divided into two parts at the junction  $VP_i$  ( $i = 1, 2$ ). As long as each peaking PA is connected with a proper offset line after the output matching network, the impedances seen into the peaking PAs from the two junction points  $VP_1$  and  $VP_2$  can be made very high [5]. Reverse power leakage is therefore prevented. In other words, the peaking branches are *isolated* from the shunt line, and this LMN is degenerated to that of the shunt stub configuration introduced before for the carrier PA. The impedance presented exhibits frequency response similar



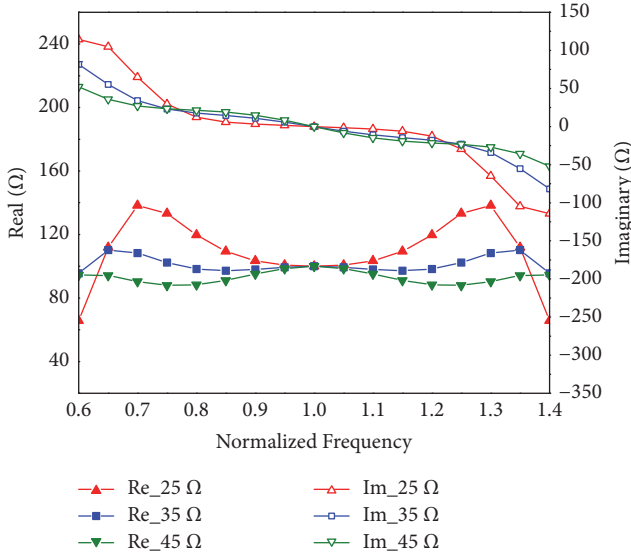


FIGURE 9: Carrier impedance of the proposed three-device DPA with shunt lines of different characteristic impedances at low-power condition.

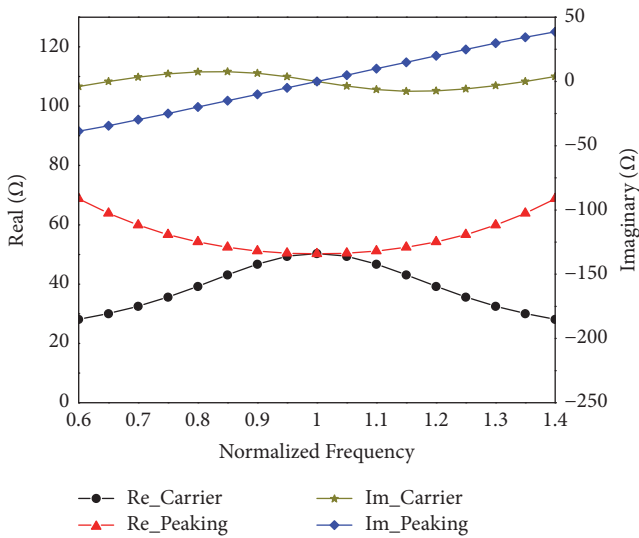


FIGURE 10: Carrier and peaking impedances for the proposed three-device DPA with  $\delta = 1$  and  $Z_{SC} = 35 \Omega$  at high-power condition.

At the input terminal, a wideband power division network is used to distribute the input power into three paths. As the same transistors are used to build the three subamplifiers, the power gain of the peaking cells is smaller than that of the carrier cell due to their lower biasing conditions. As a result, uneven power division is chosen to deliver larger power to the peaking paths. Figure 12 shows the diagram of the devised wideband power division network. Port 1 is the input terminal, and port 2 is connected to the carrier PA, whereas ports 3 and 4 are for the peaking paths. The upper and lower parts are exactly the same, and the isolation resistors  $R_1 = R_2 = 100 \Omega$ . The characteristic impedances of the six lines are  $Z_1 = 64.1 \Omega$ ,  $Z_2 = 91.7 \Omega$ ,  $Z_3 = 44.2 \Omega$ , and  $Z_4 = 57.1 \Omega$ . All the transmission lines

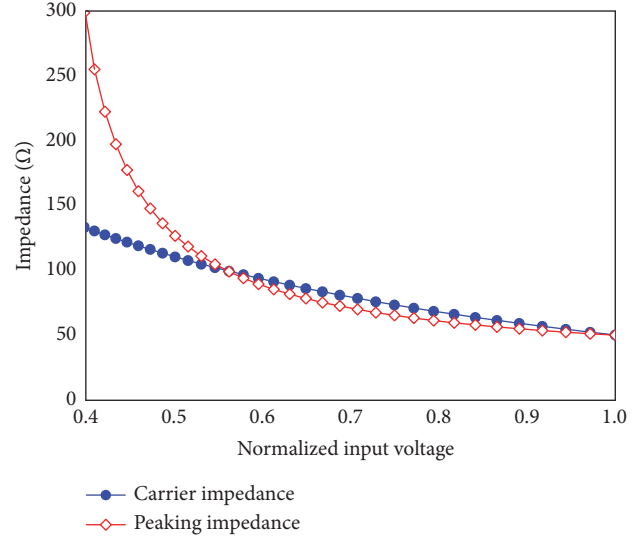


FIGURE 11: Carrier and peaking impedance variations for the proposed three-device DPA with  $\delta = 1$  and  $Z_{SC} = 35 \Omega$  as a function of input voltage.

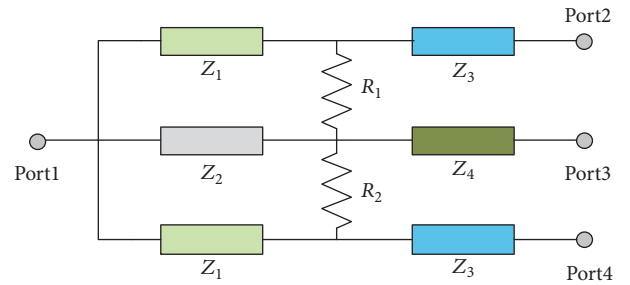


FIGURE 12: Wideband three-way uneven power divider diagram.

are  $\lambda/4$  long at the center frequency  $f_0$  ( $f_0$  equals 2.3 GHz in this particular design). Figure 13 depicts the simulated performance of the divider in Keysight ADS momentum. Note that  $S_{31}$  and  $S_{41}$  are maintained around  $-6.2$  dB and  $-4.6$  dB throughout the frequency band from 1.5 to 3.0 GHz. This means that the stimulus for peaking PAs is about 1.5 dBm larger than that for the carrier PA. This treatment is intended for identical driving capabilities at saturation among the three subamplifiers. In addition, the return losses and isolations between the output ports are all below  $-15$  dB.

As optimal source and load impedances change with operating frequency, extensive source-pull and load-pull simulations are conducted to find the frequency-dependent target impedances. Output matching networks and offset lines are carefully designed to maintain broadband operation of the whole Doherty PA. Besides, broadband input matching networks with the classical cascaded low-pass type topology are designed for all the three subamplifiers before final circuit assembly. A phase balance line is also added at the peaking input in order to maximize saturation output power. Furthermore, DC supplies can be directly added to end of the short stubs in the meantime, making DC powering more

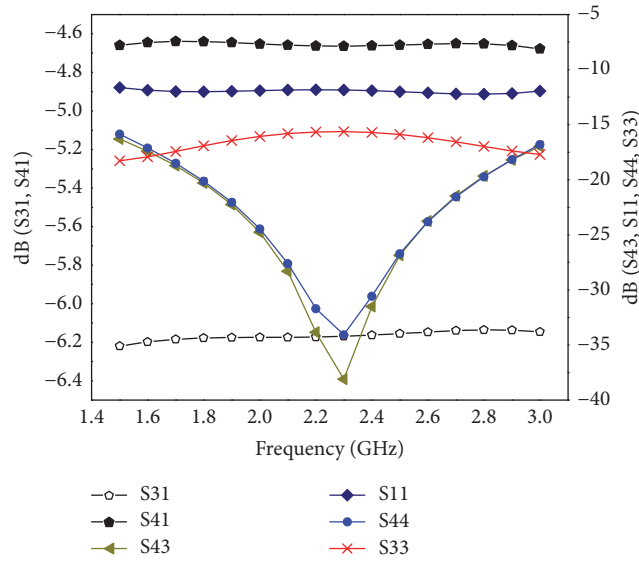


FIGURE 13: Simulated performances of the devised three-way uneven power division network.

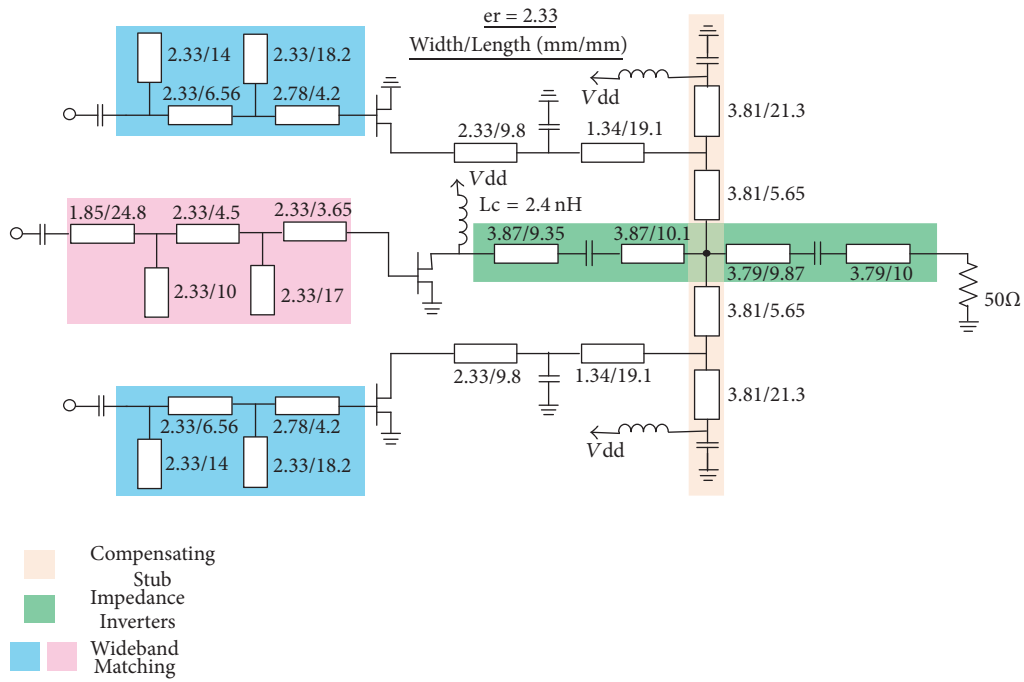


FIGURE 14: Final topology of the implemented DPA structure.

convenient. Careful optimization has been made to ensure decent performances in a large operational bandwidth.

Figure 14 gives the topology of the realized Doherty PA, shown at the bottom of this page. Input power division network is not plotted for the sake of simplicity. The prototype circuit is implemented on a Duroid 5870 substrate with permittivity of 2.33 and a height of 31 mil. The demonstrating hardware for the open stub case described in Section 2.3 is not

devised, because these two configurations have similar theoretical fundamentals for bandwidth extension as introduced above.

3.2. *Simulated and Measured Results.* This particular three-way circuit is fully characterized in Keysight ADS simulator. All subamplifiers are constructed with the 10-W GaN HEMT CGH40010 provided by Cree. Simulations are performed

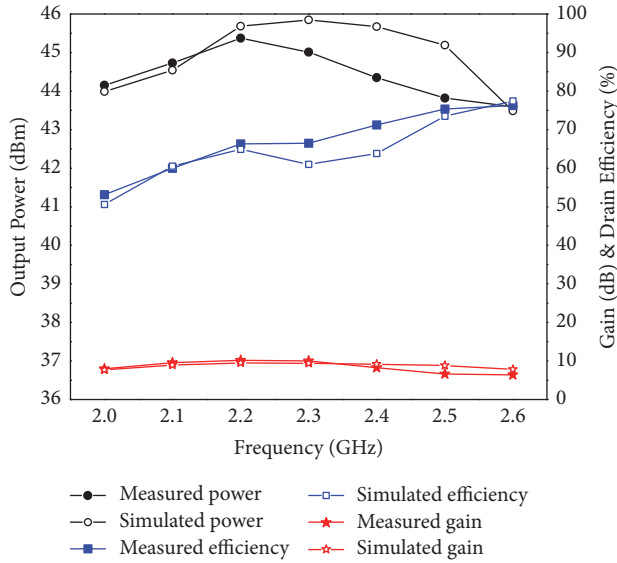


FIGURE 15: Efficiency and gain curves from simulation and measurement of the implemented prototype at saturation condition.

with a large signal transistor model provided by manufacture. Biasing conditions are carefully optimized to realize the power dependent opening sequences of the subamplifiers. To be specific, the carrier cell is biased at  $-2.7$  V, corresponding to class-AB mode. On the other hand, the biasing voltages of the two peaking cells are  $-6.5$  V, corresponding to class-C mode. The supply voltages ( $V_{dd}$ ) are all set to 28 V. By careful device alignment and wiring, the entire circuit is kept concise and symmetry.

Figure 15 shows the simulated and measured characteristics at saturation under continuous wave (CW) excitation in terms of gains, maximum output powers, and drain efficiencies of the designed Doherty PA. It is clear to see that a minimum of 53% drain efficiency is recorded in measurement in a 600 MHz bandwidth, ranging from 2.0 GHz to 2.6 GHz. 76% efficiency is obtained at 2.6 GHz, which is the highest value in this observed band. In addition, at least 43.6 dBm output power is maintained, and a peak value of 45.4 dBm appears at 2.2 GHz. The measurements and simulations agree well, and the small discrepancies may be caused by model inaccuracy, fabrication tolerance, and so on.

As two peaking amplifiers are applied, the total device periphery of the peaking part is larger than the carrier part, and thus an increased power back-off range is realized. Figure 16 compares the tested and simulated gain and drain efficiency curves at 8 dB back-off power from 2.0 GHz to 2.6 GHz. Throughout this frequency band, over 41% drain efficiency is successfully maintained. This accounts for a rational frequency bandwidth of 26%.

To better characterize the efficiency profile of the fabricated circuit, Figure 17 depicts the registered gain and drain efficiency profiles as a function of the output power in the same frequency band with a 100 MHz interval. It is readily seen that the proposed Doherty PA approximately follows the classic Doherty type efficiency profiles at all the frequency

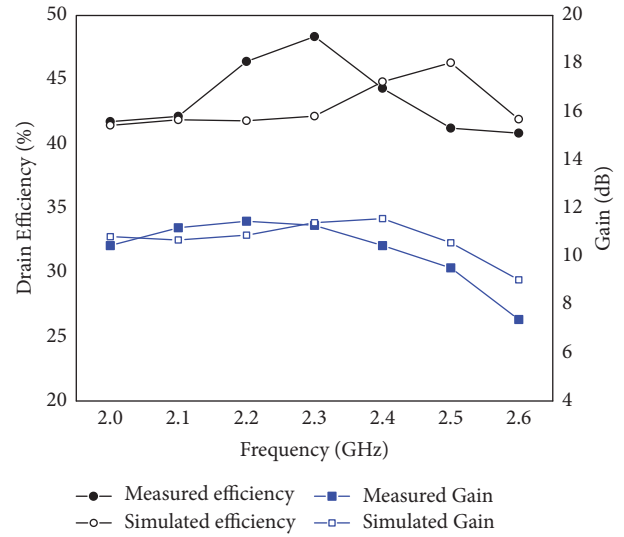


FIGURE 16: Efficiency and gain curves from simulation and measurement of the implemented prototype at 8 dB back-off range.

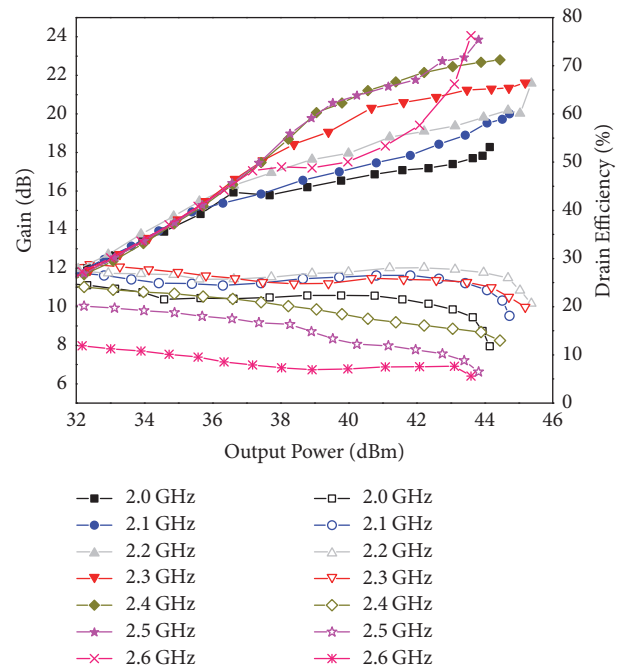


FIGURE 17: Registered gain and drain efficiency profiles as a function of output power.

components. Table 1 lists the comparison of several published wideband Doherty PAs and this work.

Moreover, a 20 MHz LTE modulated signal with 8 dB PAPR value is used to test the proposed circuit prototype for further performance evaluation. Figure 18 gives the registered average drain efficiency and adjacent channel leakage ratios (ACLR) as a function of output power at 2.3 GHz. It is readily seen that about 46% drain efficiency is achieved at 8 dB back-off power, while the corresponding ACLR value is around  $-29$  dBc. Besides, digital predistortion (DPD) technique [20]

TABLE I: Performance summary of broadband Doherty PAS.

Ref.	Config.	Freq. (GHz)	DE. @ Sat. (Max/Min%)	DE. @ OBO (Max/Min%)	Pout (dBm)
[6]	2-way	0.7–0.95	67/53	56/48 @6-dB	>43
[7]	2-way	3.0–3.6	66/55	56/38 @6-dB	43–44
[8]	2-way uneven biasing	1.7–2.6	55/50	55/41 @6-dB	42.1–45.3
[11]	2-way die	1.05–2.55	83/45	58/35 @6-dB	44.6–46.3
[12]	2-way	1.96–2.46	60/46	44/40 @6-dB	39.8–41.7
[15]	3-way	0.73–0.98	67/53	64/49 @9dB	42.7–44.6
[16]	3-stage uneven biasing	0.7–0.95	75/60	65/47 @9-dB	42.9–44.7
This work	3-device	2.0–2.6	76/53	48/41 @8-dB	43.6–45.4

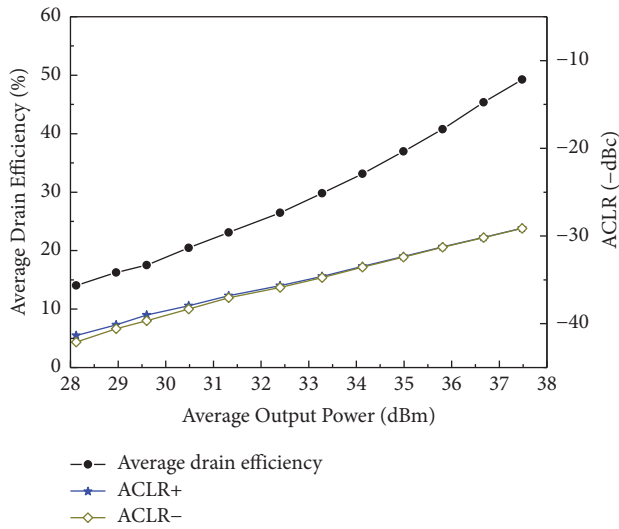


FIGURE 18: Measured average drain efficiency and ACLR values as a function of average output power at 2.3 GHz under a 20 MHz LTE signal excitation.

is applied to the devised DPA, and the ACLR value reduced to  $-51$  dBc after DPD treatment, which indicates a good linearization capability. Figure 19 depicts the photography of the fabricated Doherty PA.

#### 4. Conclusion

Two new load modulation networks with a shunt  $\lambda/4$  short stub and  $\lambda/2$  open stub to improve Doherty PA bandwidth have been proposed. Underlying principles regarding the bandwidth merits have been fully analyzed. A single-carrier dual-peaking Doherty PA circuit was implemented based on the updated topological scheme for verification. Large bandwidth and high-efficiency back-off range are achieved simultaneously.

#### Conflicts of Interest

The authors declare that they have no conflicts of interest.

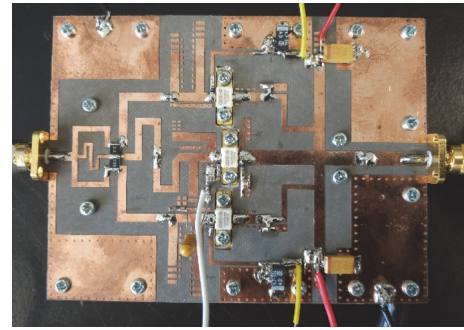


FIGURE 19: Photography of the fabricated three-device Doherty PA.

#### Acknowledgments

This work was supported in part by the National Natural Science Foundation of China under Grants no. 61601160, no. 61411136003, and no. 61331007 and by the Open Research Fund of Key Laboratory of Millimeter Waves, Southeast University, under Grant no. K201820.

#### References

- [1] S. Jin, B. Park, K. Moon et al., "A Highly Efficient CMOS Envelope Tracking Power Amplifier Using All Bias Node Controls," *IEEE Microwave and Wireless Components Letters*, vol. 25, no. 8, pp. 517–519, 2015.
- [2] S. Lee and S. Nam, "A cmos outphasing power amplifier with integrated single-ended chireix combiner," *IEEE Transactions on Circuits and Systems II: Express Briefs*, vol. 57, no. 6, pp. 411–415, 2010.
- [3] S. Chen and Q. Xue, "Optimized load modulation network for doherty power amplifier performance enhancement," *IEEE Transactions on Microwave Theory and Techniques*, vol. 60, no. 11, pp. 3474–3481, 2012.
- [4] S. Chen, Z. Cheng, G. Wang, and Q. Xue, "Compact Doherty Power Amplifier Design for  $2 \times 2$  Multiple-Input Multiple-Output System," *IEEE Microwave and Wireless Components Letters*, vol. 26, no. 3, pp. 216–218, 2016.
- [5] R. Quaglia, M. Pirola, and C. Ramella, "Offset lines in doherty power amplifiers: Analytical demonstration and design," *IEEE*

- Microwave and Wireless Components Letters*, vol. 23, no. 2, pp. 93–95, 2013.
- [6] M. N. A. Abadi, H. Golestaneh, H. Sarbishaei, and S. Boumaiza, “An extended bandwidth Doherty power amplifier using a novel output combiner,” in *Proceedings of the 2014 IEEE MTT-S International Microwave Symposium, IMS 2014*, Tampa, Fla, USA, June 2014.
  - [7] J. M. Rubio, J. Fang, V. Camarchia, R. Quaglia, M. Pirola, and G. Ghione, “3-3.6-GHz wideband GaN Doherty power amplifier exploiting output compensation stages,” *IEEE Transactions on Microwave Theory and Techniques*, vol. 60, no. 8, pp. 2543–2548, 2012.
  - [8] K. Bathich, A. Z. Markos, and G. Boeck, “Frequency response analysis and bandwidth extension of the Doherty amplifier,” *IEEE Transactions on Microwave Theory and Techniques*, vol. 59, no. 4, pp. 934–944, 2011.
  - [9] D. Gustafsson, C. M. Andersson, and C. Fager, “A modified doherty power amplifier with extended bandwidth and reconfigurable efficiency,” *IEEE Transactions on Microwave Theory and Techniques*, vol. 61, no. 1, pp. 533–542, 2013.
  - [10] R. Giofre, P. Colantonio, F. Giannini, and L. Piazzon, “New output combiner for doherty amplifiers,” *IEEE Microwave and Wireless Components Letters*, vol. 23, no. 1, pp. 31–33, 2013.
  - [11] R. Giofre, L. Piazzon, P. Colantonio, and F. Giannini, “A closed-form design technique for ultra-wideband doherty power amplifiers,” *IEEE Transactions on Microwave Theory and Techniques*, vol. 62, no. 12, pp. 3414–3424, 2014.
  - [12] M. Akbarpour, M. Helaoui, and F. M. Ghannouchi, “A transformer-less load-modulated (TLLM) architecture for efficient wideband power amplifiers,” *IEEE Transactions on Microwave Theory and Techniques*, vol. 60, no. 9, pp. 2863–2874, 2012.
  - [13] J. Qureshi, W. Sneijers, R. Keenan, L. deVreede, and F. van Rijs, “A 700-W peak ultra-wideband broadcast Doherty amplifier,” in *Proceedings of the 2014 IEEE/MTT-S International Microwave Symposium - MTT 2014*, pp. 1–4, Tampa, Fla, USA, June 2014.
  - [14] Y. Yang, J. Cha, B. Shin, and B. Kim, “A fully matched N-way Doherty amplifier with optimized linearity,” *IEEE Transactions on Microwave Theory and Techniques*, vol. 51, no. 3, pp. 986–993, 2003.
  - [15] H. Golestaneh, F. A. Malekzadeh, and S. Boumaiza, “An extended-bandwidth three-way doherty power amplifier,” *IEEE Transactions on Microwave Theory and Techniques*, vol. 61, no. 9, pp. 3318–3328, 2013.
  - [16] A. Barthwal, K. Rawat, and S. Koul, “Bandwidth Enhancement of Three-Stage Doherty Power Amplifier Using Symmetric Devices,” *IEEE Transactions on Microwave Theory and Techniques*, vol. 63, no. 8, pp. 2399–2410, 2015.
  - [17] S. Chen, G. Wang, Z. Cheng, P. Qin, and Q. Xue, “Adaptively Biased 60-GHz Doherty Power Amplifier in 65-nm CMOS,” *IEEE Microwave and Wireless Components Letters*, vol. 27, no. 3, pp. 296–298, 2017.
  - [18] S. Chen, P. Qiao, G. Wang, Z. Cheng, and Q. Xue, “A broadband three-device Doherty power amplifier based on a modified load modulation network,” in *Proceedings of the 2016 IEEE/MTT-S International Microwave Symposium (IMS)*, pp. 1–4, San Francisco, Calif, USA, May 2016.
  - [19] D. M. Pozar, *Microwave Engineering*, John Wiley & Sons, Inc, New York, NY, USA, 2nd edition, 1998.
  - [20] D. R. Morgan, Z. Ma, J. Kim, M. G. Zierdt, and J. Pastalan, “A generalized memory polynomial model for digital predistortion of RF power amplifiers,” *IEEE Transactions on Signal Processing*, vol. 54, no. 10, pp. 3852–3860, 2006.

## Research Article

# CORDIC-Based Multi-Gb/s Digital Outphasing Modulator for Highly Efficient Millimeter-Wave Transmitters

Dixian Zhao  and Pingyang He

National Mobile Communication Research Laboratory, School of Information Science and Engineering, Southeast University, Nanjing 211189, China

Correspondence should be addressed to Dixian Zhao; [dixian.zhao@seu.edu.cn](mailto:dixian.zhao@seu.edu.cn)

Received 16 December 2017; Accepted 31 March 2018; Published 7 May 2018

Academic Editor: Shichang Chen

Copyright © 2018 Dixian Zhao and Pingyang He. This is an open access article distributed under the Creative Commons Attribution License, which permits unrestricted use, distribution, and reproduction in any medium, provided the original work is properly cited.

This paper describes a high-speed CORDIC-based digital outphasing modulator. Fixed-point Matlab model of the outphasing modulator is developed to evaluate the system performance and define the circuit design parameters. Design issues such as signal quantization error, delay mismatch, and phase overflowing are addressed to enable hardware implementation. The complete outphasing modulator is fully custom designed in 40 nm CMOS, which can be integrated in a millimeter-wave outphasing transmitter to enhance the system average efficiency. Tested with 10.56 Gb/s 64-QAM, this work achieves an EVM of 3.2% and fulfils the IEEE 802.11ad spectral mask requirements.

## 1. Introduction

Linearization and efficiency enhancement techniques are always the focus in the design of power amplifiers (PAs) [1]. Figure 1 shows the characteristics of a typical linear PA. The PA only achieves the peak power-added efficiency ( $PAE_{MAX}$ ) near its saturated output power ( $P_{SAT}$ ). However, due to the high peak-to-average power ratio (PAPR), the PA has fairly low average output power ( $P_{AVG}$ ) and average power-added efficiency ( $PAE_{AVG}$ ). Note that the PDF represents the probability density function of the complex modulated signals. At millimeter-wave frequencies (mm-Wave), such issue becomes even more severe as the transistor operates at a large fraction of the  $f_T/f_{MAX}$  [2]. Therefore, the key challenge of mm-Wave multi-Gb/s transmitter (TX) is the poor average efficiency when transmitting complex modulated signals (e.g., 64-QAM).

The outphasing PA achieves linear amplification using highly efficient nonlinear PAs [3, 4], potentially alleviating the linearity/efficiency trade-off issue. The concept of outphasing is shown in Figure 2 with the phasor diagram of the outphasing vectors (i.e.,  $S_1(t)$  and  $S_2(t)$ ) and combined signal (i.e.,  $S(t)$ ). The signal component separator (SCS) is employed to generate the  $S_1(t)$  and  $S_2(t)$  based on  $S(t)$  [5]. The magnitude of the  $S(t)$  depends on the outphasing angle  $\varphi(t)$ . As a

result, the outphasing PA can achieve high linearity and high efficiency simultaneously. The work in [6] first time presents the fully integrated outphasing transmitter front-end at mm-Wave. It shows that even at mm-Wave the outphasing TX is able to perform linear amplification using switching or saturated power amplifiers (PAs), achieving nearly two times better average efficiency [6] than that of a conventional I/Q TX. Therefore, it is essential to develop a high-speed outphasing modulator to facilitate a fully integrated outphasing TX [7, 8]. The work in [9] presents an outphasing TX for 2.4-GHz WLAN with a delay-based phase modulator. However, it may require a delay resolution of 0.1 ps for a phase resolution of  $2^\circ$  when operating at 60 GHz and inevitably consumes high power. The work in [10] presents a digital outphasing modulator based on piece-wise linear functional approximation, but its speed will be limited if high-order modulation (e.g., 64-QAM) is applied due to the increased memory size of the look-up tables (LUTs) in the system.

In this paper, we report a fully custom designed digital outphasing modulator in 40 nm CMOS. Coordinate rotation digital computer (CORDIC) [11] is employed to realize the conversion between Cartesian and Polar coordinates, and different trigonometric functions. Issues such as signal quantization error, delay mismatch, and phase overflowing are

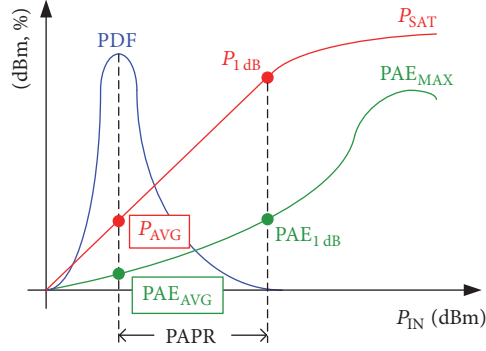


FIGURE 1: Characteristics of a typical linear PA.

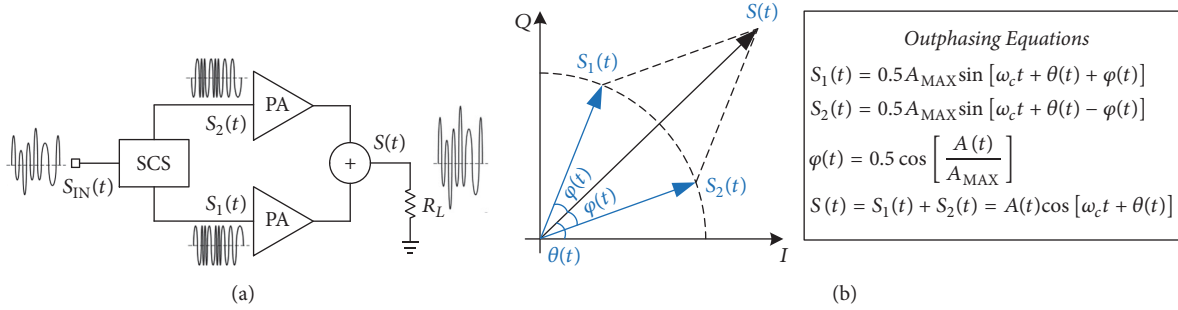


FIGURE 2: Outphasing system: (a) architecture and (b) phasor diagram.

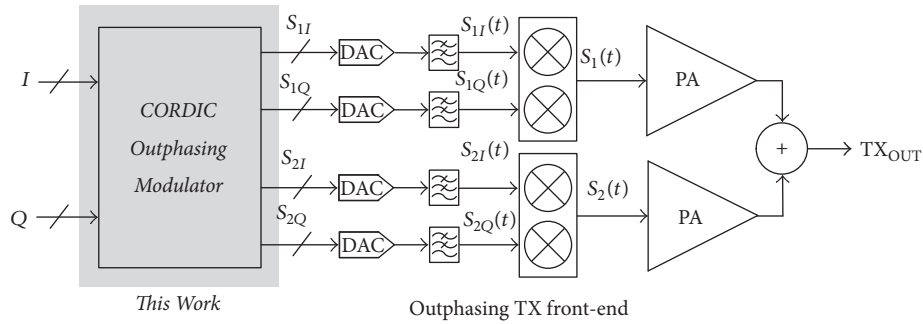


FIGURE 3: System architecture of the complete outphasing transmitter.

tackled to facilitate hardware implementation. The proposed outphasing modulator achieves simulated 10.56 Gb/s 64-QAM with an error-vector-magnitude (EVM) of 3.2% and fulfils the IEEE 802.11ad spectral mask requirements for 60 GHz communications. Section 2 describes the system architecture of the outphasing transmitter while Section 3 details the proposed CORDIC-based outphasing modulator. The circuit-level implementation and simulated results of the outphasing modulator are presented in Section 4 with the conclusion given in Section 5.

## 2. Outphasing Transmitter System Architecture

Figures 3 and 4 show the system architecture and phasor diagram of the outphasing transmitter where  $A(t)$ ,  $\theta(t)$  are

the amplitude and phase modulated signals, respectively, and outphasing angle  $\varphi(t)$  equals  $\cos^{-1}[A(t)/A_{MAX}]$ . The CORDIC-based outphasing modulator is tasked to generate the four multi-GHz digital baseband signals  $S_{1I}$ ,  $S_{1Q}$ ,  $S_{2I}$ , and  $S_{2Q}$ . They are converted to their analog counterparts  $S_{1I}(t)$ ,  $S_{1Q}(t)$ ,  $S_{2I}(t)$ , and  $S_{2Q}(t)$  through high-speed digital-to-analog converters (DACs), and up-converted by quadrature modulators to construct the desired outphasing signals  $S_1(t)$  and  $S_2(t)$  at the input of the two switching PAs. The linear amplification can be achieved at TX output by vectoring summing two outphasing signals.

It is seen that the outphasing TX requires 4 DACs, 4 reconstruction filters, and 2 I/Q modulators, twice as much as that of the conventional I/Q TX. However, the linearity requirement of these analog baseband circuits is relaxed due to the low peak-to-average-power ratio (PAPR) of the

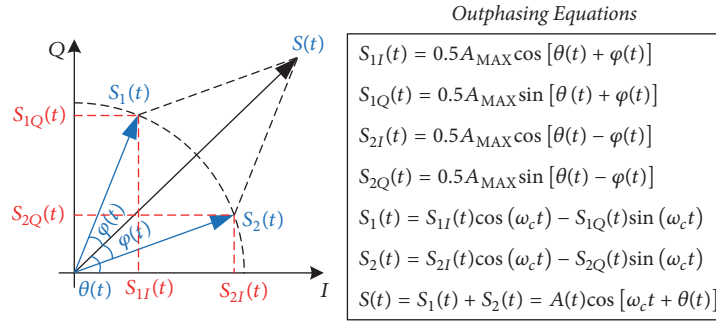


FIGURE 4: Phasor diagram of the outphasing transmitter with baseband signal decomposition.

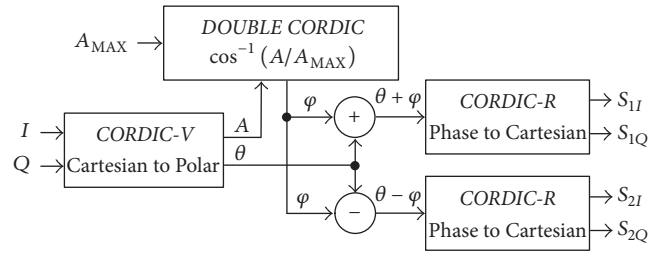


FIGURE 5: CORDIC-based outphasing modulator system diagram.

outphasing baseband signals [6]. Considering that the dc power of DAC is in exponential proportion to its linearity, the proposed outphasing system has no dc power penalty in its analog baseband circuits. In addition, prior-art 60 GHz outphasing TX front-end achieves 15% average efficiency for 16-QAM signals while conventional I/Q TX only has 7%. For a typical 60 GHz PA with 100 mW average output power for transmitting 16-QAM, the outphasing and IQ TXs consume 0.67 and 1.43 W, respectively. Depending on the data rates, the dc power of the proposed outphasing modulator varies between 30 and 150 mW, which gives outphasing TX huge efficiency benefit. Such benefit will be more pronounced for 64-QAM due to the increased PAPR.

### 3. CORDIC-Based Outphasing Modulator

CORDIC is a fast and efficient algorithm to compute common mathematical functions [11] as it only requires “add,” “subtract,” and “shift” operations. It is fully utilized in this work to realize high-speed outphasing modulator. Figure 5 shows the system diagram. The vectoring mode of CORDIC (CORDIC-V) is used to convert the input ( $I, Q$ ) signals to the polar form ( $A, \theta$ ) while the rotation mode of CORDIC (CORDIC-R) is to transform the phase signals  $\theta \pm \varphi$  to the four outphasing baseband signals. The most critical part of the outphasing modulator is to realize  $\cos^{-1}(x)$  function. The double CORDIC iterations [11, 12] are utilized in this work to compute  $\cos^{-1}(x)$ , which is also straightforward to implement in circuitry.

The fixed-point model of the outphasing modulator is developed in Matlab to evaluate the performance and define the circuit design parameters. In the simulation, the

outphasing TX front-end (see Figure 3) is assumed to be ideal. For hardware implementation, it is essential to determine the number of CORDIC iterations (i.e., CORDIC pipelined stages) and truncate the signals to balance the accuracy, speed, latency, and power consumption. Simulations indicate that CORDIC iterations have relatively minor impact on the system performance and eight iterations are sufficient to perform the coordinate conversions and to compute  $\cos^{-1}(x)$ . Quantization of each signal greatly degrades EVM and results in spectral regrowth. Regarding the number of bits required by the outphasing modulator, the limiting factor is the  $\cos^{-1}(x)$  double CORDIC block, but it is reasonable to set all the CORDIC blocks with the same word length without sacrificing the speed. Tested with 10.56 Gb/s 64-QAM signals (PAPR = 7.6 dB, root-raised cosine filter with a roll-off factor of 0.35), Figure 6 shows the simulated EVM and adjacent-channel-leakage ratio (ACLR). It is observed that when the number of bits equals 10, the EVM and ACLR flatten out to 2% and -60 dBc, respectively. It leaves sufficient margin and can be budgeted for other implementation nonidealities. To simplify the input interfacing and reduce DAC resolution, the input I/Q signals and the four outphasing signals (i.e.,  $S_{1I}$ ,  $S_{1Q}$ ,  $S_{2I}$ , and  $S_{2Q}$ ) are truncated to 8 and 7 bits, respectively. Simulation predicts that the performance degradation is negligible.

### 4. Circuit Implementation and Simulation Results

Based on the system design and simulation, all the building blocks of the CORDIC-based outphasing modulator are

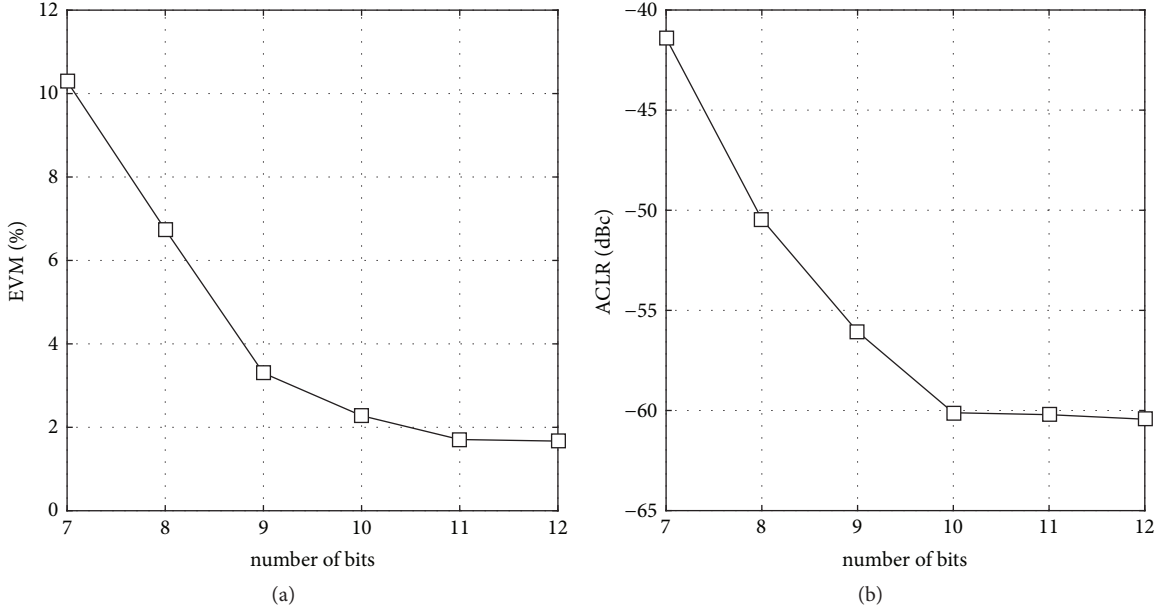


FIGURE 6: Simulated (a) EVM and (b) ACLR versus number of bits of the outphasing modulator.

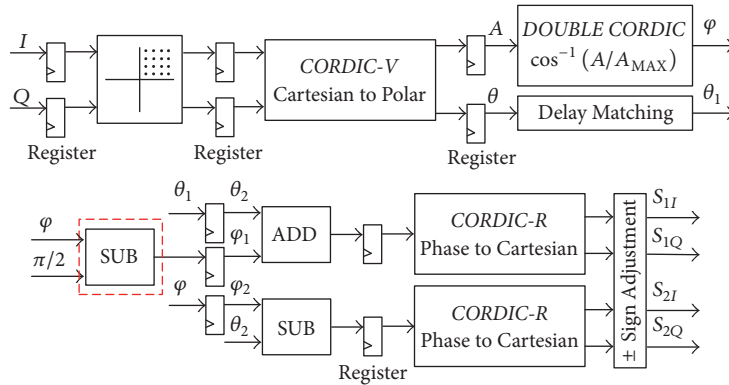


FIGURE 7: Top-level schematic of the CORDIC-based outphasing modulator.

migrated to the circuit level. The design is implemented in 40 nm CMOS. Figure 7 shows the top-level schematic of the outphasing modulator. In practice, the CORDIC-V and CORDIC-R only work properly when the phase of input  $I/Q$  signals is between  $-\pi/2$  and  $\pi/2$ , so the input  $I/Q$  signals are first transformed to the first quadrant. It is feasible thanks to the symmetrical characteristics of trigonometric functions. The resulting sign issue can be easily resolved by using flag signals and recovering the “ $\pm$ ” sign for  $S_{1I}$ ,  $S_{1Q}$ ,  $S_{2I}$ , and  $S_{2Q}$  at the output of the outphasing modulator. Simulation predicts that  $\theta + \varphi$  may be larger than  $\pi/2$ . To tackle this overflowing issue, we subtract the phase by  $\pi/2$  (i.e., the block in the red dashed box) and set  $S_{1I} = 0.5 \cdot A_{MAX} \cdot \cos(\theta + \varphi - \pi/2) = 0.5 \cdot A_{MAX} \cdot \sin(\theta + \varphi)$ ,  $S_{1Q} = 0.5 \cdot A_{MAX} \cdot \sin(\theta + \varphi - \pi/2) = -0.5 \cdot A_{MAX} \cdot \cos(\theta + \varphi)$ .  $A_{MAX}$  is set to 1. In this design, when the input signal is small (i.e.,  $|x| < 0.2$ ),  $\sin(x)$  and  $\cos(x)$  are approximated by the linear functions, given by  $\sin(x) = x$  and

$\cos(x) = 1 - |x|/8$ , which are more efficient than CORDIC-R. The delay matching block and all the registers are used to balance the latency in the signal paths.

It can be seen that the adder and the subtractor are the most critical blocks in CORDIC as well as in the complete outphasing modulator (see Figure 7), which determine the speed and power consumption. In this work, the full adder is realized by double pass-transistor logic (DPL) [13] which features relatively fast speed compared to mirror adder and complementary pass-transistor logic (CPL) adder [14] while still achieves full signal swing even at low supply voltage, as shown in Figure 8. In the design of the DPL adder, the speed of the circuit has been paid more attention. The optimum transistor size is selected upon which the delay of the critical path in the adder is minimized. In addition, the carry-select topology [14] is applied to minimize the delay of the critical path where the 10-bit adder in the  $\cos^{-1}(x)$  block is split into

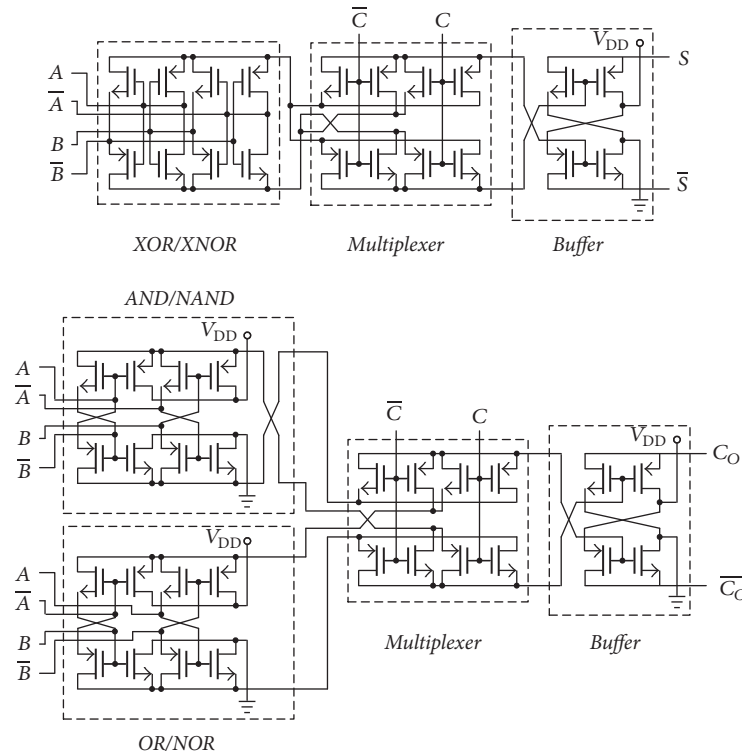


FIGURE 8: Schematic of full adder realized by double pass-transistor logic.

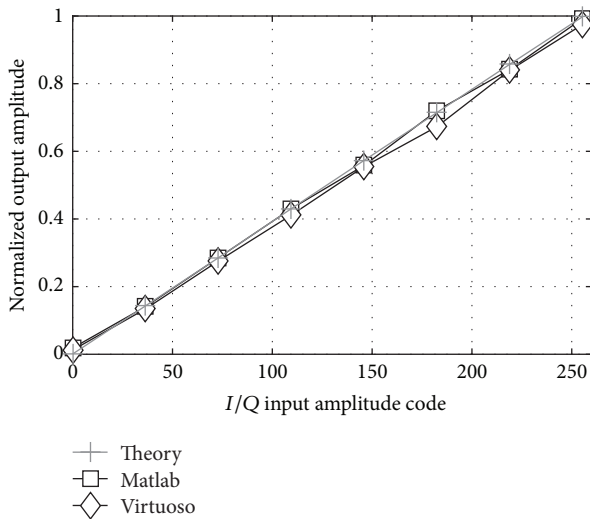


FIGURE 9: Simulated outphasing modulator linearity.

3-bit, 3-bit, and 4-bit adders. The 10-bit DPL-based adder features a simulated critical path delay of 180 ps in 40 nm CMOS. It means that a maximal clock frequency of 5.6 GHz can be applied.

In this work, the complete outphasing modulator is fully custom designed in 40 nm CMOS using Cadence Virtuoso in order to ensure high speed and low power. Figure 9 shows

the static response of the outphasing modulator. It can be seen that the modulator can operate linearly up to the peak output amplitude. The simulated results in Virtuoso are in good agreement with the theory and Matlab results. For the dynamic response, the outphasing modulator is first simulated in Virtuoso and the results are then fed to the outphasing front-end (i.e., Matlab model) to further evaluate the system performance. The complete system is tested with 10.56 Gb/s 64-QAM (i.e., 1.76 GHz signal bandwidth). Figure 10 shows the simulated 64-QAM constellation with an EVM of 3.2% and the output spectra that well fits the IEEE 802.11ad spectral mask requirements at 60 GHz. The corresponding power consumption is 112 mW at the supply voltage of 0.9 V, well competing with [10] for the same data rates.

### 5. Conclusion

A high-speed digital outphasing modulator is reported to enable fully integrated efficient outphasing TX for mm-Wave applications. CORDIC algorithm is utilized to realize coordinate conversions and  $\cos^{-1}(x)$  function. Issues such as signal quantization error, delay mismatch, and phase overflowing are tackled to facilitate hardware implementation. Fully custom designed in 40 nm CMOS, the proposed outphasing modulator achieves 10.56 Gb/s 64-QAM modulation with an EVM of 3.2% and meets the IEEE 802.11ad spectral mask requirement.

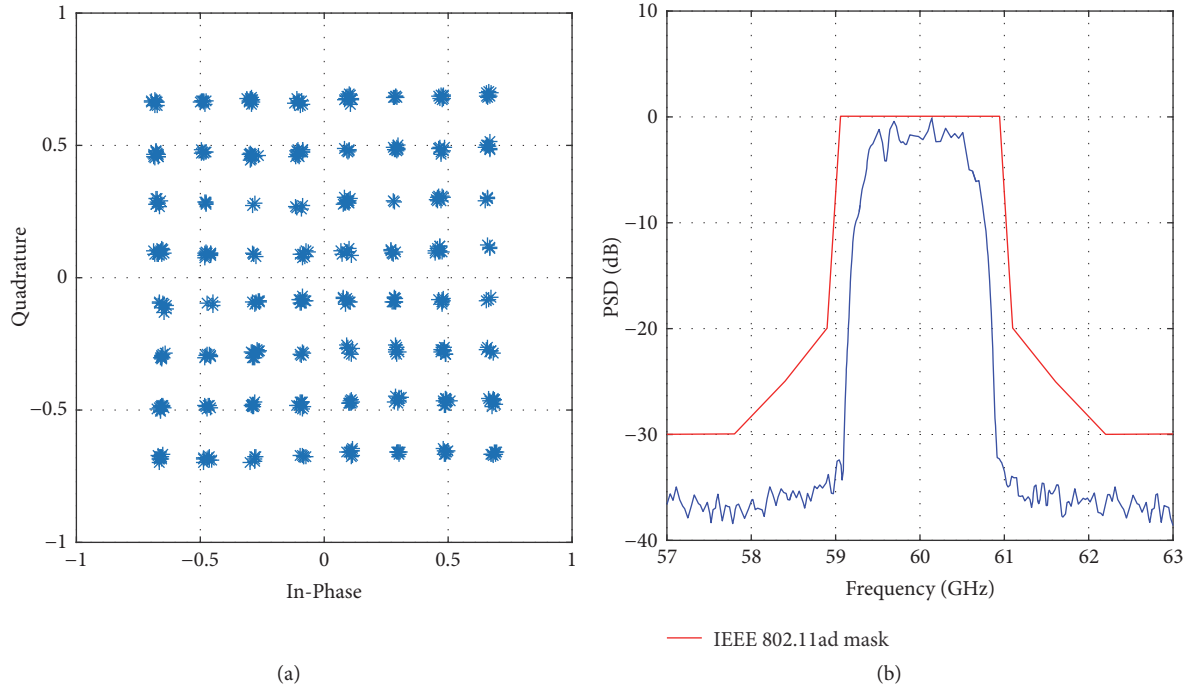


FIGURE 10: Simulated (a) 64-QAM constellation diagram and (b) power spectral density (PSD) of the output signals for IEEE 802.11ad.

## Conflicts of Interest

The authors declare that they have no conflicts of interest.

## Acknowledgments

This work is partly funded by the National Nature Science Foundation of China (no. 61674035), the Nature Science Foundation of Jiangsu Province (no. BK20160690), and the Fundamental Research Funds for the Central Universities.

## References

- [1] S. Cripps, *RF Power Amplifier for Wireless Communications*, Artech House, Norwood, Mass, USA, 2nd edition, 2006.
- [2] B. Razavi, "Design of millimeter-wave CMOS radios: a tutorial," *IEEE Transactions on Circuits and Systems I: Regular Papers*, vol. 56, no. 1, pp. 4–16, 2009.
- [3] H. Chireix, "High power outphasing modulation," *Proceedings of the Institute of Radio Engineers*, vol. 23, no. 11, pp. 1370–1392, 1935.
- [4] H. Xu, Y. Palaskas, A. Ravi, M. Sajadieh, M. A. El-Tanani, and K. Soumyanath, "A flip-chip-packaged 25.3 dBm class-D outphasing power amplifier in 32 nm CMOS for WLAN application," *IEEE Journal of Solid-State Circuits*, vol. 46, no. 7, pp. 1596–1605, 2011.
- [5] B. Shi and L. Sundström, "200-MHz IF BiCMOS signal component separator for linear LINC transmitters," *IEEE Journal of Solid-State Circuits*, vol. 35, no. 7, pp. 987–993, 2000.
- [6] D. Zhao, S. Kulkarni, and P. Reynaert, "A 60-GHz outphasing transmitter in 40-nm CMOS," *IEEE Journal of Solid-State Circuits*, vol. 47, no. 12, pp. 3172–3183, 2012.
- [7] T. W. Barton and D. J. Perreault, "Theory and implementation of RF-input outphasing power amplification," *IEEE Transactions on Microwave Theory and Techniques*, vol. 63, no. 12, pp. 4273–4283, 2015.
- [8] T. Barton, "Not just a phase: outphasing power amplifiers," *IEEE Microwave Magazine*, vol. 17, no. 2, pp. 18–31, 2016.
- [9] P. Madoglio, A. Ravi, H. Xu et al., "A 20 dBm 2.4 GHz digital outphasing transmitter for WLAN application in 32 nm CMOS," in *Proceedings of the Solid-State Circuits Conference Digest of Technical Papers (ISSCC)*, pp. 168–169, San Francisco, Calif, USA.
- [10] Y. Li, Z. Li, O. Uyar, Y. Avniel, A. Megretski, and V. Stojanovic, "High-throughput signal component separator for asymmetric multi-level outphasing power amplifiers," *IEEE Journal of Solid-State Circuits*, vol. 48, no. 2, pp. 369–380, 2013.
- [11] C. Mazenc, X. Merrheim, and J.-M. Muller, "Computing functions  $\cos^{-1}$  and  $\sin^{-1}$  using CORDIC," *IEEE Transactions on Computers*, vol. 42, no. 1, pp. 118–122, 1993.
- [12] P. K. Meher, J. Valls, T. B. Juang, and K. Maharatna, "50 years of CORDIC: algorithms, architectures, and applications," *IEEE Transactions on Circuits and Systems I: Regular Papers*, vol. 56, no. 9, pp. 1893–1907, 2009.
- [13] S. Makoto, O. Norio, T. Shinbo et al., "A 1.5-ns 32-b CMOS ALU in double pass-transistor logic," *IEEE Journal of Solid-State Circuits*, vol. 28, no. 11, pp. 1145–1151, 1993.
- [14] J. M. Rabaey, A. Chandrakasan, and B. Nikolic, *Digital Integrated Circuits: A Design Perspective*, Prentice Hall, Upper Saddle River, NJ, USA, 2nd edition, 2003.

## Research Article

# Design of a Novel Miniaturized Frequency Selective Surface Based on 2.5-Dimensional Jerusalem Cross for 5G Applications

Peng Zhao,<sup>1,2</sup> Yihang Zhang ,<sup>1</sup> Rongrong Sun,<sup>1</sup> Wen-Sheng Zhao,<sup>1</sup> Yue Hu,<sup>1</sup> and Gaofeng Wang <sup>1</sup>

<sup>1</sup>Key Lab of RF Circuits and Systems of Ministry of Education, School of Electronics and Information, Hangzhou Dianzi University, Hangzhou 310018, China

<sup>2</sup>State Key Laboratory of Millimeter Waves, Southeast University, Nanjing 211189, China

Correspondence should be addressed to Gaofeng Wang; [gaofeng@hdu.edu.cn](mailto:gaofeng@hdu.edu.cn)

Received 21 December 2017; Accepted 8 March 2018; Published 19 April 2018

Academic Editor: Ting-Yen Shih

Copyright © 2018 Peng Zhao et al. This is an open access article distributed under the Creative Commons Attribution License, which permits unrestricted use, distribution, and reproduction in any medium, provided the original work is properly cited.

A compact frequency selective surface (FSS) for 5G applications has been designed based on 2.5-dimensional Jerusalem cross. The proposed element consists of two main parts: the successive segments of the metal traces placed alternately on the two surfaces of the substrate and the vertical vias connecting traces. Compared with previous published two-dimensional miniaturized elements, the transmission curves indicate a significant size reduction (1/26 wavelengths at the resonant frequency) and exhibit good angular and polarization stabilities. Furthermore, a general equivalent circuit model is established to provide direct physical insight into the operating principle of this FSS. A prototype of the proposed FSS has been fabricated and measured, and the results validate this design.

## 1. Introduction

In recent years, frequency selective surfaces (FSSs) have drawn extensive attentions because of their wide applications in the communication equipment [1, 2]. FSSs are always designed to reflect, transmit, or absorb electromagnetic wave, and they are applied in the design of antenna radomes, reflector of low-profile antenna, electromagnetic absorbers, and so on [3–7]. The typical FSS structures consist of two-dimensional (2D) periodically arranged resonate units [8–10]. In practical design, the number of FSS units is restricted to the requirement of size. For 5G communications, the antennas are very small and the radomes covering the antennas should be small as well [11]. However, when the infinite period of the FSS is truncated, it is bound to have a significant impact on the performance of the FSS. In order to maintain original performances and compromise this constraint, compact FSS elements are required.

At present, several methods are proposed to realize the miniaturization of FSS. By adding some lumped reactive components to their design, the size of FSS element has been reduced because of the increment of the inductance and

capacitance of equivalent circuit [12]. In [13], the miniaturization of element is realized by reducing the thickness of dielectric substrate, so that the capacitance between various metallic layers has been increased. Moreover, a loop-wire structure has been introduced in [14], which consists of a metallic patch and wire-grid on the opposite layer of substrate to enhance the inductance and capacitance. The FSS element consists of four symmetrical spiral patterns of metallic meander lines which has been designed to increase the length of resonant structures in a given periodicity [15]. In [16], the spiral slot element with a compact arrangement has been proposed, which effectively increases the corresponding equivalent inductance. And the corresponding equivalent capacitance can also be increased by adjusting the distance between every two slots. More recently, square loop with vertical vias is applied to design FSS element [17]. In this design, the capacitance is increased by the capacitive coupling of adjacent via wall, and the inductance is increased by using the knitted structure alternately across different layers of substrate. The element size of this design is around 1/16 wavelengths. For 5G mobile communications, further size reduction should be investigated.

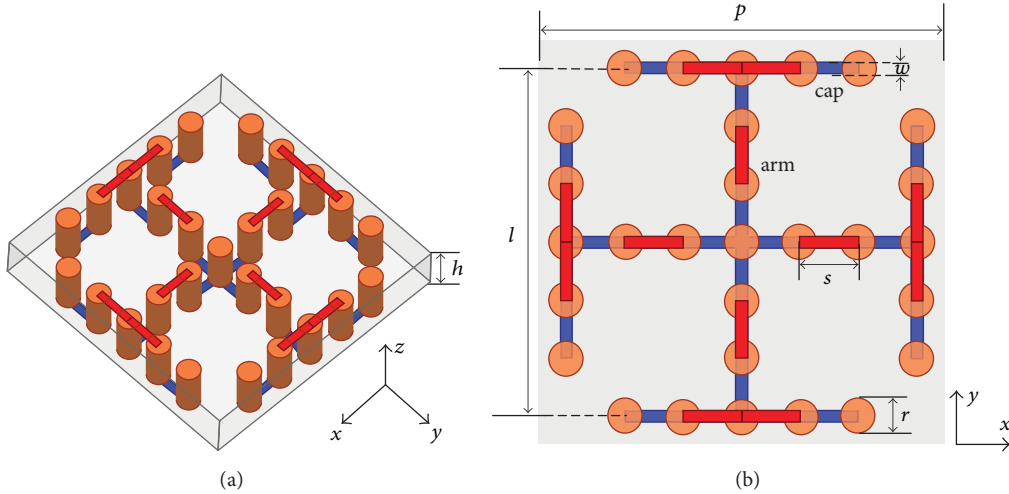


FIGURE 1: Geometry of the 2.5D straight-line type FSS element: (a) 3D perspective view and (b) top view.

In this paper, novel miniaturized FSSs based on 2.5D Jerusalem cross element have been designed, and the working frequency is around 3.3 GHz which is the potential 5G communication frequency. The FSS element uses 41 vias to provide additional inductance and capacitance due to extensive path and via wall coupling between adjacent elements. Comparing with [17], this design has more significant effect of size reduction which achieves a FSS element around  $1/26$  wavelengths at the resonant frequency. Moreover, this FSS provides good resonant stability for various polarizations and incident angles. The equivalent circuit model of the FSS has also been proposed for the analysis of its performance. Finally, to validate the results of proposed FSS, a prototype has been fabricated and measured. The proposed 2.5D FSS can be easily fabricated using low-cost PCB processing. The results show a good consistency between the full-wave simulations and measurements.

## 2. Element Design and Performance Analysis

The FSS element can be treated as a resonance circuit when it is illuminated by the incident waves. The resonant frequency is determined by the formula  $f = 1/(2\pi\sqrt{LC})$ , where  $L$  and  $C$  represent equivalent inductance and capacitance of the element, respectively. Therefore, the method of miniaturization technique is to increase the value of inductance and capacitance. Based on this theory, the proposed structure of the 2.5D miniaturized element has been designed.

In Figure 1, the metallic segments of the straight-line type FSS element are alternately placed on the top and bottom surface of the substrate and then connected through the metallic vias. The element is printed on a dielectric substrate FR-4 ( $\epsilon_r = 4.4$ ; loss tangent  $\delta = 0.025$ ), and the periodicity of unit cell is  $p$ . The length of the planar element is  $l$  and the width of its conductor is  $w$ . Each arm and cap are divided into five and seven segments, respectively. And then, the successive segments are printed on the top and bottom side of substrate connected through vias alternatively. The radius of all vias is  $r$  while the center to center spacing between adjacent

TABLE 1: Dimension of the FSS unit cell.

Parameter	Value (mm)
$p$	3.5
$l$	3
$w$	0.1
$s$	0.5
$h$	1
$r$	0.15

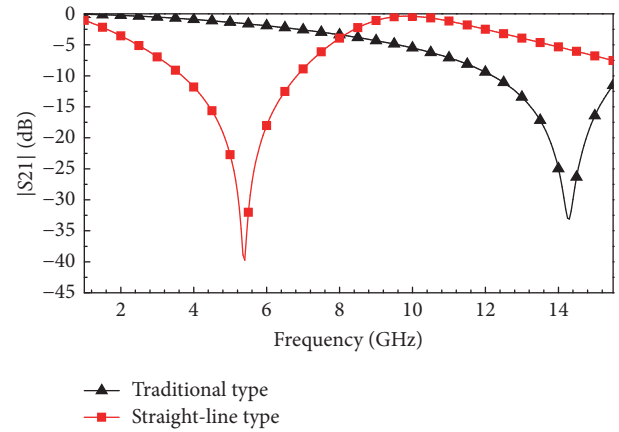


FIGURE 2: Transmission coefficients of the proposed FSS with straight-line arm with  $h = 1$  mm for normally incident TE-polarized plane wave.

vias is  $s$ . The dimensions of the designed FSS are listed in Table 1.

It can be observed from Figure 2 that the straight-line type element resonates at 5.5 GHz in contrast to the traditional Jerusalem cross element with the same design parameters that has a resonant frequency of 14.5 GHz. Thus, the size of the proposed element has been reduced from  $1/6$  to  $1/16$  wavelengths.

TABLE 2: Comparison of element sizes.

Element	Period (mm)	Thickness (mm)	Dielectric constant	Resonant frequency	Size
Ref. [12]	8.85	0.8	4.4	0.935 GHz	$0.028\lambda_0$
This FSS	3.5	0.8	4.4	3.88 GHz	$0.045\lambda_0$
Ref. [13]	7.5	0.9	2.65	1.39 GHz	$0.035\lambda_0$
This FSS	3.5	0.9	2.65	4.48 GHz	$0.052\lambda_0$
Ref. [15]	4.4	1	4.4	3.3 GHz	$0.048\lambda_0$
This FSS	3.5	1	4.4	3.3 GHz	$0.038\lambda_0$
Ref. [16]	4.8	1.6	4.4	3.82 GHz	$0.063\lambda_0$
Ref. [17]	10	1.6	4.4	1.89 GHz	$0.0625\lambda_0$
This FSS	3.5	1.6	4.4	2.29 GHz	$0.026\lambda_0$

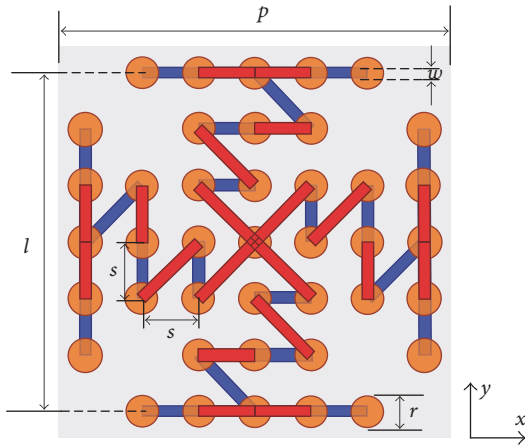


FIGURE 3: Geometry of the 2.5D meander-line type FSS element (top view).

To further miniaturize the size of element, a 2.5D Jerusalem cross with meander-line arm is proposed, as shown in Figure 3. Comparing with the previous structure, the proposed element with inserted additional vias and metal traces has a longer electric length. Therefore, the value of equivalent inductance can be increased and the resonant frequency can be decreased as well. Figure 4 shows that the transmission coefficients of the proposed FSS. The performance is simulated using finite element method incorporating with periodic boundary condition. The meander-line type element resonates at the frequency of 3.3 GHz with the same substrate thickness. Correspondingly, the period of the meandering line element is reduced to  $1/26$  wavelengths. Hence, the size of element has been reduced considerably. Furthermore, the transmission response with various substrate thicknesses has been studied. With the reduction of substrate thickness, the resonant frequency decreases due to the reduction of the inductance and capacitance of the metallic vias.

In Figure 5, the angular and polarization stabilities of proposed FSS element have been investigated. From this figure, it is observed that the maximum deviation is about 0.3% between the incidence angles  $0^\circ$  and  $60^\circ$  in both the TE and TM cases, which indicates extremely stable resonance at various polarizations and incidence angles.

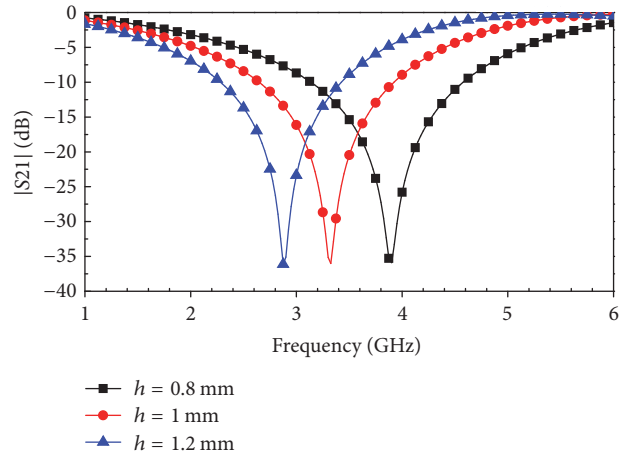


FIGURE 4: Transmission coefficients of the meander-line type FSS with various substrate thicknesses for normally incident TE-polarized plane wave.

A size comparison between the proposed and previous reported FSSs is provided in Table 2. For a fair comparison, the same substrate as that in the papers is adopted. It can be seen that the size of proposed FSS is very small. Although the size of FSS in [12] is smaller, it uses bulky lumped reactive components for the miniaturization. Similarly, the FSSs in [13] are two-dielectric layer structure. Compared with the designs on single dielectric layer [15–17], the proposed FSS has significant size reduction.

### 3. Equivalent Circuit Models Validation and Results Analysis

To provide direct physical insight into the operating principle of the 2.5D Jerusalem cross FSS, an equivalent circuit model is proposed in this section. The traditional Jerusalem cross is described by series  $LC$  circuit model. For the 2.5D Jerusalem cross, metal vias in the substrate can be treated as an additional inductor to link the top and bottom strips together, and the adjacent vias in two neighbor units can be treated as an additional capacitor, respectively.

As shown in Figure 6(a),  $L_1$  and  $L_v$  represent the equivalent inductance, respectively, generated by the serial

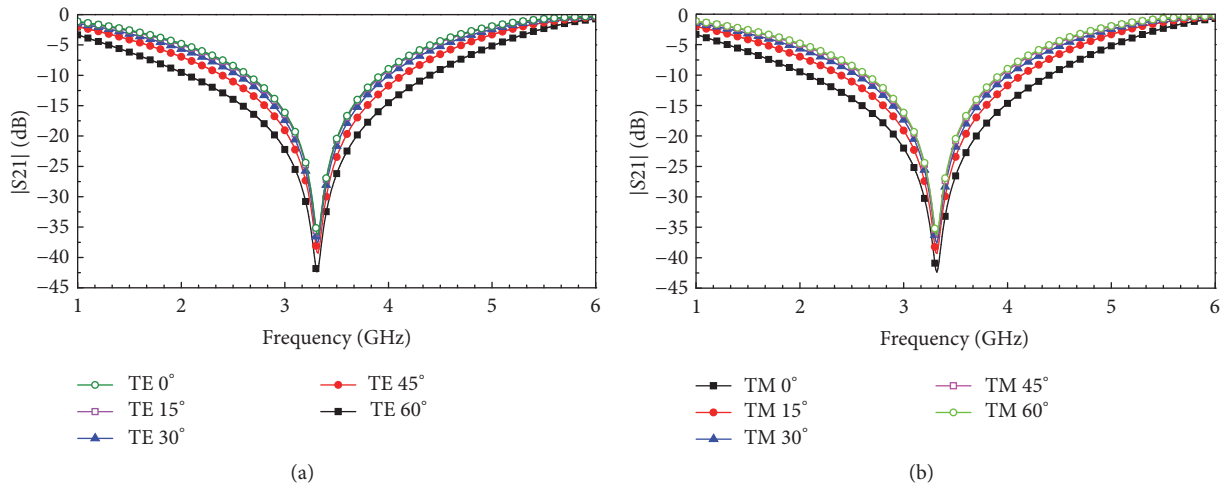


FIGURE 5: Simulated transmission coefficients of proposed FSS ( $h = 1$  mm): (a) illuminated by normally incident TE-polarized wave of different incident angles; (b) illuminated by normally incident TM-polarized wave of different incident angles.

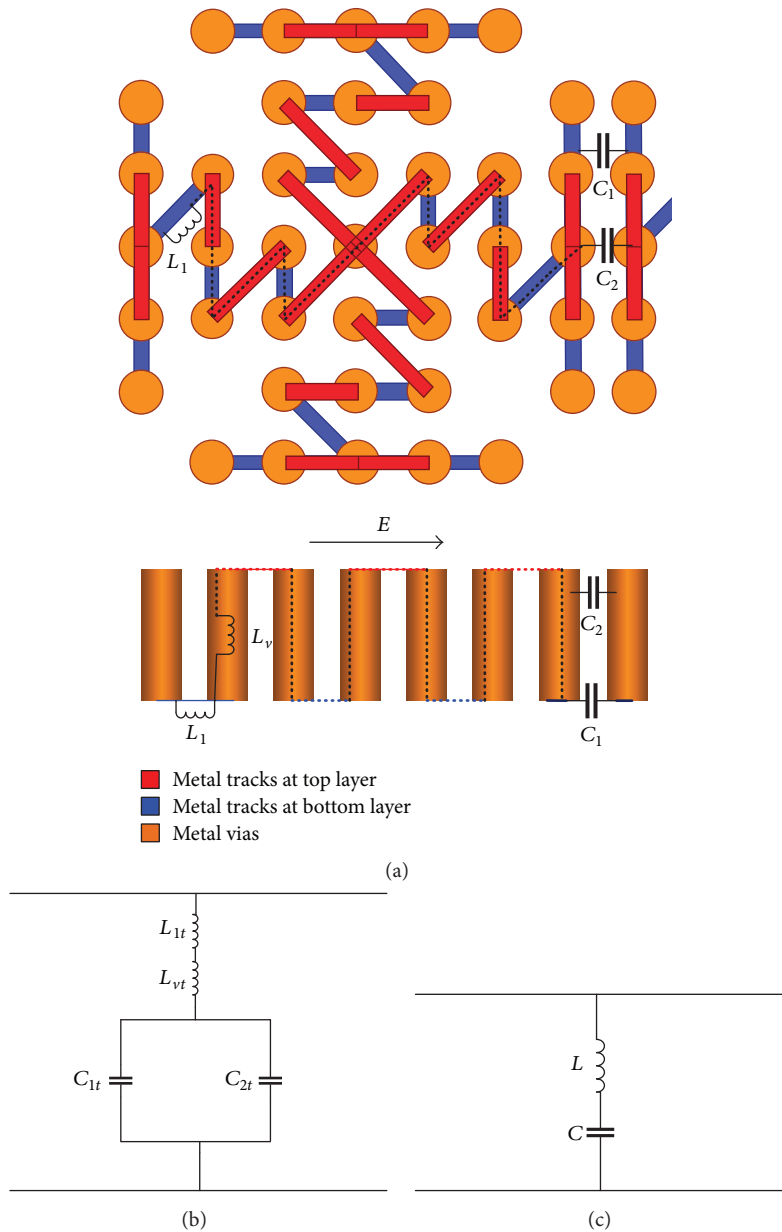


FIGURE 6: The equivalent circuit of proposed FSS element.

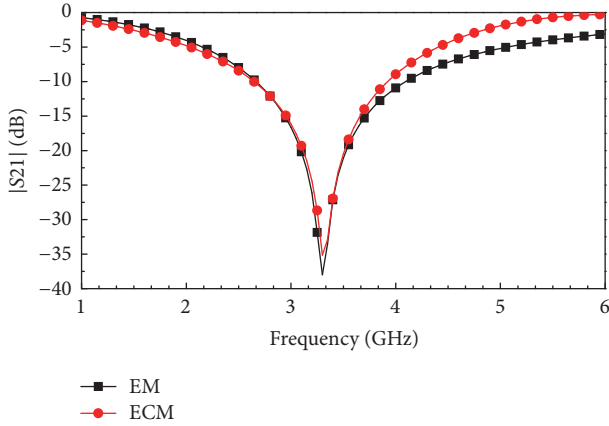


FIGURE 7: Transmission coefficients of 2.5D FSS comparison of equivalent circuit model and electromagnetic simulation.

metal strips and vertical vias, while  $C_1$  and  $C_2$  represent the equivalent capacitance, respectively, generated by the adjacent metal strips and vertical vias in two neighbor units. The equivalent circuit of the FSS element is illustrated in Figure 6(b) in which the total contribution of serial metal strips and vias for the inductance is represented by  $L_{1t}$  and  $L_{vt}$ . Similarly, the total contribution of adjacent metal strips and vertical vias for the capacitance is represented by  $C_{1t}$  and  $C_{2t}$ . By combining the inductances  $L_{1t}$  and  $L_{vt}$  into  $L$  and combining capacitances  $C_{1t}$  and  $C_{2t}$  into  $C$ , the FSS element can be described by a simpler equivalent circuit, as shown in Figure 6(c).

The equivalent inductance and capacitance of this circuit model depend on the given physical parameters. The equivalent inductance can be increased by adding substrate thickness or decreasing the spacing between adjacent vias because of the increasing electrical length. Similarly, the equivalent capacitance can be increased by narrowing the gap between neighboring element. Therefore, the resonant frequency can be tuned by adjusting the relevant parameters of the FSS element.

In order to validate the methodology of the proposed equivalent circuit, its performance is assessed against the results obtained from full-wave electromagnetic simulations. As shown in Figure 7, the transmission curves of the equivalent circuit model and electromagnetic have been illustrated. It can be observed that the frequency responding of equivalent circuit model is accurate with the electromagnetic simulations, though its bandwidth evaluation becomes slightly narrower compared with electromagnetic simulation.

#### 4. Fabrication and Measurement

In order to validate the designed structures in the above sections, the proposed FSS is fabricated using the normal PCB technique and tested in a free-space measurement environment. The design parameters of these prototype are the same as those given in Section 2. The fabricated FSS sample is shown in Figure 8. The FSS fabricated on FR-4



FIGURE 8: Measurement setup for the proposed FSS.

board and the total size is  $350 \times 350 \text{ mm}^2$  and consists of  $100 \times 100$  elements. The FSS is measured in a microwave anechoic chamber with a vector network analyzer and two standard horn antennas are placed on the two sides of the FSS as the transmitting and receiving antennas.

Figure 9 shows the transmission coefficients at various incident angles, with both TE and TM polarizations. It can be observed that the measured results are evidently consistent with the proposed models. In addition, the measurement results confirmed that the proposed FSS exhibited a stable resonant frequency. The discrepancies between the measurements and the simulations are mainly caused by the fabrication tolerance of the fine metal lines and vias and measurement uncertainties. Overall, the experimental results can demonstrate the performance of the proposed miniaturized FSS.

#### 5. Conclusion

A novel miniaturized FSS based on 2.5D Jerusalem cross has been designed for the application to 5G antenna radomes. Benefitting from the additional inductance and capacitance due to the 2.5D structure, the unit length of this FSS is only  $1/26$  wavelengths at the resonant frequency of 3.3 GHz. Furthermore, the resonant frequency of the proposed FSS exhibited a good stability at various polarizations and incident angles. The deviation of the resonant frequency is less than 0.3% even if the incident angle is  $60^\circ$  in both TE and TM cases. Moreover, an equivalent circuit model has been proposed to provide direct physical insight. The experiments' results have been given and these results validate the proposed design.

#### Conflicts of Interest

The authors declare that there are no conflicts of interest regarding the publication of this paper.

#### Acknowledgments

This work was supported in part by the National Key R&D Program of China under Grant 2017YFB0203500, in part by the National Natural Science Foundation of China under

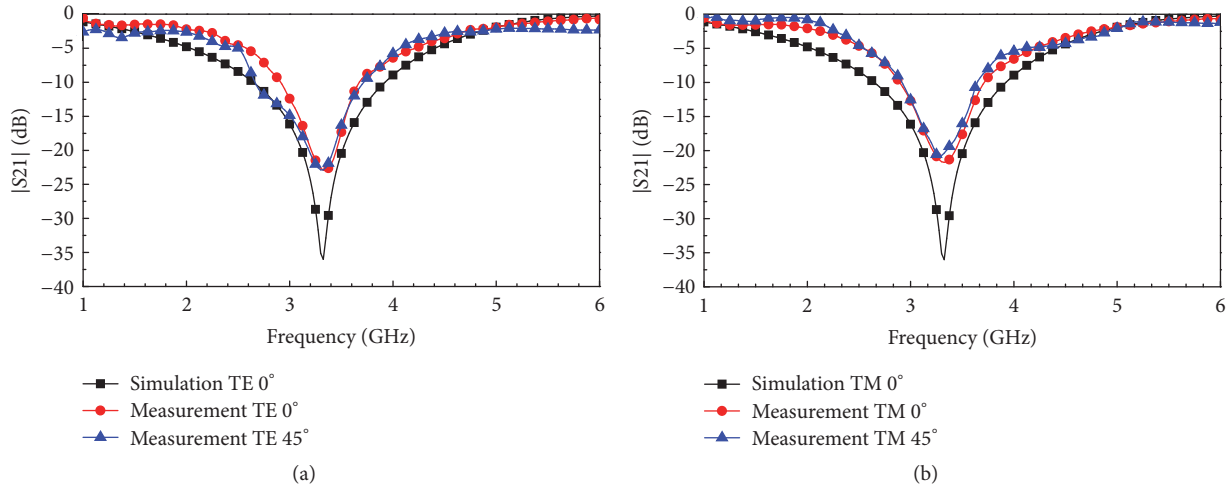


FIGURE 9: Transmission coefficients of the proposed FSS obtained from measurements and EM simulations with various incident angles: (a) for TE polarization with a substrate thickness of 1 mm; (b) for TM polarization with a substrate thickness of 1 mm.

Grants 61601163, 61331007, 61504033, and 61411136003, and in part by the State Key Laboratory of Millimeter Waves under Grant K201710.

## References

- [1] B. A. Munk, *Frequency selective surface: Theory and design*, Wiley, New York, NY, USA, 2000.
- [2] R. Mittra, C. H. Chan, and T. Cwik, "Techniques for Analyzing Frequency Selective Surfaces—a Review," *Proceedings of the IEEE*, vol. 76, no. 12, pp. 1593–1615, 1988.
- [3] C.-C. Chen, "Transmission of Microwave Through Perforated Flat Plates of Finite Thickness," *IEEE Transactions on Microwave Theory and Techniques*, vol. 21, no. 1, pp. 1–6, 1973.
- [4] F. Birbir, J. Shaker, and Y. M. M. Antar, "Chebishev bandpass spatial filter composed of strip gratings," *IEEE Transactions on Antennas and Propagation*, vol. 56, no. 12, pp. 3707–3713, 2008.
- [5] J. H. Kim, H. J. Chun, I. P. Hong, Y. J. Kim, and Y. B. Park, "Analysis of FSS radomes based on physical optics method and ray tracing technique," *IEEE Antennas and Wireless Propagation Letters*, vol. 13, pp. 868–871, 2014.
- [6] N. M. Mohamed-Hicho, E. Antonino-Daviu, M. Cabedo-Fabres, and M. Ferrando-Bataller, "A novel low-profile high-gain UHF antenna using high-impedance surfaces," *IEEE Antennas and Wireless Propagation Letters*, vol. 14, pp. 1014–1017, 2015.
- [7] J. Lee, M. Yoo, and S. Lim, "A study of ultra-thin single layer frequency selective surface microwave absorbers with three different bandwidths using double resonance," *Institute of Electrical and Electronics Engineers. Transactions on Antennas and Propagation*, vol. 63, no. 1, pp. 221–230, 2015.
- [8] T. K. Wu, *Frequency Selective Surfaces and Grid Array*, Wiley, Hoboken, NJ, USA, 1995.
- [9] J. C. Vardaxoglou, *Frequency Selective Surfaces Analysis and Design*, Wiley, Hoboken, NJ, USA, 1997.
- [10] C.-N. Chiu, Y.-C. Chang, H.-C. Hsieh, and C. H. Chen, "Suppression of spurious emissions from a spiral inductor through the use of a frequency-selective surface," *IEEE Transactions on Electromagnetic Compatibility*, vol. 52, no. 1, pp. 56–63, 2010.
- [11] W. Yadum and N. Nakajima, "The correlation of diversity/MIMO antenna for portable terminals," *Wireless Communications and Mobile Computing*, vol. 7, no. 8, pp. 995–1002, 2007.
- [12] H. L. Liu, K. L. Ford, and R. J. Langley, "Design methodology for a miniaturized frequency selective surface using lumped reactive components," *IEEE Transactions on Antennas and Propagation*, vol. 57, no. 9, pp. 2732–2738, 2009.
- [13] B.-Q. Lin, S.-H. Zhou, X.-Y. Da, Y.-W. Fang, Y.-J. Li, and W. Li, "Compact miniaturised-element frequency selective surface," *IEEE Electronics Letters*, vol. 51, no. 12, pp. 883–884, 2015.
- [14] F. Bayatpur and K. Sarabandi, "Multipole spatial filters using metamaterial-based miniaturized-element frequency-selective surfaces," *IEEE Transactions on Microwave Theory and Techniques*, vol. 56, no. 12, pp. 2742–2747, 2008.
- [15] M. Yan, S. Qu, J. Wang et al., "A novel miniaturized frequency selective surface with stable resonance," *IEEE Antennas and Wireless Propagation Letters*, vol. 13, pp. 639–641, 2014.
- [16] G. Yang, T. Zhang, W. Li, and Q. Wu, "A novel stable miniaturized frequency selective surface," *IEEE Antennas and Wireless Propagation Letters*, vol. 9, pp. 1018–1021, 2010.
- [17] T. Hussain, Q. Cao, J. K. Kayani, and I. Majid, "Miniaturization of Frequency Selective Surfaces Using 2.5-D Knitted Structures: Design and Synthesis," *IEEE Transactions on Antennas and Propagation*, vol. 65, no. 5, pp. 2405–2412, 2017.

## Research Article

# A Doherty Power Amplifier with Large Back-Off Power Range Using Integrated Enhancing Reactance

Wa Kong,<sup>1</sup> Jing Xia ,<sup>1,2</sup> Fan Meng,<sup>2</sup> Chao Yu ,<sup>2</sup> Lixia Yang,<sup>1</sup> and Xiaowei Zhu<sup>2</sup>

<sup>1</sup>School of Computer Science and Communication Engineering, Jiangsu University, Zhenjiang 212013, China

<sup>2</sup>State Key Laboratory of Millimeter Waves, Southeast University, Nanjing 210096, China

Correspondence should be addressed to Jing Xia; [ujसान@gmail.com](mailto:ujसान@gmail.com)

Received 21 December 2017; Accepted 11 March 2018; Published 15 April 2018

Academic Editor: Shichang Chen

Copyright © 2018 Wa Kong et al. This is an open access article distributed under the Creative Commons Attribution License, which permits unrestricted use, distribution, and reproduction in any medium, provided the original work is properly cited.

A symmetric Doherty power amplifier (DPA) based on integrated enhancing reactance (IER) was proposed for large back-off applications. The IER was generated using the peaking amplifier with the help of a desired impedance transformation in the low-power region to enhance the back-off efficiency of the carrier amplifier. To convert the impedances properly, both in the low-power region and at saturation, a two-impedance matching method was employed to design the output matching networks. For verification, a symmetric DPA with large back-off power range over 2.2–2.5 GHz was designed and fabricated. Measurement results show that the designed DPA has the 9 dB back-off efficiency of higher than 45%, while the saturated output power is higher than 44 dBm over the whole operation bandwidth. When driven by a 20 MHz LTE signal, the DPA can achieve good average efficiency of around 50% with adjacent channel leakage ratio of about -50 dBc after linearization over the frequency band of interest. The linearity improvement of the DPA for multistandard wireless communication system was also verified with a dual-band modulated signal.

## 1. Introduction

In future wireless communication systems, such as the 5th generation of mobile communication network (5G), the ever increasing demand for high transmission data rate results in the employment of wideband and multiband modulated signals characterized by high peak-to-average power ratios (PAPRs). To efficiently amplify these signals at back-off power (BOP) range, the Doherty power amplifier (DPA) has garnered great research attention because of its significant efficiency enhancement and ease of configuration [1–6]. Conventional symmetric DPAs, employing the same transistors to design the carrier and peaking amplifiers, always achieve high-efficiency operation over 6 dB or less BOP range [7–12], which can hardly satisfy the efficiency requirement when wideband or multiband modulated signals with the PAPRs of higher than 6 dB are employed.

To further improve the back-off efficiency, various DPAs, such as asymmetric DPAs and multistage DPAs, have been investigated to achieve large BOP range [13–16]. These two

kinds of DPAs utilize excessive modulation current of the peaking amplifier to achieve enlarged load span of the carrier amplifier for extended BOP range, leading to tradeoffs between design complexity, cost, and power utilization factor. To overcome the disadvantages of the aforementioned DPAs, modified symmetric DPAs have been proposed recently to attain larger than 6 dB high-efficiency range, which employ complex combining load technique [17] or maintain full voltage and current swings of both carrier and peaking amplifiers [18]. However, these approaches might suffer from complicated design methodology. Recently, the effect of the output impedance of the peaking stage has been investigated to extend the high-efficiency power range or bandwidth [19–21] in DPA designs. In [21], we have proposed a novel method to extend the bandwidth of the DPA based on integrated compensating reactance, which was chosen near the open-circuit area in Smith chart. However, after further analysis, it is found that a reactance near the short-circuit point can also be used to enhance the back-off efficiency and thus extend the BOP range.

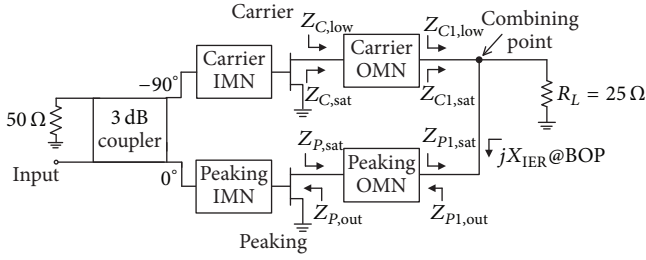


FIGURE 1: Simplified schematic of the proposed DPA.

In this paper, after analyzing the effect of a reactive load at the combining point on the back-off efficiency of the carrier amplifier, a new symmetric DPA with large BOP range based on enhancing reactance integrated in the peaking amplifier is proposed. This integrated enhancing reactance (IER) was obtained by using a two-impedance matching method to extend the BOP range. Unlike conventional DPA, the output impedance of the peaking amplifier in the proposed design has a lower reactance value for efficiency enhancement when the peaking amplifier is in off-state. For verification, a 2.2–2.5 GHz symmetric DPA with higher than 45% efficiency over 9 dB BOP range was designed. Experimental results of the output power and efficiency as well as the linearization results are also presented.

## 2. Proposed DPA for BOP Range Extension

The simplified schematic of the proposed DPA is shown in Figure 1, which comprises the carrier and peaking amplifiers, an input power divider, and a common load  $R_L$ . In Figure 1,  $Z_{C,sat}$ ,  $Z_{C1,sat}$ ,  $Z_{P,sat}$ , and  $Z_{P1,sat}$  represent the carrier and peaking load impedances at the device output and at the combining point when the DPA is at saturation, while  $Z_{P,out}$ ,  $Z_{P1,out}$ ,  $Z_{C,low}$ , and  $Z_{C1,low}$  are the output and load impedances before the peaking amplifier turns on, respectively. Moreover,  $X_{IER}$  denotes the IER generated by the peaking amplifier at BOP range for back-off efficiency enhancement. At saturation, the IER would not introduce undesirable effect on load modulation of the DPA when both carrier and peaking amplifiers turn on. The design procedure of the proposed DPA is presented as follows.

### 2.1. Effect of Shunted Reactance on Carrier Back-Off Efficiency.

To analyze the effect of the IER on the back-off efficiency of the carrier amplifier, the carrier output matching network (OMN) should be designed firstly. During the Doherty operation, the carrier OMNs should convert the load impedances to the desired values to obtain proper Doherty behavior.

By using load pull simulations based on large signal model of Wolfspeed CGH40010F GaN HEMT, the load impedances of  $18 + j2 \Omega$  and  $22 + j15 \Omega$  were chosen as  $Z_{C,sat}$  and  $Z_{C,low}$  at the frequency of 2.5 GHz, respectively. With the impedances  $Z_{C1,sat} = 50 \Omega$  and  $Z_{C1,low} = 25 \Omega$ , the carrier OMN can be designed by using stepped-impedance matching network theory [21], as shown in Figure 2. To evaluate performance over wide operation band, the simulated

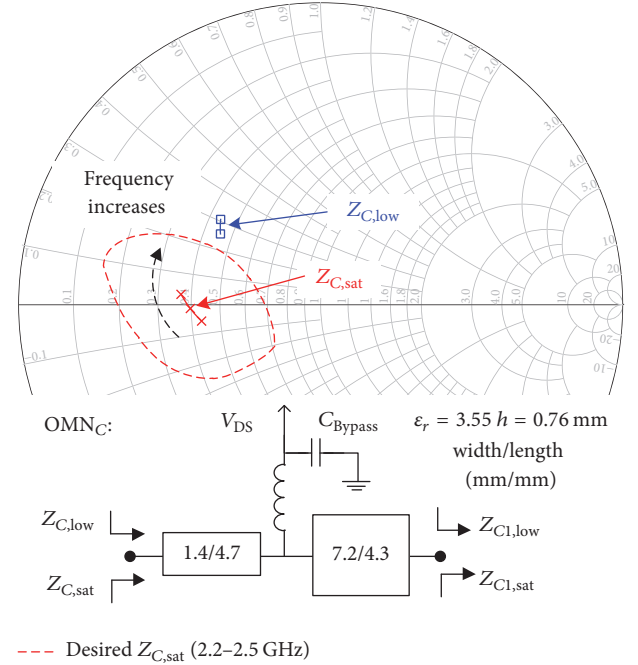


FIGURE 2: Designed carrier OMNs and the simulated impedances over the frequency band of 2.2–2.5 GHz.

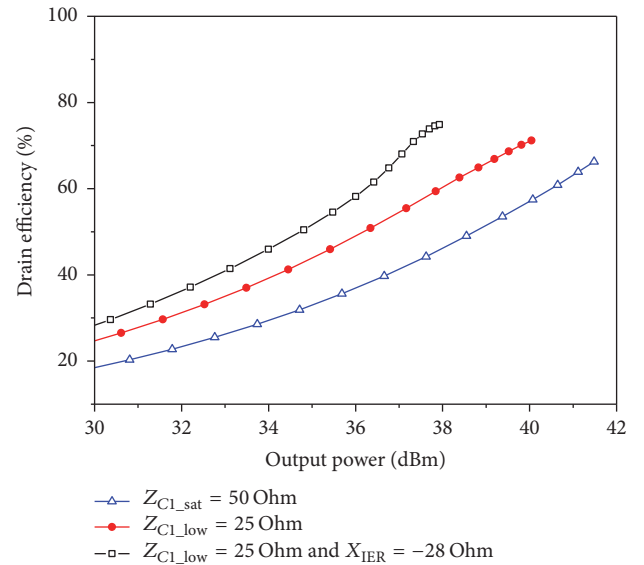


FIGURE 3: Simulated efficiency of the carrier amplifier versus output powers under different loads at 2.5 GHz.

impedances between 2.2 and 2.5 GHz are also given. After the OMN was designed, the input matching network (IMN) can also be designed to cover the required bandwidth.

Figure 3 illustrates simulated drain efficiency of the carrier amplifier versus output powers with  $Z_{C1,sat} = 50 \Omega$  and  $Z_{C1,low} = 25 \Omega$  at 2.5 GHz. It is shown that, with the load impedance of 25  $\Omega$ , the carrier amplifier can achieve enhanced efficiency at back-off powers, which implies a BOP

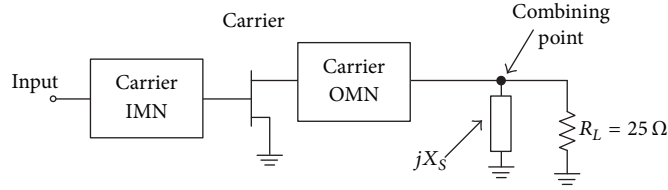
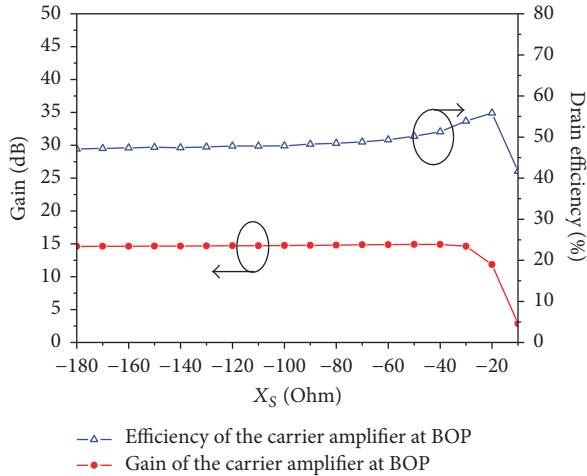


FIGURE 4: Carrier amplifier with a shunted reactance at the combining point.


 FIGURE 5: Back-off efficiency and gain of the carrier amplifier at 35 dBm output power versus  $X_S$ .

range of about 6 dB in conventional symmetric DPA theoretically. However, to achieve larger than 6 dB BOP range, the carrier back-off efficiency should be further enhanced. In the proposed DPA, a shunted reactance at the combining point was employed to achieve high efficiency of the carrier amplifier in the low-power region. To determine the value of this shunted reactance ( $X_S$ ), using the schematic in Figure 4, the effect of the reactance on the carrier back-off efficiency was analyzed. Figure 5 depicts the back-off efficiency of the carrier amplifier and the gain performance at 35 dBm output power versus the shunted reactance  $X_S$  at 2.5 GHz. It can be observed that, with  $X_S$  ranging from  $-36$  to  $-20 \Omega$ , the efficiency of the carrier amplifier remains above 52%, which corresponds to 9 dB BOP range in the proposed DPA. However, when the reactance increases to  $-20 \Omega$ , there is a large degradation of the gain performance.

After a trade-off between the back-off efficiency and gain performance, the desired value of the shunted reactance was chosen to be  $-28 \Omega$ . To illustrate the effect of the shunted reactance, simulated carrier efficiency with  $Z_{C1,low} = 25$  and  $X_S = -28 \Omega$  was also depicted in Figure 3. When compared with the case without the shunted reactance, significant efficiency enhancement can be observed in the low-power region, which means larger BOP range can be achieved. However, according to Doherty operation principle, if an additional shunted reactance at the combining point is employed as the enhancing reactance for efficiency improvement, the

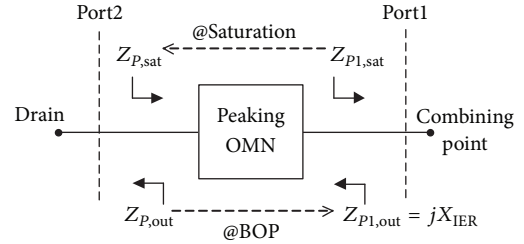


FIGURE 6: Desired impedance transformation of the peaking OMN.

load modulation at saturation will be improper, leading to unavoidable degradation of the output power and efficiency.

To solve this problem, in this paper, the output impedance of the peaking amplifier in off-state was employed to generate this enhancing reactance, which is integrated in the peaking amplifier output, that is, the IER. It should be mentioned that, unlike conventional DPA, the peaking output impedance in the proposed DPA is not an open circuit but a reactance in the low-power region. To obtain desired IER, a two-impedance matching method was employed to design the OMN of the peaking amplifier, as introduced in the following section.

**2.2. Generation of IER for BOP Range Extension.** As mentioned above, the IER used to extend the BOP range of the DPA was generated by the peaking amplifier before it turns on. The OMN of the peaking amplifier should satisfy the desired impedance transformation, as illustrated in Figure 6. The peaking OMN should convert the output impedance  $Z_{P,out}$  to desired value of  $Z_{P1,out}$  to generate the IER at BOP, while transforming  $Z_{P1,sat}$  to  $Z_{P,sat}$  at saturation, which can be achieved using the following design method.

According to network analysis, if the S parameters of a lossless reciprocal OMN can be expressed in terms of  $S_{22}$  and the phase of  $S_{21}$  ( $\theta_{21}$ ), the ABCD parameters can also be determined by these two parameters [21]:

$$\begin{bmatrix} A & B \\ C & D \end{bmatrix} = \begin{bmatrix} \frac{a+c}{2\sqrt{c}} & Z_0 \frac{b-c}{2\sqrt{c}} \\ \frac{1}{Z_0} \frac{d-c}{2\sqrt{c}} & \frac{e+c}{2\sqrt{c}} \end{bmatrix}, \quad (1)$$

where  $Z_0$  is the reference impedance and

$$a = (1 - S_{22}^* e^{j2\theta_{21}})(1 - S_{22})$$

$$b = (1 - S_{22}^* e^{j2\theta_{21}})(1 + S_{22})$$

$$c = (1 - |S_{22}|^2) e^{j2\theta_{21}}$$

$$\begin{aligned}
 d &= (1 + S_{22}^* e^{j2\theta_{21}})(1 - S_{22}) \\
 e &= (1 + S_{22}^* e^{j2\theta_{21}})(1 + S_{22}).
 \end{aligned} \tag{2}$$

Considering the peaking OMN in Figure 6, the impedances at BOP region and at saturation can be expressed as

$$\begin{aligned}
 Z_{P1,out} &= \frac{Z_{P,out}A + B}{Z_{P,out}C + D} \\
 Z_{P1,sat}^* &= \frac{Z_{P,sat}^*A + B}{Z_{P,sat}^*C + D}.
 \end{aligned} \tag{3}$$

By means of (1) and (3), the following expressions are obtained:

$$Z_{P1,out} = \frac{Z_0 Z_{P,out} a + Z_0^2 b + Z_0 (Z_{P,out} - Z_0) c}{Z_{P,out} d + Z_0 e + (Z_0 - Z_{P,out}) c} \tag{4}$$

$$\begin{aligned}
 &\frac{Z_0 Z_{P,sat}^* a + Z_0^2 b + Z_0 (Z_{P,sat}^* - Z_0) c}{Z_{P,sat}^* d + Z_0 e + (Z_0 - Z_{P,sat}^*) c} \\
 &= 1.
 \end{aligned} \tag{5}$$

According to (4) and (5), if the impedances  $Z_{P1,out}$ ,  $Z_{P,out}$ ,  $Z_{P1,sat}$ , and  $Z_{P,sat}$  are obtained, the design parameters  $S_{22}$  and  $\theta_{21}$  can be determined through solving these equations theoretically. Then, the OMN can be designed accordingly.

In the peaking OMN design, the optimum load impedance  $Z_{P,sat}$  at 2.5 GHz was obtained to be  $19 + j5 \Omega$  by using ADS load pull simulations with large signal model of CGH40010F GaN HEMT under class-C bias condition. To determine the output impedance  $Z_{P,out}$  when the peaking amplifier is in off-state, the transistor model was simulated without output matching network under small input signal stimulation in ADS large signal S-parameter simulation. According to the result, the output impedance  $Z_{P,out}$  was found to be  $0.5 - j36 \Omega$ . Considering the phase of  $\theta_{21}$  as a degree of freedom, using  $Z_{P1,sat} = 50 \Omega$ , the parameter  $S_{22}$  can then be calculated using (5), and a set of output impedance  $Z_{P1,out}$  can be plotted, as shown in Figure 7. According to Section 2.1, the desired value of IER ( $X_{IER}$ ) is  $-28 \Omega$ . From Figure 7, when  $Z_{P1,out}$  is close to  $-j28 \Omega$ , a series of  $\theta_{21} = -36^\circ - n * 180^\circ$  ( $n = 0, 1, 2, \dots$ ) can be obtained according to the periodicity of exponential function. Considering practical peaking OMN design, the  $\theta_{21}$  was chosen to be  $-216^\circ$ , while the corresponding  $S_{22}$  is calculated to be  $-0.45 + j0.1$ .

Considering the obtained S parameters, the peaking OMN can then be designed by using ADS optimization, as shown in Figure 8. The load impedances at saturation power and the peaking output impedances in class-C operation are also depicted. The results show that, using the two-point matching technique, the designed OMN can satisfy the impedance transformation of the peaking amplifier. Meanwhile, desired  $X_{IER}$  of  $-28 \Omega$  can be generated by using the peaking OMN.

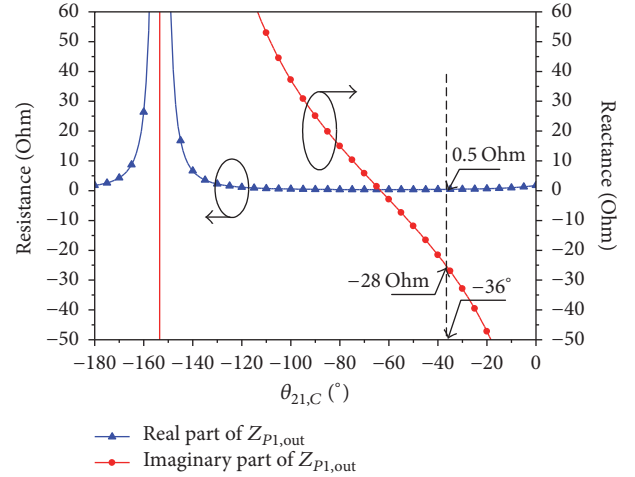


FIGURE 7: Graphical illustration of the two-impedance matching technique for the peaking OMN.

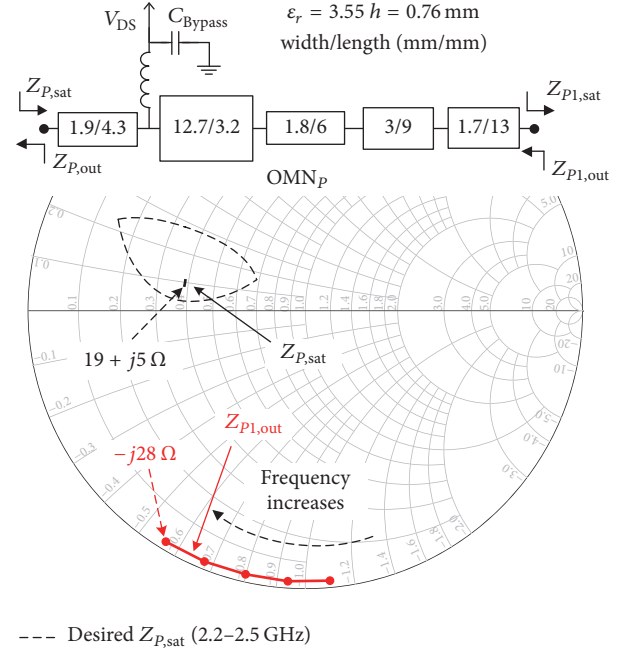


FIGURE 8: Designed peaking OMN and simulated impedances over the frequency band of 2.2–2.5 GHz.

**2.3. DPA Design and Simulations.** To verify the proposed method, a 2.2–2.5 GHz symmetric DPA with IER for BOP range extension was designed using a Taconic RF35 substrate with  $\epsilon_r = 3.55$  and thickness of 0.76 mm. Figure 9 depicts the output network topology of the DPA, including the designed OMNs and a postmatching network (PMN) for impedance transformation between the output load of  $50 \Omega$  and the common load of  $25 \Omega$ . Both the carrier and peaking IMNs are designed by using stepped-impedance matching network theory to cover the required frequency band, as shown in Figure 10.

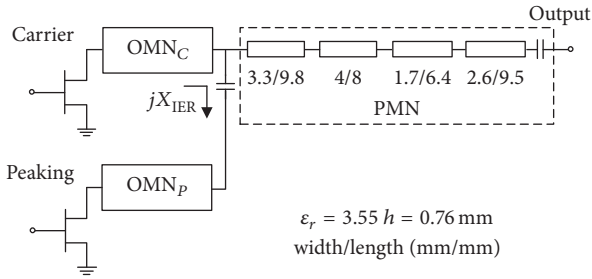


FIGURE 9: Topology of the output network of the DPA.

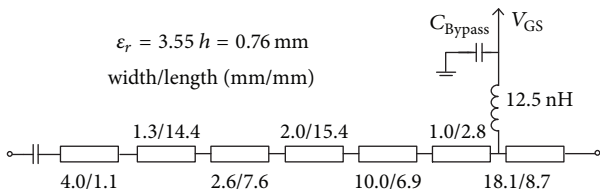


FIGURE 10: Designed IMN for the carrier and peaking amplifiers.

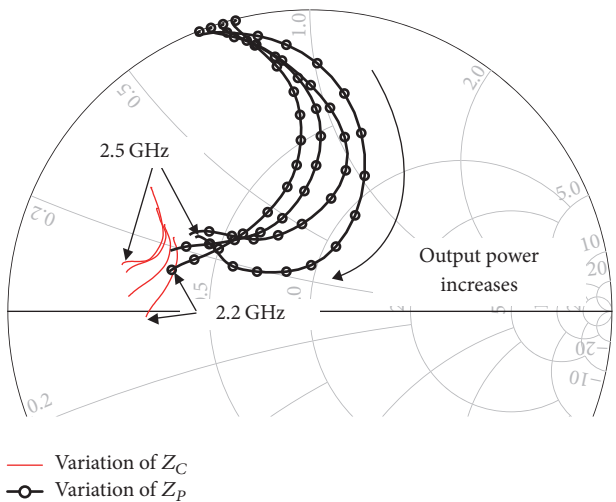


FIGURE 11: Simulated load traces of the carrier and peaking device in the Doherty operation.

After the output network and the IMNs were designed, using a 3 dB 90° hybrid coupler as the input power splitter, the whole DPA can be designed and simulated. For comparative purposes, conventional DPA using similar IMNs and OMNs with the peaking output impedance of quasi open circuit was also simulated. In both the proposed and conventional DPAs, the carrier amplifier was in a class-AB bias condition with  $I_{DS} = 0.05$  A, while the peaking one was biased in class-C mode with  $V_{GS} = -5.5$  V. For improved load modulation, the drain voltages of the carrier and peaking amplifiers were chosen to be 26 and 30 V so that these two amplifiers can generate similar output powers at saturation. In Figure 11, the simulated load impedance traces of the carrier and peaking device are depicted. The load impedances of both carrier and

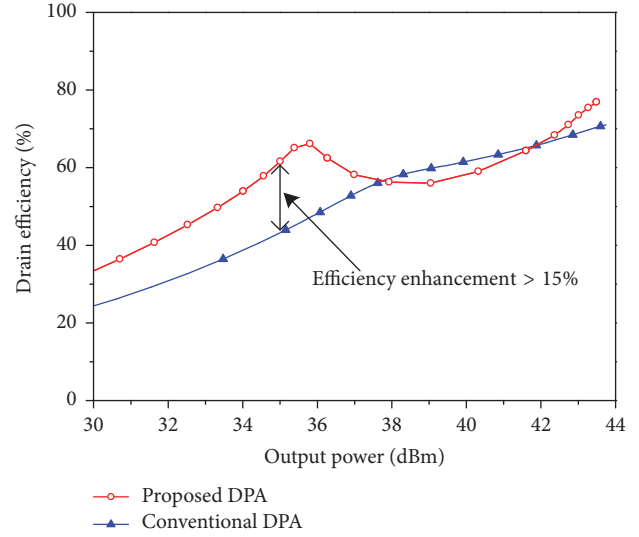


FIGURE 12: Simulated drain efficiencies of the proposed and conventional DPAs as a function of output power at 2.5 GHz.

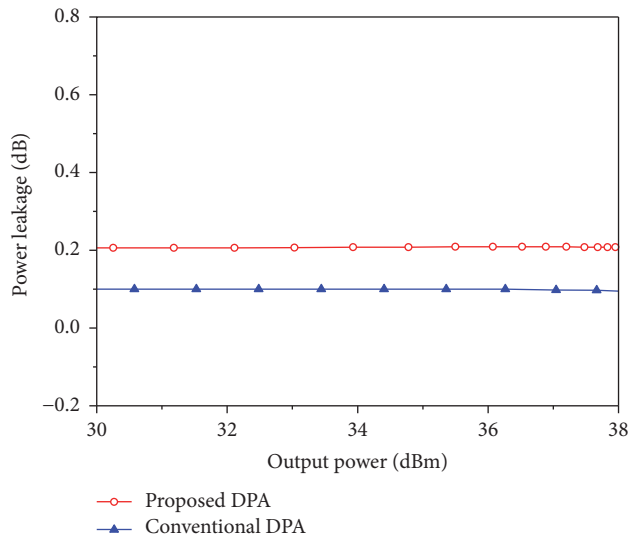


FIGURE 13: Simulated power leakages of the carrier amplifier in proposed and conventional DPAs.

peaking devices at saturation thus still satisfy the desired load impedance shown in Figures 2 and 8.

In Figure 12, the simulated drain efficiencies of the proposed and conventional DPAs are depicted. For the proposed DPA, the simulated efficiency is 58% at 9 dB BOP which is 15% higher than the one of conventional DPA. To analyze the influence of this IER on the overall performance of the DPA, the power leakages of the carrier amplifier at the combining point were simulated, as shown in Figure 13. For the proposed DPA using IER, less than 0.1 dB power leakage increment can be observed when compared with conventional DPA. The efficiency enhancement confirms that expected BOP range extension can be achieved using the proposed IER, while the output power performance is similar to conventional design.

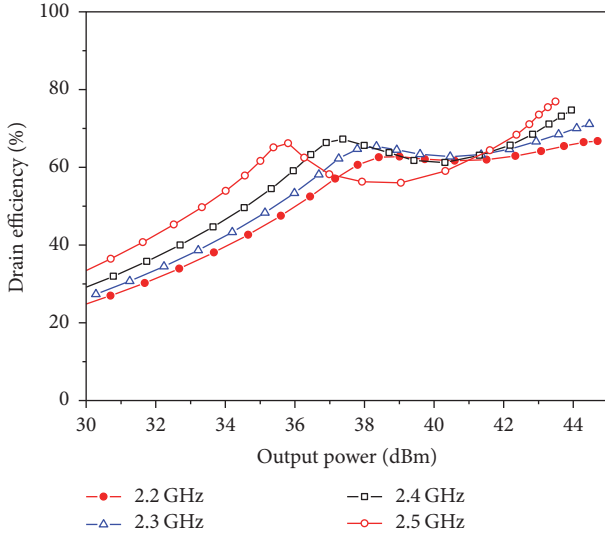


FIGURE 14: Simulated drain efficiencies of the proposed DPA at the frequencies of 2.2, 2.3, 2.4, and 2.5 GHz.

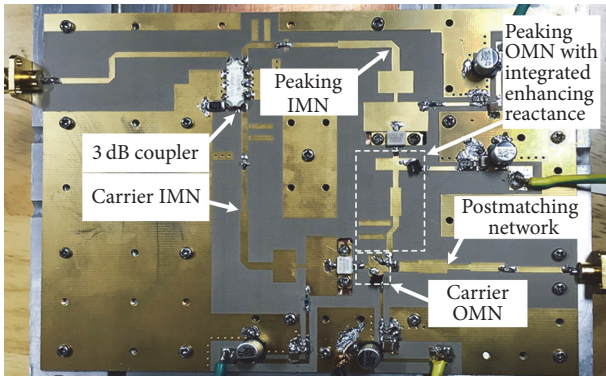


FIGURE 15: Photograph of the fabricated DPA.

To evaluate the efficiency over wide frequency band, the simulated drain efficiencies of the proposed DPA at 2.2, 2.3, 2.4, and 2.5 GHz are also given in Figure 14. The drain efficiencies are 48%–58% and 66%–75% for the 9 dB BOP and saturation regions, respectively. In addition, the efficiency plateau in large BOP range, which verifies the high-efficiency range extension based on IER, can also be observed.

### 3. Realization and Experimental Results

For experimental validation, the proposed DPA with large BOP range based on IER was fabricated, as shown in Figure 15. The measurement results using continuous wave signals and modulated signals are given as follows.

Figure 16 shows measured drain efficiencies and gains versus output powers at 2.2, 2.3, 2.4, and 2.5 GHz under continuous wave measurements. The designed DPA maintains drain efficiency of 45%–52% at about 9 dB BOP over the frequency band of interest. The peak output power ranges from 44 to 44.6 dBm with maximum efficiency of 63%–68%. One can observe that the drain efficiency can maintain

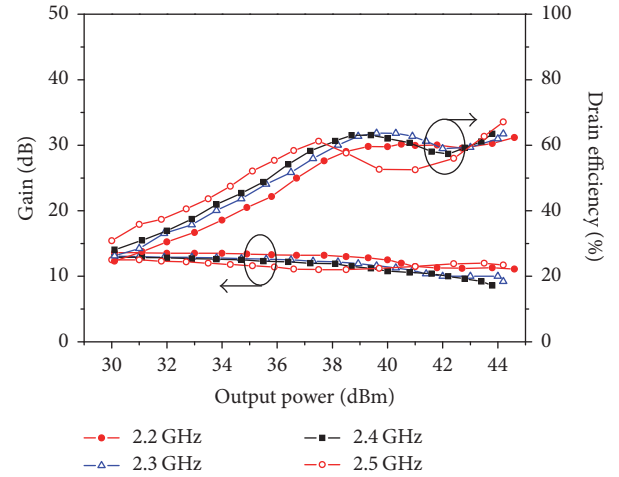


FIGURE 16: Measured drain efficiency and gain versus output power at different frequencies.

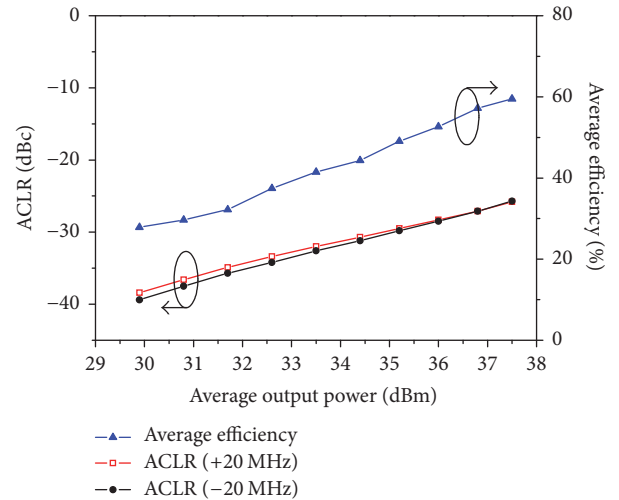


FIGURE 17: Measured average efficiencies and ACLRs for a 20 MHz LTE signal at the frequency of 2.35 GHz.

appropriate consistency over large BOP range, especially at the frequency band of 2.2–2.4 GHz.

To evaluate the performance of the proposed DPA for modulated signals application, a 20 MHz LTE signal with PAPR of about 8 dB was used to assess the efficiency and linearity performances at 2.35 GHz. Figure 17 depicts the measured average efficiencies and adjacent channel leakage ratios (ACLRs) versus the average output powers. The DPA achieved 50% average efficiency at 9 dB BOP, while ACLR is around  $-30$  dBc. Then, the DPA was linearized using the digital predistortion (DPD) technique used in [21]. The measured power spectral density (PSD) before and after DPD at 9 dB BOP is shown in Figure 18. Well-linearized ACLR of about  $-53$  dBc can be obtained. The result shows that the distortion caused by the DPA's nonlinearities and memory effects can be effectively removed. To validate the linearity improvement over the whole frequency band, the DPD linearization was implemented at the frequencies of 2.2,

TABLE I: Comparison with reported large back-off DPAs.

Ref.	Type	Freq. (GHz)	Effi.@ Sat. (%)	Effi.@ 9 dB BOP (%)	Signal BW (MHz)	ACLR (dBc)
2015 [22] <sup>1</sup>	Asym.	2.0–2.7	58–70	45–66	20	–39 <sup>4</sup>
2014 [17] <sup>2</sup>	Sym.	1.9–2.3	65–70	40–55	20	–49
2016 [18] <sup>1</sup>	Sym.	1.95–2.05	70–75	53	5	–23 <sup>3</sup>
2017 [19] <sup>1</sup>	Sym.	2.2–2.3	62.9–71	45.1–49.6	20	–51
T. W. <sup>1</sup>	Sym.	2.2–2.5	63–68	45–52	20	–53

Asym.: asymmetric DPA, Sym.: symmetric DPA. <sup>1</sup>Packaged device. <sup>2</sup>Bare-die device. <sup>3</sup>Without DPD. <sup>4</sup>With memoryless DPD.

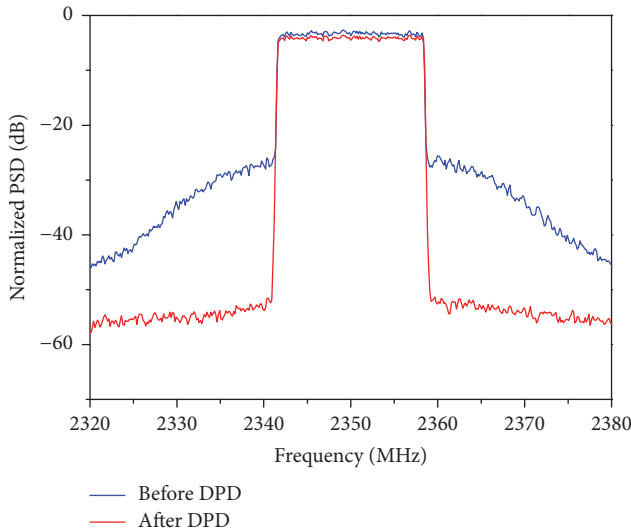


FIGURE 18: Measured power spectral density with the LTE signal at 9 dB BOP before and after DPD.

2.3, 2.4, and 2.5 GHz. Figure 19 gives the measured output powers, average efficiencies, and ACLRs versus frequencies at about 9 dB BOP. It is shown that the DPA can achieve good average efficiency of around 50% with ACLR of about –50 dBc after linearization.

For validation of the designed DPA for dual-band operations, a dual-band modulated signal with bandwidths of 10 and 20 MHz at 2.25 and 2.45 GHz, respectively, was employed to assess the efficiency and linearity performances of the DPA. The two dimensional decomposed vector rotation-based model was used for linearization [23, 24]. The measured PSD before and after DPD at the average output power of 33.7 dBm with associated efficiency of 43% is shown in Figure 20. It can be observed that the ACLRs are lower than –45 and –51 dBc for the first and second band, respectively. The linearization results show that good linearity and efficiency performance of the designed DPA can be achieved for multistandard wireless communication systems. Table I shows the performance comparison with published DPAs. When compared with most of the reported DPAs with good linearity, the proposed symmetric DPA using IER can provide high efficiency at 9 dB BOP and achieve wideband operation simultaneously.

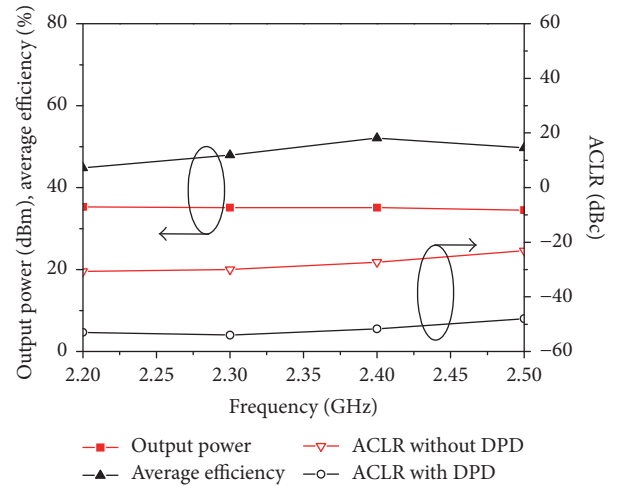


FIGURE 19: Measured output powers, average efficiencies, and ACLRs versus frequencies at about 9 dB BOP.

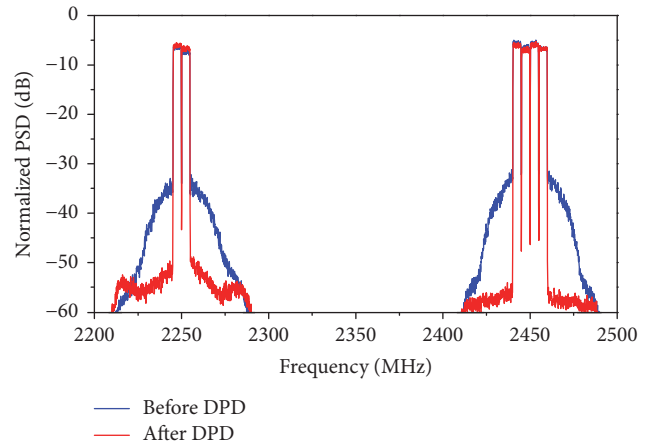


FIGURE 20: Measured power spectral density with the dual-band modulated signal before and after DPD.

#### 4. Conclusion

A DPA design approach for BOP range extension using IER was proposed. A 2.2–2.5 GHz symmetric DPA with 9 dB BOP range was developed and measured. Experimental results show that the proposed DPA has the drain efficiency of higher

than 45% at 9 dB BOP over a wide frequency band, which can satisfy the efficiency requirement when the DPA is driven by modern modulated signals with PAPRs of higher than 6 dB.

## Conflicts of Interest

The authors declare that they have no conflicts of interest.

## Acknowledgments

This work was supported by the National Science Foundation of China under Grant no. 61701199 and the Natural Science Foundation of Jiangsu Province of China under Grant no. BK20150528. This work was also supported by the Foundation of the State Key Laboratory of Millimeter Waves under Grant no. K201816 and the Natural Science Foundation of the Jiangsu Higher Education Institutions of China under Grants nos. 15KJB510007 and 16KJB510006. This work was also supported by the Research Foundation for Advanced Talents of Jiangsu University under Grant no. 15JDG080.

## References

- [1] A. Grebennikov and S. Bulja, "High-efficiency doherty power amplifiers: Historical aspect and modern trends," *Proceedings of the IEEE*, vol. 100, no. 12, pp. 3190–3219, 2012.
- [2] K. Rawat and F. M. Ghannouchi, "Design methodology for dual-band doherty power amplifier with performance enhancement using dual-band offset lines," *IEEE Transactions on Industrial Electronics*, vol. 59, no. 12, pp. 4831–4842, 2012.
- [3] S. Chen and Q. Xue, "Compact triple-transistor doherty amplifier designs: Differential/power combining," *IEEE Transactions on Microwave Theory and Techniques*, vol. 61, no. 5, pp. 1957–1963, 2013.
- [4] A. M. M. Mohamed, S. Boumaiza, and R. R. Mansour, "Electronically tunable doherty power amplifier for multi-mode multi-band base stations," *IEEE Transactions on Circuits and Systems I: Regular Papers*, vol. 61, no. 4, pp. 1229–1240, 2014.
- [5] J. Lee, J. Son, and B. Kim, "Optimised Doherty power amplifier with auxiliary peaking cell," *IEEE Electronics Letters*, vol. 50, no. 18, pp. 1299–1301, 2014.
- [6] R. Kalyan, K. Rawat, and S. K. Koul, "Design strategy of concurrent multi-band Doherty power amplifier," *IET Microwaves, Antennas & Propagation*, vol. 9, no. 12, pp. 1313–1322, 2015.
- [7] C. Musolff, M. Kamper, Z. Abou-Chahine, and G. Fischer, "A linear and efficient doherty PA at 3.5 GHz," *IEEE Microwave Magazine*, vol. 14, no. 1, pp. 95–101, 2013.
- [8] L. Piazzon, R. Giofre, P. Colantonio, and F. Giannini, "A method for designing broadband doherty power amplifiers," *Progress in Electromagnetics Research*, vol. 145, pp. 319–331, 2014.
- [9] C. Musolff, M. Kamper, Z. Abou-Chahine, and G. Fischer, "Linear and efficient Doherty PA Revisited," *IEEE Microwave Magazine*, vol. 15, no. 1, pp. 73–79, 2014.
- [10] J. Xia and X. Zhu, "Doherty power amplifier with enhanced in-band load modulation for 100 MHz LTE-advanced application," *Microwave and Optical Technology Letters*, vol. 57, no. 2, pp. 391–395, 2015.
- [11] X. Chen, W. Chen, F. M. Ghannouchi, Z. Feng, and Y. Liu, "A broadband doherty power amplifier based on continuous-mode technology," *IEEE Transactions on Microwave Theory and Techniques*, vol. 64, no. 12, pp. 4505–4517, 2016.
- [12] X. Y. Zhou, S. Y. Zheng, W. S. Chan, S. Chen, and D. Ho, "Broadband Efficiency-Enhanced Mutually Coupled Harmonic Postmatching Doherty Power Amplifier," *IEEE Transactions on Circuits and Systems I: Regular Papers*, vol. 64, no. 7, pp. 1758–1771, 2017.
- [13] S. H. Chun, D. H. Jang, J. Y. Kim, and J. H. Kim, "Inverted asymmetric Doherty power amplifier driven by two-stage symmetric Doherty amplifier," *IEEE Electronics Letters*, vol. 46, no. 17, pp. 1208–1209, 2010.
- [14] L. Piazzon, P. Colantonio, F. Giannini, and R. Giofr , "Asymmetrical Doherty power architecture with an integrated driver stage in the auxiliary branch," *International Journal of RF and Microwave Computer-Aided Engineering*, vol. 24, no. 4, pp. 498–507, 2014.
- [15] J. Xia, M. Yang, and A. Zhu, "Improved Doherty Amplifier Design with Minimum Phase Delay in Output Matching Network for Wideband Application," *IEEE Microwave and Wireless Components Letters*, vol. 26, no. 11, pp. 915–917, 2016.
- [16] H. Kang, H. Lee, H. Oh et al., "Symmetric Three-Way Doherty Power Amplifier for High Efficiency and Linearity," *IEEE Transactions on Circuits and Systems II: Express Briefs*, vol. 64, no. 8, pp. 862–866, 2017.
- [17] X. H. Fang and K.-K. M. Cheng, "Extension of high-efficiency range of doherty amplifier by using complex combining load," *IEEE Transactions on Microwave Theory and Techniques*, vol. 62, no. 9, pp. 2038–2047, 2014.
- [18] M.  zen, K. Andersson, and C. Fager, "Symmetrical Doherty Power Amplifier with Extended Efficiency Range," *IEEE Transactions on Microwave Theory and Techniques*, vol. 64, no. 4, pp. 1273–1284, 2016.
- [19] W. Shi, S. He, and N. Gideon, "Extending high-efficiency power range of symmetrical Doherty power amplifiers by taking advantage of peaking stage," *IET Microwaves, Antennas & Propagation*, vol. 11, no. 9, pp. 1296–1302, 2017.
- [20] W. Shi, S. He, F. You et al., "The Influence of the Output Impedances of Peaking Power Amplifier on Broadband Doherty Amplifiers," *IEEE Transactions on Microwave Theory and Techniques*, vol. 65, no. 8, pp. 3002–3013, 2017.
- [21] J. Xia, M. Yang, Y. Guo, and A. Zhu, "A broadband high-efficiency Doherty power amplifier with integrated compensating reactance," *IEEE Transactions on Microwave Theory and Techniques*, vol. 64, no. 7, pp. 2014–2024, 2016.
- [22] X. A. Nghiem, J. Guan, and R. Negra, "Broadband Sequential Power Amplifier with Doherty-Type Active Load Modulation," *IEEE Transactions on Microwave Theory and Techniques*, vol. 63, no. 9, pp. 2821–2832, 2015.
- [23] N. Kelly, W. Cao, and A. Zhu, "Preparing Linearity and Efficiency for 5G: Digital Predistortion for Dual-Band Doherty Power Amplifiers with Mixed-Mode Carrier Aggregation," *IEEE Microwave Magazine*, vol. 18, no. 1, pp. 76–84, 2017.
- [24] Y. Guo and A. Zhu, "Power adaptive decomposed vector rotation based digital predistortion for RF power amplifiers in dynamic power transmission," in *Proceedings of the 2017 IEEE Topical Conference on Power Amplifiers for Wireless and Radio Applications, PAWR 2017*, pp. 8–10, USA, January 2017.

## Research Article

# Single-Layer, Dual-Port, Dual-Band, and Orthogonal-Circularly Polarized Microstrip Antenna Array with Low Frequency Ratio

Min Wang , Dao-Yu Wang, Wen Wu, and Da-Gang Fang

Ministerial Key Laboratory of JGMT, School of Electronic and Optical Engineering, Nanjing University of Science and Technology, Nanjing 210094, China

Correspondence should be addressed to Min Wang; wangmin@njjust.edu.cn

Received 14 December 2017; Accepted 11 March 2018; Published 11 April 2018

Academic Editor: Shichang Chen

Copyright © 2018 Min Wang et al. This is an open access article distributed under the Creative Commons Attribution License, which permits unrestricted use, distribution, and reproduction in any medium, provided the original work is properly cited.

A single-layer, dual-port, dual-band, and dual circularly polarized (CP) microstrip array is designed for satellite communication in this paper. The operating frequencies are 8.2 and 8.6 GHz with a very low ratio of 1.05. First, a rectangular patch element is fed through microstrip lines at two orthogonal edges to excite two orthogonal dominant modes of  $TM_{01}$  and  $TM_{10}$ . The very low frequency ratio can be realized with high polarization isolations. Then, a 2-by-2 dual-band dual-CP subarray is constructed by two independent sets of sequentially rotated (SR) feed structures. An 8-by-8 array is designed on the single-layer thin substrate. Finally, by utilizing one-to-four power dividers and semirigid coaxial cables, a 16-by-16 array is developed to achieve higher gain. Measured results show that the 16-by-16 array has 15 dB return loss (RL) bandwidths of 4.81% and 6.75% and 3 dB axial ratio (AR) bandwidths of 2.84% and 1.57% in the lower and the upper bands, respectively. Isolations of 18.6 dB and 19.4 dB and peak gains of 25.1 dBic and 25.6 dBic are obtained at 8.2 and 8.6 GHz, respectively.

## 1. Introduction

In satellite communication systems, dual-band antennas are usually required for the uplink and downlink operating at different frequencies. Orthogonal polarization is much preferable to improve the isolation of separate transmit-receive channels, especially for dual-band antennas with a low frequency ratio. Circular polarization is the better choice than linear polarization because of the advantages of insensitivity to antenna orientations, elimination of the signal Faraday rotation effect caused by the ionosphere, and resistance to bad weather conditions. Various antenna types can be used to address the shared-aperture dual-band dual-circular polarized (CP) problems. Planar antennas, such as printed dipoles, slots and microstrip patches, become more favorite candidates attributing to their low profiles.

Traditionally, dual-band dual-linear or circular polarized antennas tend to adopt a multilayer and stacked-patch structure [1–5]. Separate elements are placed on different layers to achieve a dual-band dual-polarized design flexibly. Thus, appropriate frequency ratios can be easily realized [1, 2]. Agile feed networks are designed to form larger arrays with

high gain and efficiency [3, 4], improved frequency response [2], and wide bandwidth [5]. The only drawback is that the fabrication process of multilayer antennas is rather difficult and costly.

Several single-layer antenna elements have been proposed to achieve a dual-band and dual-CP radiation. Cross slots with unequal arm-lengths can be loaded on patch antenna [6] or annular-slot [7, 8] to achieve dual-band and dual-CP antennas with a single-layer configuration. Nevertheless, the bidirectional radiation property of these slot antennas limits their applications for satellite. In this context, a dual-band CP planar monopole antenna is presented in [9] by combining an “L”-shaped strip and a “C”-shaped strip. Besides, a circular patch with eight curved slots and a disk-loaded coaxial probe is presented to achieve the dual-band dual circularly polarized pattern [10]. Yet, their omnidirectional radiation is not desirable. It should be pointed out that there is also a single-layer design that can achieve dual-band and dual-CP directional pattern [11]. However, the gain of above-mentioned antennas is relatively low. Moreover, their coaxial probe feeding scheme increases

the difficulty to form a larger array that is much desirable in satellite communications.

Only a few works have been carried out on dual-band dual-polarized antenna arrays with a single-layer substrate [12–14]. In [12], two disparate patches are connected directly to construct a dual-band orthogonal-CP element fed by microstrip line, which can be extended to a larger array easily. A square patch loaded by four stubs is proposed in [13], where two pairs of orthogonal modes, that is, the  $TM_{10}/TM_{01}$  and  $TM_{30}/TM_{03}$ , are excited simultaneously. In these two cases, the dual-band orthogonal-CP microstrip array has been implemented on a single-layer substrate, but the low frequency ratio is difficult to achieve. The realized ratios of two center frequencies are 1.44 and 1.42, respectively, which are rather high for some particular satellite communication applications. In [14], a low frequency ratio of 1.14 is achieved by exciting  $TM_{10}$  and  $TM_{01}$  modes of a rectangular patch, while it is orthogonal linear polarized (LP). In addition, these configurations tend to have only a single port, which is not suitable for systems with separate transmit-receive antennas.

In this paper, a dual-port, dual-band, and dual-CP microstrip array on a single-layer substrate is presented. First, by exciting two orthogonal dominant modes of  $TM_{01}$  and  $TM_{10}$ , a rectangular patch is adopted to realize a very low frequency ratio, while radiating the orthogonal-LP waves. For a specific satellite communication system, the element is designed at 8.2 GHz and 8.6 GHz with a ratio of 1.05. Then, the sequentially rotated (SR) feeding scheme is utilized to construct a dual-port, dual-band, and dual-CP array with improved impedance and axial ratio (AR) bandwidth. For demonstration, a 2-by-2 subarray is constructed by two independent sets of sequentially feed network. Afterwards, an 8-by-8 array is proposed on the single-layer thin substrate. Finally, by utilizing the one-to-four power dividers and semirigid coaxial cables, a 16-by-16 array is successfully developed with high gain of more than 25 dBic. Measured results indicate that the two antenna arrays exhibit ideal radiation patterns and good isolations of better than 18 dB between two ports.

## 2. Design Concept

The specifications of the antenna to be designed are shown in Table 1. It is dual-port, dual-band, and orthogonal-CP at 8.2 and 8.6 GHz. The targeted gains of 25 dBic are not very high for single-band microstrip antenna arrays, which can be achieved with about 100 elements. However, they must be met for a dual-port shared-aperture array as well as specified frequencies and polarization. The bandwidths of 15 dB return loss (RL) and 3 dB axial ratio are 80 MHz in both bands. The fractional bandwidths are about 1%.

The frequency ratio is only 1.05. It is convenient to construct a shared-aperture array with equal element spacing in two bands, but it causes restrictions on the designs of the feed networks and shared-aperture elements (or subarray). For such a low frequency ratio, it is difficult to implement a diplexer with desirable isolations between two bands, so that two independent feed networks are required for dual-port

TABLE 1: Design parameters for dual port, dual-band, orthogonal-CP antenna.

Parameters	Receiving	Transmitting
Frequency (GHz)	8.2	8.6
Bandwidth (MHz)	80	80
Polarization	RHCP	LHCP
Return loss (dB)	$\geq 15$	$\geq 15$
Axial ratio (dB)	$< 3$	$< 3$
Gain (dBic)	$> 25$	$> 25$
Isolation (dB)	$> 20$	$> 20$

designs. Shared-aperture elements (or subarray) can be designed with single-layer or multilayer configuration. For the former, four appropriate modes should be excited simultaneously in one patch to implement orthogonal-CP in dual bands; however, it is difficult for the frequency ratio of 1.05. For the latter, the overlapped patches on two layers are required, but strong coupling significantly increases the design complexity. Moreover, the fabrication of multilayer antennas is rather difficult and costly. Therefore, we choose to design with a single-layer configuration.

After a preliminary investigation, two candidates of the shared-aperture array on a single-layer substrate were investigated: (1) interlaced array consisting of two independent CP arrays in two bands; (2) shared-aperture array with sequential-rotated CP subarrays consisting of LP elements.

The first configuration is formed by using two independent interlaced arrays consisting of CP patch elements and feed networks. It is difficult to interlace two independent corporate-fed arrays with appropriate element spacing and without crossing in a single layer. Series-fed arrays are relatively easy; however, they suffer from very low bandwidth and tilted beam at frequencies off the center.

The second configuration of shared-aperture array adopts the sequentially rotated CP subarray as a unit cell. The SR technique was first proposed in [15], which substantially improves the bandwidth and polarization purity of CP arrays in spite of using the narrow band elements [16, 17]. Either LP or CP elements can be adopted to construct a SR array; however, LP rectangular patch has two orthogonal dominant modes which can realize dual-band radiation with very small frequency ratio as well as desired isolation. The following design is based on this configuration.

The patch with edges  $L_1$  and  $L_2$  of unequal length is adopted and shown in Figure 1. Two orthogonal dominant modes  $TM_{01}$  and  $TM_{10}$  are excited by two microstrip lines at the center of the orthogonal edges  $L_1$  and  $L_2$  for 8.2 and 8.6 GHz, respectively.

A basic SR subarray has its elements arranged in a 2-by-2 square or rectangular grid configuration with element angular orientation and feed phase arranged in either  $0^\circ$ ,  $90^\circ$ ,  $0^\circ$ ,  $90^\circ$  or  $0^\circ$ ,  $90^\circ$ ,  $180^\circ$ ,  $270^\circ$  fashion. In the latter arrangement, the axial ratio bandwidth of the array can be increased substantially [17]. Either parallel feed or serial feed can be used for a SR array [18]. Here, both of them are utilized to construct a dual-band dual-CP subarray with dual ports based on the dual-band dual-LP elements.

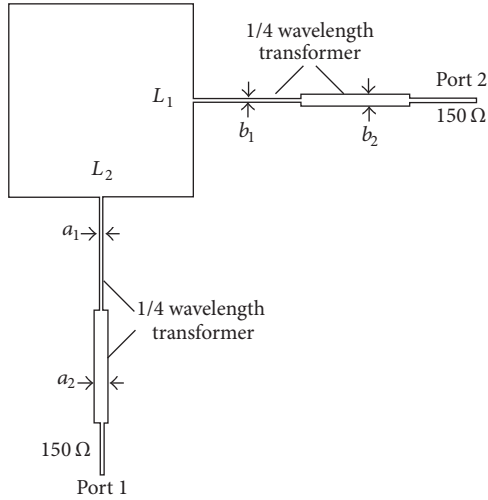


FIGURE 1: Structure of dual-band dual-LP element.

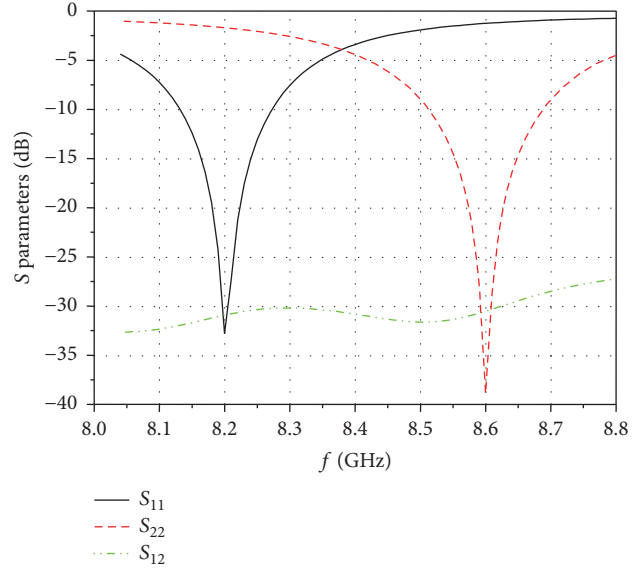


FIGURE 3: S parameters of the element.

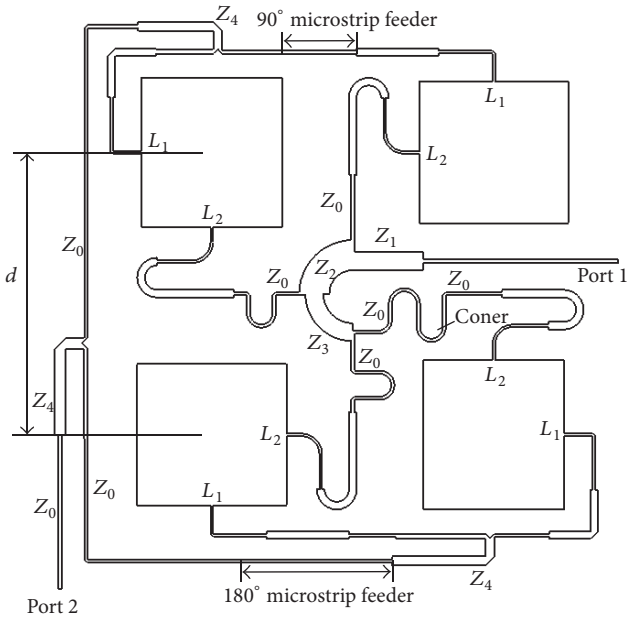


FIGURE 2: Structure of dual-band dual-CP subarray.

The 2-by-2 subarray is shown in Figure 2. Both the element angular orientation and feed phase are arranged in the  $0^\circ$ ,  $90^\circ$ ,  $180^\circ$ ,  $270^\circ$  fashion. A serial feed network is placed at the array center and connected to  $L_2$  to form right-hand circularly polarization (RHCP) for the lower band. Meanwhile, a parallel feed structure is placed outside the subarray and connected to  $L_1$  to form left-hand circularly polarization (LHCP).

The proposed 2-by-2 subarray possesses all the desired features: being single-layer, dual-port, dual-band, dual-circular polarization and with a low frequency ratio. This subarray is taken as the unit cell to form an 8-by-8 array by using two independent sets of parallel feed networks. The cross-over of the feed lines in the two sets of the feed networks can be avoided through careful arrangement. By utilizing

one-to-four power dividers and semirigid coaxial cables, a 16-by-16 array is further developed. The performances of this design in various stages of development are provided below in detail.

### 3. Dual-Band Dual-LP Element

As illustrated in Figure 1, a dual-band dual-LP rectangular patch is designed on a single-layer substrate of Rogers RT/duroid 5880 with the relative permittivity of 2.2 and a thickness of 0.787 mm. The dimensions of edges  $L_1$  and  $L_2$  are 11.65 mm and 11.04 mm, corresponding to the frequencies  $f_1 = 8.2$  GHz and  $f_2 = 8.6$  GHz, respectively. Two orthogonal dominant modes  $TM_{01}$  and  $TM_{10}$  are excited by two microstrip lines at a pair of orthogonal edge-centers. In each feed line, a dual-section transformer consisting of two quarter-wavelength segments with impedance of 160 ohms and 100 ohms is introduced to match the patch to the feed line of 150 ohms. The line widths of the impedance transformers  $a_1$ ,  $a_2$ ,  $b_1$ , and  $b_2$  are 0.2 mm, 0.8 mm, 0.2 mm, and 0.6 mm, respectively. Simulated S parameters of the element are shown in Figure 3. We can see that it matches well at two center frequencies, respectively. The corresponding 15 dB return loss bandwidths are 0.97% (8.16–8.24 GHz) and 1.05% (8.56–8.65 GHz). The isolations of two ports are better than 30 dB.

In this design, the frequency ratio is approximately equal to the ratio between the two orthogonal edges  $L_1$  and  $L_2$  of the patch. Because of the narrowband property and good polarization purity, two operating frequencies with a very low frequency ratio can be achieved with good isolations.

### 4. Dual-Band Dual-CP Subarray

4.1. Subarray Structure. As indicated in Figure 2, a 2-by-2 subarray is constructed by SR dual-band orthogonal-LP

TABLE 2: Impedance transformation values.

Feeder section	$Z_0$	$Z_1$	$Z_2$	$Z_3$	$Z_4$
Impedance values ( $\Omega$ )	150	75	50	75	106

patches. All the elements match microstrip lines with characteristic impedance  $Z_0$ . The topological structure in Figure 2 is useful where dual-band, dual-port, and dual-circular polarization are required.

A serial feed network is placed at the array center and connected to  $L_2$  to form RHCP for the lower band. It is modified from the one in Ref. [18]. The curved segments  $Z_2$  and  $Z_3$  perform as transitions rather than as quarter-wavelength impedance transformers. Only one-quarter-wavelength impedance transformer  $Z_1$  is used to match the subarray to impedance  $Z_0$ . Therefore, the network can be more compact to be accommodated in an array with small element spacing. To meet the feed phase requirements,  $90^\circ$  phase shifts are achieved by stretching the length of corners along with the arcs.

A corporate network is placed outside the subarray and connected to  $L_1$  to form LHCP. It is a combination of three 3 dB T-junction power dividers, in which a quarter-wavelength impedance transformer  $Z_4$  is used. Impedance values of the transitions and impedance transformers are shown in Table 2, which ensure equal power required for each element. The  $90^\circ$  phase shifts are achieved by adding two  $90^\circ$  and one  $180^\circ$  microstrip segments.

**4.2. Element Spacing Selection.** For a conventional microstrip patch array, maximum directivity is obtained when the element spacing is in the range of  $0.8\text{--}0.9\lambda_0$ , where  $\lambda_0$  denotes the wavelength in free space [19]. However, for a SR CP array with LP elements, gain bandwidth broadens for reduced spacing [20]. Therefore, element spacing  $d$  of the proposed array should be chosen as small as possible. To accommodate the patch and feed networks,  $d$  is chosen as 22 mm, about  $0.6\lambda_1$  and  $0.63\lambda_2$ , where  $\lambda_1$  and  $\lambda_2$  are the free space wavelengths of  $f_1 = 8.2$  GHz and  $f_2 = 8.6$  GHz, respectively.

**4.3. Simulated Results.** Simulated  $S$  parameters of the subarray are shown in Figure 4. It is seen that desired matching at two ports is obtained for both frequency bands. The 15 dB RL bandwidths are 3.92% (8.00–8.32 GHz) and 3.15% (8.43–8.7 GHz) in the lower and upper bands, respectively. The bandwidths are obviously broadened. The isolations between two ports are 20 dB and 16 dB at 8.2 GHz and 8.6 GHz, respectively. We can see that the isolation performance deteriorates obviously. This is the result of the broadening of the bandwidth and the coupling between the feeder and the patch. However, the insertion of a bandpass filter in an independent feed network can easily increase the isolation of up to 20 dB.

Simulated ARs versus frequency are shown in Figure 5. The 3 dB AR bandwidths are 3.23% (8.075–8.34 GHz) and 1.28% (8.57–8.68 GHz) in the lower and upper bands, respectively.

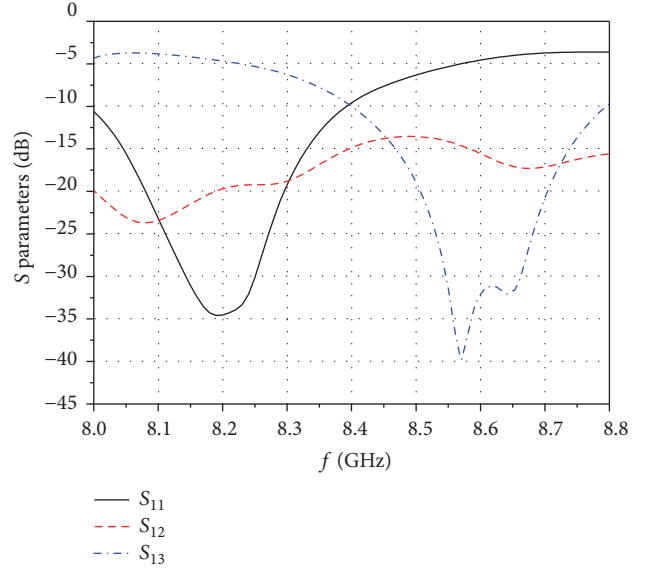
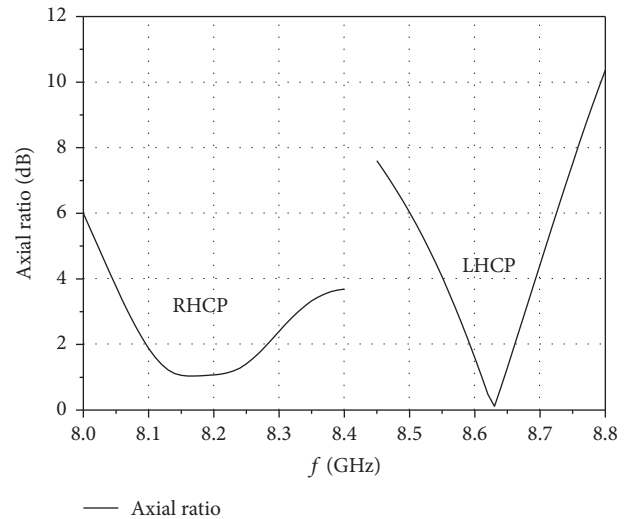
FIGURE 4:  $S$  parameters of the subarray.

FIGURE 5: ARs of the subarray versus frequencies.

Gain patterns are shown in Figure 6. Maximum gains of 10.5 dBic and 11.29 dBic are obtained at 8.2 GHz and 8.6 GHz, respectively. It is seen that the patterns are much symmetrical and the cross polarization levels are below  $-20$  dB in two principle planes. However, high cross-polarized lobes appear in the  $\varphi = 45^\circ$  plane. The high diagonal lobes can be significantly reduced when the sequential array is placed in a larger array environment that will be shown in Section 5.

For SR arrays, the gain bandwidth is dependent on the elements' polarization properties. The array factor (AF) of the 4-element subarrays with different polarized elements is investigated in [21]. It shows that, for an SR array with LP elements, the AF is generally independent of frequency, but the maximum is 3 dB lower than an array with CP elements. That is the reason why the gains of the propose dual-band array are about 3 dB lower than those of a conventional

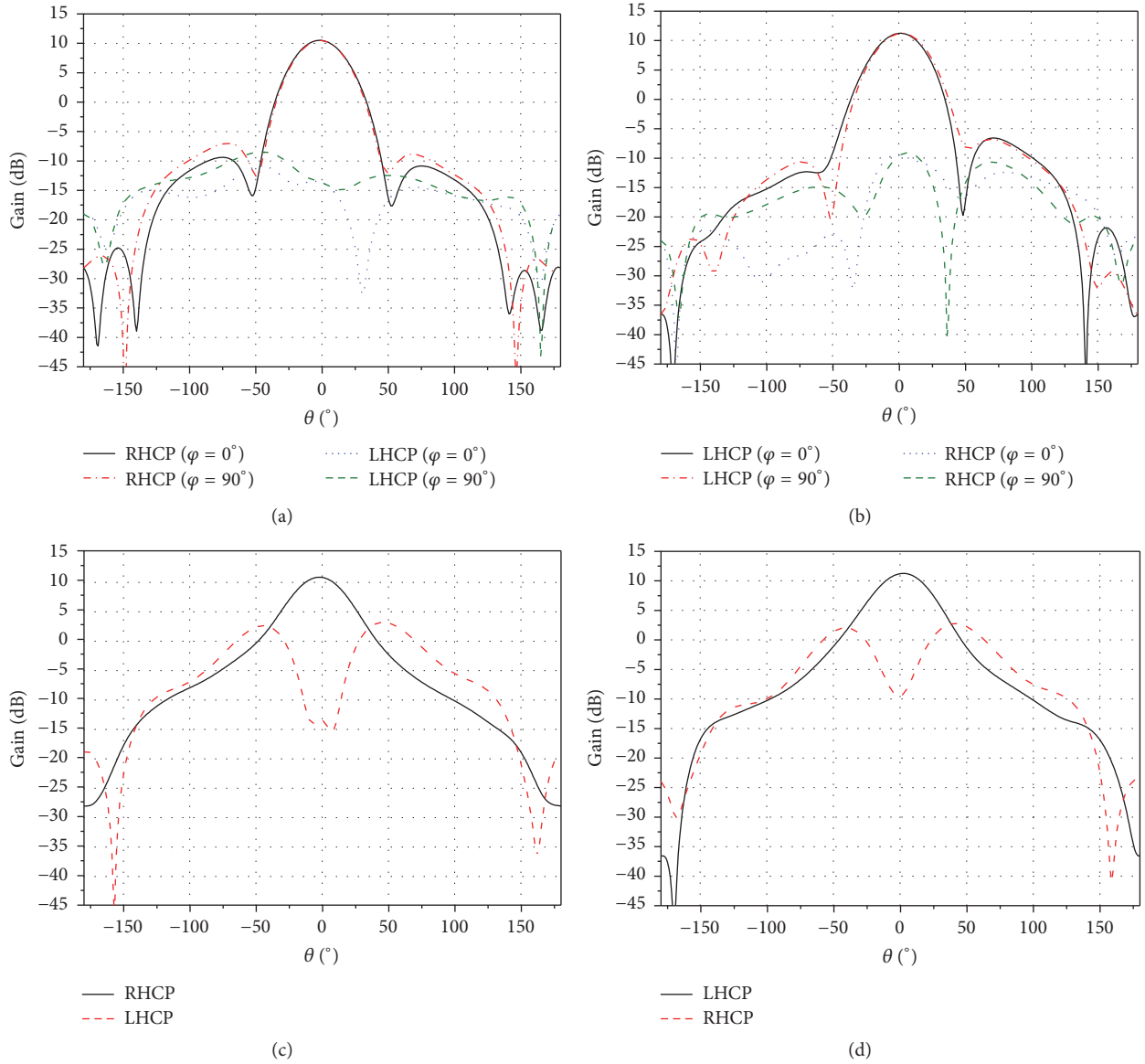


FIGURE 6: Gain patterns at two center frequencies: (a) gain patterns in two principle planes at 8.2 GHz; (b) gain patterns in two principle planes at 8.6 GHz; (c) gain patterns in the  $\varphi = 45^\circ$  plane at 8.2 GHz; (d) gain patterns in the  $\varphi = 45^\circ$  plane at 8.6 GHz.

4-element microstrip array, and the gain bandwidth is mainly determined by the minimum of the impedance and AR bandwidth.

## 5. 8-by-8 Dual-Band Dual-CP Array

**5.1. 8-by-8 Array Structure.** Considering the 2-by-2 subarray as a dual-port unit, an 8-by-8 array on a single-layer substrate is designed and fabricated. As shown in Figure 7, a hard plastic plate with a thickness of 4 mm is set on the back. Two independent sets of parallel feed networks are used to feed 16 subarrays. It is seen that the designed layout can avoid the cross-over of feed lines in the two sets of the feed networks.

To accommodate the networks and reduce the coupling between feed lines, the spacing is chosen as  $d = 22$  mm,

TABLE 3: Optimized values of S parameters and ARs.

Port	$S_{11}$ (dB)	$S_{12}$ (dB)	$S_{22}$ (dB)	AR (dB)
1@8.2 GHz	-18.8	-23.6	-9.0	1.67
2@8.6 GHz	-5.71	-20.2	-24.7	1.41

$d_1 = 28$  mm,  $d_2 = 26$  mm, and  $d_3 = 32$  mm. The feed networks should be adjusted carefully for appropriate amplitudes and phases. The array dimension is 220 mm  $\times$  220 mm.

**5.2. Simulated and Measured Results.** S parameters and ARs are optimized at two center frequencies, and the optimal values are shown in Table 3. Good impedance matching, moderate isolations, and desired CP radiation are achieved

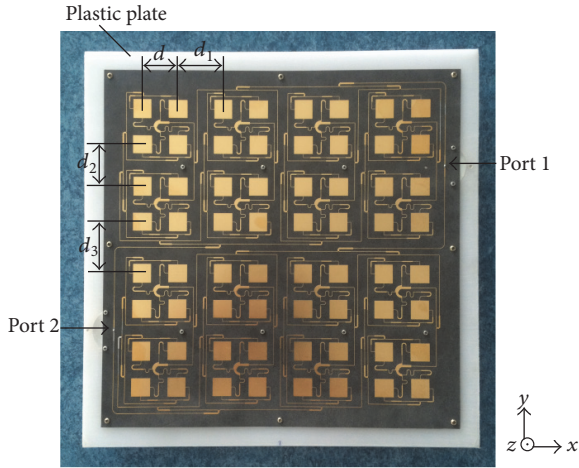


FIGURE 7: Photo of the fabricated antenna array.

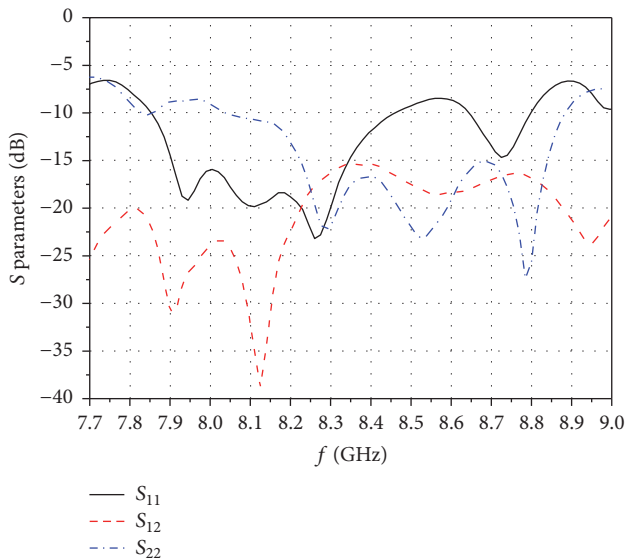


FIGURE 8: S parameters of the 8 by 8 array.

simultaneously. Measured S parameters with desired performances are shown in Figure 8. The 15 dB RL bandwidths are 5.3% (7.91–8.34 GHz) and 7% (8.23–8.83 GHz) in the lower and upper bands, respectively. The isolations between two ports are 22.4 dB and 18.5 dB at 8.2 GHz and 8.6 GHz, respectively. We found that the impedance bandwidths are further broadened, which can be attributed to the increase of loss and coupling in the array. However, the isolations do not deteriorate further, even though two band overlap to some extent. It can be explained by the measured ARs shown in Figure 9. The 3 dB AR bandwidths are 3.23% (8.02–8.22 GHz) and 1.39% (8.54–8.66 GHz) in the lower and upper bands, respectively, which are close to those of the subarray. The minimum ARs of 0.45 dB and 0.4 dB are obtained, respectively, at 8.1 GHz and 8.6 GHz. This is ideal for CP performance to ensure good isolation. It is also found that the frequency deviation of the minimum AR is very small, which is due to the error in simulation and

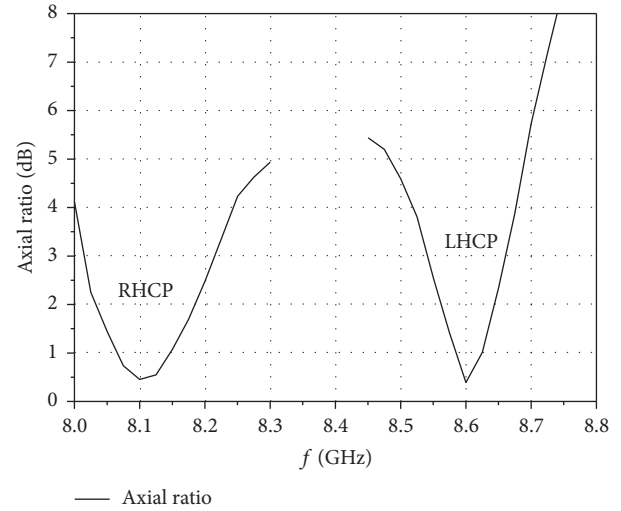


FIGURE 9: ARs of the 8-by-8 array versus frequencies.

manufacturing process. At 8.2 GHz, the AR of 2.48 dB is acceptable.

Patterns at 8.1 GHz and 8.6 GHz are simulated and measured. Normalized patterns in the  $\varphi = 0^\circ$  plane are shown in Figure 10. Measured and simulated results maintain good consistency. The patterns are very symmetric and have very low cross polarization level in the main beam. Half-power beamwidths of  $9.1^\circ$  and  $8.8^\circ$ , and side lobes of  $-11$  dB and  $-10$  dB are obtained at 8.1 GHz and 8.6 GHz, respectively. Normalized patterns in the  $\varphi = 45^\circ$  plane at 8.1 GHz are also given in Figure 11. It can be seen that the cross polarization reduces to  $-11.3$  dB and is far away from the main beam. This is because of the small spacing of the subarray and the averaging effects of the large array.

The measured gains of 20.1 dBic and 20.5 dBic are obtained at 8.2 GHz and 8.6 GHz, respectively. While simulated gains are 21.3 dBic and 21.9 dBic. The deviations are mainly attributed to the fabrication tolerances and the dielectric and conductive loss.

**5.3. Discussion on Array Configuration.** In the above discussion, two independent sets of parallel feed networks are used to extend the subarray to the 8-by-8 array. The SR feed networks can be adopted again to further broaden the 15 dB RL and 3 dB AR bandwidth [18]. In that case, however, the gain bandwidth will decrease. In addition, the complexity of array arrangement will also increase dramatically for the dual-band shared-aperture antenna array.

## 6. 16-by-16 Dual-Band Dual-CP Array

To achieve higher gains, a 16-by-16 array is designed. Because of the rapid increase of loss, microstrip line is not the advisable choice to expand the feed network. A one-to-four power divider (PD) and semirigid coaxial cables are used to set up the 16-by-16 array, which are shown in Figures 12 and 13, respectively. The PD consists of four symmetric quarter-wavelength impedance transformers to achieve complete

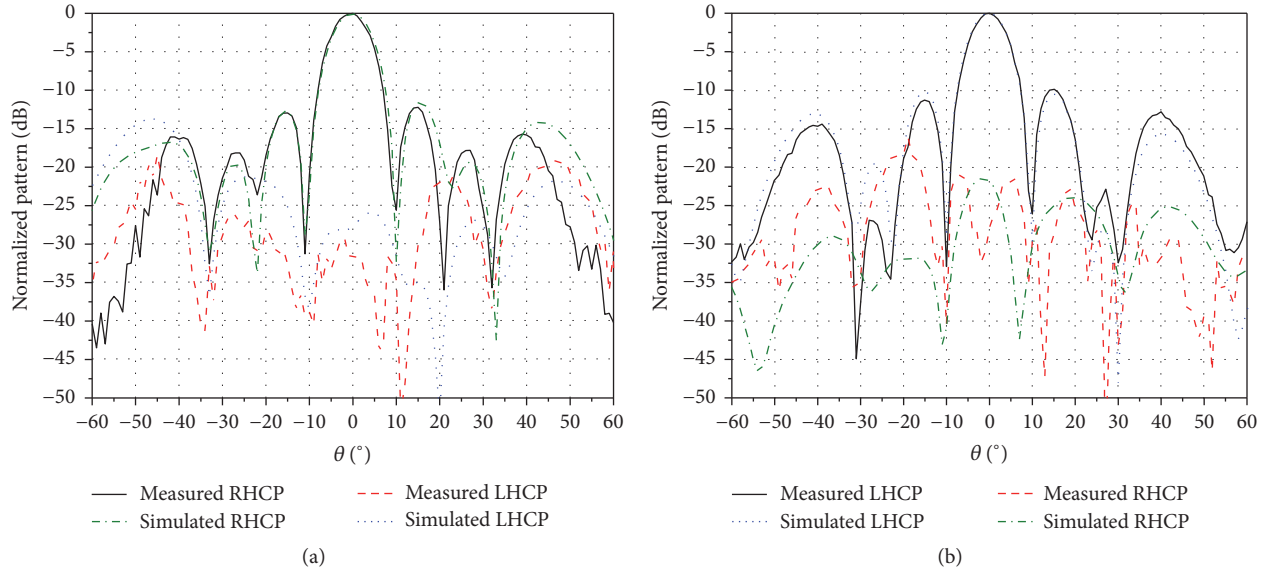


FIGURE 10: Normalized patterns in the  $\varphi = 0^\circ$  plane: (a) 8.1 GHz; (b) 8.6 GHz.

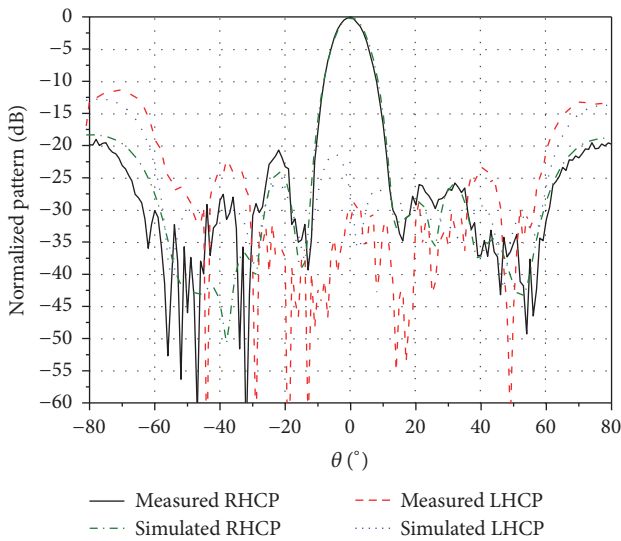


FIGURE 11: Normalized patterns in the  $\varphi = 45^\circ$  plane at 8.1 GHz.

impedance matching. Two independent PDs are designed for upper and lower bands, respectively. Measured return losses at the input ports are better than 20 dB over the operating bands. Insertion losses between input and output ports are less than 6.5 dB. Amplitude and phase deviations between four ways are less than 0.15 dB and  $2^\circ$ , respectively. The semirigid coaxial cables have a low insertion loss of about 0.1 dB and a small phase deviation less than  $2^\circ$ . Therefore, desired balance of amplitude and phase can be achieved. The total insertion loss, including the PD, the coaxial cables, and SMA connectors, is about 1 dB.

The fabricated 16-by-16 array is shown in Figure 14. It is seen from Figure 14(a) that the array consists of four 8-by-8 arrays with spacing values  $d_4$  and  $d_5$  of 32 mm, about  $0.87\lambda_1$

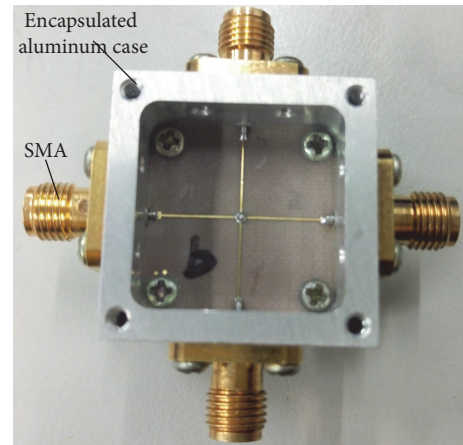


FIGURE 12: Photo of one-to-four power divider.



FIGURE 13: Photo of a semirigid coaxial cable.

and  $0.92\lambda_2$ . The array has a size of  $424 \times 424 \text{ mm}^2$  and is fixed on a hard plastic plate with a thickness of 4 mm. Figure 14(b) shows the connections between the 8-by-8 subarray ports connected by the one-to-four power dividers and semirigid coaxial cables.

Measured  $S$  parameters are shown in Figure 15. The impedance bandwidths are 4.81% (7.91–8.30 GHz) and 6.75% (8.30–8.88 GHz) for 15 dB RL in the lower and upper bands, respectively. At 8.2 GHz and 8.6 GHz, the isolations between

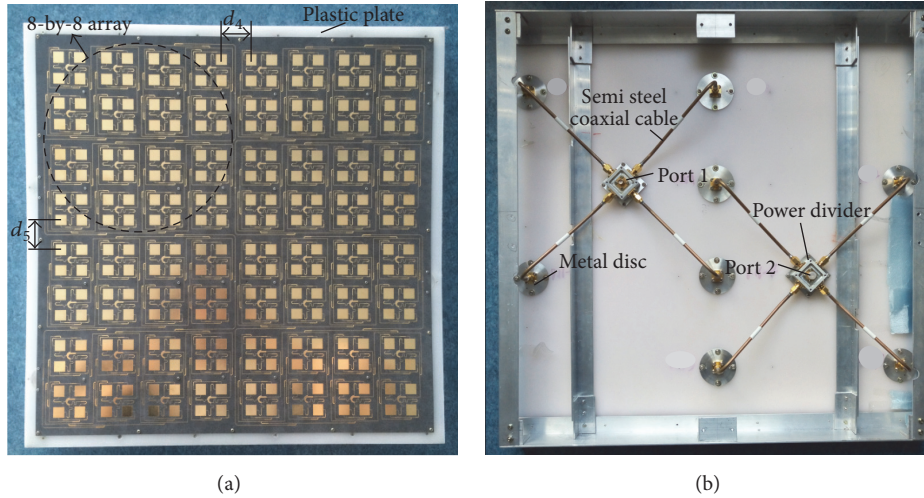


FIGURE 14: Photos of the fabricated 16-by-16 antenna array: (a) top view; (b) bottom view.

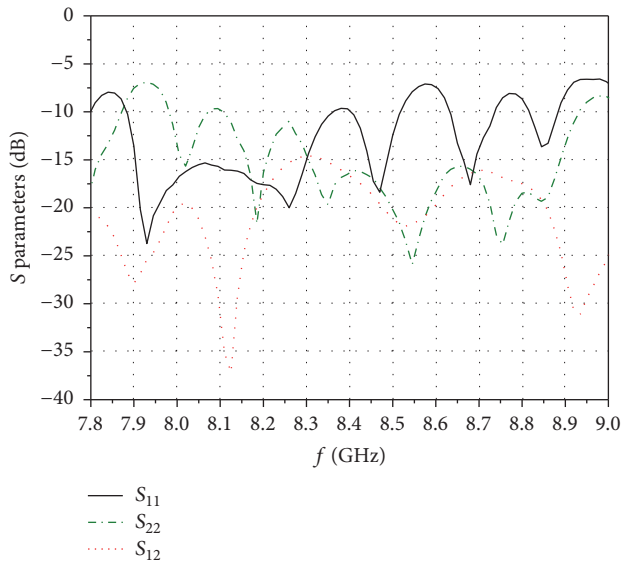


FIGURE 15: S parameters of the 16-by-16 array.

two ports are 18.6 dB and 19.4 dB, respectively. Measured ARs are shown in Figure 16. The 3 dB AR bandwidths are 2.84% (7.99–8.22 GHz) and 1.57% (8.52–8.66 GHz) in the lower and upper bands, respectively, which are close to those of the subarray and the 8-by-8 array. Minimum ARs of 0.4 dB and 0.6 dB are obtained at 8.1 GHz and 8.6 GHz, respectively. The small deviation of the minimum AR frequency in the lower band is in accordance with the deviation of the 8-by-8 array. At 8.2 GHz, the AR of 2.8 dB is acceptable.

Patterns are measured at 8.1 GHz and 8.6 GHz. Normalized patterns in the  $\varphi = 0^\circ$  plane are shown in Figure 17. The patterns are very symmetrical and have very low cross polarization levels in the main beam. Half-power beamwidths of  $4.4^\circ$  and  $4.1^\circ$ , and side lobes of  $-11.7$  dB and  $-11$  dB are obtained at 8.1 GHz and 8.6 GHz, respectively. Normalized patterns in the  $\varphi = 45^\circ$  plane at 8.1 GHz are also given in

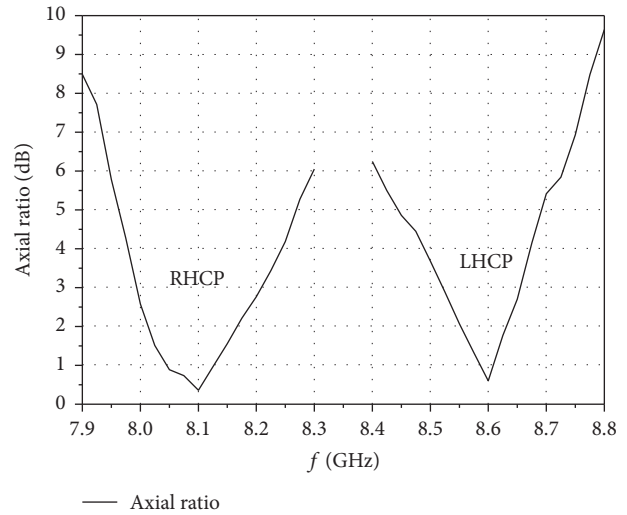


FIGURE 16: ARs of the 16-by-16 array versus frequencies.

Figure 18. It can be seen that the cross polarization level is decreased to  $-15.9$  dB and far away from the main beam. This demonstrates that better cross polarization performance can be obtained for larger arrays.

Measured gains of 25.1 dBic and 25.6 dBic are obtained at 8.2 GHz and 8.6 GHz, respectively, which are in accordance with the measured results of the 8-by-8 array and the connection networks.

## 7. Conclusion

In this paper, a single-layer, dual-port, dual-band, and dual-CP microstrip antenna array is proposed. The frequencies of 8.2 GHz and 8.6 GHz with a ratio of 1.05 have been realized by adopting a dual-band orthogonal-LP rectangular patch as the elements. Two independent sets of SR feed networks are utilized to combine the dual-band, dual-LP elements into a

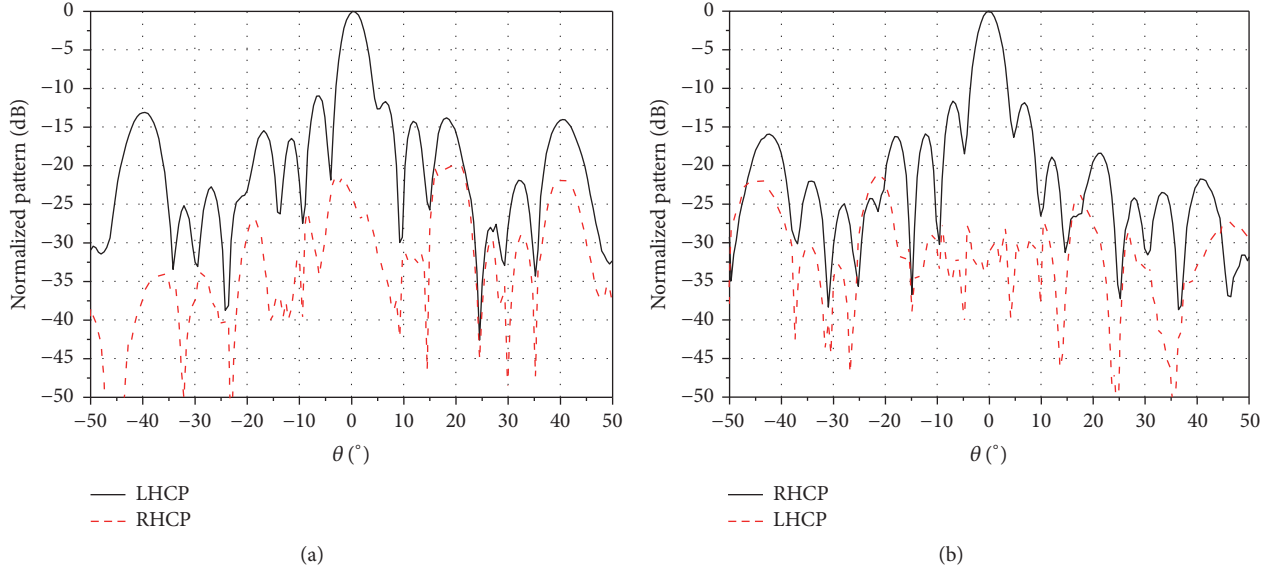


FIGURE 17: Measured normalized patterns in the  $\varphi = 0^\circ$  plane: (a) normalized patterns in the  $\varphi = 0^\circ$  plane at 8.1 GHz; (b) normalized patterns in the  $\varphi = 0^\circ$  plane at 8.6 GHz.

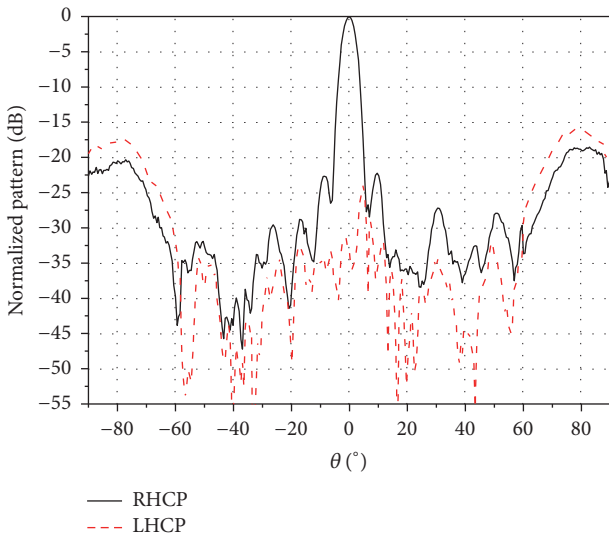


FIGURE 18: Measured normalized patterns in the  $\varphi = 45^\circ$  plane.

2-by-2 dual-band, dual-CP subarray. This subarray is taken as the unit cell and the 8-by-8 array is successfully designed on the single-layer substrate. Furthermore, with the help of the one-to-four power dividers and semirigid coaxial cables, a 16-by-16 array is also developed to achieve higher gains. Measured results of the 8-by-8 and 16-by-16 arrays show that good CP performance, impedance, and AR bandwidths have been obtained. Measured gains more than 25 dBic have been achieved for the 16-by-16 array. Isolations between two ports can be improved up to 20 dB conveniently by inserting bandpass filters into the independent feed networks.

The proposed array has advantages of the single-layer and dual-port structure and dual-band dual-polarized performance. Therefore, it would be a good candidate for

satellite communication systems, especially for dual-band applications with a very low frequency ratio.

### Conflicts of Interest

The authors declare that they have no conflicts of interest.

### Acknowledgments

The authors would like to acknowledge National Natural Science Foundation of China for funding this study under the General Program entitled “Pattern Synthesis on the Conical Beam Antennas for the Applications of Vehicle-Borne Satellite Communication and Missile-Borne Detection System” (Project Code 61771242).

### References

- [1] S. Du, Q.-X. Chu, and W. Liao, “Dual-band circularly polarized stacked square microstrip antenna with small frequency ratio,” *Journal of Electromagnetic Waves and Applications*, vol. 24, no. 11-12, pp. 1599–1608, 2010.
- [2] C.-X. Mao, S. Gao, Y. Wang, Q. Luo, and Q.-X. Chu, “A shared-aperture dual-band dual-polarized filtering-antenna-array with improved frequency response,” *Institute of Electrical and Electronics Engineers. Transactions on Antennas and Propagation*, vol. 65, no. 4, pp. 1836–1844, 2017.
- [3] S. Kumar, B. K. Kanaujia, M. K. Khandelwal, and A. K. Gautam, “Stacked dual-band circularly polarized microstrip antenna with small frequency ratio,” *Microwave and Optical Technology Letters*, vol. 56, no. 8, pp. 1933–1937, 2014.
- [4] K. Wincza and S. Gruszczynski, “Series-Fed Dual-Band Dual-Polarized Antenna Lattice Fed by Slot-Coupled Power Dividers,” *IEEE Antennas and Wireless Propagation Letters*, vol. 15, pp. 1065–1068, 2016.

- [5] M. Fakheri, M. Naser-Moghadasi, and R. A. Sadeghzadeh, "A broad band circularly polarized cross slot cavity back array antenna with sequentially rotated feed network for improving gain in X-band application," *International Journal of Microwave and Wireless Technologies*, pp. 1–6, 2016.
- [6] X. L. Bao and M. J. Ammann, "Compact annular-ring embedded circular patch antenna with cross-slot ground plane for circular polarisation," *IEEE Electronics Letters*, vol. 42, no. 4, pp. 192–193, 2006.
- [7] S. Feng, E. Nishiyama, and M. Aikawa, "Broad-band circularly polarized ring-slot array antenna for simultaneous use of the orthogonal polarizations," *IEICE Transactions on Electronics*, vol. E93-C, no. 7, pp. 1105–1110, 2010.
- [8] Q. Zhang and W. Wu, "Dual-band microstrip-fed cavity-backed slot array of circular polarization," in *Proceedings of the IEEE Antennas and Propagation Society International Symposium (APSURSI '13)*, pp. 1720–1721, July 2013.
- [9] M.-T. Tan and B.-Z. Wang, "A Dual-Band Circularly Polarized Planar Monopole Antenna for WLAN/Wi-Fi Applications," *IEEE Antennas and Wireless Propagation Letters*, vol. 15, pp. 670–673, 2016.
- [10] D. Yu, S.-X. Gong, Y.-T. Wan, and W.-F. Chen, "Omnidirectional dual-band dual circularly polarized microstrip antenna Using  $TM_{01}$  and  $TM_{02}$  modes," *IEEE Antennas and Wireless Propagation Letters*, vol. 13, pp. 1104–1107, 2014.
- [11] Z.-X. Liang, D.-C. Yang, X.-C. Wei, and E.-P. Li, "Dual-Band Dual Circularly Polarized Microstrip Antenna with Two Eccentric Rings and an Arc-Shaped Conducting Strip," *IEEE Antennas and Wireless Propagation Letters*, vol. 15, pp. 834–837, 2016.
- [12] J.-D. Zhang, W. Wu, and D.-G. Fang, "Dual-band and dual-circularly polarized shared-aperture array antennas with single-layer substrate," *Institute of Electrical and Electronics Engineers. Transactions on Antennas and Propagation*, vol. 64, no. 1, pp. 109–116, 2016.
- [13] J.-D. Zhang, L. Zhu, N.-W. Liu, and W. Wu, "Dual-band and dual-circularly polarized single-layer microstrip array based on multiresonant modes," *Institute of Electrical and Electronics Engineers. Transactions on Antennas and Propagation*, vol. 65, no. 3, pp. 1428–1433, 2017.
- [14] M. Wang, W. Wu, and D.-G. Fang, "Uniplanar single cornerfed dual-band dual-polarization patch antenna array," *Progress in Electromagnetics Research Letters*, vol. 30, pp. 41–48, 2012.
- [15] T. Teshirogi, M. Tanaka, and W. Chujo, "Wideband circularly polarised array antenna with sequential rotations and phase shift of elements," in *Proceedings of the in Proceedings of IEEE International Symposium on Antennas and Propagation*, vol. 1, pp. 117–120, Tokyo, Japan, 1985.
- [16] P. S. Hall, J. S. Dahele, and J. R. James, "Design principles of sequentially fed, wide bandwidth, circularly polarised microstrip antennas," *IEE Proceedings Part H Microwaves, Antennas and Propagation*, vol. 136, no. 5, pp. 381–389, 1989.
- [17] P. S. Hall, J. Huang, E. Rammos, and A. Roederer, "Gain of circularly polarised arrays composed of linearly polarised elements," *IEEE Electronics Letters*, vol. 25, no. 2, pp. 124–125, 1989.
- [18] M. N. Jazi and M. N. Azarmanesh, "Design and implementation of circularly polarised microstrip antenna array using a new serial feed sequentially rotated technique," *IEE Proceedings Microwaves, Antennas and Propagation*, vol. 153, no. 2, pp. 133–140, 2006.
- [19] E. Levine, G. Malamud, S. Shtrikman, and D. Treves, "A Study of Microstrip Array Antennas with the Feed Network," *IEEE Transactions on Antennas and Propagation*, vol. 37, no. 4, pp. 426–434, 1989.
- [20] P. S. Hall, "Application of sequential feeding to wide bandwidth, circularly polarised microstrip patch arrays," *IEE Proceedings Part H Microwaves, Antennas and Propagation*, vol. 136, no. 5, pp. 390–398, 1989.
- [21] T. Zhang, W. Hong, and K. Wu, "Analysis and optimum design of sequential-rotation array for gain bandwidth enhancement," *Institute of Electrical and Electronics Engineers. Transactions on Antennas and Propagation*, vol. 63, no. 1, pp. 142–150, 2015.

## Research Article

# Magnetolectric Dipole Antenna with Dual Polarization and High Isolation

Xujun Yang,<sup>1</sup> Lei Ge ,<sup>1</sup> Dengguo Zhang ,<sup>1</sup> and Chow-Yen-Desmond Sim <sup>2</sup>

<sup>1</sup>College of Electronic Science and Technology, Shenzhen University, Shenzhen, China

<sup>2</sup>Department of Electrical Engineering, Feng Chia University, Taichung, Taiwan

Correspondence should be addressed to Lei Ge; [leige@szu.edu.cn](mailto:leige@szu.edu.cn)

Received 5 December 2017; Accepted 28 February 2018; Published 11 April 2018

Academic Editor: Eva Antonino-Daviu

Copyright © 2018 Xujun Yang et al. This is an open access article distributed under the Creative Commons Attribution License, which permits unrestricted use, distribution, and reproduction in any medium, provided the original work is properly cited.

A dual-polarized aperture-coupled magnetolectric (ME) dipole antenna is presented in this paper. The feeding network is based on substrate-integrated coaxial lines (SICLs). To describe the effect of the SICL on improving the isolation, the ME dipole with another two different feeding configurations, microstrip lines and striplines, respectively, is compared. As such, the coupling between the transmission lines is tremendously reduced and the isolation between the two input ports of different polarization is enhanced. An antenna prototype is fabricated and tested, exhibiting good performances, including an isolation level of higher than 30 dB between the two input ports and gains of more than 9.5 dBi. Besides, the proposed design is capable of achieving stable directional radiation patterns with cross-polarization levels lower than  $-22$  dB and back radiation levels lower than  $-24$  dB.

## 1. Introduction

Since the 5G (fifth-generation) wireless communication technology will be commercially available in the early 2020s, the number of mobile subscribers will rise enormously and mobile wireless services will unceasingly expand. Due to limited frequency resources, antennas with higher performances are desired to enhance the traffic capacity and spectrum utilization for wireless cellular networks.

Dual-polarized antennas are widely used in radio frequency communication systems, especially in mobile cellular base stations. Compared to linearly polarized antennas, dual-polarized antennas are more attractive because they can combat the multipath fading and increase the channel capacity [1]. Up to now, in order to obtain stable electrical performances, several dual-polarized antenna designs have been reported [2–4] on the basis of a wideband complementary antenna, namely, magnetolectric (ME) dipole [5, 6]. This type of antenna comprises a vertically oriented quarter-wavelength shorted patch and a planar dipole, which behave as a magnetic dipole and an electric dipole. By exciting both the magnetic and electric dipoles with equal amplitudes and phases simultaneously, the antenna can achieve excellent performances, such as a wide impedance bandwidth, a stable gain, low back

radiation, low cross-polarization levels, and symmetric  $E$ -plane and  $H$ -plane radiation patterns across the operating frequency band. Moreover, due to the aforementioned advantages, the ME dipole antenna can also be developed in the millimeter-wave band [7].

In this paper, we demonstrate a dual-polarized aperture-coupled ME dipole antenna. Its feeding network is based on substrate-integrated coaxial lines (SICLs), which is able to reduce the coupling between the transmission lines and therefore enhance the isolation between the two input ports of different polarization. In addition, a two-way power divider is used to realize a twin feed for balanced excitation. This leads to the proposed design with symmetric radiation patterns over its entire operating frequency band. Furthermore, nearly identical impedance matching and radiation performances are obtained for the two polarization levels.

## 2. Antenna Configuration

The geometry of the proposed dual-polarized aperture-coupled ME dipole antenna is given in Figure 1. Its detailed geometry dimensions are shown in Table 1. The antenna consists of three parts, including an ME dipole, a feeding

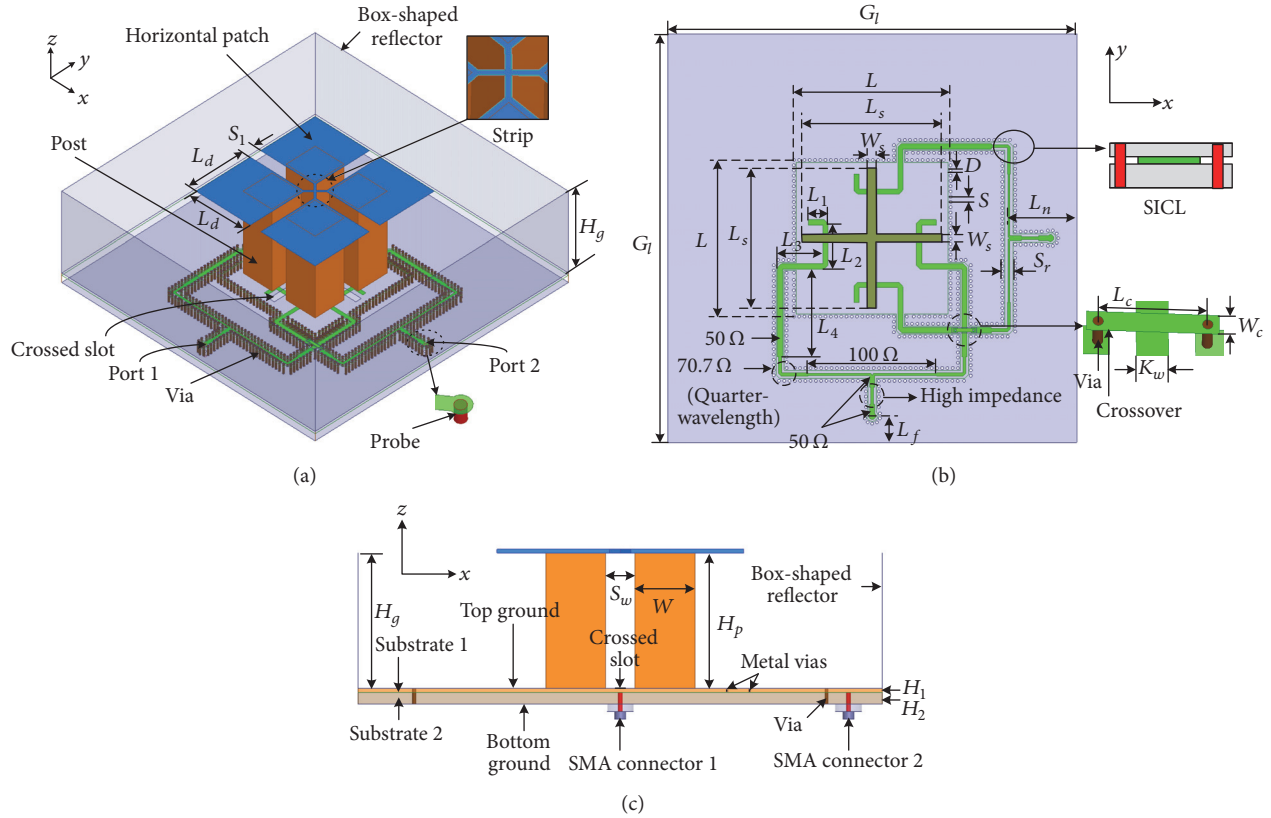


FIGURE 1: Geometry of the proposed dual-polarized aperture-coupled magnetoelectric dipole antenna. (a) 3D view. (b) Top view. (c) Side view.

network, and a box-shaped reflector. As shown in Figure 1(a), the ME dipole is composed of four parts which are located symmetrically with respect to the center of the ground plane. The four horizontal patches of the ME dipole are connected by a cross-shaped strip in the perpendicularly diagonal directions for impedance matching as analyzed in [7]. The ME dipole is aperture-coupled fed by a crossed slot. The structure of the feeding network is fabricated on two stacked substrates, namely, *Substrate 1* (Taconic RF-30, height of  $H_1 = 1$  mm,  $\epsilon_r = 3$ ) and *Substrate 2* (Taconic TLC, height of  $H_2 = 3.18$  mm,  $\epsilon_r = 3.2$ ). As illustrated in Figure 1(b), a two-way power divider is used to realize a twin feed for balanced excitation of the crossed slot. In order to locate the feeding network of the two polarization levels, a crossover is built in *Substrate 1*. As such, the ME dipole can be excited by the crossed slot. In this configuration, *Substrate 1* is reallocated on the top of *Substrate 2*, as shown in Figure 1(c). Lastly, a box-shaped reflector is employed to achieve stable radiation patterns and reduce the back lobe.

In this design, the SICL is realized by loading shorting vias with a periodic spacing along a stripline that is used to form the feeding network, and a backed cavity is also used (for the crossed slot) to suppress the back radiation of the ME dipole.

Here, *Substrate 2* (with a higher profile) is located below *Substrate 1* (with a lower profile), and they are firmly stacked together by applying several plastic screws. By doing so, the

current distribution on the top ground of the two stacked substrates can be concentrated, which in this case will strengthen the excitation field around the cross slot loaded on the top ground [8].

### 3. Simulated and Measured Results

To verify the proposed design, a prototype was fabricated and tested. Simulated results were achieved by using the commercial EM software Ansys HFSS, including reflection coefficients ( $S_{11}$  and  $S_{22}$ ), isolation ( $|S_{12}|$ ), antenna gains, and radiation patterns. Measured results were obtained by using Agilent N5225A network analyzer and a Satimo Starlab near-field measurement system.

Figures 2(a) and 2(b) present the simulated and measured reflection coefficients of the proposed antenna at Port 1 and Port 2, respectively. Here, it can be seen that two resonances are excited, and the corresponding simulated impedance bandwidths ( $VSWR \leq 1.5$ ) via both ports ( $S_{11}$  and  $S_{22}$ ) are identical to each other at 23.4% (2.11–2.67 GHz), because of the symmetric structure of the proposed antenna. As for the measured reflection coefficients of the proposed antenna, Figures 2(a) and 2(b) show that the two resonances are slightly shifted to the higher frequency band. Notably, the differences between the measured and simulated reflection coefficients of the proposed antenna via both ports can be due to the

TABLE 1: Dimensions of the proposed antenna.

Parameters	$G_I$	$L$	$L_S$	$L_d$	$W_S$	$H_p$	$W$	$H_g$	$S_W$	$S_I$	$D$	$S$	$S_r$	$L_n$	$L_C$	$L_f$	$K_W$	$W_C$	$L_1$	$L_2$	$L_3$	$L_4$
Values/mm	140	52	48	30	1.5	36	16	36	7.8	5.8	1	1.8	4.4	23.3	6.1	9.1	1.8	1.2	6.8	15	15.5	30.2

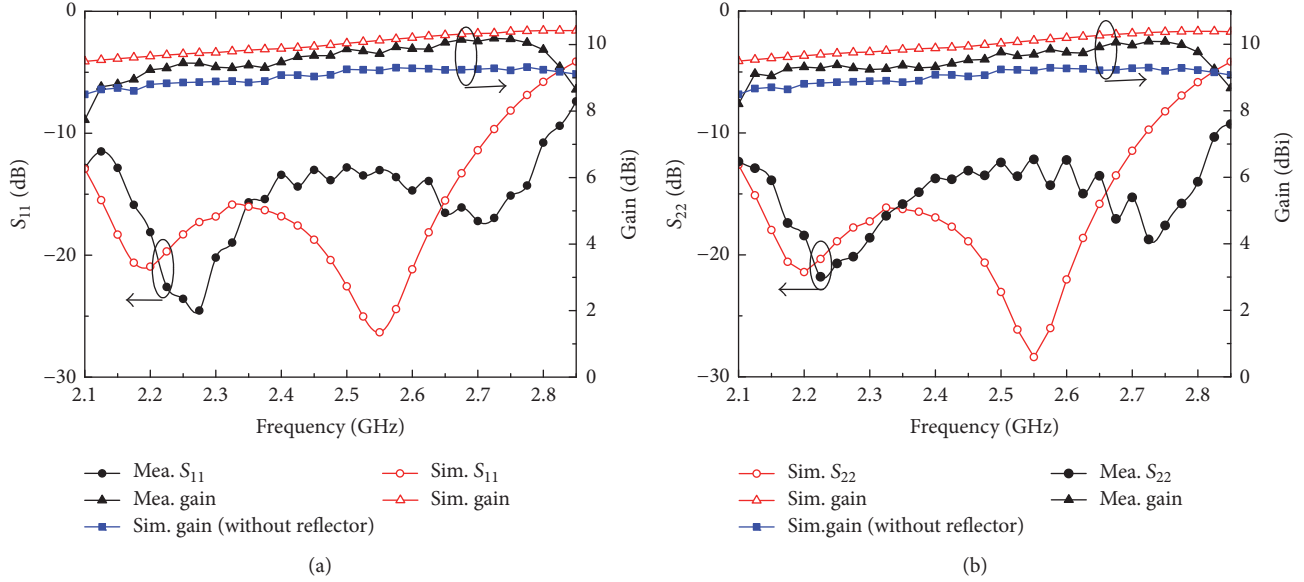


FIGURE 2: Simulated and measured reflection coefficients and broadside gains of the proposed antenna: (a) Port 1; (b) Port 2.

inevitable variations (because of fabrication inaccuracy) that exist between the exact dimensions of the fabricated prototype and the simulated one. Other effects such as imperfect SMA connector assembly and unavoidable small air gap between the two substrate layers may have also contributed to the differences.

The simulated and measured broadside gains of Ports 1 and 2 are also plotted in Figure 2. Within the operating frequency band, the measured gains are approximately 9.4 dBi with a variation of 0.6 dBi, which agrees well with the simulated result of 10 dBi with a variation of 0.5 dBi. Meanwhile, to evaluate how well the box-shaped reflector can increase the gains of both ports, the gain curves without reflector are presented for comparison. As observed from Figure 2, approximately 1.2 dBi of the increments is obtained at two ports. Figure 3 depicts the simulated and measured isolation between Ports 1 and 2. Over the operating frequency band, the simulated and measured results are very consistent with an isolation level of higher than 30 dB. Figure 3 also illustrates the measured antenna efficiencies of the proposed antenna. In the whole operating frequency band, the measured antenna efficiency is always larger than 83%.

The  $E$ -plane ( $xoz$ -plane) and  $H$ -plane ( $yo$  $z$ -plane) radiation patterns of Port 1 at frequencies of 2.2, 2.4, and 2.6 GHz were illustrated in Figure 4. The radiation patterns of Port 2 are similar to that of Port 1 and are not given here for brevity. It can be observed that a good agreement between the measurement and the simulation is obtained. Across the operating frequency band, the proposed antenna is capable of realizing stable directional radiation patterns with cross-polarization levels lower than  $-22$  dB and back radiation levels lower than  $-24$  dB for both ports. The slight difference between the measured and simulated radiation patterns is mainly caused by fabrication inaccuracy and manufacturing soldering tolerances.

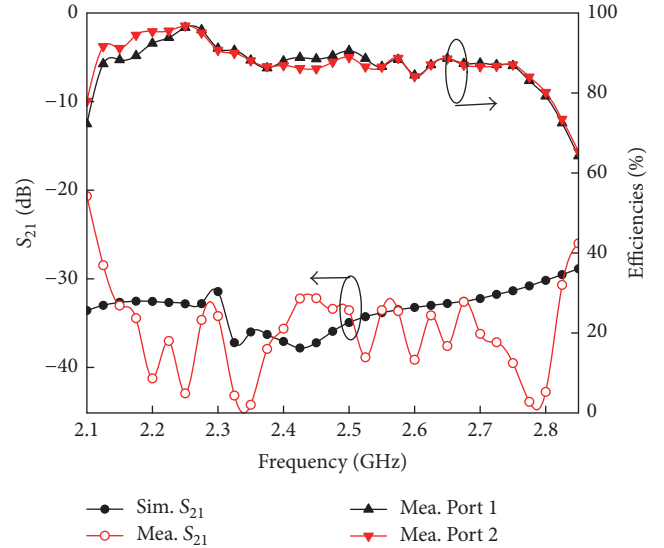


FIGURE 3: Simulated and measured  $S_{21}$  and efficiencies of the proposed antenna.

## 4. Comparison and Discussion

**4.1. Feeding Configurations.** For a dual-polarized antenna, the isolation between the two polarization levels is one of the most significant characteristics. To show how well the SICL feeding network can improve the isolation of the proposed ME dipole antenna, two different (typically used) feeding configurations are also investigated via simulation. Figures 5 and 6 show the impedance matching and isolation of the proposed ME dipole antenna when applying the microstrip lines and striplines as transmission lines of the feeding network, respectively.

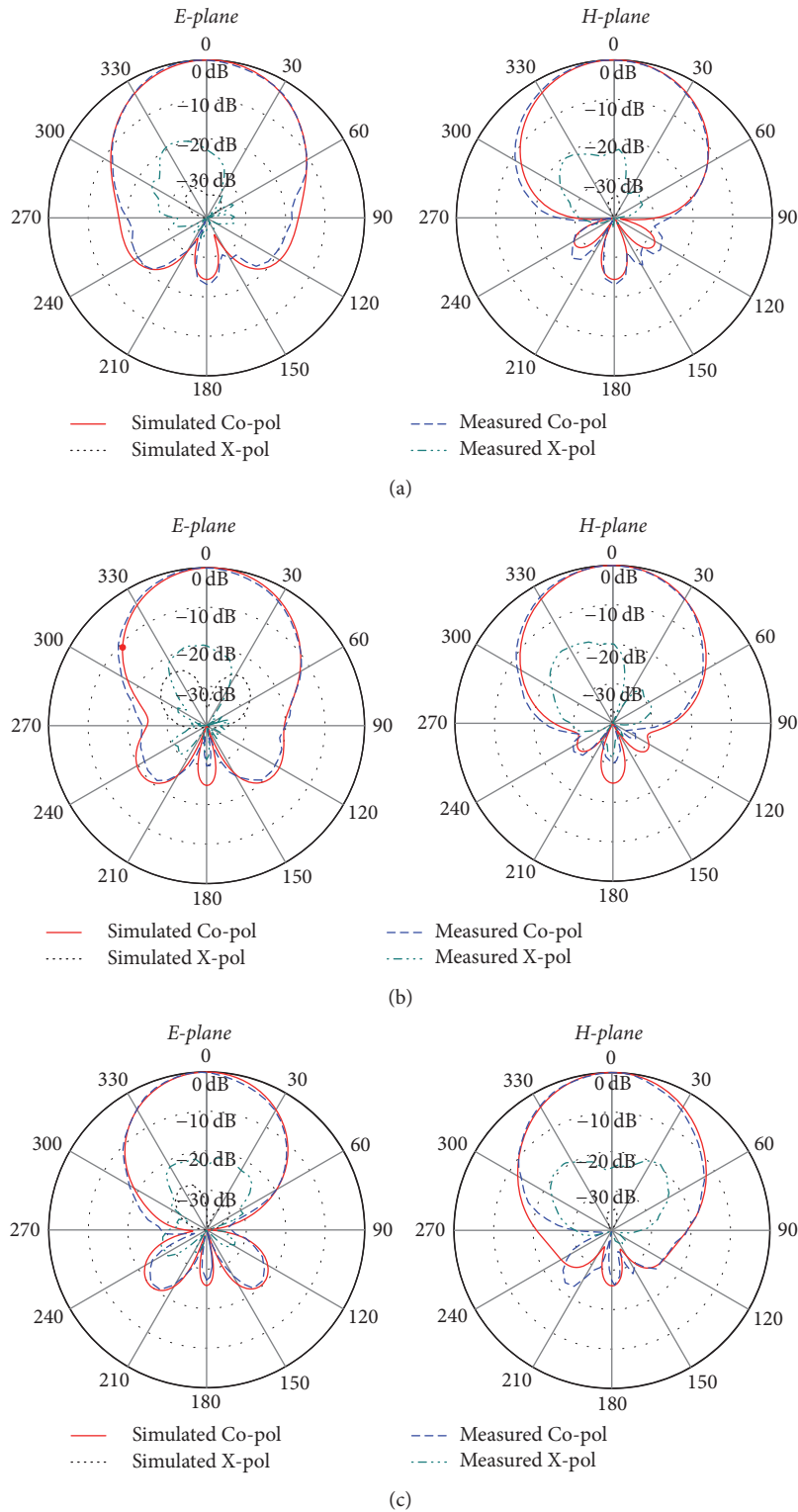


FIGURE 4: Simulated and measured radiation patterns of  $E$ -plane and  $H$ -plane at Port 1. (a) 2.2 GHz; (b) 2.4 GHz; (c) 2.6 GHz.

As shown in Figure 5, the two resonances are separated farther away from each other, leading to two operating modes with narrow 10-dB impedance bandwidths at approximately 2.1 and 2.7 GHz. By further observing  $S_{21}$  across the operating

frequency, isolation level of up to 23 dB is observed. As shown in Figure 6, much poorer impedance matching is observed across the operating frequency when the SICLs are replaced by the striplines. As for its corresponding  $S_{21}$ , undesirable

TABLE 2: Comparison between proposed and reported dual-polarized ME dipole antennas.

Ref.	Antenna size ( $\lambda_0^3$ )	Impedance bandwidth %	Average gain (dBi)	Isolation (dB)
[2]	1.28 * 1.28 * 0.23	65.9 (SWR < 2)	9.5	36
[3]	0.82 * 0.82 * 0.15	25.2 and 32.2 (SWR < 2)	8.2	29
[4]	1.3 * 1.3 * 0.24	68 (SWR < 2)	8.1	36
This work	1.12 * 1.12 * 0.32	23.4 (SWR < 1.5)	9.5	30

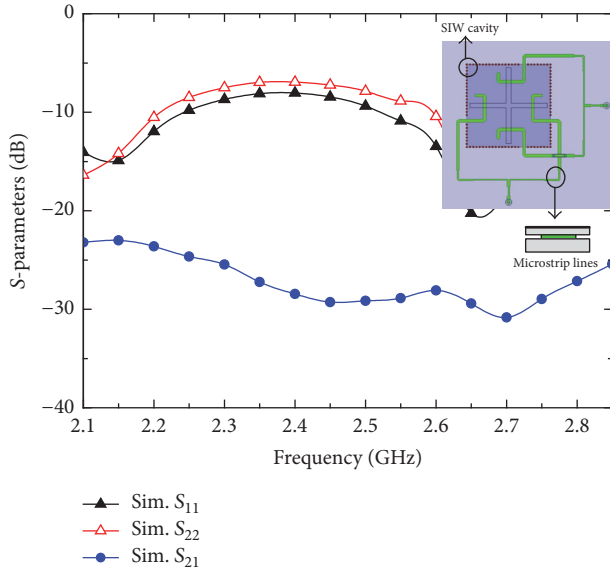


FIGURE 5: Proposed ME dipole antenna fed by microstrip lines.

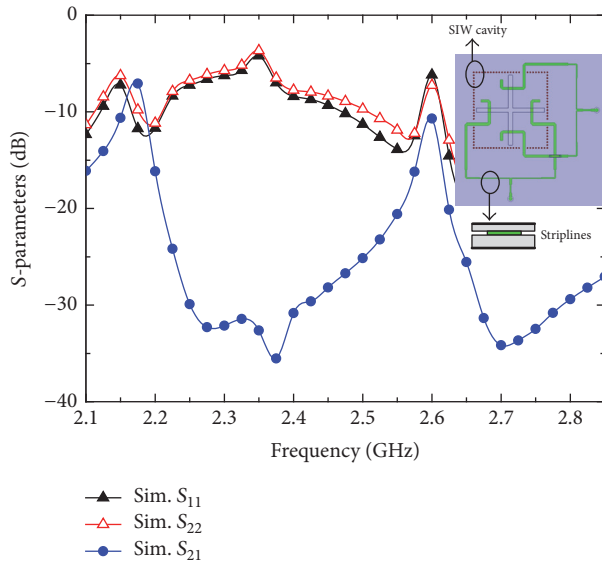


FIGURE 6: Proposed ME dipole antenna fed by striplines.

isolation of approximately 7 dB and 11 dB is realized at 2.18 GHz and 2.59 GHz, respectively. Here, it is worth noting that because of the change in characteristic impedance of the transmission lines, even though the impedances of the above two different feeding configurations are not well matched, the

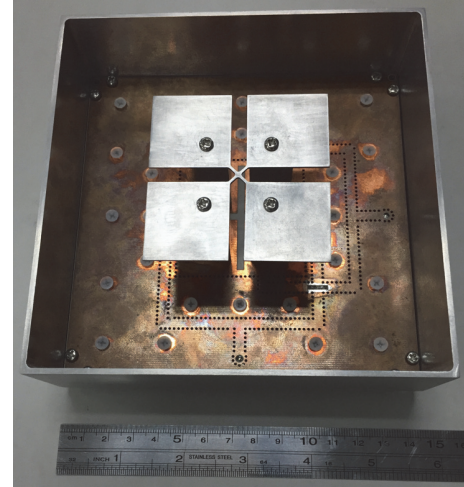


FIGURE 7: Prototype of the fabricated antenna.

isolation levels can still be used as a reference, because the isolation levels of the above two investigated cases will be even lower when the proposed antenna is impedance matched. Therefore, if the above two investigated cases have been modified to attain good impedance matching, the isolation of the microstrip lines case will not be better than 23 dB, and the isolation level of the striplines case will be even worse than 9 dB (at 2.16 GHz). For comparison, the isolation level is higher than 30 dB over the entire operating band when SICLs are applied to the proposed antenna. This is because the electromagnetic field is well sealed in the SICLs; therefore, the coupling between adjacent transmission lines is weak. Lastly, the photograph of the fabricated prototype is presented in Figure 7.

**4.2. Performances.** Table 2 compares the proposed ME dipole antenna's performances with other published dual-polarized ME dipole antennas. In terms of the bandwidth and isolation, although [2, 4] can achieve more than 60% impedance bandwidths and larger than 36 dB isolation, their horizontal geometry dimensions are slightly wider. Especially in [4], a higher isolation is realized by differential feeding, and thus the complexity will be raised inevitably. The design in [3] can reduce the size of the antenna with dielectric loading but suffer from asymmetrical impedance bandwidths and lower gains between the two ports. By comparison, this work still has significant value with a stable gain of 9.5 dBi and high isolation and wide bandwidths via both ports.

## 5. Conclusion

A dual-polarized aperture-coupled ME dipole antenna with feeding network that is based on the SICL has been successfully investigated. To validate the performances of the design, an elevated prototype was fabricated and measured. The measured results show that the proposed ME dipole antenna has wide bandwidths, stable gains, well-controlled radiation patterns, and high isolation between different polarization levels.

## Conflicts of Interest

The authors declare that they have no conflicts of interest.

## References

- [1] S. Gao, A. Sambell, and S. S. Zhong, "Polarization-agile antennas," *IEEE Antennas and Propagation Magazine*, vol. 48, no. 3, pp. 28–37, 2006.
- [2] B. Q. Wu and K. M. Luk, "A broadband dual-polarized magneto-electric dipole antenna with simple feeds," *IEEE Antennas and Wireless Propagation Letters*, vol. 8, pp. 60–63, 2009.
- [3] L. Siu, H. Wong, and K. M. Luk, "A dual-polarized magneto-electric dipole with dielectric loading," *IEEE Transactions on Antennas and Propagation*, vol. 57, no. 3, pp. 616–623, 2009.
- [4] Q. Xue, S. W. Liao, and J. H. Xu, "A differentially-driven dual-polarized magneto-electric dipole antenna," *IEEE Transactions on Antennas and Propagation*, vol. 61, no. 1, pp. 425–430, 2013.
- [5] K. M. Luk and H. Wong, *A complementary wideband antenna*, U.S. Patent No. 11/373,518, Mar. 10, 2006.
- [6] K. M. Luk and H. Wong, "A new wideband unidirectional antenna element," *Int. J. Microw. Opt. Technol*, vol. 1, no. 1, pp. 35–44, 2006.
- [7] Y. Li and K. M. Luk, "60-GHz Dual-Polarized Two-Dimensional Switch-Beam Wideband Antenna Array of Aperture-Coupled Magneto-Electric Dipoles," *IEEE Transactions on Antennas and Propagation*, vol. 64, no. 2, pp. 554–563, 2016.
- [8] P. Brachat and J. M. Baracco, "Dual-Polarization Slot-Coupled Printed Antennas Fed by Stripline," *IEEE Transactions on Antennas and Propagation*, vol. 43, no. 7, pp. 738–742, 1995.

## Research Article

# A Wide Stopband Balun Bandpass Filter with Its Application to Balanced Quasi-Yagi Antenna

Gang Zhang , Zhenyao Qian, Yushou Chen , and Yang Zhao 

*School of Electrical and Automation Engineering, Nanjing Normal University, Nanjing, China*

Correspondence should be addressed to Yushou Chen; [yushou.chen\\_nnu@126.com](mailto:yushou.chen_nnu@126.com)

Received 11 December 2017; Accepted 6 March 2018; Published 10 April 2018

Academic Editor: Lei Ge

Copyright © 2018 Gang Zhang et al. This is an open access article distributed under the Creative Commons Attribution License, which permits unrestricted use, distribution, and reproduction in any medium, provided the original work is properly cited.

A new microstrip balun bandpass filter (BPF) with wide stopband is presented. It is realized by utilizing the out-of-phase feature of standing-wave distribution on a half-wavelength ( $\lambda/2$ ) open-ended microstrip line and the resonant characteristics of the triple-mode resonators. For demonstration, a prototype balun BPF operating at central frequency ( $f_0$ ) of 2.34 GHz with fractional bandwidth (FBW) of about 16.7% is designed. The presented balun BPF not only exhibits nice balanced response with 0.47 dB magnitude imbalance and  $4.3^\circ$  phase difference but also achieves 30-dB harmonic suppression up to 6.40 GHz ( $2.7f_0$ ). Afterward, this presented design is embedded into a balanced quasi-Yagi antenna to obtain high-selective radiation and wide stopband rejection. Experimental results of the implemented antenna indicate less than  $-10$  dB reflection coefficient, 4.49–5.38 dBi gain, and 12.71–19.62 dB front-to-back ratio within the operating bandwidth.

## 1. Introduction

A balun bandpass filter (BPF) is an important multifunctional integrated component, which provides both balanced conversion of a balun and bandpass frequency selectivity of a BPF simultaneously, since it can reduce the cost and size of the functional block for modern compact wireless communication systems. Therefore, the studies on balun BPFs have been receiving more attention [1–7].

In [1], a multilayer balun BPF with small size and high performance was proposed. But, the involved design structure and procedure of this circuit are complicated. Based on Marchand balun, a dual-band coupled-line balun filter is proposed in [3]. However, two terminals of the coupled lines utilized by the balun have to be terminated to ground by via holes to obtain the desired characteristics. Another type of balun filter is implemented by combining of microstrip lines, slotlines, and coplanar striplines [4]. Although good performance can be achieved, the balun filter still requires via holes connected to the ground and a large size, which cannot accommodate the growth of modern wireless communication system. In addition, a single dual-mode square-loop resonator or patch resonator was introduced to realize a novel dual-mode balun BPF in [5, 6], respectively. While

the method itself is simple and ingenious, it is restrained in the loop-type dual-mode resonator or patch resonator, thus limiting its application in other types of dual-mode resonator. Moreover, open-type resonator, which is widely used in microwave circuit design, is utilized to realize balun BPFs with good balanced performance and high frequency selectivity [2, 7]. But its limited bandwidth [7] and stopband suppression [2] of the balun BPFs are not satisfactory and need further improvement, while considering its practical application for feeding antenna. Apart from these above listed designs, a balun BPF [8] based on substrate integrated waveguide cavity concept has also been reported. This design is suitable for high frequency application and exhibits very narrow bandwidth.

This paper is aimed to explore a wide stopband balun BPF design with moderate bandwidth and investigate the feasibility of its practical application into antenna feeding network. At first, by selecting proper coupling topologies between the  $\lambda/2$  open-circuited transmission line and triple-mode open-stub loaded resonators, a new planar type triple-mode balun BPF with moderate band, wide stopband, and high selectivity is presented in this paper. Our research demonstrates that the proposed balun BPF possesses nice balanced responses across the operation passband with about

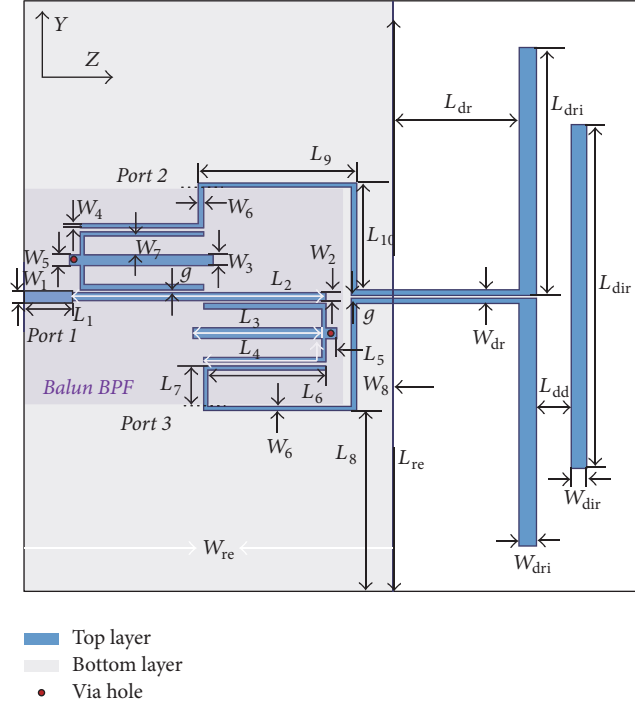


FIGURE 1: Layout of quasi-yagi antenna fed by the proposed balun BPF.

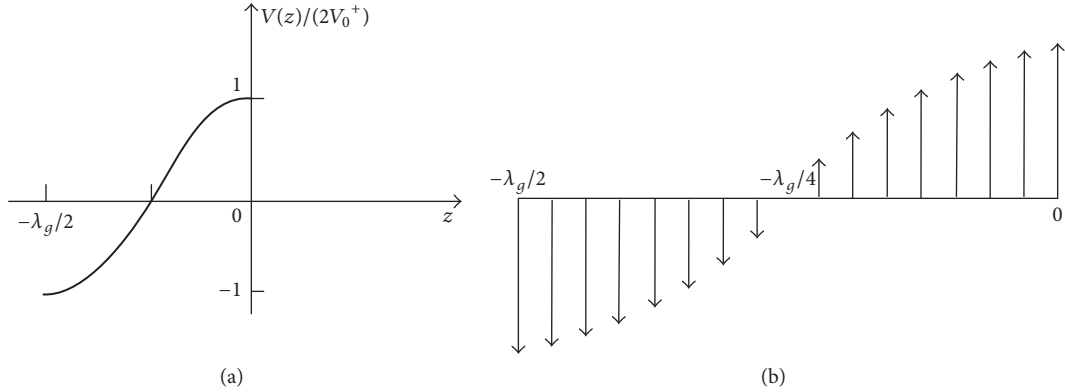


FIGURE 2: (a) Variation on normalized voltage along a  $\lambda/2$  open-circuited line and (b) its relevant electric field distribution.

16.7% 3-dB fractional bandwidth and  $2.7f_0$  harmonic suppression with better than 30 dB rejection level. Further, the proposed design is embedded into quasi-Yagi antenna as a feeder, for sake of getting high-selective radiation and wide stopband rejection. Both simulated and measured results are displayed to verify these properties predicted in theory.

## 2. Proposed Broadband Balun Bandpass Filter

The configuration of the proposed balun BPF is depicted in the purple shadow section of Figure 1 which mainly consists of a pair of triple-mode resonators and an open-ended transmission line. Based on the transmission line theory, it can be derived that a standing wave pattern will be yielded when the length of the transmission line is about  $\lambda/2$ . The corresponding voltage distribution and electric field distribution are described in Figure 2 [9] in which two

distinct regions can be observed with out-of-phase and identical magnitude. These inherent properties can be effectively utilized to meet both the magnitude and the phase requirements of a balun.

Figure 3(a) describes the employed triple-mode resonator in this design, which is symmetrical with respect to its centre plane. Thus, the odd/even-mode method can be applied to analyse its resonance property [10]. The corresponding equivalent circuits are given in Figures 3(b)-3(c). Correspondingly, design equations for the first three resonant frequencies (queued as  $f_1$ ,  $f_2$ , and  $f_3$ ) and one inherent transmission zero ( $f_{TZ1}$ ) can be derived from input admittances of the odd- and even-mode circuits ( $Y_{ino}$  and  $Y_{ine}$ ), which are given as

$$Y_{ino} = -jY_4 \cdot \cot \theta_4$$

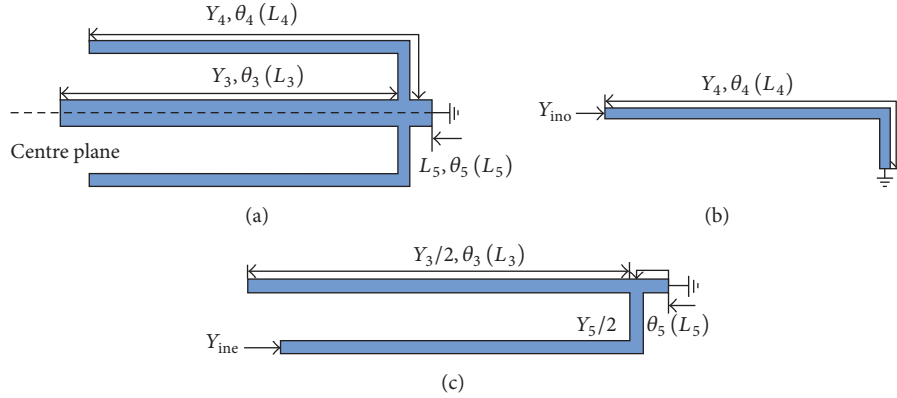


FIGURE 3: Triple-mode resonator and its corresponding equivalent circuits, (a) configuration of the proposed triple-mode resonator, (b) odd-mode equivalent circuit, and (c) even-mode equivalent circuit.

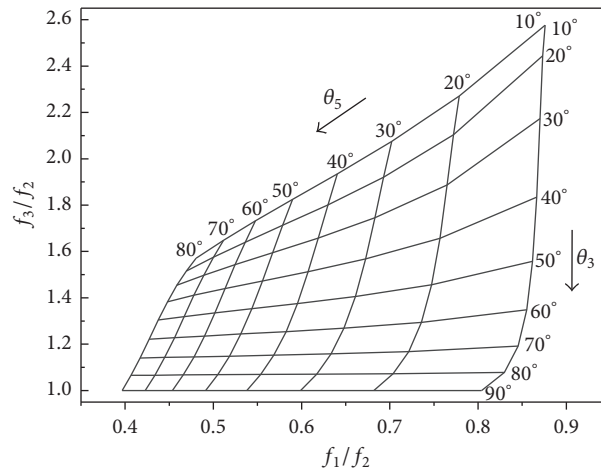


FIGURE 4: Design graph for the triple-mode resonator.

$$Y_{\text{ino}} = Y_4 \cdot \frac{K_e + jY_4 \cdot \tan \theta_4}{Y_4 + jK_e \cdot \tan \theta_4}, \quad (1)$$

where  $K_e = (-jY_5 \cdot \cot \theta_5)/2 + (jY_3 \cdot \tan \theta_3)/2$ .

By setting  $Y_{\text{ino}} = 0$ , the odd-mode resonant frequency can be solved as  $\theta_4 = 90^\circ$  (for  $f_2$ ). Meanwhile, when  $Y_{\text{ino}} = 0$ , the even-mode resonant conditions can be simplified as  $Y_5 \cdot \cot \theta_5 - Y_3 \cdot \tan \theta_3 = 2Y_4 \tan \theta_4$  (for  $f_1, f_3$ ). In addition, by solving  $Y_{\text{ino}} = Y_{\text{ine}}$ , one inherent TZ frequency  $f_{\text{TZ1}}$  can be calculated as  $\theta_3 = 90^\circ$ .

Based on the above analysis, a triple-mode resonator can be realized and designed. Specifically, we can figure out from (1) that  $f_2$  is only determined by  $\theta_4$ , while  $f_1/f_2$  and  $f_3/f_2$  are mainly influenced by  $\theta_5$  and  $\theta_3$ , respectively. Figure 4 shows the design graph of the tri-mode resonators with a admittance ratio  $K = Y_5/Y_3 = 1.6$ . It can be seen that the smaller  $\theta_5$  is, the larger  $f_3/f_2$  will be, while the smaller  $\theta_3$  is, the larger  $f_1/f_2$  will be. The admittance ratio  $K$  is added in the design to increase the degree of freedom in determining resonant frequencies  $f_1$  and  $f_3$  allocation. Thus, one can decide  $f_1$  and  $f_3$  by properly adjusting  $\theta_5, \theta_3$ , and  $K$ , while remaining  $f_2$  unchanged. On the other hand,  $Y_{\text{ino}} = Y_{\text{ine}}$  indicates that

the inherent  $f_{\text{TZ1}}$  could be controlled by  $\theta_3$ . Therefore, these demonstrated properties are very useful for one to realize a balun BPF with filtering performance of desired bandwidth and high selectivity.

Based on the aforementioned illustration, a balun BPF is constructed as depicted in Figure 1. As it presents, two identical stubs-loaded resonators are placed symmetrically in the two above regions in Figure 2 featured with equal magnitude and contrary phase. Due to this arrangement, the couplings between the transmission line and two resonators can be characterized with the same amplitude and out of phase. Thus, a pair of balanced signals between ports 2 and 3 is finally achieved. Additionally, the input/output coupled structures are introduced by properly orienting the resonators to realize good filtering behaviour. Since the desired absolute bandwidth of triple-mode Balun BPF is approximate to  $f_3 - f_1$  and the centre frequency can be deemed as  $f_2$ , initial dimensions of the resonators and open-ended transmission line can be obtained. Besides, dimensions of the input/output (I/O) coupling line structure can be determined by fine tuning the parameters, that is, width ( $W_2$ ) and gap ( $g$ ) of the I/O coupled-lines so as to satisfy the given bandwidth.

TABLE 1: Dimensions of the proposed Balun BPF.

Parameter	$W_1$	$W_2$	$W_3$	$W_4$	$W_5$	$W_6$	$W_7$	$W_8$	$L_1$	$L_2$	$L_3$	$L_4$	$L_5$	$L_6$	$L_7$	$L_8$	$L_9$	$L_{10}$	$g$	$L_{re}$	$L_{dr}$	$L_{dri}$	$L_{dd}$	$L_{dir}$	$W_{re}$	$W_{dr}$	$W_{dri}$	$W_{dir}$
Value (mm)	1.17	0.9	1.4	0.6	1.4	0.6	2.5	5.0	6.0	33.5	17	18.2	1.4	15.7	3.6	30	20.9	14.2	0.2	77.2	16.4	32.5	4.6	45	49	1.8	2.4	2.0

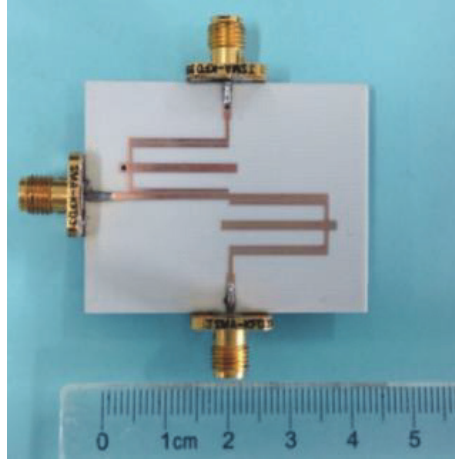


FIGURE 5: Photograph of the fabricated balun BPF.

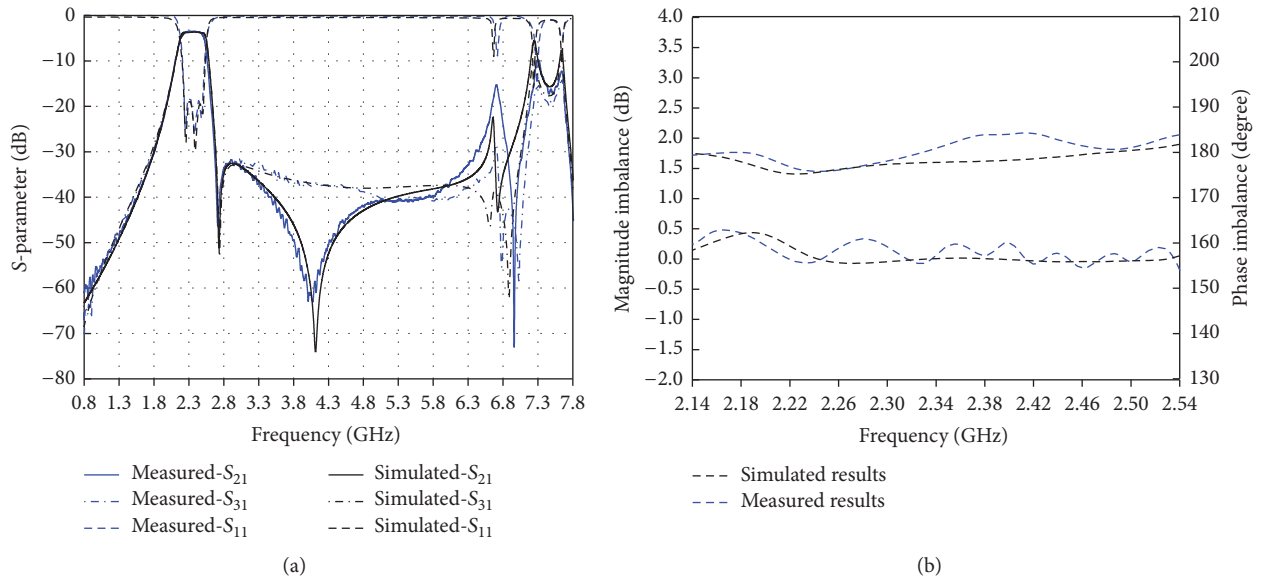


FIGURE 6: Simulated and measured results of the proposed balun BPF, (a) S-parameters of the balun BPF, and (b) magnitude imbalance and phase imbalance of the presented balun BPF.

For validation, a prototype centered at 2.34 GHz is designed in this work. It is implemented on the substrate of Rogers RO4003C with a dielectric constant  $\epsilon_r = 3.55$ , a loss tangent  $\tan \delta = 0.0027$ , and a thickness  $h = 0.508$  mm. The optimal physical dimensions of the design are denoted as Table 1 with the diameter ( $D = 0.4$  mm) of the metallic via hole. The balun BPF was simulated by commercial software ANSYS EM 16.1, and the corresponding fabricated circuit shown in the inset plot of Figure 5 was measured with the Agilent N5244A four-port vector network analyzer. Simulated and measured results depicted in Figure 6 show a good agreement with each other. Measured results indicate that the proposed balun BPF operates at the central frequency of

2.34 GHz with a 3-dB fractional bandwidth of 17.6%. Within the passband, the balun filter exhibits with a minimum insertion loss of 0.7 dB and maximum return loss of 17.8 dB. Outside the passband, one common TZ located at 2.71 GHz is observed for both  $S_{21}$  and  $S_{31}$ . Besides, an additional TZ located at 4.01 GHz for  $S_{21}$  can be seen, which might be caused by the resonance of the input transmission line. These TZs ensure high out-of-band selectivity of the Balun BPF. What is more, the balun BPF also exhibits 30-dB harmonic suppression up to 6.40 GHz ( $2.7f_0$ ). For the performance between two output ports, the maximum in-band magnitude imbalance is about 0.47 dB and the phase difference is within  $4.3^\circ$ . The small discrepancies between measured results and

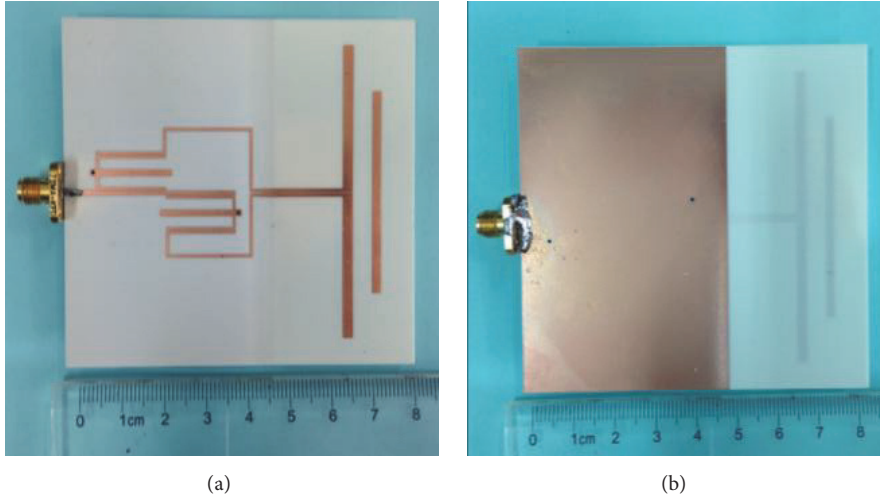


FIGURE 7: Photograph of the fabricated antenna, (a) top view, and (b) bottom view.

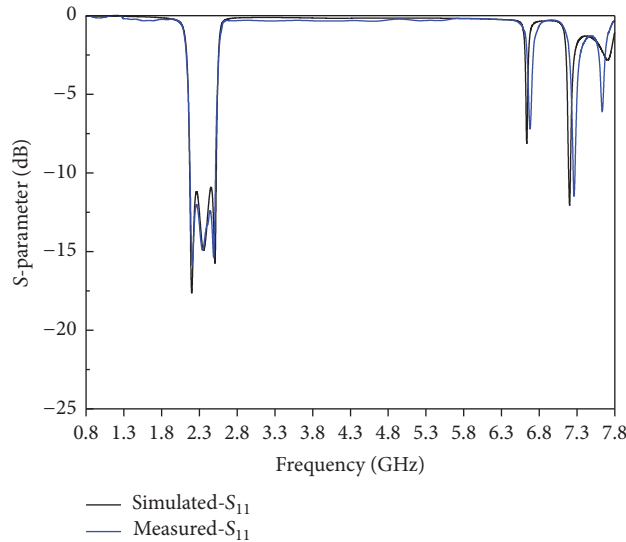


FIGURE 8: Simulated and measured reflection coefficient of the quasi-Yagi antenna.

simulated results are mainly attributed to the fabrication error and minor SMA connection difference between port 2 and port 3. Table 2 tabulates the performances in comparison with the proposed BPF and other reported ones. It can be seen that our work exhibits wider operation bandwidth, low phase imbalance, and good harmonic suppression against others.

### 3. Balun BPF Feeding Broadband Quasi-Yagi Antenna

Aiming to achieve good radiation performance, wide stop-band rejection, and high selective radiation, the proposed balun BPF is further employed to feed a moderate-band balanced quasi-Yagi antenna as shown in Figure 1. The quasi-Yagi is designed with two rectangle-shaped radiation arms as the dipole driver and one rectangle-shaped patch as the director [11]. One sectional folded microstrip line is utilized herein for the integration of the balun and antenna and the input impedance matching. Besides, to achieve desired bandwidth,

the spacing  $L_{dd}$  between the parasitic director and dipole driver is chosen less than a quarter-wavelength. As for the spacing  $L_{dr}$  between the dipole driver and truncated ground plane, it should be chosen as about a quarter-wavelength so as to create an in-phase reflected wave along the end-fire direction. The detailed geometric parameters are listed in Table 1. The designed antenna fed by balun BPF is then fabricated and tested. Figure 7 shows its top- and bottom-view photographs. The reflection coefficient is measured by the N5244A Network Analyzer, while the radiation patterns, gains, and efficiency of this antenna were measured by employing the Microwave Vision Group's Starlab near-field antenna measurement system. Measured reflection coefficient plotted in Figure 8 indicates that the operating band of the antenna ranges from 2.17 GHz to 2.52 GHz (FBW of about 15%) with smaller than  $-10$  dB reflection coefficient. It can be found that the implemented quasi-Yagi antenna possesses a well-defined return-loss curve without undesired radiation up to  $2.75 f_0$  outside the passband. Figures 9(a)–9(f)

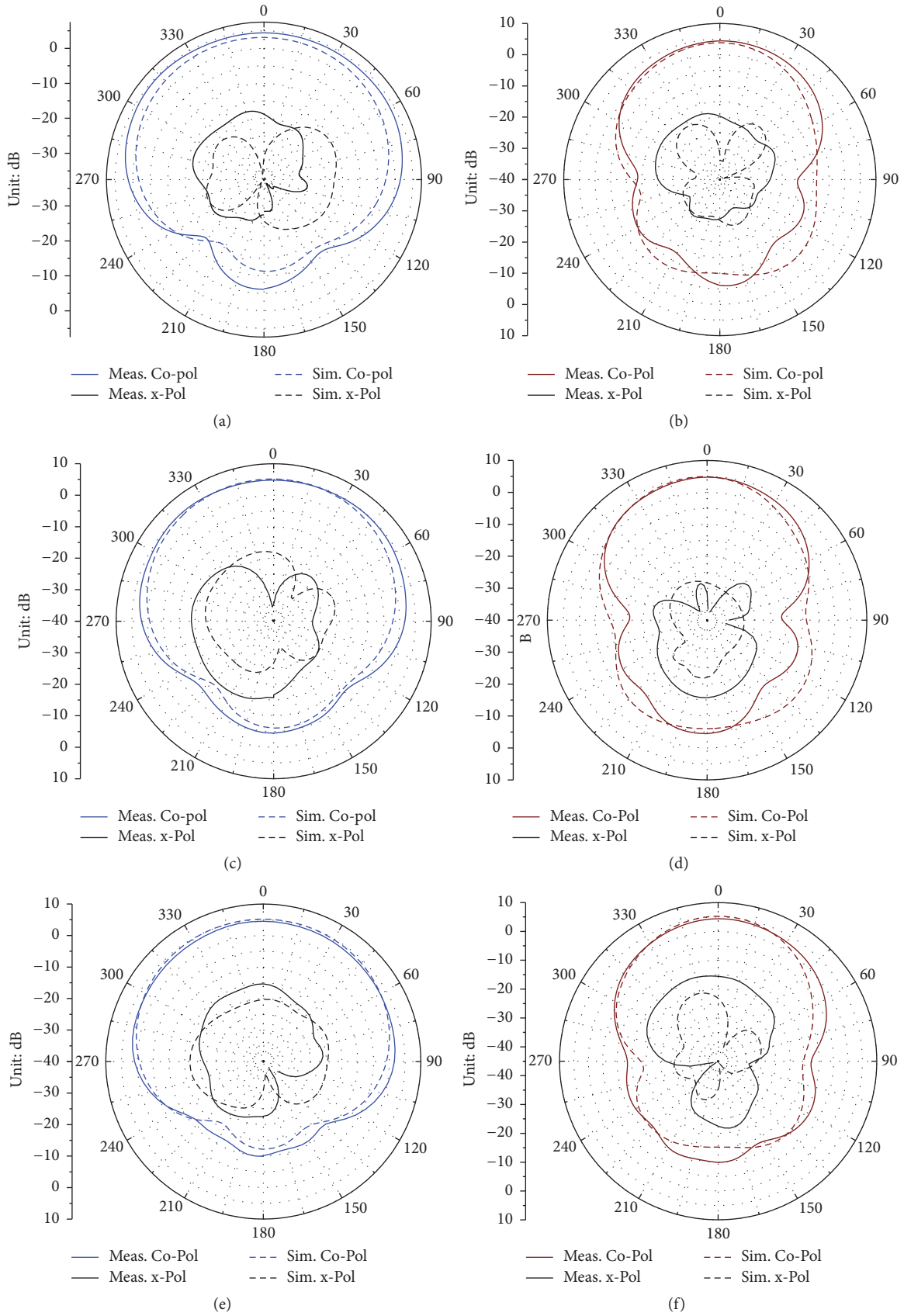


FIGURE 9: Simulated and measured radiation patterns at two frequencies, (a)  $xz$ -plane at 2.34 GHz, (b)  $yz$ -plane at 2.34 GHz, (c)  $xz$ -plane at 2.2 GHz, (d)  $yz$ -plane at 2.2 GHz, (e)  $xz$ -plane at 2.5 GHz, and (f)  $yz$ -plane at 2.5 GHz.

TABLE 2: Comparisons among proposed and other reported Balun BPFs.

Ref.	$f_0$ (GHz)	3-dB FBW	Amplitude imbalance	Phase imbalance	30-dB harmonic suppression
[5]	2.55	3.5%	<1.10 dB	<5°	$1.5f_0$
[6]	3.48	5.8%	<0.50 dB	<5°	None
[7]	2.00	11.0%	<0.35 dB	<5°	None
This work	2.34	16.7%	<0.47 dB	<4.3°	$2.7f_0$

Ref.: references,  $f_0$ : centre frequency, and FBW: fractional bandwidth.

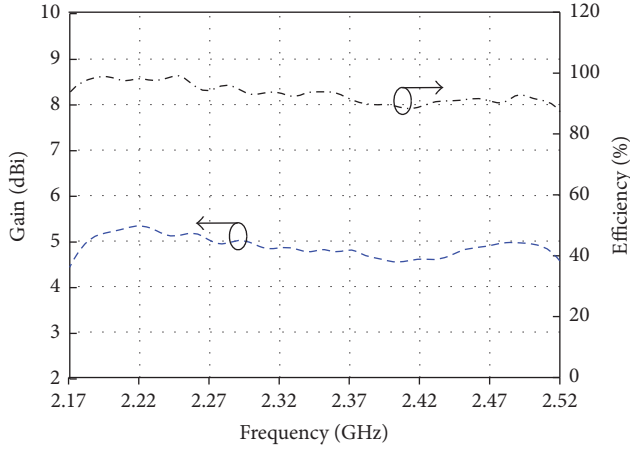


FIGURE 10: Measured gain and efficiency of the integrated quasi-Yagi antenna.

indicate the measured radiation patterns on  $YZ$ -plane ( $E$ -plane) and  $XZ$ -plane ( $H$ -plane). The results depicted in Figure 9 confirm the directive properties of the antenna. The front-to-back ratio of the antenna varies from 10.6 dB at 2.35 GHz to 14.4 dB at 2.5 GHz. In addition, Figure 10 illustrates the measured gain and efficiency. The realized gain is approximately 4.49–5.38 dBi and the efficiency is more than 88.6% across the band from 2.17 GHz to 2.52 GHz.

#### 4. Conclusion

In this paper, a new design of wide stopband balun BPF has been proposed. Owing to the standing-wave distribution on a half-wavelength open-ended microstrip line, signals with equal magnitude and contrary phase are simultaneously obtained at two output ports. Furthermore, by using the even-/odd-mode analysis method, the filtering responses have been figured out with the bisected equivalent circuit of the employed resonator. To further explore it in the practical antenna application, a quasi-Yagi antenna fed by the proposed balun BPF is designed for high selective radiation and wide stopband rejection. Both simulated and measured results verify the feasibility of the presented designs.

#### Conflicts of Interest

The authors declare that there are no conflicts of interest regarding the publication of this paper.

#### References

- [1] X. F. Liu, X. Y. Zhang, and K.-X. Wang, "Compact LTCC balun filter using folded half-wavelength resonators," in *Proceedings of the IEEE International Wireless Symposium, IWS 2015*, China, April 2015.
- [2] G. Zhang, J. Wang, and W. Wu, "Wideband balun bandpass filter explored for a balanced dipole antenna with high selectivity," *IEEE Electronics Letters*, vol. 52, no. 13, pp. 1153–1155, 2016.
- [3] L. K. Yeung and K. L. Wu, "A dual-band coupled-line balun filter," *IEEE Transactions on Microwave Theory and Techniques*, vol. 55, no. 11, pp. 2406–2411, 2007.
- [4] Y.-W. Lin, J.-C. Lu, and C.-Y. Chang, "Design of high-order wideband planar balun filter in S-plane bandpass prototype," *IEEE Transactions on Microwave Theory and Techniques*, vol. 60, no. 7, pp. 2124–2130, 2012.
- [5] P. Cheong, T.-S. Lv, W.-W. Choi, and K.-W. Tam, "A compact microstrip square-loop dual-mode balun-bandpass filter with simultaneous spurious response suppression and differential performance improvement," *IEEE Microwave and Wireless Components Letters*, vol. 21, no. 2, pp. 77–79, 2011.
- [6] X. F. Ye, Y. Z. Shi, E. Guo, and S. Y. Zheng, "A bandpass filtering balun based on circular sector patch," in *Proceedings of the 5th IEEE Asia-Pacific Conference on Antennas and Propagation, APCAP 2016*, pp. 21–22, Taiwan, July 2016.
- [7] F. Huang, J. Wang, and L. Zhu, "A New Approach to Design a Microstrip Dual-Mode Balun Bandpass Filter," *IEEE Microwave and Wireless Components Letters*, vol. 26, no. 4, pp. 252–254, 2016.
- [8] H. Gu, J. Wang, G. Zhang, and J.-L. Li, "Design of a SIW balun bandpass filter with high selectivity," *Journal of Electromagnetic Waves and Applications*, vol. 30, no. 1, pp. 61–69, 2016.
- [9] D. M. Pozar, *Microwave Engineering*, John Wiley Sons Press, New York, 3rd edition, 2005.
- [10] J. Hong and M. J. Lancaster, *Microstrip Filters for RF/Microwave Applications*, John Wiley & Sons, New York, NY, USA, 2001.
- [11] Y. Qian, W. R. Deal, N. Kaneda, and T. Itoh, "Microstrip-fed quasi-Yagi antenna with broadband characteristics," *IEEE Electronics Letters*, vol. 34, no. 23, pp. 2194–2196, 1998.

## Research Article

# A Compact Differential-Mode Wide Stopband Bandpass Filter with Good and Wideband Common-Mode Suppression

Gang Zhang , Yang Zhao , and Wei Yan

*School of Electrical and Automation Engineering, Nanjing Normal University, Nanjing 210046, China*

Correspondence should be addressed to Yang Zhao; yang\_zhao\_nnu@126.com

Received 21 December 2017; Accepted 18 February 2018; Published 21 March 2018

Academic Editor: Lei Ge

Copyright © 2018 Gang Zhang et al. This is an open access article distributed under the Creative Commons Attribution License, which permits unrestricted use, distribution, and reproduction in any medium, provided the original work is properly cited.

This letter presents a microstrip differential-mode (DM) bandpass filter (BPF) with high and wide stopband suppression under both DM and common-mode (CM) operations. A new coupling topology is formed up to realize the DM BPF by integrating a pair of  $\lambda/2$  microstrip transmission lines and two multimode resonators. The DM and CM equivalent half-circuits are established to explain the operating principal. For validation, a DM BPF operating at 2.2 GHz is implemented. Experimental results indicate that the presented DM BPF exhibits not only sharp DM passband selectivity but also deep and ultrawide stopband suppression of more than 30 dB for both DM and CM.

## 1. Introduction

Recently, the great development of modern wireless communication system has put forward higher requirements on RF devices with high performance and miniaturized size. To meet these requirements, one effective approach is to design multifunction embedded component by integrating multiple functions into one component. Since differential-mode circuits play an important role in the modern communication system as they can reduce the environmental noise as well as crosstalk in the system and bandpass filters (BPFs) can realize the passband frequency selective response, differential-mode bandpass filter as one typical integrated component has been proposed accordingly. It can provide both functions of differential-mode (DM) passband selectivity and common-mode (CM) rejection has been receiving increased attention. Over the past few years, much effort has been made in the exploration of various DM BPFs [1–9].

In [1], a DM BPF is proposed by adopting lumped-element loaded half-wavelength resonators. In the design, the common-mode suppression can be tuned independently of the differential-mode response in the differential-mode filter via making full use of a center-loaded half-wavelength resonator. Although the DM BPF exhibits sharp frequency selectivity and high CM suppression, the involved design configuration and procedure are very complicated. Besides, another

DM BPF based on short-ended self-coupled ring resonator is presented in [2]. By periodically and symmetrically arranging short-ended SCRRs between the microstrip differential lines, the common-mode suppression can be realized at desired frequency easily with wideband differential-mode passband. But its circuit usually suffers from bulky size. In addition, by utilizing inherent common-mode rejection property of slotline, a compact DM BPF is developed in [3]. In this design, by properly placing the slotline resonator, the coupling between the slotline mode and the differential-mode signals can be maximized, while that between the slotline mode and the common-mode signals can be minimized. However, the employed slotline itself often results in a high insertion loss due to its high radiation loss. Moreover, based on the mode degeneration properties of the square patch resonator, a dual-mode differential mode has also been presented by adopting appropriate coupling structure among four isosceles right triangular patch resonators in [4]. But CM rejection level needs to be improved. On the other hand, stemming from the differential-mode coupled-line prototype, DM BPFs [5, 6] are proposed with improved performance by utilizing balanced coupled-line structure to realize the passband response in differential-mode operation and meanwhile give nice stopband in common-mode operation. Nevertheless, these designs are still difficult to achieve high and wide stopband rejection for DM and CM simultaneously. Apart

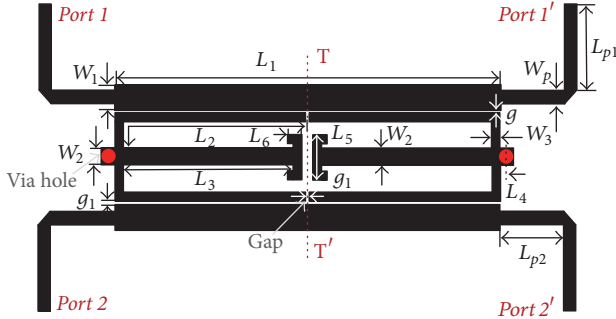


FIGURE 1: Schematic of the proposed differential-mode BPF.

from these above reported works, other differential-mode bandpass filters based on coplanar waveguide resonator, substrate integrated waveguide resonator, or dielectric resonator are also reported in [7–9].

In this letter, a microstrip differential-mode BPF is presented with new coupling topology by properly arranging multimode resonators between input/output transmission lines. High selective passband and wide stopband for DM and a wide and deep stopband for CM are realized at the same time in the design. For demonstration, a prototype differential-mode BPF is implemented. Both simulated and measured results are in good agreement, which validates the design concept.

## 2. Proposed Differential-Mode BPF Design

Figure 1 depicts the layout of the designed DM BPF, which only consists of a pair of  $\lambda/2$  microstrip transmission input/output lines and two triple-mode resonators. The entire structure is symmetrical with respect to the vertical central plane T-T'. Under DM operation, the central plane T-T' behaves as a perfect electrical wall. On this occasion, parallel coupled line prototype with two different terminations of one open-ended circuit and one short-ended circuit will be formed up between the input/output lines and the arms of the resonators. It will provide a bandpass response. Therefore, the DM equivalent circuit of its half symmetrical bisections can be simply treated as a triple-mode bandpass filter with a pair of bandpass coupled feeding lines. Meanwhile, for common-mode operation, the central plane becomes a perfect magnetic wall. With this case, parallel coupled line prototype with two same short-ended terminations will be generated between the input/output lines and the arms of the resonators, which will exhibit an all stopband response. Correspondingly, the CM equivalent-half-circuit can be directly deemed as all-stopband circuit, since the feeding lines exhibit all-stop characteristic [10].

In order to illustrate the resonant properties of the employed resonator, Figure 2 describes the corresponding even-mode and odd-mode equivalent circuits of its half symmetrical bisections by utilizing the even-mode/odd-mode method in [11]. Therefore, assuming that the even-mode input admittance and odd-mode input admittance  $Y_{in,even}$

and  $Y_{in,odd}$ , respectively, are equal to zero, the resonant condition equations can be derived as

$$\cot \theta_3 - \tan \theta_2 = \frac{2}{K} \tan \theta_1 \quad (1a)$$

$$\theta_1 = \frac{\pi}{2}, \quad (1b)$$

where  $K = Y_2/Y_1$  is the admittance ratio of the resonator.

In addition, one inherent TZ can be found when  $\theta_2 = \pi/2$  under  $Y_{in,odd} = Y_{in,even}$ . Based on the above analysis, the first three even-mode and odd-mode resonant frequencies can be deduced as  $f_{even1}$ ,  $f_{odd}$ , and  $f_{even2}$ , respectively. Figure 3 shows the design chart of the employed triple-mode resonators with  $K = 1.6$ . We can figure out that  $f_{even1}/f_{odd}$  and  $f_{even2}/f_{odd}$  are mainly, respectively, determined by  $\theta_3$  and  $\theta_2$ , while  $f_{odd}$  is only determined by  $\theta_1$ . More specially, it can be observed that  $f_{even1}/f_{odd}$  almost remains unchanged versus  $\theta_2$  but decreases as  $\theta_3$  increases.

Furthermore,  $f_{even2}/f_{odd}$  significantly decreases as  $\theta_2$  decreases, while it causes a small reduction when  $\theta_3$  rises up. Figure 4 describes the impedance ratio of  $Y_1/Y_2$  influence on resonant frequencies and frequency bandwidth. It can be seen that when  $Y_1/Y_2$  increases,  $f_{even1}$  and  $f_{odd}$  fall down, while the bandwidth between  $f_{even1}$  and  $f_{even2}$  increases. Therefore, the impedance ratio of  $Y_1/Y_2$  can be utilized to increase the design freedom. These above demonstrated properties are meaningful for one to realize a differential-mode BPF with desired DM passband bandwidth and high selectivity. Figure 5 gives the corresponding coupling scheme of the DM BPF under differential-mode operation, where nodes 1, 2, and 3 denote the even and odd modes of the resonator which form up the triple-mode DM filtering response, respectively. Due to the symmetry of the DM equivalent circuit, the coupling coefficients in Figure 5 satisfy the relationship of  $M_{S,1/2/3} = M_{L,1/2/3}$ .

Herein, a prototype differential-mode BPF with the central frequency of  $f_0 = 2.2$  GHz and desired 3 dB bandwidth of 240 MHz is designed for an instance. The design procedure is listed in the following steps. At the beginning, according to the above (1a)-(1b), calculate the parameters ( $L_2 = 20.4$  mm,  $L_3 = 18.0$  mm, and  $L_4 = 0.8$  mm) of the resonator with the derived frequencies  $f_{even1} = 2.11$  GHz,  $f_{odd} = 2.24$  GHz, and  $f_{even2} = 2.33$  GHz from a targeted coupling matrix [12]. Secondly, based on the required external Q-factors to even and odd modes ( $Q_{exe1} = 37.0$ ,  $Q_{exe2} = 66.3$ , and  $Q_{exo} = 23.8$ ) from the matrix, determine the values of the width ( $W_1 = 2.3$  mm) and gap ( $g = 0.2$  mm) through extracting the two group delays, that is,  $\tau_{S11}(f_{even})$  and  $\tau_{S11}(f_{odd})$ . In the end, the designed differential-mode circuit is initially built and fine tuning is performed to obtain optimal performance.

## 3. Experimental Results

To validate the design concept, the differential-mode filter has been designed and fabricated on the substrate with a relative dielectric constant of 3.55, thickness of 0.508 mm, and loss tangent of 0.0027. The final layout parameters are  $L_1 = 35.6$  mm,  $L_2 = 19.5$  mm,  $L_3 = 17.1$  mm,  $L_4 = 0.8$  mm,  $L_5 =$

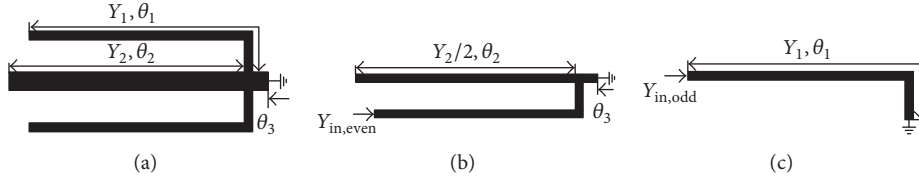


FIGURE 2: Equivalent circuits of employed multimode resonator. (a) Entire structure. (b) Even-mode bisection. (c) Odd-mode bisection.

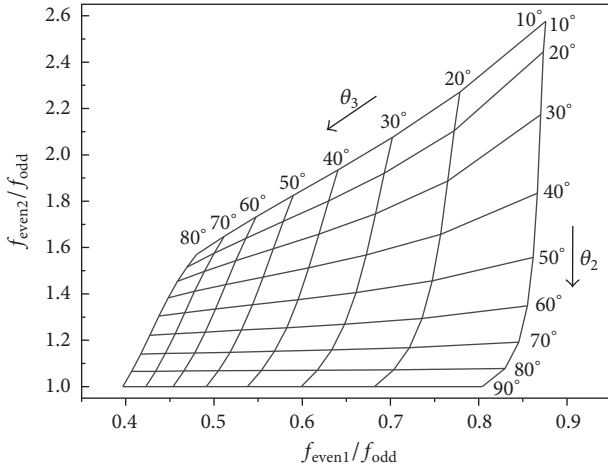


FIGURE 3: Design chart of the triple mode resonator.

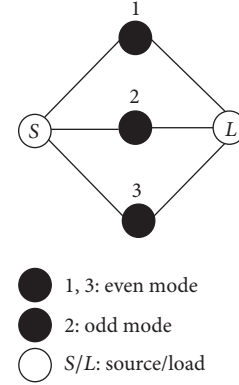
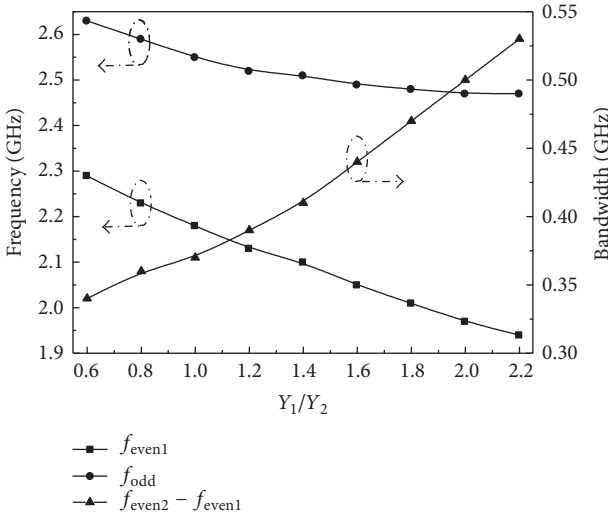


FIGURE 5: Equivalent-half-coupling scheme of the proposed DM BPF under differential-mode operation.


 FIGURE 4: Resonant frequencies and bandwidth versus  $Y_1/Y_2$ .

4.2 mm,  $L_6 = 1.3$  mm,  $L_{p1} = 7.9$  mm,  $L_{p2} = 6.0$  mm,  $W_1 = 2.3$  mm,  $W_2 = 1.6$  mm,  $W_3 = 0.7$  mm,  $W_p = 1.17$  mm, and  $g = 0.2$  mm. The photograph of the fabricated circuit is displayed in Figure 6. Figure 7 shows the simulated and measured results. Simulation is accomplished by the commercial full-wave simulator ANSOFT HFSS, while the measurement is carried out in the Agilent N5244A four-port vector network analyzer. As shown in the figure, under DM operation, the measured DM central frequency is 2.2 GHz with the 3 dB Bandwidth of 230 MHz. Three transmission poles inside the

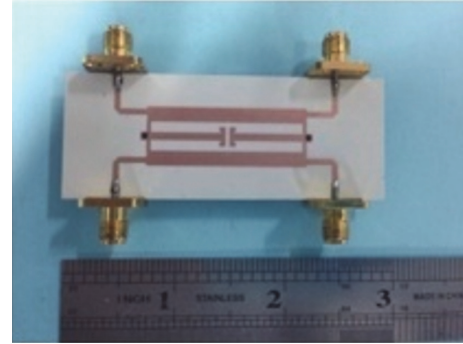


FIGURE 6: The photograph of the fabricated DM BPF.

passband can be clearly observed. Meanwhile, one transmission zero can also be obviously found as expected. Within this DM operating band, the measured minimum insertion loss (IL) is 0.8 dB, while the return loss (RL) is better than 15.8 dB. Besides, the proposed differential-mode BPF exhibits sharp frequency selectivity and good harmonic suppression with more than 30 dB suppression level up to  $2.7f_0$ . On the other hand, for CM excitation, the differential-mode filter shows an ultrawide stopband with the rejection higher than 30 dB from DC to  $2.8f_0$ .

Table 1 compares the performances of the proposed DM BPF with other published works in terms of the specifications, that is, roll-off, differential-mode stopband, and common-mode suppression. It indicates that our differential-mode filter exhibits not only sharp DM passband selectivity and wide upper stopband but also good ultrawide CM stopband rejection against others.

TABLE 1: Comparisons with previous works.

Refs.	Sharp roll-off	DM suppression >30 dB	CM rejection >30 dB	CM rejection (0 to $2.5f_0$ )
[4]	Yes	None	None	None
[5]	Yes	Up to $2.0f_0$	Up to $1.9f_0$	>26 dB
[6]	No	None	Up to $2.7f_0$	>30 dB
[7]	Yes	Up to $2.3f_0$	Up to $1.3f_0$	>10 dB
This work	Yes	Up to $2.7f_0$	Up to $2.8f_0$	>31.4 dB

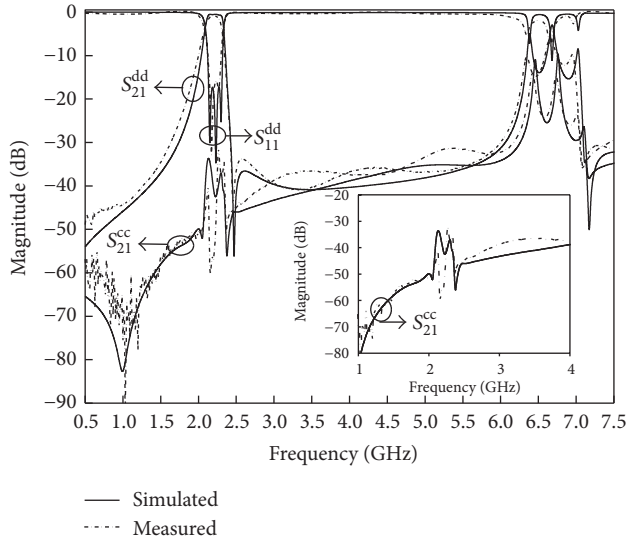


FIGURE 7: Measured and simulated results of the DM BPF.

## 4. Conclusion

In this letter, a compact differential-mode bandpass filter (BPF) has been presented with an ingenious coupling topology, achieving wide and deep stopband rejection for both differential mode and common mode. The explicit design procedure has been described and a prototype example has been manufactured. The experimental results agree well with simulated ones, validating the feasibility of the proposed design concept for modern differential communication system.

## Conflicts of Interest

The authors declare that they have no conflicts of interest.

## References

- [1] J. Shi and Q. Xue, "Balanced bandpass filters using center-loaded half-wavelength resonators," *IEEE Transactions on Microwave Theory and Techniques*, vol. 58, no. 4, pp. 970–977, 2010.
- [2] H. Wang, K.-W. Tam, S.-K. Ho, W. Kang, and W. Wu, "Short-ended self-coupled ring resonator and its application for balanced filter design," *IEEE Microwave and Wireless Components Letters*, vol. 24, no. 5, pp. 312–314, 2014.
- [3] D. Chen, H. Bu, L. Zhu, and C. Cheng, "A differential-mode wideband bandpass filter on slotline multi-mode resonator with controllable bandwidth," *IEEE Microwave and Wireless Components Letters*, vol. 25, no. 1, pp. 28–30, 2015.
- [4] Q. Liu, J. Wang, and Y. He, "Compact balanced bandpass filter using isosceles right triangular patch resonator," *IEEE Electronics Letters*, vol. 53, no. 4, pp. 253–254, 2017.
- [5] T. Yan, D. Lu, J. Wang, and X.-H. Tang, "High-Selectivity Balanced Bandpass Filter with Mixed Electric and Magnetic Coupling," *IEEE Microwave and Wireless Components Letters*, vol. 26, no. 6, pp. 398–400, 2016.
- [6] D. Chen, L. Zhu, H. Bu, and C. Cheng, "Differential-mode bandpass filter on microstrip line with wideband common-mode suppression," *IEEE Electronics Letters*, vol. 53, no. 3, pp. 163–165, 2017.
- [7] A. Fernández-Prieto, J. Bhatker, A. Lujambio, J. Martel, F. Medina, and R. R. Boix, "Balanced bandpass filter based on magnetically coupled coplanar waveguide folded-stepped impedance resonators," *IEEE Electronics Letters*, vol. 52, no. 14, pp. 1229–1231, 2016.
- [8] K. Zhou, W. Kang, and W. Wu, "Compact dual-band balanced bandpass filter based on double-layer SIW structure," *IEEE Electronics Letters*, vol. 52, no. 18, pp. 1537–1539, 2016.
- [9] J.-X. Chen, Y. Zhan, W. Qin, Z.-H. Bao, and Q. Xue, "Novel narrow-band balanced bandpass filter using rectangular dielectric resonator," *IEEE Microwave and Wireless Components Letters*, vol. 25, no. 5, pp. 289–291, 2015.
- [10] L. Yang, W.-W. Choi, K.-W. Tam, and L. Zhu, "Balanced Dual-Band Bandpass Filter With Multiple Transmission Zeros Using Doubly Short-Ended Resonator Coupled Line," *IEEE Transactions on Microwave Theory and Techniques*, vol. 63, no. 7, pp. 2225–2232, 2015.
- [11] D. M. Pozar, *Microwave Engineering*, Wiley, New York, NY, USA, 3rd edition, 2005.
- [12] J. Hong and M. J. Lancaster, *Microstrip Filters for RF/Microwave Applications*, John Wiley & Sons, New York, NY, USA, 2nd edition, 2001.

## Research Article

# Uplink Multiuser MIMO-OFDM System in the Presence of Phase Noises, Power Imbalance, and Correlation

Xiaoming Chen <sup>1</sup>, Andreas Wolfgang <sup>2</sup> and Tommy Svensson <sup>3</sup>

<sup>1</sup>*School of Electronic and Information Engineering, Xi'an Jiaotong University, Xi'an 710049, China*

<sup>2</sup>*Qamcom Research & Technology AB, 41285 Gothenburg, Sweden*

<sup>3</sup>*Department of Electrical Engineering, Chalmers University of Technology, 41296 Gothenburg, Sweden*

Correspondence should be addressed to Xiaoming Chen; [xiaoming.chen@mail.xjtu.edu.cn](mailto:xiaoming.chen@mail.xjtu.edu.cn)

Received 3 December 2017; Accepted 14 January 2018; Published 8 February 2018

Academic Editor: Ting-Yen Shih

Copyright © 2018 Xiaoming Chen et al. This is an open access article distributed under the Creative Commons Attribution License, which permits unrestricted use, distribution, and reproduction in any medium, provided the original work is properly cited.

The effects of phase noises (PNs), power imbalances, and correlations on multiuser orthogonal frequency division multiplexing (OFDM) multiple-input multiple-output (MIMO) systems are studied. It is assumed that each user is equipped with a single antenna, whereas the base station (BS) has multiple antennas and use zero-forcing (ZF) decoder for multiuser detection. Since each user has an independent oscillator, the received uplink (UL) signal at each BS antenna is corrupted by all of these independent PNs. Furthermore, there may be power imbalances and correlations (due to common scatterers) between different users. These impairments are jointly analyzed in this work. A closed-form expression of the mean square error (MSE) performance of the multiuser MIMO-OFDM system is derived. The analytical results are verified by simulations.

## 1. Introduction

The orthogonal frequency division multiplexing (OFDM) technique [1] can effectively turn a frequency-selective channel [2] into multiple frequency-flat subchannels at different subcarriers, allowing the simple one-tap channel equalization to mitigate the multipath effect. Recently, it is chosen as the main fifth generation (5G) waveform for sub-6 GHz as well as millimeter-wave bands [3, 4] by the 3rd generation partnership project (3GPP) standardization [5]. The OFDM can be readily combined with multiple-input multiple-output (MIMO) techniques [6–8] to exploit spatial multiplexing and/or diversity gain. As a result, MIMO-OFDM systems are ubiquitously employed in modern telecommunications, such as long-term evolution (LTE) and wireless local area network (WLAN) systems, for example, [9, 10].

Unfortunately, MIMO-OFDM systems are sensitive to oscillator phase noises [11–23], which cause common phase error (CPE) and intercarrier interference (ICI). While the CPE is a common phase rotation for all the subcarriers (of one OFDM symbol), the ICI represents the interferences caused by nonorthogonal subcarriers. The PN effect on single-user MIMO-OFDM (SU-MIMO-OFDM) systems has been well

studied in the literature [11–19]. Most of the works assume a common oscillator for all the antennas at the transceiver [11–16], whereas the case of an independent oscillator for each antenna has been studied in [17–19]. Assuming the base station (BS) antennas share a common oscillator, the downlink (DL) of the multiuser MIMO-OFDM (MU-MIMO-OFDM) system (at each user) is similar to the single-user case (in that the user see only a single transmit PN). In the uplink (UL) transmission, however, the received signal at the BS is corrupted by multiple transmit PNs. Since the PNs from different users are independent, the PN estimation in the UL is more complex than that in the DL. For this reason, we focus on the UL multiuser PN effect in this work.

There are a few works studying the PN effect on uplink MU-MIMO-OFDM systems, for example, [20, 21]. While [20] considered multiple PNs from the users together with another PN at the BS, [21] considered multiple PNs at the BS (with large antenna array) with PN-free users. The PNs from multiple users are mixed at each BS antenna, whereas the PNs (of multiple oscillators) at the BS are uncoupled. Therefore, PN estimation in the former is more challenging than that in the latter. For example, the CPEs of multiuser PNs must

be jointly estimated [20], whereas the CPE of each of the BS PNs can be tracked separately in an easier way [21, 22]. It is difficult to compensate the ICI effects of multiple transmit PNs at the receiver. As a result, a PN compensation scheme that mitigates the multiple transmit PNs and a receive PN separately was proposed in [23] for multinode backhauling. Nevertheless, the scheme requires a feedback loop with direct RF sampling at each transmitting node and, therefore, is not feasible for the considered multiuser scenario in this work.

In this work, we focus on the ICI effects of multiuser PNs. Specifically, we derive a closed-form expression of the mean square error (MSE) performance of the uplink MU-MIMO-OFDM system with and without power imbalance and correlation, assuming the CPEs of different PNs can be perfectly estimated. (Given the fact that the CPE is just the time average of the PN over one OFDM symbol, the CPE can usually be estimated accurately [11, 14, 15]. The effect of imperfect CPE estimation is included in simulations.) Unlike [20] where the multiuser PN effects were studied by simulation solely, the analytical results derived in this work give more insight into the ICI effect of multiuser PNs. Moreover, the derived MSE expression can take into account of power imbalances and correlations between different users. (In the literature, it is usually assumed that spatially separated users are uncorrelated. Nevertheless, measurements and simulations confirm that spatially separated users can still have correlations due to common scatterers [24–26].) To the best knowledge of the authors, the joint effects of multiuser PNs, power imbalance, and correlation of the uplink MU-MIMO-OFDM system have not been studied analytically in the previous literature. Finally, the ICI effect of multiuser PNs for different numbers of BS antennas and users are studied analytically and experimentally (by simulations). Good agreements between simulated and theoretical MSEs are observed.

*Notations 1.* Throughout this paper, boldface lower and uppercase letters (e.g.,  $\mathbf{x}$  and  $\mathbf{X}$ ) represent column vector and matrix, respectively;  $\text{diag}(\mathbf{x})$  denotes a diagonal matrix whose diagonal elements are given by  $\mathbf{x}$ ;  $\|\mathbf{x}\|$  is the Euclidean norm of  $\mathbf{x}$ ;  $\text{Tr}(\mathbf{X})$  represents the trace of  $\mathbf{X}$ ;  $\mathbf{I}_M$  is an  $M \times M$  identity matrix;  $j = \sqrt{-1}$ ;  $\otimes$  denotes the Kronecker product;  $E$  represents mathematical expectation; and  $T$ ,  $H$ , and  $\dagger$  denote transpose, transpose conjugate (Hermitian), and Moore-Penrose pseudoinverse, respectively.

## 2. System Model

For simplicity, we assume  $K$  users (each equipped with a single antenna along with a free-running oscillator) and  $M (> K)$  antennas at the BS (see Figure 1). The BS uses zero-forcing (ZF) decoder for multiuser detection. Throughout this paper, we assume that the cyclic prefix (CP) of the OFDM symbol is longer than the channel spread.

Let  $N$  be the number of OFDM subcarriers and  $\mathbf{F}$  be an  $N \times N$  unitary discrete Fourier transform (DFT) matrix, whose elements are given by  $\exp(-j2\pi nl/N)/\sqrt{N}$ , ( $n, l = 0, \dots, N-1$ ), and  $\boldsymbol{\varphi}_k$  and  $\boldsymbol{\theta}$  be  $N \times 1$  vectors consisting of

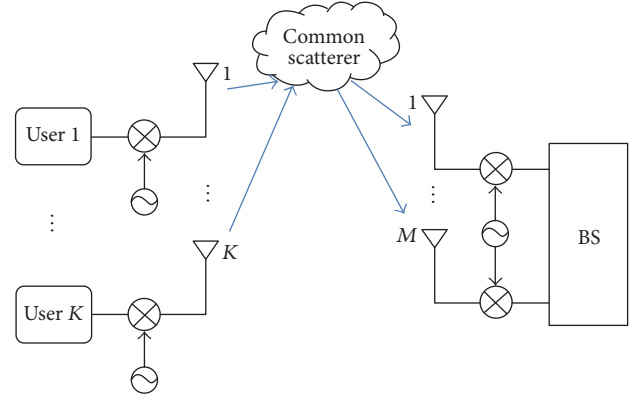


FIGURE 1: Block diagram of the considered MU-MIMO-OFDM system with illustrations of oscillators and a common scatterer.

the time-domain PNs within one OFDM symbol at the  $k$ th user ( $k = 1, \dots, K$ ) and at the BS, respectively. The frequency-domain expression of the UL transmission (from  $K$  users to the BS) in the presence of PNs is given as follows [17]:

$$\mathbf{y} = (\mathbf{G}_R \otimes \mathbf{I}_M) \mathbf{H} \mathbf{G}_T \mathbf{x} + \mathbf{w}, \quad (1)$$

where  $\mathbf{H}$  is an  $MN \times KN$  block diagonal channel matrix whose  $n$ th diagonal block entry  $\mathbf{H}_n$  is an  $M \times K$  channel transfer function (CTF) matrix at the  $n$ th subcarrier,  $\mathbf{x} = [\mathbf{x}_1^T \ \mathbf{x}_2^T \ \dots \ \mathbf{x}_N^T]^T$  is the  $KN \times 1$  signal vector with  $\mathbf{x}_n$  denoting the  $K \times 1$  transmitted signal vector at the  $n$ th subcarrier,  $\mathbf{y} = [\mathbf{y}_1^T \ \mathbf{y}_2^T \ \dots \ \mathbf{y}_N^T]^T$  is the  $MN \times 1$  signal vector with  $\mathbf{y}_n$  denoting the  $M \times 1$  received signal vector at the  $n$ th subcarrier,  $\mathbf{w}$  is an  $MN \times 1$  additive white Gaussian noise (AWGN) vector,  $\mathbf{G}_R = \mathbf{F} \text{diag}(\exp(j\boldsymbol{\theta})) \mathbf{F}^H$  is an  $N \times N$  matrix of the PN spectral components of the BS oscillator, and  $\mathbf{G}_T$  is a  $KN \times KN$  matrix consisting of the  $N$  spectral components of the PNs of all the  $K$  users. The  $(n, l)$ th entry of  $\mathbf{G}_R$  is denoted as  $g_{(n-l)_N}^{\text{Rx}}$ , where  $(n-l)_N$  denotes  $(n-l) \bmod N$ . The  $(n, l)$ th block of  $\mathbf{G}_T$  is  $\text{diag}(\mathbf{g}_{(n-l)_N}^{\text{Tx}})$ , where the  $K \times 1$  vector  $\mathbf{g}_{(n-l)_N}^{\text{Tx}}$  consists of the corresponding spectral components of all the PNs from the  $K$  users. Note that (1) only holds approximately since the PN in the CP and the end of the time-domain OFDM symbol are different. Nevertheless, it is a good approximation [11, 15, 17]. By separating the CPE and ICI terms  $\mathbf{G}_T = \mathbf{I}_N \otimes \text{diag}(\mathbf{g}_0^{\text{Tx}}) + \mathbf{P}_T$  and  $\mathbf{G}_R = g_0^{\text{Rx}} \mathbf{I}_N + \mathbf{P}_R$ , (1) can be rewritten as

$$\mathbf{y} = g_0^{\text{Rx}} \mathbf{H} (\mathbf{I}_N \otimes \text{diag}(\mathbf{g}_0^{\text{Tx}})) \mathbf{x} + \mathbf{e} + \mathbf{w}, \quad (2)$$

where  $g_0^{\text{Rx}}$  is the CPE of the PN at the BS,  $\mathbf{g}_0^{\text{Tx}}$  consists of the CPEs of the PNs from the  $K$  users, and the ICI term  $\mathbf{e}$  is

$$\begin{aligned} \mathbf{e} = & (\mathbf{P}_R \otimes \mathbf{I}_M) \mathbf{H} \mathbf{P}_T \mathbf{x} + g_0^{\text{Rx}} \mathbf{H} \mathbf{P}_T \mathbf{x} \\ & + (\mathbf{P}_R \otimes \mathbf{I}_M) \mathbf{H} (\mathbf{I}_N \otimes \text{diag}(\mathbf{g}_0^{\text{Tx}})) \mathbf{x}. \end{aligned} \quad (3)$$

The received signal at the  $n$ th subcarrier can be expressed as

$$\mathbf{y}_n = \mathbf{H}_n \text{diag}(\mathbf{g}_0) \mathbf{x}_n + \mathbf{e}_n + \mathbf{w}_n, \quad (4)$$

where  $\mathbf{g}_0 = g_0^{\text{Rx}} \mathbf{g}_0^{\text{Tx}}$ ,  $\mathbf{e}_n$  and  $\mathbf{w}_n$  denote ICIs and AWGNs at the  $n$ th subcarrier, respectively. The CPEs  $\mathbf{g}_0$  of multiple PNs can be jointly estimated as follows [20]:

$$\hat{\mathbf{g}}_0 = \frac{1}{N_p} \sum_{n \in S_p} (\mathbf{H}_n \text{diag}(\mathbf{x}_n))^{\dagger} \mathbf{y}_n, \quad (5)$$

where  $S_p$  denotes the set of the  $N_p$  scattered pilots. The CPEs can be corrected at the ZF decoder as

$$\hat{\mathbf{x}}_n = \text{diag}(\hat{\mathbf{g}}_0)^{-1} \mathbf{H}_n^{\dagger} \mathbf{y}_n, \quad (6)$$

where  $\hat{\mathbf{x}}_n$  denotes the detected signals at the  $n$ th subcarrier. Note that, in order to focus on the PN effect, we assume perfect channel estimation. In practice, the estimated channel in the preamble will contain an initial CPE. In the payload, the CPE will be different. Thus, it is necessary to estimate the relative CPE with respect to the initial CPE. Mathematically, it is equivalent to assume that the estimated channel contains the preamble CPE and then the relative CPE in the payload can still be estimated using (5).

For simplicity, we assume the Wiener PN model for the free-running oscillator, whose discrete-time expression is given as follows [11, 13–15]:

$$\phi(i+1) = \phi(i) + \zeta(i), \quad (7)$$

where  $\phi$  is the PN and  $\zeta$  is a zero-mean Gaussian random variable, whose variance is  $4\pi\beta T_s$  with  $T_s$  denoting the sampling duration and  $\beta$  representing the 3 dB bandwidth of the PN. The 3 dB bandwidth is related to the carrier frequency  $f_c$  as  $\beta = \zeta\pi f_c^2$ , where  $\zeta$  is a parameter characterizing the quality of the oscillator [27]. Nevertheless, the value of  $\beta$  is usually given instead of  $\zeta$  in the literature.

In order to include power imbalances and correlations of different users, the MIMO channel impulse response of the  $l$ th tap is modeled as  $\tilde{\mathbf{H}}_l = \mathbf{H}_w \mathbf{R}^{1/2}$ ,  $\mathbf{H}_w$  denotes the spatially white MIMO channel with independent and identically distributed (i.i.d.) complex Gaussian variables, and  $\mathbf{R}^{1/2}$  is the Hermitian square root of the correlation matrix  $\mathbf{R}$ , defined as

$$\mathbf{R} = \text{diag}(\sqrt{\boldsymbol{\eta}}) \boldsymbol{\Phi} \text{diag}(\sqrt{\boldsymbol{\eta}}), \quad (8)$$

where  $\boldsymbol{\eta}$  is a vector consisting of the mean effective gains (MEGs) [28] of the users' antennas,  $\sqrt{\cdot}$  represents element-wise square root, and the matrix  $\boldsymbol{\Phi}$  consists of correlation coefficients due to the common scatters. The power imbalances are the MEG differences (in dB) between the elements in  $\boldsymbol{\eta}$ . It is noted that the path loss differences between different users can be included in the power imbalances.

### 3. Performance Analysis

In order to focus on the ICI effects of multiuser PNs, we assume perfect estimation of CPEs. Since the BS can afford high quality oscillator with negligible PN whereas the users are usually equipped with low-cost oscillators with nonnegligible PNs, we ignore the BS PN and focus on

multiuser PNs. (The BS PN and imperfect CPE estimation are considered in the simulations in the next section.) For notational convenience, we drop the superscript Tx hereafter.

The signal at the  $n$ th subcarrier after the ZF decoder is given as

$$\mathbf{r}_k = \text{diag}(\mathbf{g}_0) \mathbf{x}_n + \sum_{l=0, l \neq n}^{N-1} \text{diag}(\mathbf{g}_{(n-l)_N}) \mathbf{x}_l + \mathbf{H}_n^{\dagger} \mathbf{w}_n. \quad (9)$$

The (normalized) MSE at the  $n$ th subcarrier is

$$\xi_n = \frac{E \left[ \left\| \sum_{l=0, l \neq n}^{N-1} \text{diag}(\mathbf{g}_{(n-l)_N}) \mathbf{x}_l \right\|^2 \right] + E \left[ \left\| \mathbf{H}_n^{\dagger} \mathbf{w}_n \right\|^2 \right]}{E \left[ \left\| \text{diag}(\mathbf{g}_0) \mathbf{x}_n \right\|^2 \right]}. \quad (10)$$

Note that the normalized MSE is also referred to as error vector magnitude (EVM) [15], which is a popular performance metric in the industry.

Assuming the subcarrier symbols are independent and identically distributed with a variance of  $\sigma_x^2$ , that is,  $E[\mathbf{x}_n \mathbf{x}_n^H] = \sigma_x^2 \mathbf{I}_K$ , the power contributions of the useful signal (with known CPEs) and ICI term can be expressed as

$$E \left[ \left\| \text{diag}(\mathbf{g}_0) \mathbf{x}_n \right\|^2 \right] = \sigma_x^2 E \left[ \left\| \mathbf{g}_0 \right\|^2 \right],$$

$$E \left[ \left\| \sum_{l \neq n} \text{diag}(\mathbf{g}_{(n-l)_N}) \mathbf{x}_l \right\|^2 \right] = \sigma_x^2 E \left[ \sum_{l \neq n} \left\| \mathbf{g}_{(n-l)_N} \right\|^2 \right], \quad (11)$$

respectively.

Assuming the oscillators at different users are of the same quality (i.e., PNs from different users have the same 3 dB bandwidth  $\beta$ , the same CPE term  $\sigma_{\text{CPE}}^2 = E[|g_0|^2]$ , and the same ICI term  $\sigma_{\text{ICI}}^2 = E[\sum_{l \neq n} |g_{(n-l)_N}|^2]$ ),

$$E \left[ \left\| \mathbf{g}_0 \right\|^2 \right] = KE \left[ |g_0|^2 \right] = K\sigma_{\text{CPE}}^2,$$

$$E \left[ \sum_{l \neq n} \left\| \mathbf{g}_{(n-l)_N} \right\|^2 \right] = KE \left[ \sum_{l \neq n} |g_{(n-l)_N}|^2 \right] = K\sigma_{\text{ICI}}^2. \quad (12)$$

Note that  $E[\sum_{l \neq n} |g_{(n-l)_N}|^2] = E[\sum_{n \neq 0} |g_n|^2]$ . Let

$$g_{(n-l)_N}|_{l=0} = g_n = \frac{1}{N} \sum_i \exp(j\phi(i)) \exp\left(-\frac{j2\pi ni}{N}\right), \quad (13)$$

and the total power of the PN is given as

$$\begin{aligned} \sum_{n=0}^{N-1} |g_n|^2 &= \frac{1}{N^2} \sum_{n=0}^{N-1} \sum_i \sum_p \exp(j(\phi(i) - \phi(p))) \\ &\quad \times \exp\left(j \frac{2\pi k(p-i)}{N}\right) \\ &= \frac{1}{N^2} \sum_i \sum_p \exp(j(\phi(i) - \phi(p))) \\ &\quad \times \sum_{n=0}^{N-1} \exp\left(j \frac{2\pi k(p-i)}{N}\right), \end{aligned} \quad (14)$$

where

$$\exp\left(j\frac{2\pi n(p-i)}{N}\right) = \begin{cases} N, & p = i \\ 0, & p \neq i. \end{cases} \quad (15)$$

Hence,

$$\sigma_{\text{CPE}}^2 + \sigma_{\text{ICI}}^2 = E\left[\sum_{n=0}^{N-1} |g_n|^2\right] = \frac{1}{N^2} (N \times N) = 1. \quad (16)$$

Using the DFT expression (13),  $\sigma_{\text{CPE}}^2$  can be derived as

$$\begin{aligned} E[|g_0|^2] &= E\left[\sum_i \sum_p \exp(j(\phi(i) - \phi(p)))\right] \\ &= \frac{1}{N^2} \sum_i \sum_p \exp(-2\pi\beta|i-p|T_s), \end{aligned} \quad (17)$$

where the last step is derived using the characteristic function (i.e., the Fourier transform of the probability density function) of the PN. Once  $\sigma_{\text{CPE}}^2$  is known,  $\sigma_{\text{ICI}}^2$  can be readily derived as

$$E\left[\sum_{n \neq 0} |g_n|^2\right] = 1 - \frac{1}{N^2} \sum_i \sum_p \exp(-2\pi\beta|i-p|T_s). \quad (18)$$

Equations (16)–(18) imply that the total energy of the PN is fixed and that reducing the subcarrier spacing reduces the CPE term and increases the ICI term.

Since  $\mathbf{H}_n^\dagger = (\mathbf{H}_n^H \mathbf{H}_n)^{-1} \mathbf{H}_n^H$  and  $E[\mathbf{w}_n \mathbf{w}_n^H] = \sigma_w^2 \mathbf{I}_M$ , the noise power (after the ZF decoder) is given as

$$\begin{aligned} E\left[\|\mathbf{H}_n^\dagger \mathbf{w}_n\|^2\right] &= \text{Tr}\left\{E\left[\mathbf{H}_n^\dagger \mathbf{w}_n \mathbf{w}_n^H (\mathbf{H}_n^\dagger)^H\right]\right\} \\ &= \sigma_w^2 \text{Tr}\left\{E\left[(\mathbf{H}_n^H \mathbf{H}_n)^{-1}\right]\right\}. \end{aligned} \quad (19)$$

In the case of a Rayleigh fading multipath channel  $\mathbf{H}_n^H$  and  $M > K$ ,  $(\mathbf{H}_n^H \mathbf{H}_n)^{-1}$  follows the inverse (noncentral) Wishart distribution, whose mean is  $\mathbf{R}^{-1}/(M-K)$  [29]. Hence (19) boils down to

$$E\left[\|\mathbf{H}_n^\dagger \mathbf{w}_n\|^2\right] = \frac{\sigma_w^2}{M-K} \text{Tr}(\mathbf{R}^{-1}). \quad (20)$$

Note that the distribution of  $(\mathbf{H}_n^H \mathbf{H}_n)^{-1}$  is unknown when  $M = K$ . Due to the singularity in (20), simulations for the case of  $M = K$  do not converge. When  $M < K$ , the degree of freedom at the BS will be insufficient for detecting  $K$  data streams. As a result, we only consider the case of  $M > K$  in this paper.

Denoting the signal-to-noise ratio (SNR) as  $\gamma_0 = \sigma_x^2/\sigma_w^2$ , the MSE at the  $n$ th subcarrier can be derived as follows:

$$\xi_n = \frac{\gamma_0 K \left(1 - \frac{1}{N^2} \sum_{i=0}^{N-1} \sum_{p=0}^{N-1} \exp(2\pi\beta|i-p|T_s)\right) + (\text{Tr}(\mathbf{R}^{-1})) / (M-K)}{(\gamma_0 K/N^2) \sum_{i=0}^{N-1} \sum_{p=0}^{N-1} \exp(2\pi\beta|i-p|T_s)}. \quad (21)$$

As can be seen,  $\xi_n$  is independent of the subcarrier index  $n$ ; hence, the MSE averaged over all the subcarriers  $\xi$  is also given by (21), that is,  $\xi_n = \xi$ . It can be concluded from (21) that the MSE performance degrades with increasing  $\beta$  (the 3 dB bandwidth of the PN) and/or with increasing number of users  $K$  (for a given number of BS antennas  $M$ ) and improves with increasing  $M$  (for a given  $K$ ).

For two users ( $K = 2$ ) with a correlation of  $\rho$  and power imbalance of  $\eta_1/\eta_2$  (where  $\eta_1$  and  $\eta_2$  denote the MEGs of the two users' antennas, resp.),

$$\text{Tr}(\mathbf{R}^{-1}) = \left(\frac{1}{\eta_1} + \frac{1}{\eta_2}\right) \frac{1}{1 - |\rho|^2}. \quad (22)$$

In the absence of phase noises, the MSE reduces to

$$\xi|_{K=2} = \frac{\eta_1 + \eta_2}{2\gamma_0 (M-2) \eta_1 \eta_2 (1 - |\rho|^2)}. \quad (23)$$

As can be seen from (23) the MSE performance degrades with increasing correlation and/or power imbalance and that the effects of correlation and power imbalance are separable (independent). Note that the two-user case is assumed in (22) and (23) in order to illustrate the effects of correlation and power imbalance explicitly, whereas (21) holds for any  $K$  ( $< M$ ).

## 4. Simulation

Throughout the section, we make the following assumptions. There are 512 subcarriers including 32 scattered pilots. The remaining active subcarriers are loaded with QAM symbols. The multipath fading channel is a 4-tap Rayleigh fading channel, where the taps are at the 0, 20, 30, and 60th time samples with equal average tap gain of 1/4, and that the channel stays constant within 40 OFDM symbols after which an independent channel realization is drawn (i.e., block fading channel). In total, 100 channel realizations are generated. (The analysis in the previous section holds for Rayleigh fading channel with arbitrary number of channel taps; the 4-tap Rayleigh fading channel is used here as an example.) The CP length is set to 64. The PNs from different users are independent yet follow the same (Wiener process) distribution with the same 3 dB PN bandwidth  $\beta$ . Without further specification, we assume  $T_s = 10$  ns, corresponding to a bandwidth of 100 MHz, which can be realized using carrier aggregation in the current long-term evolution advanced (LTE-A) system and is decided as a typical bandwidth for 5G communications according to the 3GPP standardization [5]. For simplicity and in order to focus on the effects of PN, power imbalance, and correlation, we assume the channel has

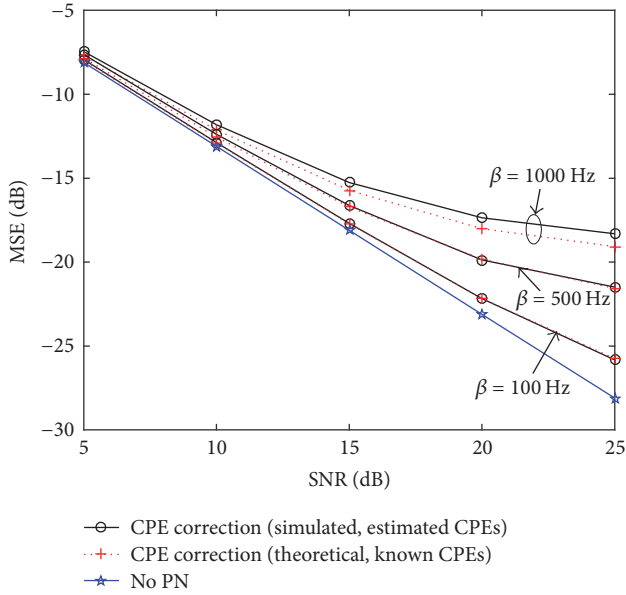


FIGURE 2: MSE performance of MU-MIMO-OFDM ( $K = 2$ ,  $M = 4$ ) with different 3 dB PN bandwidths in spatially white and power-balanced MIMO channels.

been perfectly estimated in the preamble. The 32 scatter pilots are used for CPE estimation in the payload using (5).

Figure 2 shows the MSE performance of the MU-MIMO-OFDM system with two users and four BS antennas in spatially white and power-balanced MIMO channels. As a reference, the ideal case (no PN) is also plotted in the same figure. As can be seen, with modest PN ( $\beta \leq 500$  Hz), the simulated MSE with CPE correction agrees well with that of the theoretical one (21). This implies that the CPE correction (cf. Section 2) can eliminate the CPEs of the multiple PNs. Note that as  $\beta$  increases, the joint CPE estimation (5) becomes less accurate. As a result, it is also shown that the MSE performance with CPE correction is slightly worse than its theoretical counterpart as  $\beta$  increases up to 1000 Hz.

Figure 3 shows the MSE performance of the MU-MIMO-OFDM system in spatially white and power-balanced MIMO channels as a function of subcarrier spacing  $1/(NT_s)$ . Since the ICI effect reduces with increasing subcarrier spacing, the MSE performance improves with increasing subcarrier spacing. At 5 dB SNR, the noises have more profound effect than the PNs do, whereas the PNs dominates at 25 dB SNR. Therefore, the improvement of the MSE performance (due to the increase of the subcarrier spacing) is more prominent at high SNR. Note that the channel length is assumed to be 61 time samples, whose absolute value (in seconds) decreases with increasing subcarrier spacing. For a fixed channel length (independent of the subcarrier spacing), it may not be a good idea to increase the subcarrier spacing unlimitedly in that a larger subcarrier spacing may necessitate a longer CP length (increased overhead) and multitap channel equalization (increased complexity).

Figure 4 shows the MSE performance of the PN corrupted MU-MIMO-OFDM system (with four users) in spatially white and power-balanced MIMO channels as a function of

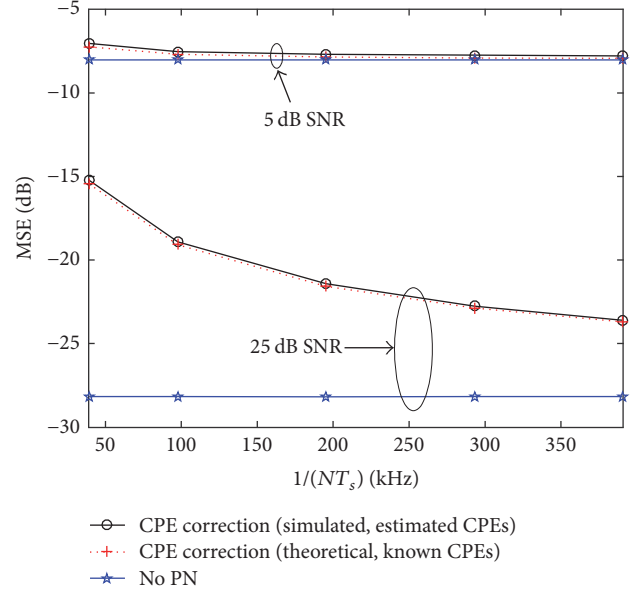


FIGURE 3: MSE performance of MU-MIMO-OFDM ( $K = 4$ ,  $M = 4$ ,  $\beta = 500$  Hz) as a function of subcarrier spacing  $1/(NT_s)$  under different SNRs in spatially white and power-balanced MIMO channels.

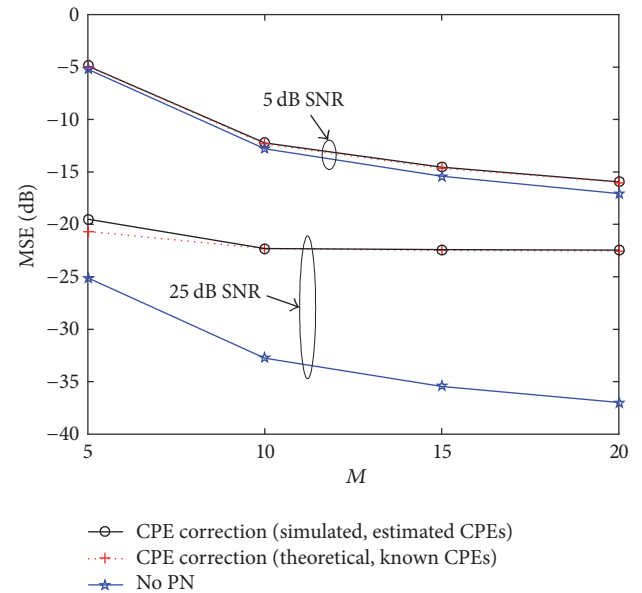


FIGURE 4: MSE performance of MU-MIMO-OFDM ( $K = 4$ ,  $\beta = 500$  Hz) as a function of  $M$  under different SNRs in spatially white and power-balanced MIMO channels.

number of BS antennas (under different SNRs). The 3 dB PN bandwidth is set to 500 Hz. As references, the MSEs of the corresponding ideal cases (no PN) are also plotted in the same figure. As can be seen, the MSE performance improves as the number of BS antennas increases at low (5 dB) SNR. At high (25 dB) SNR, however, the MSE performance improvement becomes insignificant beyond ten BS antennas. This is because that, given  $K$ , the diversity gain of the ZF

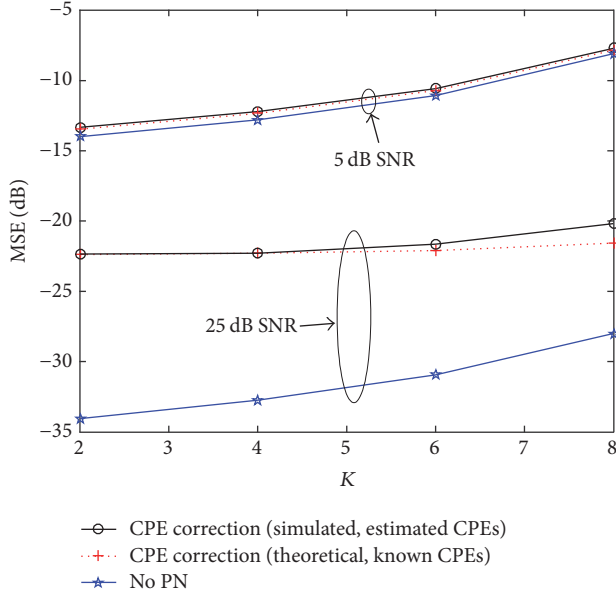


FIGURE 5: MSE performance of MU-MIMO-OFDM ( $M = 10$ ,  $\beta = 500$  Hz) as a function of  $K$  under different SNRs in spatially white and power-balanced MIMO channels.

decoder increases with increasing  $M$ ; and the increasing diversity gain is more effective at low SNR.

Figure 5 shows the MSE performance of the PN corrupted MU-MIMO-OFDM system (with ten BS antennas) in spatially white and power-balanced MIMO channels as a function of number of users (under different SNRs). The 3 dB PN bandwidth is set to 500 Hz. As references, the MSE of the corresponding ideal cases (no PN) are also plotted in the same figure. As can be seen, the MSE performance degrades as the number of users increases (for a given number of BS antennas). This is because that, given  $M$ , the diversity gain of the ZF decoder decreases with increasing  $K$ . Analogous to the results in Figure 4, the MSE dependence on the number of users is more obvious at low SNR than that at high SNR. Note that as the number of BS antennas ( $M$ ) decreases or as the number of users ( $K$ ) increases, the joint CPE estimation becomes less accurate, resulting in small discrepancies between the simulated and theoretical results in Figures 4 and 5.

To further illustrate the multiuser PN effects, we plot the MSE performances of MU-MIMO-OFDM systems with four BS antennas and two and three users, respectively, in Figure 6. The 3 dB PN bandwidth is set to 100 Hz. As references, the MSEs of the corresponding ideal cases (no PN) are also plotted in the same figure. Given  $M$ , increasing  $K$  decreases the degree of freedom at the BS and, therefore, degrades the MSE performance of the MU-MIMO-OFDM system. As can be seen from Figure 6, the MSE with the three users is higher than that with two users and that the theoretical results agree reasonably well with the simulated ones over the whole SNR range.

The above simulation results are for spatially white and power-balanced MIMO channels. The MSE performance of

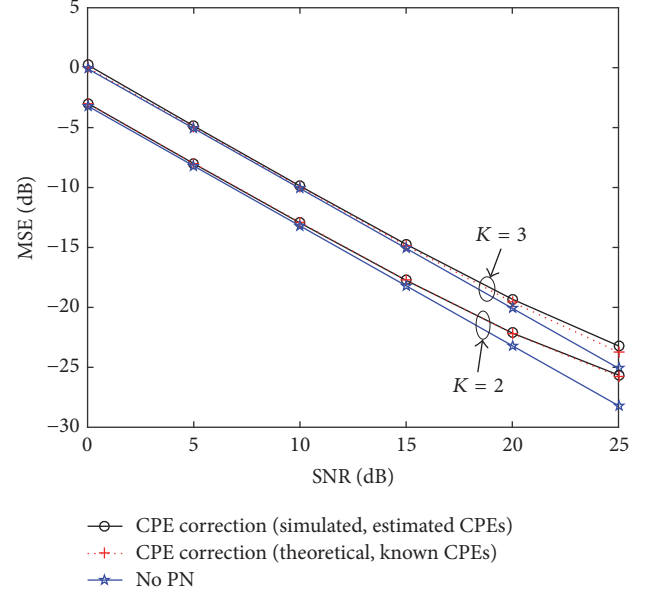


FIGURE 6: MSE performance of MU-MIMO-OFDM ( $M = 4$ ,  $\beta = 100$  Hz) in spatially white and power-balanced MIMO channels.

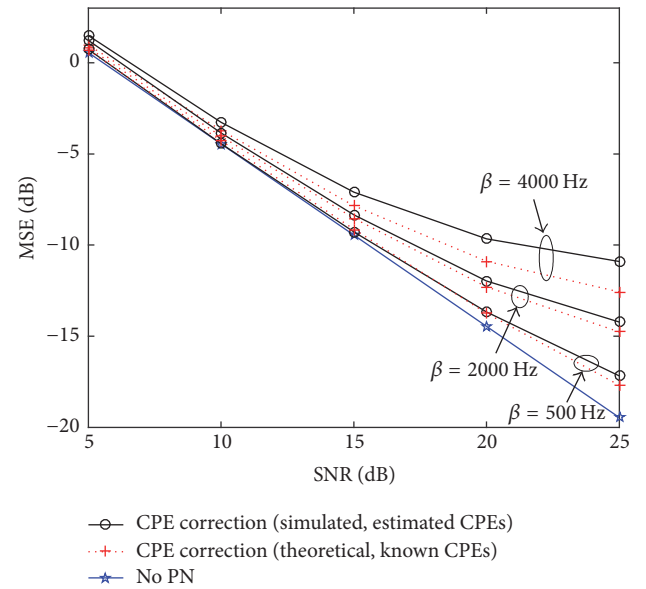


FIGURE 7: MSE performance of MU-MIMO-OFDM ( $K = 2$ ,  $M = 4$ ) with different 3 dB PN bandwidths in the presence of 0.5 correlation and 10 dB power imbalance.

the MU-MIMO-OFDM system with two users and four BS antennas in the presence of 0.5 correlation and 10 dB power imbalance is shown in Figure 7. Comparing Figures 2 and 7, it can be seen that the power imbalance and the correlation significantly degrade the MSE performance of the MU-MIMO-OFDM system. Similar to Figure 2, as  $\beta$  increases, the joint CPE estimation (5) becomes less accurate, and the difference between the simulated and theoretical MSE increases.

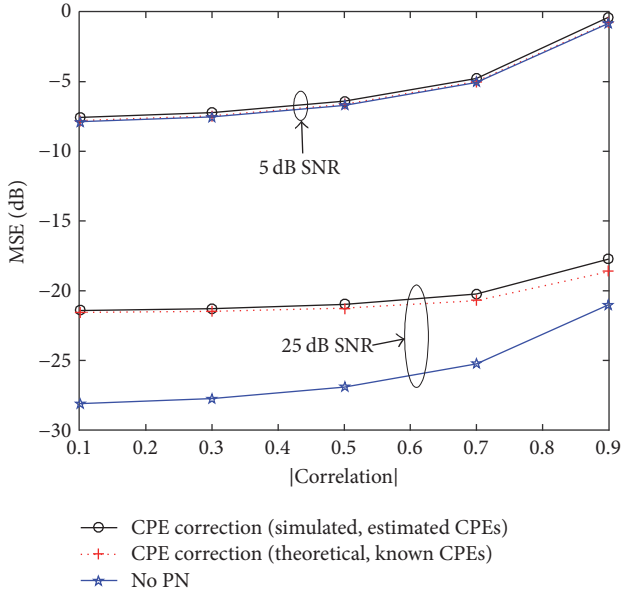


FIGURE 8: MSE performance of MU-MIMO-OFDM ( $K = 2$ ,  $M = 4$ ,  $\beta = 500$  Hz) as a function of user correlation in power-balanced MIMO channels.

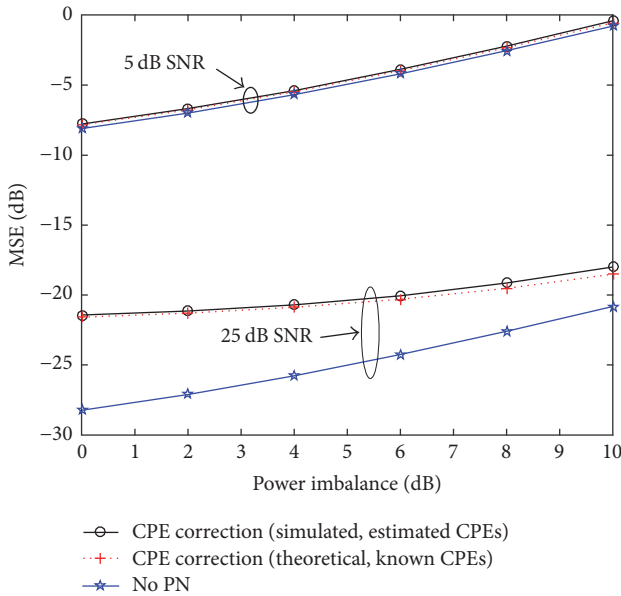


FIGURE 9: MSE performance of MU-MIMO-OFDM ( $K = 2$ ,  $M = 4$ ,  $\beta = 500$  Hz) as a function of power imbalance in spatially white MIMO channels.

It is shown from (22) that the effects of correlation and power imbalance are separable. Thus, we show their effects on the MU-MIMO-OFDM system with two users and four BS antennas in Figures 8 and 9, respectively. As can be seen, the MSE performance degrades with increasing correlation and/or power imbalance and that the theoretical MSE expression (21) can well predict the simulated MSE. The small discrepancy at high correlation (power imbalance) is

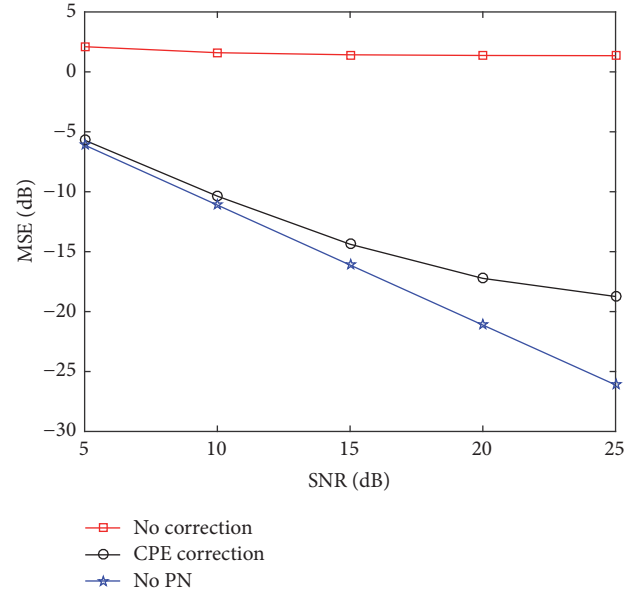


FIGURE 10: MSE performance of MU-MIMO-OFDM ( $K = 2$ ,  $M = 4$ ,  $\beta = 500$  Hz) with PNs at both users and the BS in the presence of 0.3 correlation and 3 dB power imbalance.

due to the fact that the estimated CPEs become less accurate at high correlation (power imbalance) values.

So far, we have been focusing on the effect of multiuser PNs, while omitting the PN at the BS. As shown in Section 2, the CPE of the PN at the BS can be corrected together with the multiuser CPEs using the CPE correction method. Figure 10 shows the MSE performance of the MU-MIMO-OFDM system with two users and four BS antennas in the presence of 0.3 correlation and 3 dB power imbalance, and PNs (with  $\beta = 500$  Hz) at users and the BS. As can be seen, the PNs of the users and the BS can be greatly mitigated by using the CPE correction method.

## 5. Conclusions

In this work, we studied the phase noise (PN) effect on the uplink multiuser MIMO-OFDM system. It was assumed that each user is equipped with a single antenna along with a free-running oscillator, whereas the base station (BS) has multiple antennas and use zero-forcing for multiuser detection. An analytical mean square error (MSE) expression was derived for the case where the common phase errors (CPEs) can be perfectly estimated. The analytical MSE expression can take into account of correlations and power imbalances between different users. It was shown that the MSE performance improves with increasing number of BS antennas ( $M$ ) yet degrades with increasing power imbalance, correlation, number of users ( $K$ ), and/or 3 dB PN bandwidth and that the MSE dependence on  $M$  or  $K$  is more obvious at low SNR. In the special case of two users, the correlation and power imbalance effects are separable (independent) and can be shown explicitly in the analytical MSE expression. The analytical results were verified by simulations.

## Conflicts of Interest

The authors declare that they have no conflicts of interest.

## Acknowledgments

The research leading to these results received funding from the European Commission H2020 Programme under Grant Agreement no. 671650 (5G PPP mmMAGIC project).

## References

- [1] J. A. C. Bingham, "Multicarrier modulation for data transmission: an idea whose time has come," *IEEE Communications Magazine*, vol. 28, no. 5, pp. 5–14, 1990.
- [2] R. He, B. Ai, G. L. Stüber, G. Wang, and Z. Zhong, "Geometrical based modeling for millimeter wave MIMO mobile-to-mobile channels," *IEEE Trans. Veh. Technol.*, vol. 67, 2018.
- [3] K. Guan, B. Ai, A. Fricke et al., "Excess Propagation Loss of Semi-Closed Obstacles for Inter/Intra-Device Communications in the Millimeter-Wave Range," *Journal of Infrared, Millimeter, and Terahertz Waves*, vol. 37, no. 7, pp. 676–690, 2016.
- [4] R. He, Q. Li, B. Ai et al., "A Kernel-power-density based algorithm for channel multipath components clustering," *IEEE Trans. Wireless Commun.*, vol. 16, no. 11, pp. 7138–7151, 2017.
- [5] <http://www.3gpp.org/>.
- [6] G. J. Foschini, "Layered space-time architecture for wireless communication in a fading environment when using multi-element antennas," *Bell Labs Technical Journal*, vol. 1, no. 2, pp. 41–59, 1996.
- [7] W. Fan, I. Carton, P. Kyosti et al., "A Step Toward 5G in 2020: Low-cost OTA performance evaluation of massive MIMO base stations," *IEEE Antennas and Propagation Magazine*, vol. 59, no. 1, pp. 38–47, 2017.
- [8] B. Ai, K. Guan, R. He et al., "On Indoor Millimeter Wave Massive MIMO Channels: Measurement and Simulation," *IEEE J. Sel. Areas Commun.*, vol. 35, no. 7, pp. 1678–1690, 2017.
- [9] M. Barazzetta, D. Micheli, L. Bastianelli et al., "A Comparison between Different Reception Diversity Schemes of a 4G-LTE Base Station in Reverberation Chamber: A Deployment in a Live Cellular Network," *IEEE Transactions on Electromagnetic Compatibility*, vol. 59, no. 6, pp. 2029–2037, 2017.
- [10] R. Recanatini, F. Moglie, and V. M. Primiani, "Performance and immunity evaluation of complete wlan systems in a large reverberation chamber," *IEEE Transactions on Electromagnetic Compatibility*, vol. 55, no. 5, pp. 806–815, 2013.
- [11] T. C. W. Schenk, X.-J. Tao, P. F. M. Smulders, and E. R. Fledderus, "On the influence of phase noise induced ICI in MIMO OFDM systems," *IEEE Communications Letters*, vol. 9, no. 8, pp. 682–684, 2005.
- [12] J. Li and W. Wu, "Performance of MIMO-OFDM Systems with Phase Noise at Transmit and Receive Antennas," in *Proceedings of the 2011 7th International Conference on Wireless Communications, Networking and Mobile Computing (WiCOM)*, pp. 1–4, Wuhan, China, September 2011.
- [13] S. Bittner, E. Zimmermann, and G. Fettweis, "Exploiting phase noise properties in the design of MIMO-OFDM receivers," in *Proceedings of the IEEE Wireless Communications and Networking Conference, WCNC 2008*, pp. 940–945, USA, April 2008.
- [14] R. Corvaja and A. G. Armada, "SINR degradation in MIMO-OFDM systems with channel estimation errors and partial phase noise compensation," *IEEE Transactions on Communications*, vol. 58, no. 8, pp. 2199–2203, 2010.
- [15] R. Hamila, Ö. Özdemir, and N. Al-Dhahir, "Beamforming OFDM Performance Under Joint Phase Noise and I/Q Imbalance," *IEEE Transactions on Vehicular Technology*, vol. 65, no. 5, pp. 2978–2989, 2016.
- [16] O. H. Salim, W. Xiang, and A. A. Nasir, "Joint data detection and phase noise mitigation for light field video transmission in MIMO-OFDM systems," <https://arxiv.org/abs/1602.02834>.
- [17] X. Chen, H. Wang, W. Fan et al., "Phase Noise Effect on MIMO-OFDM Systems with Common and Independent Oscillators," *Wireless Communications and Mobile Computing*, vol. 2017, pp. 1–12, 2017.
- [18] P. Xu, Y. Xiao, S. Zhou, and M. Zhao, "ICI analysis of MIMO-OFDM systems with independent phase noise at both transmit and receive antennas," in *Proceedings of the 5th International Conference on Wireless Communications, Networking and Mobile Computing (WiCOM '09)*, Beijing, China, September 2009.
- [19] R. Krishnan, M. R. Khanzadi, N. Krishnan et al., "On the impact of oscillator phase noise on the uplink performance in a massive MIMO-OFDM system," <https://arxiv.org/abs/1405.0669>.
- [20] S. Wu and Y. Bar-Ness, "Multiple phase noise correction for OFDM/SDMA," in *Proceedings of the GLOBECOM '03. IEEE Global Telecommunications Conference*, pp. 1311–1315, San Francisco, CA, USA.
- [21] A. Pitarokoilis, E. Björnson, and E. G. Larsson, "Performance of the Massive MIMO Uplink with OFDM and Phase Noise," *IEEE Communications Letters*, vol. 20, no. 8, pp. 1595–1598, 2016.
- [22] A. Puglielli, G. Laccaille, A. M. Niknejad, G. Wright, B. Nikolic, and E. Alon, "Phase noise scaling and tracking in OFDM multi-user beamforming arrays," in *Proceedings of the 2016 IEEE International Conference on Communications (ICC '16)*, 6, 1 pages, Kuala Lumpur, Malaysia, May 2016.
- [23] X. Chen, "OFDM Based Multi-Node Transmission in the Presence of Phase Noises for Small Cell Backhaul," *IEEE Communications Letters*, vol. 21, no. 5, pp. 1207–1210, 2017.
- [24] W. Xu, S. A. Zekavat, and H. Tong, "A novel spatially correlated multiuser MIMO channel modeling: Impact of surface roughness," *IEEE Transactions on Antennas and Propagation*, vol. 57, no. 8, pp. 2429–2438, 2009.
- [25] A. Adhikary, E. Al Safadi, M. K. Samimi et al., "Joint spatial division and multiplexing for mm-Wave channels," *IEEE Journal on Selected Areas in Communications*, vol. 32, no. 6, pp. 1239–1255, 2014.
- [26] X. Gao, O. Edfors, F. Rusek, and F. Tufvesson, "Linear precoding performance in measured very-large MIMO channels," in *Proceedings of the IEEE Vehicular Technology Conference (VTC Fall '11)*, pp. 1–5, IEEE, San Francisco, Calif, USA, September 2011.
- [27] X. Chen, S. Zhang, and A. Zhang, "On MIMO-UFMC in the Presence of Phase Noise and Antenna Mutual Coupling," *Radio Science*, vol. 52, no. 11, pp. 1386–1394, 2017.
- [28] X. Chen and S. Zhang, "Multiplexing efficiency for MIMO antenna-channel impairment characterisation in realistic multipath environments," *IET Microwaves, Antennas & Propagation*, vol. 11, no. 4, pp. 524–528, 2017.
- [29] P. Graczyk, G. Letac, and H. Massam, "The complex Wishart distribution and the symmetric group," *The Annals of Statistics*, vol. 31, no. 1, pp. 287–309, 2003.

## Research Article

# Impact of Probe Configurations on Maximum of Test Volume Size in 3D MIMO OTA Testing

**Weimin Wang, Huaqiang Gao, Yongle Wu, and Yuanan Liu**

*The Beijing Key Laboratory of Work Safety Intelligent Monitoring, School of Electronic Engineering, Beijing University of Posts and Telecommunications, Beijing 100876, China*

Correspondence should be addressed to Yongle Wu; wuyongle138@gmail.com

Received 16 October 2017; Accepted 5 December 2017; Published 26 December 2017

Academic Editor: Lei Ge

Copyright © 2017 Weimin Wang et al. This is an open access article distributed under the Creative Commons Attribution License, which permits unrestricted use, distribution, and reproduction in any medium, provided the original work is properly cited.

With the development of multiple-input-multiple-output (MIMO) technology, the over-the-air (OTA) testing of MIMO capable devices with different sizes needs to be conducted for performance evaluation. The device under test (DUT) should be within a tridimensional test volume created by multiprobe configurations. Thus, determining the maximum size of test volume could be vital to test the DUT of different size and larger test volumes should be adopted to evaluate larger DUTs. All types of probe configurations including the fixed and the flexible probe configurations are investigated in this paper to address this issue. The maximum of test volume size (MTVS) is determined within the given error threshold of spatial correlation for a given probe configuration. Simultaneously, the impact of different probe configurations on MTVS is studied in order to obtain larger MTVSs. Simulation results show that larger MTVSs can be obtained by utilizing the optimal probe configuration with any given 3D channel model for 3D MIMO OTA testing.

## 1. Introduction

Multiple-input-multiple-output (MIMO), an important technology of high-speed wireless communication, has been adopted in Long Term Evolution (LTE) and LTE-Advanced [1]. Massive MIMO systems employing a large number of antennas are used in radio base stations (BSs). As a multiuser MIMO technology, it would be applied to the fifth-generation (5G) mobile communication system in the future [2]. MIMO capable devices include user equipment (UE) assembled with several antennas and massive MIMO BS equipped with hundreds of antennas. In order to evaluate the performance of MIMO capable devices, they need to be tested under realistic channel propagation environment in the laboratory. MIMO over-the-air (OTA) testing [3] has been considered as a promising method for evaluation of the performance of MIMO capable devices by 3GPP, CTIA, and COST. Among the several MIMO OTA testing methods, the MIMO OTA testing method based on multiprobe anechoic chamber (MPAC) becomes one of the most competitive methods for its ability to reproduce the multipath wireless channel environment and obtain higher emulation precision [4].

Three main modules are involved in the MPAC method, namely, BS emulator or UE emulator (BS emulator adopted for UE testing and UE emulator adopted for massive BS testing), channel emulator, and anechoic chamber. The anechoic chamber is mainly composed of multiprobe setup, absorbers and device under test (DUT). The multiprobe setup is distributed with multiple probes, each of which includes two polarized antennas (i.e., vertical polarization and horizontal polarization); the absorbers could attenuate the electromagnetic waves projected on their surface greatly and eliminate the reflected electromagnetic waves; the DUT is placed in the center of the anechoic chamber with the multiprobe setup. An ideal realistic communication environment for the DUT could be created by the multiprobe setup and absorbers. The MPAC method could provide a tridimensional test volume around the DUT where the performance test of DUT can be imitated in the realistic channel environment. Note that the DUT size is less than the test volume.

The MPAC method includes two different dimensions of condition due to the different channel models, namely, two-dimensional (2D) and three-dimensional (3D). Most of the standard channel models are 2D channel models; that

is, only horizontal azimuth angles are defined without the extension of vertical elevation angles. Some of the literatures adopted the 2D MPAC method to emulate a 2D standard channel model in a 2D multiprobe setup [5–7], in which eight probes are placed horizontally on a probe ring. However, the assumption of a 2D channel model is not sufficient to reproduce the realistic channel environment because the elevation angle cannot be neglected in the propagation environment. Hence, an accurate realistic channel propagation environment should be reproduced when an elevation extension is introduced. Reference [8] extends the 2D MPAC method to the 3D MPAC method, in which the multiprobe setup is 3D and the probes are distributed on a sphere. These probes compose several probe planes of different elevations where the probes are placed evenly in a circle on each plane, that is, probe circle. Taking sixteen probes as an example, there are three probe circles including the upper, middle, and lower one. Eight probes are on the middle probe circle, while four probes are on the upper one and the other on the lower one, respectively.

The channel environment in the test volume is mostly generated by geometry-based stochastic models (GBSM), which introduce the concept of clusters, each of which has a specific angle power spectrum. The prefaded signal synthesis (PFS) technique reproduces the channel spatial characteristics in the test volume as a channel emulation technique [9]. Meanwhile, it generates a prefaded signal in each probe of the multiprobe setup based on the angular power spectrum of the cluster. The prefaded signals that could synthesize the target channel environment in the test volume are generated by assigning the corresponding power weights to the respective probes. References [10, 11] apply the PFS technique to the 3D MPAC method. The power spectrum of the cluster is extended from the original 2D power azimuth spectrum (PAS) to a 3D spherical power spectrum (SPS). Different 3D channel models have variable SPSs, and different SPSs produce altered 3D channel spatial characteristics. The spatial correlation is utilized frequently as a figure of merit (FoM) to evaluate the 3D channel spatial characteristics. Thus, the error between the target and emulated spatial correlation is employed to measure the reconstruction accuracy of the 3D channel emulation.

Several contributions have reported that 3D channel spatial characteristics are reconstructed in 3D multiprobe setups for the UE testing. Four different diameters of spherical test volume are compared to obtain the maximum diameter in [10]. However, the test volume is sampled on the three axes, which might lead to the bad reconstruction accuracy at certain locations. In other words, the maximum diameter is just considered for three directions and not exact for all directions. In [8], the test volume is sampled by selecting locations on the surface of the ellipsoid, but the size of test volume is fixed to a certain value, without considering how to determine the maximum size of test volume within given accepted correlation error. If the maximum of test volume size (MTVS) for DUT can be determined in spherical multiprobe setups, the MIMO terminals of different size can be evaluated in the anechoic chamber. A few works have also reported the OTA evaluation of massive MIMO BSs where a sectorized

MPAC configuration is proposed [12]. Compared with the UE, the electrical size of the massive MIMO BS is much larger. Hence, larger test volumes are needed to evaluate larger MIMO capable devices. Importantly, the test volume size depends directly on the number of probe antennas and is limited owing to the limited number of probe antennas and output ports of the radio channel emulator [13]. Thus, it becomes significant to increase the test volume size with a limited number of probe antennas. So as to increase MTVS, it would be a desirable solution to assess the impact of different probe configurations on MTVS. However, few contributions have addressed this issue.

In this paper, a novel method is presented to obtain MTVS. The MTVS for DUT is determined in spherical multiprobe setups. The test volume is sampled on the surface of a sphere. Meanwhile, this paper investigates the impact of probe configurations on MTVS to obtain larger MTVSs. The probe configurations include the fixed probe configuration and the flexible probe configurations. The fixed probe configuration means that there are several probe circles in the probe setup, each of which is with probes placed uniformly. The flexible probe configuration stands for that the probes of the setup are distributed arbitrarily for both elevation angles and azimuth angles. The fixed probe configuration is adopted to consider the effect of azimuth and elevation angles independently. The flexible probe configuration is employed to study the effect of both azimuth and elevation angles simultaneously. Moreover, the effect of number of probes is discussed in the flexible configuration as well.

The aim of this paper is multifold:

- (1) The MTVS can be determined by calculated results of spatial correlation error directly and effectively without complicated system validation and electromagnetic calculation [14]. The maximum of DUT size can be achieved for a given probe configuration.
- (2) Different probe configurations including the fixed and the flexible probe configurations are assessed for MTVS. The azimuth and elevation angles are varied independently for the fixed probe configuration, while the azimuth and elevation angles are changed simultaneously for the flexible probe configuration. In the flexible probe configuration, two kinds of optimization algorithms are combined to acquire the optimal probe configuration for larger MTVSs than those in the fixed probe configuration.
- (3) The proposed method that could determine and increase the MTVS provides a general framework to decide MTVS for any channel model and probe configuration. Simultaneously, larger MTVSs for any channel model can be obtained with the optimal probe configuration.

## 2. Method

*2.1. 3D Spherical Power Spectrum.* The 3D spherical power spectrum (SPS) could be modeled as a function of both elevation angle ( $\theta$ ) and azimuth angle ( $\phi$ ). It consists of power

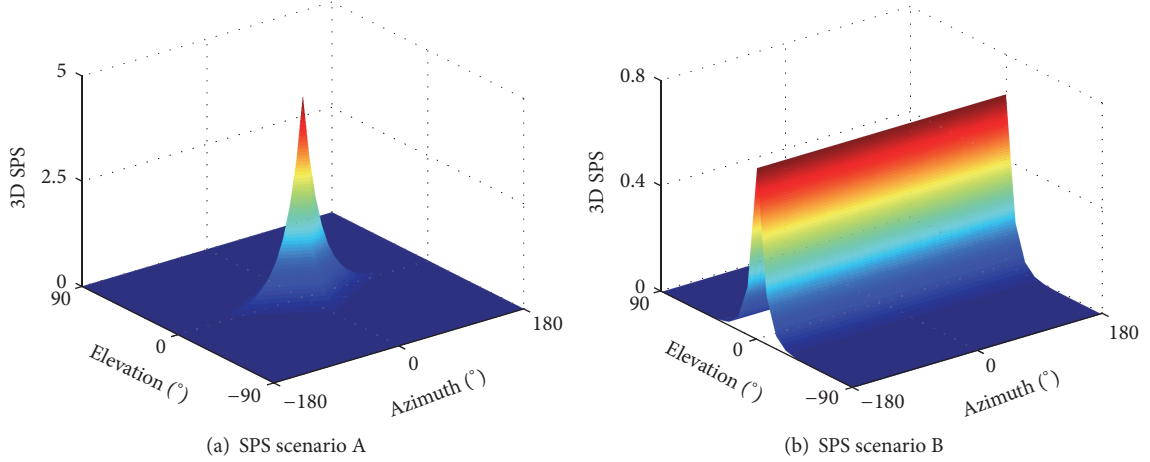


FIGURE 1: Two considered SPS scenarios.

elevation spectrum (PES) and power azimuth spectrum (PAS) [15]:

$$\text{SPS}(\Omega) = \text{SPS}(\theta, \phi) = \text{PES}(\theta) \text{PAS}(\phi). \quad (1)$$

where  $\Omega$  is the solid angle. The PES and PAS are functions of  $\theta$  and  $\phi$ , respectively. Moreover, the SPS satisfies the condition of  $\oint \text{SPS}(\Omega) d\Omega = 1$ .

The PAS represents the power distribution of different incoming waves in the horizontal azimuth, and PES denotes the power distribution of the different incoming waves at the vertical height. The PAS is characterized by azimuth of arrival (AoA) and azimuth spread (AS), while the PES is characterized by elevation of arrival (EoA) and elevation spread (ES). AoA and EoA are the mean values of the angles of the different incoming waves in the horizontal azimuth and at the vertical height, respectively, and AS and ES represent the standard deviations of the angles of the different incoming waves in the horizontal azimuth and at the vertical height, respectively.

Two target SPS scenarios (A and B) are considered in this paper.

### 2.1.1. SPS Scenario A: SPS of Laplacian Distribution for Both PES and PAS

$$\begin{aligned} \text{PES}(\theta) &= Q_\theta \exp\left(-\frac{\sqrt{2}|\theta - \bar{\theta}|}{\sigma_\theta}\right), \quad \left[-\frac{\pi}{2}, \frac{\pi}{2}\right] \\ \text{PAS}(\phi) &= Q_\phi \exp\left(-\frac{\sqrt{2}|\phi - \bar{\phi}|}{\sigma_\phi}\right), \quad [-\pi, \pi]. \end{aligned} \quad (2)$$

### 2.1.2. SPS Scenario B: SPS of Laplacian Distribution for PES and Uniform Distribution for PAS

$$\begin{aligned} \text{PES}(\theta) &= Q_\theta \exp\left(-\frac{\sqrt{2}|\theta - \bar{\theta}|}{\sigma_\theta}\right), \quad \left[-\frac{\pi}{2}, \frac{\pi}{2}\right] \\ \text{PAS}(\phi) &= \frac{1}{2\pi}, \quad [-\pi, \pi], \end{aligned} \quad (3)$$

where  $\bar{\theta}$  and  $\bar{\phi}$  are the mean elevation and azimuth angles of arrival of incoming waves, respectively.  $\sigma_\theta$  and  $\sigma_\phi$  are the elevation and azimuth angular spreads, respectively.  $Q_\theta$  and  $Q_\phi$  are scaling constants for PES and PAS, respectively, ensuring that  $\oint \text{SPS}(\Omega) d\Omega = 1$  is fulfilled. In this paper, it is assumed that mean elevation angle is  $0^\circ$  ( $\bar{\theta} = 0^\circ$ ) and mean azimuth angle is  $0^\circ$  as well ( $\bar{\phi} = 0^\circ$ ), while elevation spread (ES) is  $10^\circ$  ( $\sigma_\theta = 10^\circ$ ), and azimuth spread is  $35^\circ$  ( $\sigma_\phi = 35^\circ$ ). The two considered SPS scenarios are illustrated in Figures 1(a) and 1(b).

**2.2. Criteria to Evaluate MTVS.** The spatial correlation error is adopted as a FoM to evaluate the test volume size of 3D MIMO OTA setups in this paper. The spatial correlation at DUT antenna elements  $u$  and  $v$  can be expressed as follows [16]:

$$\begin{aligned} \rho_a &= \frac{\oint \mathbf{F}_u(\Omega) \mathbf{F}_v^*(\Omega) \text{SPS}(\Omega) d\Omega}{\sqrt{\oint |\mathbf{F}_u(\Omega)|^2 \text{SPS}(\Omega) d\Omega} \sqrt{\oint |\mathbf{F}_v(\Omega)|^2 \text{SPS}(\Omega) d\Omega}}, \end{aligned} \quad (4)$$

where  $()^*$  denotes complex conjugate operation and  $\mathbf{F}_u(\Omega)$  and  $\mathbf{F}_v(\Omega)$  are the complex radiation patterns of DUT antennas  $u$  and  $v$ , respectively, with a common phase center.

Considering the OTA probes are in the far field with respect to the test volume and DUT antenna pattern is isotropic, (4) can be rewritten as [8]

$$\begin{aligned} \rho_{3D}(d, m) &= \oint \exp\left(jk(\vec{r}_{u,m} - \vec{r}_{v,m}) \cdot \vec{\Omega}\right) \text{SPS}(\Omega) d\Omega, \end{aligned} \quad (5)$$

where  $\vec{r}_{u,m}$  and  $\vec{r}_{v,m}$  are two sample points at the opposite position of the surface of the fixed spherical test volume in the anechoic chamber, which are defined as the  $m$ th location pair. The length of  $\vec{r}_{u,m} - \vec{r}_{v,m}$  represents the DUT antenna separation  $d$ , that is, the diameter of spherical test volume.  $\vec{\Omega}$

is a 3D unit vector denoting the solid angle  $\Omega$ .  $k$  is the wave number. Note that the diameter  $d$  of spherical test volume represents the test volume size. Therefore, the target spatial correlation  $\rho_{3D}(d, m)$  is the function of the test volume size  $d$  for the  $m$ th location pair.

In 3D multiprobe OTA setups with a limited number of antennas  $N$ , the emulated spatial correlation could be calculated:

$$\rho_{OTA}(\mathbf{w}, d, m) = \sum_{n=1}^N w_n \exp\left(jk(\vec{r}_{u,m} - \vec{r}_{v,m}) \cdot \vec{\Phi}_n\right), \quad (6)$$

where  $\mathbf{w} = [w_1, \dots, w_n, \dots, w_N]^T$  is a power weighting vector to be optimized.  $\vec{\Phi}_n$  is a 3D unit position vector of the  $n$ th probe. The total number of probes is defined as  $N$ . Once the power weighting vector  $\mathbf{w}$  is determined, the emulated spatial correlation  $\rho_{OTA}(d, m)$  is only the function of the test volume size  $d$  for the  $m$ th location pair.

The spatial correlation error ( $|\rho_{3D}(d, m) - \rho_{OTA}(d, m)|$ ) is obtained from the absolute value of the difference between target spatial correlation  $\rho_{3D}(d, m)$  and emulated spatial correlation  $\rho_{OTA}(d, m)$  for the  $m$ th location pair. Hence, the MTVS could be determined according to the root mean square (rms) of the spatial correlation error  $|\rho_{3D}(d) - \rho_{OTA}(d)|$ . For  $M$  location pairs, the rms error  $\sigma_{rms}(d)$  that is a function of the test volume size  $d$  can be expressed as follows:

$$\sigma_{rms}(d) = \sqrt{\frac{1}{M} \sum_{m=1}^M |\rho_{3D}(d, m) - \rho_{OTA}(d, m)|^2}. \quad (7)$$

The threshold of 0.05 [10] is given for  $\sigma_{rms}(d)$  to determine the MTVS. Therefore, MTVS can be obtained within a maximum rms error of 0.05. It should be mentioned that the MTVS is recommended for MIMO OTA testing in the multiprobe anechoic chamber.

**2.3. Optimal OTA Antenna Power Weights.** The power weighting vector  $\mathbf{w}$  in (6) could be determined by convex optimization [17]. The objective function  $f_O(d)$  of convex optimization is described as

$$\begin{aligned} f_O(d) &= \min_{\mathbf{w}} \|\rho_{3D}(d) - \rho_{OTA}(\mathbf{w}, d)\|_2^2 \\ \text{s.t.} \quad &0 \leq w_i \leq 1 \quad (\forall i \in [1, N]), \quad \|\mathbf{w}\|_1 = 1, \end{aligned} \quad (8)$$

where  $\rho_{3D}(d)$  and  $\rho_{OTA}(\mathbf{w}, d)$  are the target spatial correlation and emulated spatial correlation vectors, respectively, with each element corresponding to the spatial correlation between two isotropic antennas at a certain location pair inside the fixed test volume.

**2.4. Probe Location Optimization.** Combined with the aforementioned convex optimization, what is called probe location optimization algorithm (PLOA) is adopted to obtain the optimal probe location and probe weights in flexible probe configurations.

The convex optimization and genetic algorithm (GA) are used to obtain the minimal rms error of spatial correlation

in a fixed test volume [18]. In [18], the convex optimization is adopted to optimize power weights for each probe once the probe locations are selected in the iterative process of GA. The objective function of convex optimization in (8) is adopted as the fitness function of GA. Therefore, the minimal rms error of spatial correlation is not achieved until the maximum iterative number is reached. The method description in [18] is not detailed here. On the basis of [18], the different test volume sizes are considered in this paper. Differently, the objective in this paper is to minimize the sum of rms errors in different test volume sizes using convex optimization and PLOA. It is clear that different test volume sizes have different objective function values of convex optimization in (8). The sum of objective function values for different test volume sizes is employed as the fitness function  $f_F$  of PLOA as follows:

$$f_F = \sum_{l=1}^L f_O(d_l), \quad (9)$$

where  $\mathbf{d} = [d_1, \dots, d_l, \dots, d_L]$  with  $d_l = d_{l-1} + d_{step}$  being a vector representing the different test volume sizes.  $L$  is the number of test volume sizes. In addition,  $d_{step}$  is the step of  $\mathbf{d}$ .

Three PLOAs are adopted for comparison in this paper, namely, the GA [19], the chicken swarm optimization (CSO) [20], and the improved chicken swarm optimization (ICSO) [21].

**2.4.1. GA.** GA is an optimization method for mimicking natural selection and genetic mechanism. It is based on Darwin's theory of biological evolution and Mendel's theory of genetics. Gene hybridization and gene mutations would produce offspring with strong environmental adaptability, and the genetic structure with high fitness is preserved by natural selection of the survival of the fittest. Therefore, GA is formed by imitating the biological genetic, evolutionary principle, and citing the principle of random statistics. Nevertheless, its ability to explore the new space is limited and it can converge to the local optimal solution easily. Moreover, the search speed is relatively slow so that more training time is needed to obtain the more accurate solution scheme. In addition, the programming implementation is quite complex, that is, coding the problem first and decoding the problem after finding the optimal solution. The algorithm description of GA is given in [19] and not detailed here briefly.

**2.4.2. CSO.** CSO is a novel bionic algorithm that fully inherits the characteristics of swarm intelligence optimization. Individual classification and cooperative optimization are utilized in this algorithm. Thus, the optimal solution maximally can be dug and prematureness can be avoided simultaneously. The CSO mimics the hierarchal order and the individual foraging behavior of the chicken swarm. According to the fitness value of the chicken swarm, it can be divided into several groups, each of which consists of one rooster and some hens and chicks. Each individual corrects its position to get a better feeding position according to its own laws of motion, so that its fitness value is as small as possible. Mimicking this chicken wisdom can be a good solution to practical optimization problems. The detailed algorithm description of CSO could be referred to in [20].

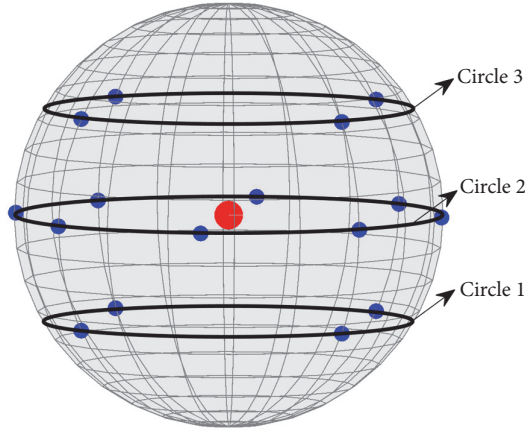


FIGURE 2: An original 3D probe setup with 16 probes. Red mark denotes the center of 3D sphere and blue marks denote the position of probes on the sphere.

2.4.3. *ICSO*. Considering that the original CSO is easy to fall into local optimum and premature convergence when solving high-dimensional optimization problem, the ICSO algorithm is presented in [21]. The algorithm adds the part of chicks learning from the rooster in chicks' own group to chick's position update equation and introduces the learning factor and inertia weight. Therefore, it is easier to find the global optimal value using ICSO for high-dimensional optimization problem. The algorithm description of ICSO could be found in [21].

### 3. Simulation Results

3.1. *Effect of Azimuth Angle of Probe on MTVS*. The effect of azimuth angle of probe on MTVS is assessed based on an original 3D probe setup with 16 probes, as shown in Figure 2. The setup has three elevation-separated circles of OTA probes, named circle 1, circle 2, and circle 3, respectively. In the setup, circle 1, circle 2, and circle 3 are composed of four, eight, and four probes, with elevation angle of  $-30^\circ$ ,  $0^\circ$ , and  $+30^\circ$ , respectively. The probes are placed evenly on three circles where circle 1 and circle 3 are symmetrical with regard to circle 2; that is, there are four probes having the same azimuth angle in three circles, respectively.

In the original setup with 16 probes, the rms error of spatial correlation is presented as a function of test volume size  $d$  for two SPS scenarios that can be seen from Figure 3. The rms monotonically increases within the rms interval of  $[0, 0.05]$ . There is only one value of  $d$  when fixing rms = 0.05, as marked in Figure 3. In addition, the MTVS can be obtained within the given maximum rms error of 0.05 for each SPS scenario, that is,  $0.75\lambda$  and  $0.95\lambda$  for SPS scenarios A and B, respectively. Compared with the MTVS for SPS scenario A, a larger MTVS can be obtained for SPS scenario B.

The effect of azimuth angle of probe on MTVS is assessed by rotating the probe circle horizontally. There are three setup cases of rotating the probe circle considered here. The azimuth angles of probe for each elevation circle for three

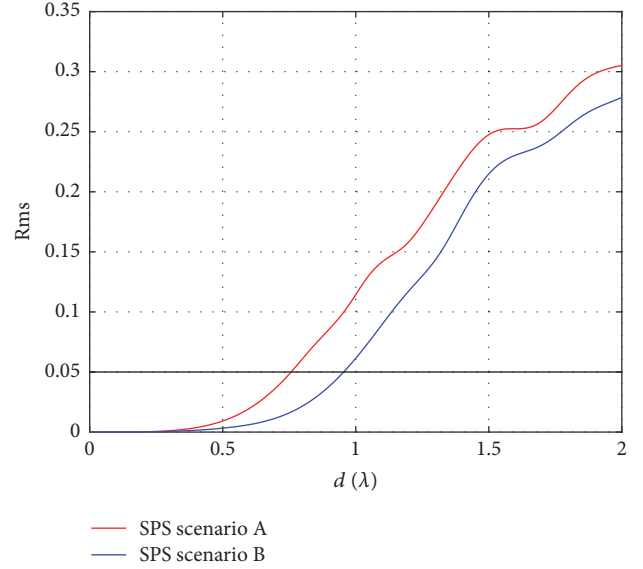


FIGURE 3: Rms error of spatial correlation with test volume size  $d$  for two SPS scenarios in the original setup.

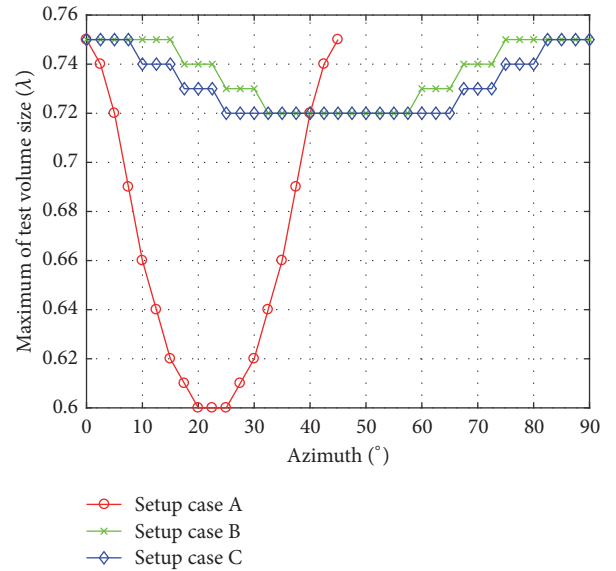


FIGURE 4: MTVS with different rotation angles for three setup cases (cases A, B, and C) employing the SPS scenario A.

setup cases are tabulated in Table 1. The variables  $x$ ,  $y$ ,  $z$  represent the rotation angle of probe circle.

Figure 4 displays the MTVS with different rotation angles for three setup cases employing the SPS scenario A. It can be found that the MTVS decreases with probe circle rotating from  $0^\circ$  to  $22.5^\circ$ , while the MTVS increases as increasing the rotation angle from  $22.5^\circ$  to  $45^\circ$  in setup case A. For both setup cases B and C, the curves are both symmetrical with regard to rotation angle  $45^\circ$ . Therefore, the largest MTVS of  $0.75\lambda$  is obtained without rotation (i.e., the original setup) for three setup cases employing the SPS scenario A.

TABLE 1: Azimuth angles of probe for each elevation circle for three setup cases.

Setup case	Probe azimuth angles		
	Circle 1	Circle 2	Circle 3
A	$-180^\circ + j \cdot 90^\circ$ , $j \in [1, \dots, 4]$	$-180^\circ + x + j \cdot 45^\circ$ , $j \in [1, \dots, 8]$ $x \in [0, \dots, 45]$	$-180^\circ + j \cdot 90^\circ$ , $j \in [1, \dots, 4]$
B	$-180^\circ + j \cdot 90^\circ$ , $j \in [1, \dots, 4]$	$-180^\circ + j \cdot 45^\circ$ , $j \in [1, \dots, 8]$	$-180^\circ + y + j \cdot 90^\circ$ , $j \in [1, \dots, 4]$ $y \in [0, \dots, 90]$
C	$-180^\circ - z + j \cdot 90^\circ$ , $j \in [1, \dots, 4]$ $z \in [0, \dots, 90]$	$-180^\circ + j \cdot 45^\circ$ , $j \in [1, \dots, 8]$	$-180^\circ + z + j \cdot 90^\circ$ , $j \in [1, \dots, 4]$ $z \in [0, \dots, 90]$

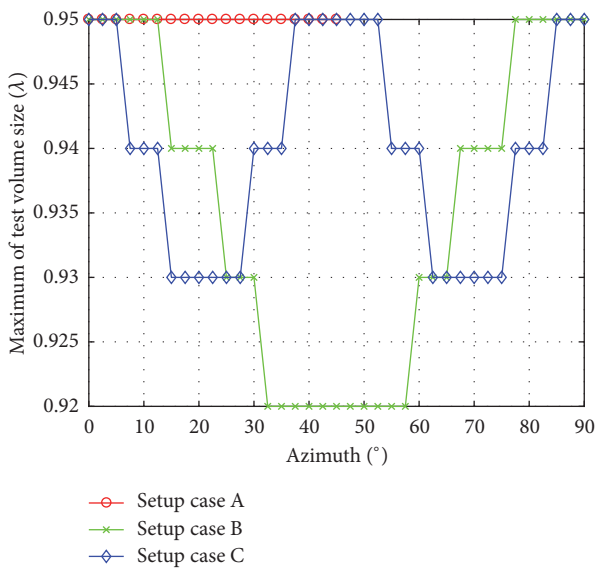


FIGURE 5: MTVS with different rotation angles for three setup cases (cases A, B, and C) employing the SPS scenario B.

The MTVS with variable rotation angle for three setup cases is illustrated in Figure 5 by adopting the SPS scenario B. For setup case A, the MTVS keeps constant with probe circle rotating from  $0^\circ$  to  $45^\circ$ . The curves are symmetrical with regard to rotation angle  $45^\circ$  for both setup case B and setup case C. However, the largest MTVS of  $0.95\lambda$  is obtained at rotation angle  $45^\circ$  besides  $0^\circ$  for setup case C, unlike setup case B.

For setup case C, circle 1 and circle 3 are symmetrical with regard to circle 2 at rotation angle  $45^\circ$  as well but the azimuth distribution of probes is changed compared with rotation angle  $0^\circ$ . Comparing two SPS scenarios for setup case C, the varied symmetrical setups with different azimuth distributions of probes (i.e., at rotation angle  $45^\circ$  and  $0^\circ$ ) have the same MTVS for PAS of uniform distribution, while different for PAS of Laplacian distribution.

**3.2. Effect of Elevation Angle of Probe Circle and ES on MTVS.** In this part, the effects of elevation angle of probe circle and ES on MTVS are investigated based on the original setup.

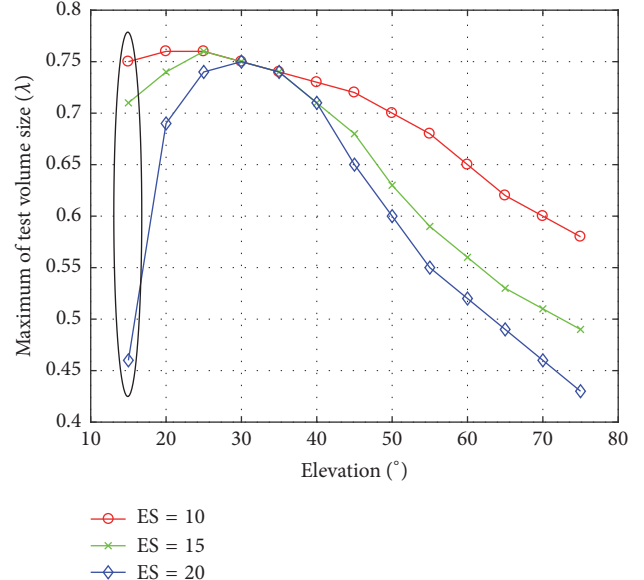


FIGURE 6: MTVS as a function of EPC with different values of ES for SPS scenario A.

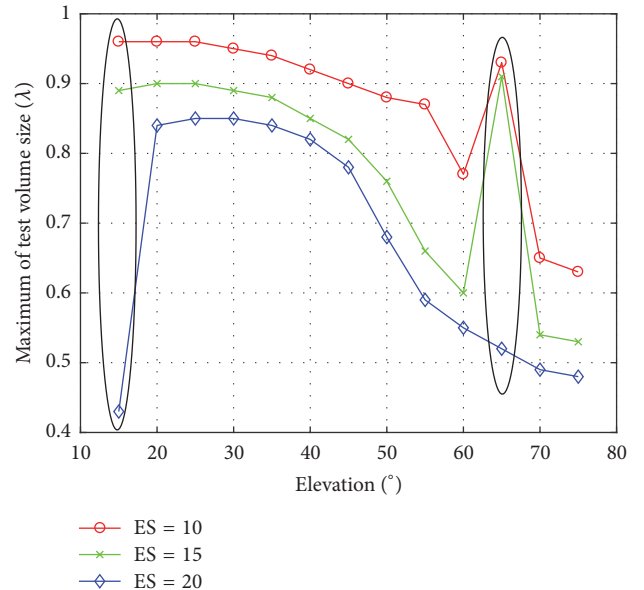


FIGURE 7: MTVS as a function of EPC with different values of ES for SPS scenario B.

The elevation angle of probe circle (EPC) investigated in this paper means the elevation angle of circle 3 mentioned in Section 3.1 where circle 1 and circle 3 are equidistant with regard to circle 2. Considering the practical spherical setup in the anechoic chamber, the EPC is selected from  $15^\circ$  to  $75^\circ$  with an interval of  $5^\circ$  for exploring the effect of EPC. In the practical SPS of 3D channel model, ES is selected from  $15^\circ$  to  $20^\circ$  with an interval of  $5^\circ$  to investigate the effect of ES. Figure 6 plots the MTVS as a function of EPC for SPS scenario A with different values of ES. For SPS scenario B, the MTVS with varying EPC is shown in Figure 7.

TABLE 2: The parameters of vector representing different test volume sizes for different number of probes.

Number of probes	Parameters of vector ( $\lambda$ )		
	$d_1$	$d_{\text{step}}$	$d_L$
8	0	0.1	1
12	0	0.3	1.5
16	0	0.2	2

Firstly, the effect of EPC on MTVS is investigated. Fixing  $ES = 10^\circ$ , varied EPCs lead to different MTVSs, as shown in Figures 6 and 7. For SPS scenario A, the function MTVS with  $15^\circ \leq EPC \leq 75^\circ$  has two same global maxima of  $0.76\lambda$  at  $EPC = 20^\circ$  and  $EPC = 25^\circ$ . For SPS scenario B, the function MTVS with  $15^\circ \leq EPC \leq 75^\circ$  has three same global maxima of  $0.96\lambda$  at  $EPC = 15^\circ$ ,  $EPC = 20^\circ$ , and  $EPC = 25^\circ$ . Hence, the optimal EPC for the largest MTVS can be found when azimuth angle of probe, the number of probes, and ES are given.

Then the influence of ES on MTVS is studied when fixing  $EPC = 30^\circ$ . The identical MTVS of  $0.75\lambda$  is obtained with three different values of ES for SPS scenario A from Figure 6. As shown in Figure 7, ES of  $10^\circ$  can achieve the largest MTVS of  $0.95\lambda$  among three different values of ES for SPS scenario B, while ES of  $20^\circ$  can obtain the smallest one. Hence, the optimal ES for the largest MTVS can be found when azimuth angle of probe, the number of probes, and EPC are given.

Finally, the effects of combining EPC and ES on MTVS are researched. For SPS scenario A, the effect of ES becomes more evident when EPC is not in an interval of  $[25^\circ, 40^\circ]$ . For instance, when setting  $EPC = 15^\circ$ , as highlighted in Figure 6, MTVS is  $0.75\lambda$  with  $ES = 10^\circ$ ,  $0.72\lambda$  with  $ES = 15^\circ$ , and  $0.46\lambda$  with  $ES = 20^\circ$ . However, three different values of ES have the same MTVS at  $EPC = 30^\circ$  and  $35^\circ$ . For SPS scenario B, the effect of ES is clear when EPC is  $15^\circ$  and  $65^\circ$ , as highlighted in Figure 7. When setting the EPC as  $15^\circ$ , MTVS is  $0.96\lambda$  with  $ES = 10^\circ$ ,  $0.89\lambda$  with  $ES = 15^\circ$ , and  $0.42\lambda$  with  $ES = 20^\circ$ . When considering EPC of  $65^\circ$ , MTVS is  $0.93\lambda$  with  $ES = 10^\circ$ ,  $0.91\lambda$  with  $ES = 15^\circ$ , and  $0.52\lambda$  with  $ES = 20^\circ$ . The function MTVS with  $ES = 10^\circ$  and the function MTVS with  $ES = 15^\circ$  both have a local maximum at  $EPC = 65^\circ$ .

Due to the effects of both EPC and ES on MTVS for two SPS scenarios, it can be found that the EPC for the largest MTVS increases as the value of ES increases. For SPS scenario A, the minimal EPC for the largest MTVS is  $10^\circ$  larger than ES for each ES. For SPS scenario B, the minimal EPC for the largest MTVS is  $5^\circ$  larger than ES for each ES. In addition, the MTVS decreases generally along with an augmentation of ES for different EPCs. Therefore, the optimal combination of EPC and ES for the largest MTVS can be acquired for each SPS scenario.

**3.3. Effect of Number of Probes on MTVS.** The effect of different number of probes in the flexible probe configuration on MTVS is investigated in this part where eight probes, twelve probes, and sixteen probes are considered, respectively. The parameters of vector  $\mathbf{d}$  representing variable test volume sizes for different number of probes are summarized in Table 2.

TABLE 3: Test cases considered for algorithm comparison.

Test case	PLOA	Algorithm parameters	
		Maximum number of iterations	Population size
A	GA	100	50
B	CSO	100	50
C	ICSO	100	50
D	CSO	200	100

TABLE 4: Statistics of the MTVS results for two SPS scenarios and test case A employing different number of probes.

Number of probes	MTVS ( $\lambda$ )	
	SPS scenario A	SPS scenario B
8	0.92	0.56
12	1.45	0.72
16	1.57	0.94

TABLE 5: Statistics of the MTVS results for SPS scenario A and the test cases A, B, and C employing different number of probes.

Number of probes	MTVS ( $\lambda$ )		
	Test case A	Test case B	Test case C
8	0.92	1.02	0.89
12	1.45	1.18	1.44
16	1.57	1.57	1.84

Four test cases of PLOA are considered in Table 3, which summarizes two parameters used in the PLOA except the other default parameters.

Considering the test case A firstly, the rms error of spatial correlation is presented as a function of test volume size for two SPS scenarios employing different number of probes that can be found from Figure 8. Fixing  $rms = 0.05$ , statistics of the MTVS results for different number of probes and SPS scenarios are summarized in Table 4. It can be seen that as the number of probes increases, so does the MTVS. In addition, compared with the MTVS results in the original setup with 16 probes, a larger MTVS can be obtained in the flexible probe configuration for SPS scenario A, while the MTVS is smaller for SPS scenario B. Therefore, the fixed probe configuration is more suitable for channel model with uniform distribution while the flexible probe configuration is more suitable for channel model with nonuniform distribution in terms of obtaining larger MTVSs.

Then considering SPS scenario A, three PLOAs are compared for different number of probes. Figure 9 presents the rms error of spatial correlation as a function of test volume size employing different number of probes for SPS scenario A and the test cases A, B, and C. The corresponding MTVS results are summarized in Table 5.

CSO can achieve a larger MTVS for eight probes and ICSO can obtain a larger MTVS for sixteen probes

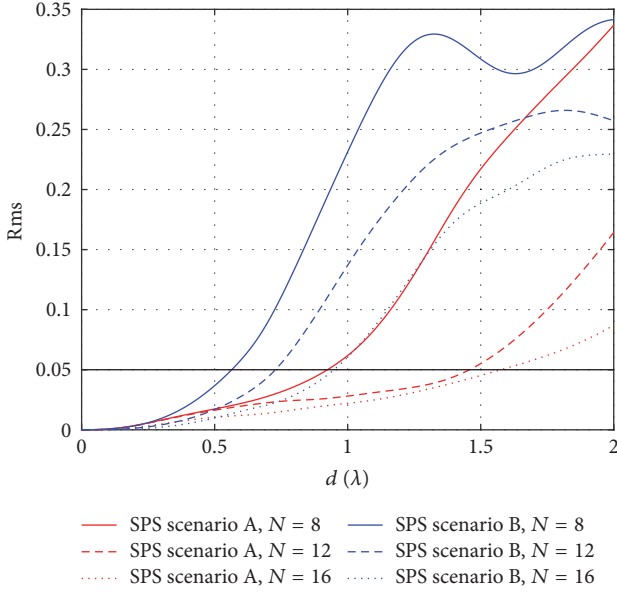


FIGURE 8: Rms error of spatial correlation as a function of test volume size  $d$  for two SPS scenarios and test case A employing different number of probes.

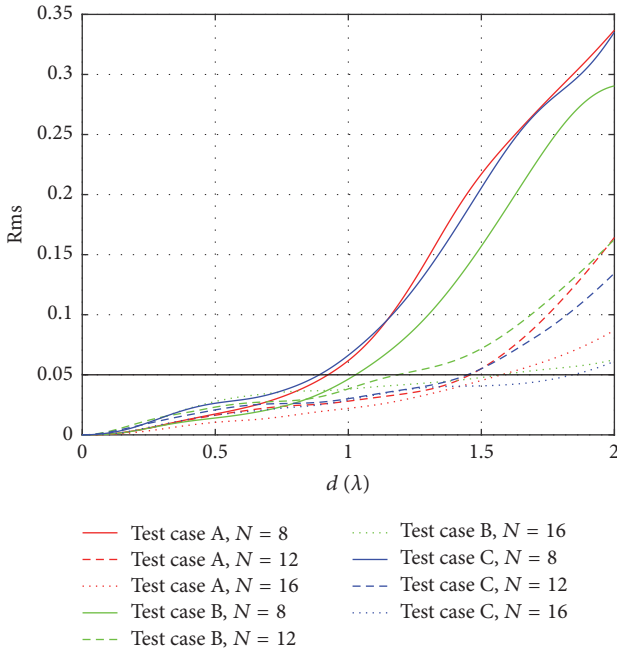


FIGURE 9: Rms error of spatial correlation as a function of test volume size employing different number of probes for SPS scenario A and the test cases A, B, and C.

because CSO is suitable for solving low-dimensional optimization problem while ICSO is appropriate for solving high-dimensional optimization problem.

Considering CSO finally, different maximum number of iterations and population size are compared for SPS scenario A employing different number of probes. Figure 10 presents the rms error of spatial correlation as a function of test volume

TABLE 6: Statistics of the MTVS results for SPS scenario A and the test cases B and D employing different number of probes.

Number of probes	MTVS ( $\lambda$ )	
	Test case B	Test case D
8	1.02	1
12	1.18	1.55
16	1.57	1.9

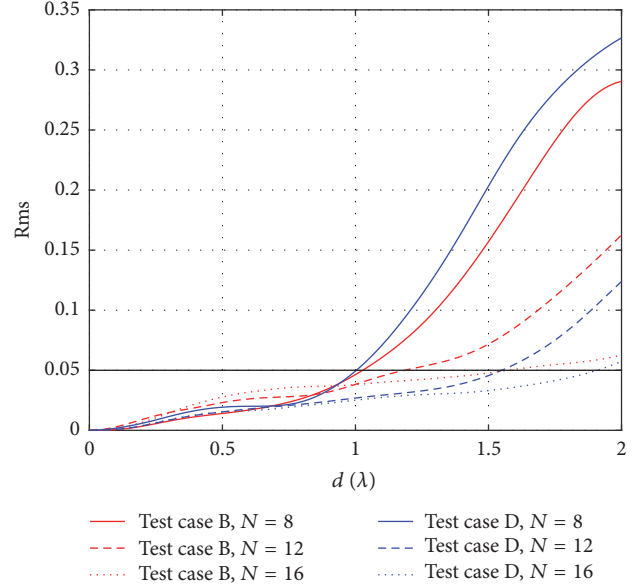


FIGURE 10: Rms error of spatial correlation as a function of test volume size employing different number of probes for SPS scenario A and the test cases B and D.

size employing different number of probes for SPS scenario A and the test cases B and D. The corresponding MTVS results are summarized in Table 6. It can be demonstrated that larger MTVSs can be obtained by increasing the maximum number of iterations and population size.

## 4. Conclusion

This paper presents a method to determine MTVS and investigates the impact of probe configurations on MTVS in order to obtain larger MTVSs. From the simulation results, it can be deduced that symmetrical configuration is optimal for larger MTVSs considering the effect of azimuth angle of probe on MTVS in the fixed probe configuration. Moreover, the optimal combination of EPC and ES for the largest MTVS can be found for each SPS scenario. In the flexible probe configuration, larger MTVSs can be obtained than those in the fixed probe configuration employing the same number of probes for PAS of nonuniform distribution. In addition, larger MTVSs can be achieved when more probes are employed with PLOA and convex optimization. It is obtained that the PLOA solving high-dimensional optimization problem is more suitable for a larger number of probes. The determination and increasing of MTVS are

meaningful to determine the maximum of DUT size for a given probe configuration and increase the MTVS for MIMO OTA testing.

## Conflicts of Interest

The authors declare that there are no conflicts of interest regarding the publication of this paper.

## Acknowledgments

This work was supported by the National Natural Science Foundations of China (no. 61327806 and no. 61701041) and by the National Key Basic Research Program of China (973 Program) (no. 2014CB339900).

## References

- [1] Y. Jing, Z. Wen, H. Kong, S. Duffy, and M. Rumney, "Two-stage over the air (OTA) test method for MIMO device performance evaluation," in *Proceedings of the 2011 IEEE International Symposium on Antennas and Propagation and USNC/URSI National Radio Science Meeting, APSURSI 2011*, pp. 71–74, Washington, DC, USA, June 2011.
- [2] P. K. Agyapong, M. Iwamura, D. Staehle, W. Kiess, and A. Benjebbour, "Design considerations for a 5G network architecture," *IEEE Communications Magazine*, vol. 52, no. 11, pp. 65–75, 2014.
- [3] "Verification of radiated multi-antenna reception performance of user equipment, 3GGP TR 37.977 V14.1.0," Sep. 2016.
- [4] M. Rumney, R. Pirkel, M. H. Landmann, and D. A. Sanchez-Hernandez, "MIMO over-the-air research, development, and testing," *International Journal of Antennas and Propagation*, vol. 2012, Article ID 467695, 2012.
- [5] Y. Okano, K. Kitao, and T. Imai, "Impact of number of probe antennas for MIMO OTA spatial channel emulator , in," in *Proceedings of the European Conference on Antennas and Propagation*, pp. 1–5, April 2010.
- [6] A. Khatun, T. Laitinen, V.-M. Kolmonen, and P. Vainikainen, "Dependence of error level on the number of probes in over-the-air multiprobe test systems," *International Journal of Antennas and Propagation*, vol. 2012, Article ID 624174, 6 pages, 2012.
- [7] L. Foged, A. Scannavini, N. Gross, and J. Estrada, "MIMO OTA testing using a multiprobe system approach," in *Proceedings of the European Conference on Antennas and Propagation*, pp. 1673–1677, Gothenburg, Sweden, April 2013.
- [8] W. Fan, P. Kyosti, S. Fan et al., "3D Channel Model Emulation in a MIMO OTA Setup," in *Proceedings of the 2013 IEEE 78th Vehicular Technology Conference (VTC Fall)*, pp. 1–5, Las Vegas, NV, USA, September 2013.
- [9] I. C. Llorente, W. Fan, and G. F. Pedersen, "Mimo ota testing in small multiprobe anechoic chamber setups," *IEEE Antennas and Wireless Propagation Letters*, vol. 15, pp. 1167–1170, 2016.
- [10] P. Kyosti and A. Khatun, "Probe configurations for 3D MIMO Over-the-Air testing," in *Proceedings of the 2013 7th European Conference on Antennas and Propagation, EuCAP 2013*, pp. 1421–1425, Gothenburg, Sweden, April 2013.
- [11] M. Belhabib, R. D'Errico, and B. Uguen, "Spatial correlation in spherical and cylindrical 3D MIMO Over-The-Air tests setups," in *Proceedings of the 10th European Conference on Antennas and Propagation, EuCAP 2016*, Davos, Switzerland, April 2016.
- [12] P. Kyösti, W. Fan, G. F. Pedersen, and M. Latva-Aho, "On dimensions of OTA setups for massive MIMO base stations radiated testing," *IEEE Access*, vol. 4, pp. 5971–5981, 2016.
- [13] W. Fan, X. Carreño, P. Kyösti, J. Ø. Nielsen, and G. F. Pedersen, "Over-the-air testing of MIMO-capable terminals: evaluation of multiple-antenna systems in realistic multipath propagation environments using an OTA method," *IEEE Vehicular Technology Magazine*, vol. 10, no. 2, pp. 38–46, 2015.
- [14] "Test Plan for 2x2 Downlink MIMO and Transmit Diversity Over-the-Air Performance," CTIA Certification, Tech. Rep. Version 1.1, 2016.
- [15] M. B. Knudsen and G. F. Pedersen, "Spherical outdoor to indoor power spectrum model at the mobile terminal," *IEEE Journal on Selected Areas in Communications*, vol. 20, no. 6, pp. 1156–1169, 2002.
- [16] R. Vaughan and J. Bach-Anderson, *Channels, Propagation and Antennas for Mobile Communications*, IET, London, UK, 2003.
- [17] S. Boyd and L. Vandenberghe, *Convex Optimization*, Cambridge University Press, Cambridge, UK, 2004.
- [18] H. Gao, W. Wang, Y. Wu, and Y. Liu, "3D Flexible Multi-probe Setups for MIMO OTA Testing," in *Proceedings of the 5th International Symposium on EMC*, Beijing, China, 2017.
- [19] R. L. Haupt and D. H. Werner, *Genetic Algorithms in Electromagnetics*, Wiley-IEEE Press, Hoboken, NJ, USA, 2007.
- [20] X. B. Meng, L. Yu, X. Z. Gao, and H. Z. Zhang, "A new bio-inspired algorithm: chicken swarm optimization," in *Advances in Swarm Intelligence*, vol. 8794 of *Lecture Notes in Computer Science*, pp. 86–94, Springer International, Brussels, Belgium, 2014.
- [21] D. Wu, F. Kong, W. Gao, Y. Shen, and Z. Ji, "Improved chicken swarm optimization," in *Proceedings of the 5th Annual IEEE International Conference on Cyber Technology in Automation, Control and Intelligent Systems, IEEE-CYBER 2015*, pp. 681–686, China, June 2015.